

THE MINISTRY OF EDUCATION AND SCIENCE OF THE RUSSIAN FEDERATION



**ST. PETERSBURG STATE  
POLYTECHNICAL UNIVERSITY  
JOURNAL**

---

---

Physics  
and Mathematics

---

---

**VOLUME 11, No. 1**  
**2018**

Polytechnical University Publishing House  
Saint Petersburg  
2018

# ST. PETERSBURG STATE POLYTECHNICAL UNIVERSITY JOURNAL. PHYSICS AND MATHEMATICS

## JOURNAL EDITORIAL COUNCIL

*Zh.I. Alferov* – full member of RAS, head of the editorial council;  
*A.I. Borovkov* – vice-rector for perspective projects;  
*V.A. Glukhikh* – full member of RAS;  
*D.A. Indeitsev* – corresponding member of RAS;  
*V.K. Ivanov* – Dr.Sc.(phys.-math.), prof.;  
*A.I. Rudskoy* – corresponding member of RAS, deputy head of the editorial council;  
*R.A. Suris* – full member of RAS;  
*D.A. Varshalovich* – full member of RAS;  
*A.E. Zhukov* – corresponding member of RAS, deputy head of the editorial council.

## JOURNAL EDITORIAL BOARD

*V.K. Ivanov* – Dr. Sc. (phys.-math.), prof., SPbPU, St. Petersburg, Russia, – editor-in-chief;  
*A.E. Fotiadi* – Dr. Sc. (phys.-math.), prof., SPbPU, St. Petersburg, Russia, – deputy editor-in-chief;  
*V.M. Kapralova* – Candidate of Phys.-Math. Sc., associate prof., SPbPU, St. Petersburg, Russia, – executive secretary;  
*V.I. Antonov* – Dr. Sc. (phys.-math.), prof., SPbPU, St. Petersburg, Russia;  
*I.B. Bezprozvanny* – Dr. Sc. (Biology), prof., The University of Texas Southwestern Medical Center, Dallas, TX, USA;  
*A.V. Blinov* – Dr. Sc. (phys.-math.), prof., SPbPU, St. Petersburg, Russia;  
*D.V. Donetski* – Dr. Sc. (phys.-math.), prof., State University of New York at Stony Brook, NY, USA;  
*D.A. Firsov* – Dr. Sc. (phys.-math.), prof., SPbPU, St. Petersburg, Russia;  
*A.S. Kheifets* – Ph.D., prof., Australian National University, Canberra, Australia.  
*J.B. Malherbe* – Dr. Sc. (Physics), prof., University of Pretoria, Republic of South Africa;  
*V.M. Ostryakov* – Dr. Sc. (phys.-math.), prof., SPbPU, St. Petersburg, Russia;  
*V.E. Privalov* – Dr. Sc. (phys.-math.), prof., SPbPU, St. Petersburg, Russia;  
*A.V. Solov'yov* – Dr. Sc. (phys.-math.), prof., MBN Research Center, Frankfurt am Main, Germany;  
*A.K. Tagantsev* – Dr. Sc. (phys.-math.), prof., Swiss Federal Institute of Technology, Lausanne, Switzerland;  
*I.N. Toptygin* – Dr. Sc. (phys.-math.), prof., SPbPU, St. Petersburg, Russia;  
*E.A. Tropp* – Dr. Sc. (phys.-math.), prof., SPbPU, St. Petersburg, Russia.

*The journal is published under the scientific and methodical guidance of RAS since 1995.*

The journal is included in the List of leading peer-reviewed scientific journals and other editions to publish major findings of theses for the research degrees of Doctor of Sciences and Candidate of Sciences.

The publications are presented in the VINITI RAS Abstract Journal and Ulrich's Periodical Directory International Database.

The journal is published since 2008 as part of the periodical edition 'Nauchno-tekhnicheskie vedomosti SPb-GPU'.

The journal is registered with the Federal Service for Supervision in the Sphere of Telecom, Information Technologies and Mass Communications (ROSKOMNADZOR). Certificate ПИ № ФС77-52144 issued December 11, 2012.

The journal is distributed through the CIS countries catalogue, the «Press of Russia» joint catalogue and the «Press by subscription» Internet catalogue. The subscription index is **71823**.

The journal is in the Russian Science Citation Index (RSCI) database.

© Scientific Electronic Library (<http://www.elibrary.ru>).

No part of this publication may be reproduced without clear reference to the source.

The views of the authors may not represent the views of the Editorial Board.

Address: 195251 Politekhnikeskaya St. 29, St. Petersburg, Russia.

Phone: (812) 294-22-85.

<http://ntv.spbstu.ru/physics>

© Peter the Great St. Petersburg Polytechnic University, 2018



# НАУЧНО-ТЕХНИЧЕСКИЕ ВЕДОМОСТИ

САНКТ-ПЕТЕРБУРГСКОГО ГОСУДАРСТВЕННОГО  
ПОЛИТЕХНИЧЕСКОГО УНИВЕРСИТЕТА

---

---

Физико-математические  
науки

---

---

**ТОМ 11, № 1**  
**2018**

**НАУЧНО-ТЕХНИЧЕСКИЕ ВЕДОМОСТИ САНКТ-ПЕТЕРБУРГСКОГО  
ГОСУДАРСТВЕННОГО ПОЛИТЕХНИЧЕСКОГО УНИВЕРСИТЕТА.  
ФИЗИКО-МАТЕМАТИЧЕСКИЕ НАУКИ**

**РЕДАКЦИОННЫЙ СОВЕТ ЖУРНАЛА**

Алферов Ж.И., академик РАН – председатель;  
Боровков А.И., проректор по перспективным проектам;  
Варшалович Д.А., академик РАН;  
Глухих В.А., академик РАН;  
Жуков А.Е., чл.-кор. РАН – зам. председателя;  
Иванов В.К., д-р физ.-мат. наук, профессор;  
Индейцев Д.А., чл.-кор. РАН;  
Рудской А.И., чл.-кор. РАН – зам. председателя;  
Сулис Р.А., академик РАН.

**РЕДАКЦИОННАЯ КОЛЛЕГИЯ ЖУРНАЛА**

Иванов В.К., д-р физ.-мат. наук, профессор, СПбПУ, СПб., Россия, – главный редактор;  
Фотиади А.Э., д-р физ.-мат. наук, профессор, СПбПУ, СПб., Россия, – зам. главного редактора;  
Каприлова В.М., канд. физ.-мат. наук, доцент, СПбПУ, СПб., Россия – ответственный секретарь;  
Антонов В.И., д-р физ.-мат. наук, профессор, СПбПУ, СПб., Россия;  
Безпрозванный И.Б., д-р биол. наук, профессор, Юго-Западный медицинский центр  
Техасского университета, Даллас, США;  
Блинов А.В., д-р физ.-мат. наук, профессор, СПбПУ, СПб., Россия;  
Донецкий Д.В., д-р физ.-мат. наук, профессор, университет штата Нью-Йорк в Стоуни-Брук, США;  
Малерб Й.Б., Dr.Sc. (Physics), профессор, университет Претории, ЮАР;  
Остряков В.М., д-р физ.-мат. наук, профессор, СПбПУ, СПб., Россия;  
Привалов В.Е., д-р физ.-мат. наук, профессор, СПбПУ, СПб., Россия;  
Соловьёв А.В., д-р физ.-мат. наук, профессор, Научно-исследовательский центр  
мезобионаносистем (MBN), Франкфурт-на-Майне, Германия;  
Таганцев А.К., д-р физ.-мат. наук, профессор, Швейцарский федеральный институт технологий,  
Лозанна, Швейцария;  
Топтыгин И.Н., д-р физ.-мат. наук, профессор, СПбПУ, СПб., Россия;  
Тропп Э.А., д-р физ.-мат. наук, профессор, СПбПУ, СПб., Россия;  
Фирсов Д.А., д-р физ.-мат. наук, профессор, СПбПУ, СПб., Россия.  
Хейфец А.С., Ph.D. (Physics), профессор, Австралийский национальный университет,  
Канберра, Австралия.

*Журнал с 1995 года издается под научно-методическим руководством Российской академии наук.*

Журнал с 2002 г. входит в Перечень ведущих рецензируемых научных журналов и изданий, в которых должны быть опубликованы основные результаты диссертаций на соискание ученых степеней доктора и кандидата наук.

Сведения о публикациях представлены в Реферативном журнале ВИНТИ РАН, в международной справочной системе «Ulrich's Periodical Directory».

С 2008 года выпускается в составе сериального периодического издания «Научно-технические ведомости СПбГПУ».

Журнал зарегистрирован Федеральной службой по надзору в сфере информационных технологий и массовых коммуникаций (Роскомнадзор). Свидетельство о регистрации ПИ № ФС77-52144 от 11 декабря 2012 г.

Распространяется по Каталогу стран СНГ, Объединенному каталогу «Пресса России» и по Интернет-каталогу «Пресса по подписке». Подписной индекс **71823**.

Журнал включен в базу данных «Российский индекс научного цитирования» (РИНЦ), размещенную на платформе Научной электронной библиотеки на сайте <http://www.elibrary.ru>

При перепечатке материалов ссылка на журнал обязательна.

Точка зрения редакции может не совпадать с мнением авторов статей.

Адрес редакции и издательства: Россия, 195251, Санкт-Петербург, ул. Политехническая, д. 29.  
Тел. редакции (812) 294-22-85.  
<http://ntv.spbstu.ru/physics>

© Санкт-Петербургский политехнический университет Петра Великого, 2018



## Contents

### Condensed matter physics

<b>Abrosimov A.S., Agarev V.N.</b> Numerical simulation of the resonance-tunnel structure based on the Schottky barrier and a GaAs/AlGaAs heterojunction .....	9
<b>Tregulov V.V., Stepanov V.A., Melnik N.N.</b> Properties of the semiconductor structure with a p-n-junction created in a porous silicon film under laser radiation .....	18
<b>Platko A.P., Sotova Yu.I., Gorokhovatskiy Yu.A., Karulina E.A., Galikhanov M.F.</b> Electret effect in biodecomposed polylactide films filled with nanoscale magnesia .....	26
<b>Zhukov N.N., Marchenko A.V., Shakhovich K.B.</b> Mössbauer emission spectra of stannum daughter isotopes measured under condition of a dynamic radioactive equilibrium of tellurium parent isotopes and antimony daughter ones .....	34
<b>Klinkov V.A.</b> Spectral and luminescent properties of doped fluoroaluminate glasses promising for optical temperature sensors .....	44

### Simulation of physical processes

<b>Isaenko I.I., Makhnov A.V., Smirnov E.M., Schmidt A.A.</b> Simulation of high-speed cavitating flows in channels.....	55
<b>Chulyaeva E.G., Kuznetsov S.N., Ognev B.I.</b> The concept of building a wireless optical communication network between surface ships.....	66
<b>Chumakov Yu.S., Levchenya A.M., Malah H.</b> The vortex structure formation around a circular cylinder placed on a vertical heated plate .....	73
<b>Bykov N.Yu.</b> On simulation of cluster formation process under water vapor spherical expansion into vacuum .....	86

### Physical materials technology

<b>Mamontov A.I., Petrakov A.P., Zimin S.P.</b> Porosity and surface morphology of lead selenide – tin selenide layers on silicon substrates: X-ray diffraction studies .....	102
<b>Khripunov A.K., Stepanova T.P., Saprykina N.N., Astapenko E.P., Romanov D.P., Tkachenko A.A., Kapralova V.M.</b> Morphology of dried nanogel films of bacterial cellulose impregnated with the silver nitrate solution .....	112

### Nuclear physics

<b>Basalaev A.E., Naryshkin Yu.G.</b> Dark matter searches at the Large Hadron Collider .....	122
---	-----

### Radiophysics

<b>Cherepanov A.S.</b> Electromagnetic wave propagation in the three-layer ferrite-dielectric structure .....	138
---	-----

**Theoretical physics**

<b>Gorobey N.N., Lukyanenko A.S.</b> <i>Quantization of the energy density in a closed universe</i> .....	147
---	-----

**Mechanics**

<b>Belyaev A.K., Shurpatov A.O., Ma Ch.-Ch.</b> <i>Determining the contact force of an axial collision of an elastic rod with a rigid impactor</i> .....	157
--	-----

<i>Author index</i> .....	167
---------------------------	-----

## Содержание

### Физика конденсированного состояния

<b>Абросимов А.С., Агарев В.Н.</b> Численное моделирование резонансно-туннельных структур на основе барьера Шоттки и гетероперехода GaAs/AlGaAs .....	9
<b>Трегулов В.В., Степанов В.А., Мельник Н.Н.</b> Свойства полупроводниковой структуры с p–n-переходом, сформированной в пленке пористого кремния под действием лазерного излучения (статья на английском языке) .....	18
<b>Платко А.П., Сотова Ю.И., Гороховатский Ю.А., Карулина Е.А., Галиханов М.Ф.</b> Электретный эффект в биоразлагаемых полимерных пленках полилактида с наноразмерным оксидом магния в качестве наполнителя .....	26
<b>Жуков Н.Н., Марченко А.В., Шахович К.Б.</b> Эмиссионные мёссбауэровские спектры дочерних атомов олова, измеренные в условиях подвижного радиоактивного равновесия материнских изотопов теллура с дочерними изотопами сурьмы .....	34
<b>Клинков В.А.</b> Спектрально-люминесцентные свойства активированных фторалюминатных стекол, перспективных для создания оптических температурных сенсоров .....	44

### Математическое моделирование физических процессов

<b>Исаенко И.И., Махнов А.В., Смирнов Е.М., Шмидт А.А.</b> Моделирование кавитации в высокоскоростных течениях в каналах .....	55
<b>Чуляева Е.Г., Кузнецов С.Н., Огнев Б.И.</b> Концепция построения сети беспроводной оптической связи между надводными кораблями .....	66
<b>Чумаков Ю.С., Левченя А.М., Малах Х.</b> Формирование вихревой структуры в окрестности стыка кругового цилиндра с вертикальной нагретой поверхностью .....	73
<b>Быков Н.Ю.</b> О моделировании процесса образования кластеров при сферическом расширении водяного пара в вакуум .....	86

### Физическое материаловедение

<b>Мамонтов А.И., Петраков А.П., Зимин С.П.</b> Пористость и морфология поверхности слоев селенида свинца – селенида олова на кремниевых подложках по данным рентгено-дифракционных исследований .....	102
<b>Хрипунов А.К., Степанова Т.П., Сапрыкина Н.Н., Астапенко Э.П., Романов Д.П., Ткаченко А.А., Капралова В.М.</b> Морфология высушенных наногель-пленок бактериальной целлюлозы, пропитанных раствором нитрата серебра .....	112

### Ядерная физика

<b>Басалаев А.Е., Нарышкин Ю.Г.</b> Поиски частиц темной материи на Большом адронном коллайдере .....	122
---	-----

### Радиофизика

<b>Черепанов А.С.</b> Распространение электромагнитных волн в трехслойной феррит-диэлектрической структуре .....	138
--	-----

**Теоретическая физика**

<b>Горобей Н.Н., Лукьяненко А.С.</b> <i>Квантование плотности энергии в замкнутой Вселенной .....</i>	147
---	-----

**Механика**

<b>Беляев А.К., Шурпатов А.О., Ма Ч.-Ч.</b> <i>Определение контактной силы осевого соударения упругого стержня и недеформируемого ударника.....</i>	157
---	-----

<i>Авторский указатель .....</i>	167
----------------------------------	-----

## NUMERICAL SIMULATION OF THE RESONANCE-TUNNEL STRUCTURE BASED ON THE SCHOTTKY BARRIER AND A GaAs/AlGaAs HETEROJUNCTION

**A.S. Abrosimov, V.N. Agarev**

Lobachevsky State University of Nizhny Novgorod,  
Nizhny Novgorod, Russian Federation

The resonance tunneling diode has been widely studied because of its importance in the field of nanoelectronic technology and its potential applications in very high speed/functionality devices and circuits. Even though much progress has been made in this regard, the most popular structure of these diodes consists of barriers created by heterojunctions only. In this paper, we present numerical simulation results for a two-barrier resonance-tunnel structure consisting of the Schottky barrier and a GaAs/AlGaAs heterojunction. We considered its potential application to the resonance-tunnel diodes working at room temperature. The configuration of this structure was optimized using numerical simulation methods. A current voltage characteristic was simulated by the example of the optimized structure, and the influence of the thermal current on the obtained dependence was analyzed.

**Key words:** numerical simulation; resonance-tunnel structure; Schottky barrier; heterojunction

**Citation:** A.S. Abrosimov, V.N. Agarev, Numerical simulation of the resonance-tunnel structure based on the Schottky barrier and a GaAs/AlGaAs heterojunction, St. Petersburg Polytechnical State University Journal. Physics and Mathematics. 11 (1) (2018) 5 – 12. DOI: 10.18721/JPM.11101

### Introduction

Resonant tunneling diodes based on nanoscale semiconductor heterostructures have an  $N$ -shaped current-voltage characteristic ( $I$ – $V$  curve) with a negative differential resistance region and short response times of the tunneling process (lasting on the order of  $10^{-13}$  s). For this reason, these diodes show great potential for applications in high-speed terahertz devices and digital devices with switching times on the order of  $10^{-12}$  s or less. Iogansen was the first to propose using the effect of resonant electron tunneling in layered thin-film metal–insulator structures for creating electronic interferometers, thin-film diodes, triodes, etc. [1 – 3].

### Investigation of resonant tunneling structures

Ref. [4] studied the  $I$ – $V$  curve of an  $\text{Al}_{1-x}\text{Ga}_x\text{As}/\text{GaAs}/\text{Al}_{1-x}\text{Ga}_x\text{As}$  structure with

different barrier thickness to quantum well ratios. Resonant current was observed only at low temperatures (77 K and below) for all structures under consideration; all effects associated with tunneling disappeared at room temperature. The authors explained this by thermal smearing of the local levels in the quantum well and by a low barrier which electrons whose energies are relatively high energies for room temperature pass through easily.

On the other hand, a decrease in temperature to 4.2 K does not lead to the expected ‘sharpened’ tunneling, which is probably due to scattering by structural fluctuations and impurities; this scattering also results in a broadening of the local levels.

A current peak caused by the resonant tunneling effect is observed on the  $I$ – $V$  curve at 77 K, while the curve’s simulated shape agrees with the experimental one. This feature disappears at room temperature.

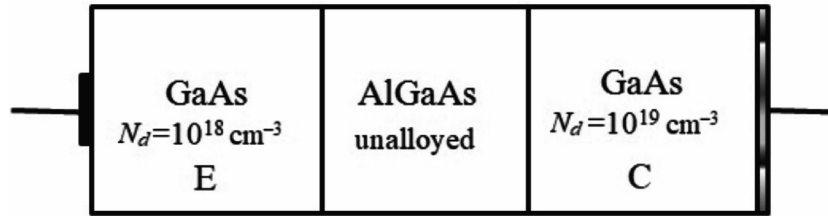


Fig. 1. Schematic of a resonant tunneling structure  
GaAs collector metal (Schottky barrier); GaAs/AlGaAs heterojunction (the second barrier);  
E and C are the emitter and the collector, respectively

Four factors influence the magnitude of the tunneling current [5]: the thickness of the barrier, the width of the well, the height of the barrier and the concentration of impurities in the contact region. While the first three factors determine the height of the peak and the behavior of the dependence of the transparency coefficient on the electron energy, the fourth one determines the energy distribution of these electrons at the input to the two-barrier structure.

The  $I$ – $V$  curve of a resonant-tunnel diode is also affected by its material. For example, the height of the  $i_{\max}$  peak for InAlAs/InGaAs structures is almost an order of magnitude higher than for AlAs/GaAs, with approximately the same  $i_{\max}/i_{\min}$  ratio [6]. Multi-barrier structures have also yielded good results. The electron energies in such a system containing a sequence of monotonically narrowing quantum wells are the same at equivalent levels of all wells [7]. This is achieved by tailoring the widths of the wells so that the value of the potential difference applied to the structure is equal to the height difference between the ground level of the narrowest quantum well and the Fermi level.

A sharp resonance peak is observed on the  $I$ – $V$  curve of the structure at sufficiently low barrier permeability, when level splitting due to overlapping of electron wavefunctions in adjacent wells is small. This peak is formed by electrons whose energy lies in a narrow range near the ground state energy of the narrowest quantum well.

### Simulation procedure

In this paper, we have investigated a two-barrier resonant tunneling structure where the Schottky barrier, which is natural for metal–

gallium arsenide (GaAs) contact and caused by surface states, is necessarily present (Fig. 1). Its height for various metals is about 0.8 eV [8].

The second barrier is a GaAs/AlGaAs heterojunction, which can have different heights (depending on the aluminum fraction). The thickness of the AlGaAs layer responsible for the heterojunction barrier width is also varied.

We assumed that the carrier density  $n$  reached  $10^{19} \text{ cm}^{-3}$  for the simulated structure. The Schottky barrier with such an impurity concentration has the smallest thickness, and this concentration is technologically obtained with the least number of implantation defects.

Within our model, the region of the Schottky barrier is a depleted layer, so the distribution of external potential is assumed to be linear, with its maximum at the point  $x = 0$ , and its zero at the metal–semiconductor interface (Fig. 2). The external voltage falls between the Schottky barrier (this is a metal–GaAs transition, which is a collector) and the heavily doped GaAs region which serves as the second contact. The structure's emitter is located on the left, on the side of the heterojunction barrier, and the collector is on the right, the side of the Schottky barrier (see Fig. 1).

In practice, it is possible to create resonant tunneling diodes with heterojunction barrier heights up to 0.4 eV. This limit is due to recombination centers emerging in a semiconductor, and, as a consequence, high noise on the  $I$ – $V$  curve of the structure.

In this study we have analyzed resonant tunneling structures with barrier heights from 0.3 to 0.4 eV. The current in these structures was calculated as created by electrons moving from the emitter to the collector [5]; as a result, its density followed the expression

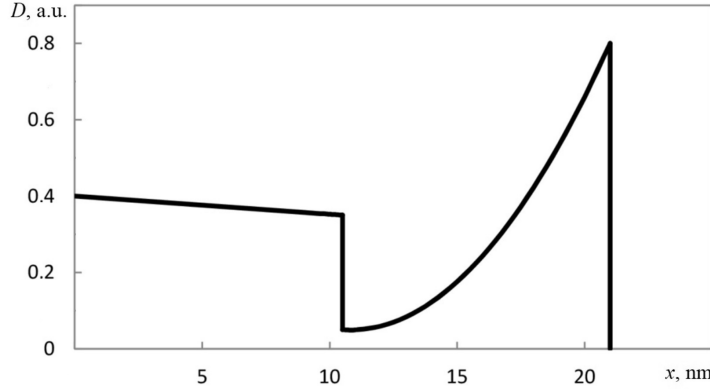


Fig. 2. The energy diagram of the structure with an external voltage of 0.1 V applied

$$j = \frac{em^*k_B T}{2\pi^2\hbar^3} \int_0^\infty D(E) \times \ln \left[ 1 + \exp \left( \frac{E_F - E}{k_B T} \right) \right] dE - \frac{em^*k_B T}{2\pi^2\hbar^3} \int_0^\infty D(E) \times \ln \left[ 1 + \exp \left( \frac{E_F - E - eV}{k_B T} \right) \right] dE, \quad (1)$$

where  $E$  is the energy;  $V$  is the voltage applied to the structure;  $D(E)$  is the transmission coefficient;  $E_F$  is the energy of the Fermi level;  $T$  is the temperature;

$k_B$  is the Boltzmann constant;  $e$  and  $m^*$  the electron charge and effective mass.

The  $E_F$  value is determined from the solution of the electroneutrality equation

$$\frac{N_d}{1 + \beta^{-1} \exp \left( \frac{E_F - E_d}{k_B T} \right)} = N_c F_{1/2} \left( \frac{E_F}{k_B T} \right), \quad (2)$$

where  $\beta$  is the spin degeneracy factor ( $\beta = 1/2$ );  $N_d$  is the donor impurity concentration ( $N_d = 10^{19} \text{ cm}^{-3}$  in the present study, it is taken for the GaAs layer adjacent to the Schottky barrier);  $N_c$  is the effective density of states in the conduction band;  $F_{1/2}$  is the Fermi integral with the index  $1/2$ ;  $E_d$  is the energy of the donor level.

The donor level in gallium arsenide is created by silicon with a depth of  $-6 \text{ meV}$  relative to the bottom of the conduction band. We obtained the  $D(E)$  dependence by the method

proposed in [9], by solving the Schrödinger equation in the one-electron approximation without scattering effects taken into account.

Let the two-barrier structure be located at distances from 0 to  $L$ ; then the wave function is taken from the Schrödinger equation:

$$\psi'' + \frac{2m^*}{\hbar^2} (E - U(x))\psi = 0, \quad (3)$$

where  $m^*$  is the effective electron mass (for simplicity, it is assumed to be the same in the entire region under consideration).

The solution of the equation in the outer regions are functions of the following form:

$$\begin{aligned} x \leq 0, \quad \psi &= e^{ikx} + re^{-ikx}; \\ x \geq L, \quad \psi &= de^{ik(x-L)}, \end{aligned} \quad (4)$$

where  $r$  and  $d$  are the amplitudes of reflection and transmission, respectively;  $k$  is the wave vector magnitude.

The reflection and transmission coefficients follow the expression

$$R = |r|^2, \quad D = |d|^2, \quad (5)$$

The boundary conditions are obtained from functions (4):

$$\begin{aligned} \psi(0) &= 1 + r, \quad \psi(L) = d, \\ \psi'(0) &= ik(1 - r), \quad \psi'(L) = ikd. \end{aligned} \quad (6)$$

Let us express the amplitudes  $r$  and  $d$  through functions  $\psi(0)$  and  $\psi(L)$ ; the boundary conditions can be then written as

$$\begin{aligned} \psi'(0) + ik\psi(0) &= 2ik, \\ \psi'(L) - ik\psi(L) &= 0. \end{aligned} \quad (7)$$



Equation (3) together with conditions (7) determine the problem in the inner region at distances from 0 to  $L$ . Solving this problem and finding  $\psi(x)$ , we can find the reflection and transmission coefficients in the following form:

$$D = |d|^2 = |\psi(L)|^2, R = |r|^2 = |\psi(0) - 1|^2. \quad (8)$$

Let us take the structure's total length  $L$  for unity, then the Schrödinger equation takes the form

$$\psi'' + (\varepsilon - U(x))\psi = 0, \quad (9)$$

where the energy  $\varepsilon$  and the potential  $U(x)$  are counted in units  $\hbar^2 / 2mL^2$ .

Let us divide the section from 0 to  $L$  into  $N$  regions of length  $a$ . Then  $L = Na$ ; if  $L = 1$ , then  $a = 1/N$ .

For an arbitrary point inside the region, equation (9) can be written in a discrete form:

$$\psi_{n+1} + \psi_{n-1} + \varepsilon_n \psi_n = 0, \quad (10)$$

$$\varepsilon_n = -2 + a^2(\varepsilon - V_n). \quad (11)$$

For the first of boundary conditions (7), let us replace the wave function derivative with its discrete equivalent

$$\psi'(0) \approx (\psi_1 - \psi_{-1}) / 2a.$$

Then the boundary condition and the Schrödinger equation for  $x = 0$  have the form

$$\psi_1 - \psi_{-1} + 2ika\psi_0 = 4ika, \quad (12)$$

$$\psi_1 - \psi_{-1} + \varepsilon_0\psi_0 = 0.$$

Adding up the two equations of (12) and dividing this sum by 2, we obtain the first boundary condition:

$$\psi_1 + \left( \frac{\varepsilon_0}{2} + ika \right) \psi_0 = 2ika. \quad (13)$$

For the second boundary condition ( $x = N$ ), we similarly find:

$$\psi_{N+1} - \psi_{N-1} - 2ika\psi_N = 0, \quad (14)$$

$$\psi_{N+1} - \psi_{N-1} + \varepsilon_N\psi_N = 0,$$

and from this we obtain this condition in the form

$$\psi_{N-1} + \left( \frac{\varepsilon_N}{2} + ika \right) \psi_N = 0. \quad (15)$$

Thus, the problem consists in solving the

system of equations (10), (13), and (15).

The tridiagonal system of equations (10) is solved by the modified sweep method [10].

## Results and discussion

At the first stage of the simulation, the resonant tunneling structure was optimized based on the transmission coefficient  $D(E)$  depending on the width and height of the GaAs/AlGaAs heterojunction barrier; we selected the geometric parameters (height and width) of this barrier with which the transmission coefficient took the greatest value, at least 70 %.

An example of the simulation result is shown in Fig. 3. Notice that the barriers in this structure are rather wide (up to 11 nm) and the width of the peaks on the  $D(E)$  dependence does not exceed several tens of millielectronvolts (specifically, it was varied from 0.01 to 20 meV). The  $D(E)$  dependences we have obtained did not take into account the scattering effects in solving the Schrödinger equation in the one-electron approximation with the help of the above-described numerical method.

The highest transmission coefficients were observed in structures with Schottky barrier heights of 0.30 – 0.35 eV and widths of 6 – 9 nm. The transmission coefficient was more than 95 % in some of these structures. Additionally, resonant tunneling with peaks of 10 % or higher was observed for all configurations of the heterojunction barrier.

Fig. 4 shows examples of the dependence of the maximum value of the transmission coefficient on the external voltage with varying barrier width (from 6 to 11 nm) and fixed barrier height (0.4 eV). As the width of the barrier decreased, the height of the peaks increased; the form of the dependence changed from decreasing at the maximum width to increasing (up to the value of the transmission coefficient over 90 %).

An examination of the selected models of resonant tunneling structures revealed that the transmission coefficient value depends more on the height of the heterojunction barrier than on its width. The transmission coefficient values determine the simulated behavior of the  $I$ – $V$  curve of the resonant tunneling diode (see Eq. (1)); however, while analysis of these coefficients is important, it does provide a

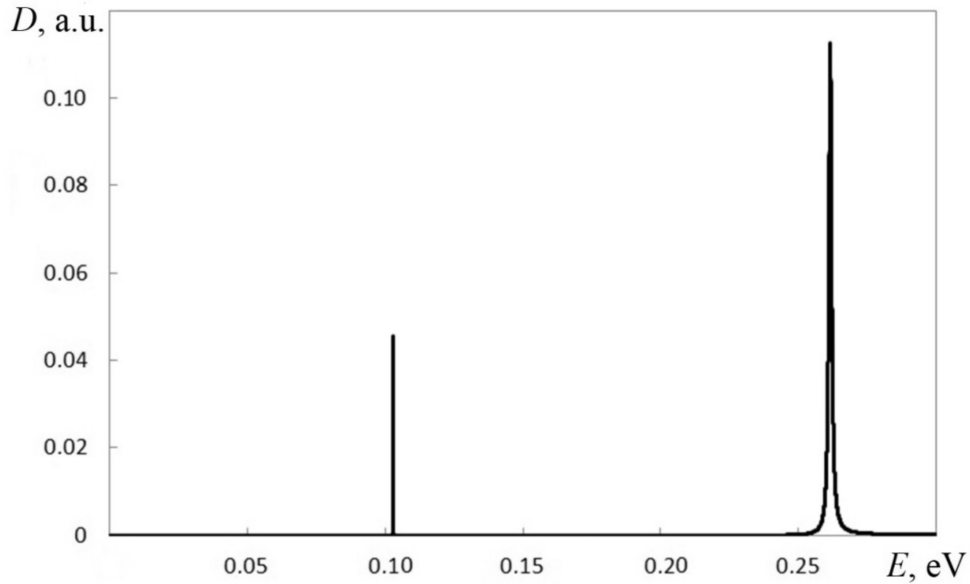


Fig. 3. Transmission coefficient versus energy with a heterojunction barrier width of 6 nm and height of 0.3 eV (the result of simulation)

complete picture of the optimization. For this reason, we also simulated the  $I$ – $V$  curves of these structures at two temperatures: 100 and 300 K.

Fig. 5 shows the  $I$ – $V$  curves of a resonant tunneling structure with a barrier height of 0.3 eV and a thickness of 6 nm; the highest and broadest current peak is observed at these

parameters. The calculated  $I$ – $V$  curves were obtained at 100 and 300 K.

It can be seen from the dependences that the current density peak reaches a value that is acceptable for experimental observation (up to  $10^8$  A/m<sup>2</sup>) at 300 K. The current density for the resonant tunneling structures under

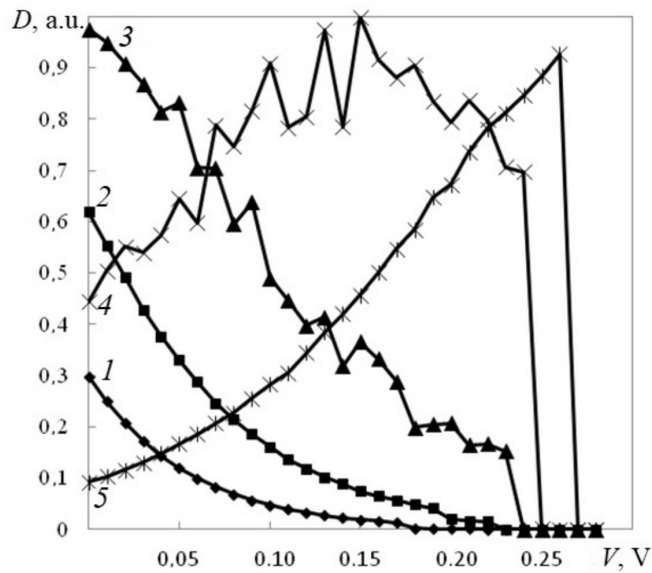


Fig. 4. Dependences of the maximum transmission coefficient on the external voltage with a variation in the heterojunction barrier width, nm: 11 (curve 1), 10 (2), 9 (3), 7 (4), 6 (5); barrier width was 0.4 eV

consideration has two components at nonzero temperatures, the thermal and the tunneling one. The tunneling current has been discussed above, and the thermal current is expressed by the following formula:

$$j_{therm} = ne \left( \frac{k_B T}{2\pi m^*} \right)^{1/2} \exp \left( -\frac{e\phi}{k_B T} \right) \times \left( \exp \left( \frac{eV}{k_B T} \right) - 1 \right). \quad (16)$$

As a result, the current density  $J$  is expressed by the sum

$$J = j_{therm} + j_{tunnel} \quad (17)$$

where  $j_{tunnel}$  is the tunneling current density (1).

Due to the high Schottky barrier

( $\phi = 0.8$  eV), the thermal current injected through it is extremely small compared to the tunneling current. The thermal component at room temperature (300 K) is two orders of magnitude lower than the tunneling one.

The  $I$ – $V$  curves shown in Fig. 5 were obtained without taking into account the effects of electron scattering. The main contribution to the current is made by resonant tunneling through the second level (see Fig. 3), for which the transmission coefficient peak is much wider and higher.

However, electron scattering in doped gallium arsenide can significantly affect the values of the transmission coefficient and current. This effect can be estimated by assuming that the transmission coefficient peak is described by the Lorentz formula [11]:

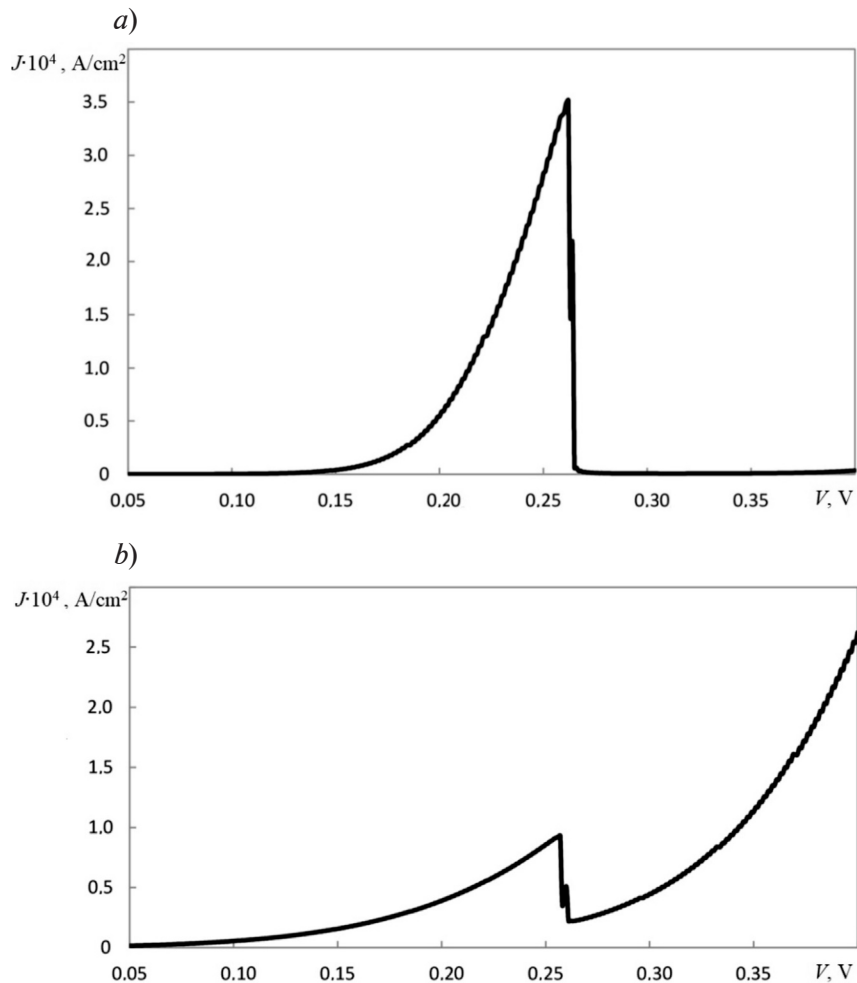


Fig. 5.  $I$ – $V$  curve of a resonant tunneling structure with the heterojunction barrier width of 6 nm and the height of 0.3 eV at temperatures of 100 K (a) and 300 K (b)



$$D(E) = \frac{4D_1D_2}{(D_1 + D_2)^2} \frac{\Delta E_b^2}{\Delta E_t^2 + 4(E - E_p)^2}, \quad (18)$$

where  $D_1$  and  $D_2$  are the coefficients of transmission through the first and the second barrier;  $\Delta E_t$  is the total width of the peak;  $\Delta E_b$  is the peak width without taking into account the scattering processes,  $E_p$  is the position of the maximum peak value.

The full width of the peak

$$\Delta E_t = \Delta E_b + \Delta E_r,$$

where  $\Delta E_r$  is the width of the peak caused by relaxation processes;  $\Delta E_r = \hbar / \tau_r$  ( $\tau_r$  is the momentum relaxation time).

If we assume that electron mobility in doped gallium arsenide is  $\mu = 0.4 \text{ m}^2/(\text{V}\cdot\text{s})$  at 300 K, then  $\tau_r = 1.5 \cdot 10^{-13}$ ,  $\Delta E_r = 4.4 \text{ meV}$ .

Thus, the influence of scattering processes manifests in a decrease in the height of the transmission coefficient peak by 4.4 times and in its broadening by 2.1 times. This should lead to a significant decrease in the tunneling current (current should decrease due to a decrease in the height of the resonant peak, but this decrease should be partially compensated by its broadening).

To estimate the effect of scattering on negative differential conductivity (NDC), we can assume that its maximum value  $g_{\max}$  is proportional to the ratio  $\Delta E_b^2 / \Delta E_t^2$ , and then  $g_{\max}$  will decrease by 4.4 times.

The above estimates prove that the effect of scattering in the structure under consideration reduces the peak current on the  $I$ - $V$  curve by several times and expands the NDC region, making the current decay slower compared with the  $I$ - $V$  curve in Fig. 5

However, NDC at normal temperature and the simplified technology (compared with a two-barrier heterostructure) are still important for practical applications, in comparison with a two-barrier heterostructure.

## Conclusion

The paper presents the results of numerical simulation of promising resonant tunneling structures. We have established that tunneling effects in these structures persist at high temperatures up to room temperature, while the position and shape of the current density peak change with the configuration, i. e., the height and width of the GaAs/AlGaAs barrier of the resonant tunneling structure.

## REFERENCES

- [1] **L.V. Iogansen**, The possibility of resonance transmission of electrons in crystals through a system of barriers, JETP. 18 (1) (1964) 146–150.
- [2] **L.V. Iogansen**, Resonance tunneling of electrons in crystals, JETP. 20 (1) (1965) 180–185.
- [3] **L.V. Iogansen**, Thin-film electron interferometers, Physics-Uspekhi. 8 (3) (1965) 413–416.
- [4] **L.L. Chang, L. Esaki, R. Tsu**, Resonant tunneling in semiconductor double barriers, Appl. Phys. Lett. 24 (12) (1974) 593–595.
- [5] **V.P. Dragunov, I.G. Neizvestnyy, V.A. Gridchin**, Osnovy nanoelektroniki [Nanoelectronics fundamentals]. Novosibirsk: Izd-vo NGTU, 2000.
- [6] **E.V. Buzaneva**, Mikrostruktury integralnoy elektroniki [Microstructures of integrated electronics], Moscow, Radio i svyaz, 1990.
- [7] **M. Cahoy, M. McLennan, S. Datta, M.S. Lundstrom**, Importance of space-charge effects in resonant tunneling devices, Appl. Phys. Lett. 50 (10) (1987) 612–614.
- [8] **R. Irsigler, R. Geppert, R. Goppert, J. Ludwig, M. Rogalla, K. Runge, Th. Schmidt, M. Weber**, Influence of contacts and substrate on semi-insulating GaAs detectors, Nucl. Instrum. Meth. Phys. A. 395 (1) (1997) 71–75.
- [9] **A.M. Satanin**, Chislennyye metody v nanofizike [Numerical methods in nanophysics], Nizhni Novgorod, Izd-vo Nizhegorodskogo gosuniversiteta, 2006.
- [10] **T.Y. Na**, Computational methods in engineering boundary value problems, New York, London, Academic Press, 1979.
- [11] **V.Ya. Demikhovskiy, G.A. Vugalter**, Fizika kvantovykh nizkorazmernykh struktur [Physics of quantum low-dimensional structures], Moscow, Logos, 2000.

Received 18.06.2016, accepted 24.10.2017.

#### THE AUTHORS

**ABROSIMOV Alexander S.**

*Lobachevsky State University of Nizhny Novgorod*

23, Gagarin Ave., Nizhny Novgorod, 603950, Russian Federation

MANOWAR89@mail.ru

**AGAREV Vladimir N.**

*Lobachevsky State University of Nizhny Novgorod*

23, Gagarin Ave., Nizhny Novgorod, 603950, Russian Federation

agarev\_v\_n@mail.ru



## PROPERTIES OF THE SEMICONDUCTOR STRUCTURE WITH A $p$ - $n$ -JUNCTION CREATED IN A POROUS SILICON FILM UNDER LASER RADIATION

V.V. Tregulov<sup>1</sup>, V.A. Stepanov<sup>1</sup>, N.N. Melnik<sup>2</sup>

<sup>1</sup>Ryazan State University named for S.A. Yesenin, Ryazan, Russian Federation;

<sup>2</sup>Lebedev Physical Institute, Russian Academy of Science, Moscow, Russian Federation

The possibility of formation of a  $p$ - $n$ -junction in a film of porous silicon by means of pulse laser radiation have been shown. Methods of Raman spectroscopy and photoluminescence spectroscopy were used to investigate features of transformation of a microstructure of a film of porous silicon under the influence of laser radiation. It was established that influence of a single laser impulse lasting 18 ns with the wavelength of 355 nanometers and energy of an impulse in the range of 85 – 200 mJ lead to disappearance of an amorphized phase and an increase in the sizes of crystallites in a film of porous silicon. In the paper it was shown that the  $p$ - $n$ -junction was formed under the influence of laser radiation inside the largest silicon crystallites of a porous silicon film. To study the features of the electrophysical characteristics of the obtained semiconductor structure, methods for measuring the current-voltage and the capacitance-voltage characteristics were used. The obtained  $p$ - $n$ -junction was sharp. The mechanisms of current flow had a complex character and were mainly determined by the processes of generation and recombination of carriers in the space-charge region of the  $p$ - $n$ -junction involving the energy levels of the traps.

**Key words:** porous silicon film;  $p$ - $n$ -junction, laser radiation; Raman scattering; photoluminescence

**Citation:** V.V. Tregulov, V.A. Stepanov, N.N. Melnik, Properties of the semiconductor structure with a  $p$ - $n$ -junction created in a porous silicon film under laser radiation, St. Petersburg Polytechnical State University Journal. Physics and Mathematics. 11 (1) (2018) 13 – 18. DOI: 10.18721/JPM.11102

### Introduction

Silicon photo diodes with nanosecond speed can be created on the basis of a heterojunction between a por-Si film and a single crystal [2]. Currently, developing methods for fabricating semiconductor structures with por-Si films for improving the technical and economic characteristics of semiconductor devices created on the basis of these films is an important problem.

Some properties of a semiconductor structure with a  $p$ - $n$ -junction created in a por-Si film under laser radiation have been investigated in this study. This film contained phosphorus impurity. The por-Si film was saturated by phosphorus during its growth [3]. This method allows reducing the number of technological operations in comparison with the traditional technological scheme [1], and decreases the prime cost of the end products which is very important for production of photo-electric converters of solar energy. Using a laser beam scanning on a substrate surface, it is possible

to form a  $p$ - $n$ -junction with a rather complex topology without resorting to photolithography. It should be noted that the possibility of forming a  $p$ - $n$ -junction in silicon under laser radiation was shown in the monograph [4].

### Experimental samples

The semiconductor structure was made as follows. A por-Si film was grown on the surface of a silicon single-crystal plate of  $p$ -type with a specific resistance of 1 Ohm·cm and a (100) orientation of the surface. The anode electrochemical etching method was used in galvanostatic mode at a current density of 20 mA/cm<sup>2</sup> for 10 min. An electrolyte consisting of HF, C<sub>2</sub>H<sub>5</sub>OH and H<sub>3</sub>PO<sub>4</sub> (1 : 1 : 1 ratio) was applied. The resulting por-Si film contained phosphorus impurity. The electrolyte was then washed off the film surface and the samples were dried.

The surface of the prepared por-Si film was exposed to polyharmonic emission by an LS-2147A (Nd:YAG) laser. Ablation of samples



was carried out by a single 18 ns pulse at a wavelength of 532 nm with the energy ranging from 100 to 240 mJ and at that of 355 nm with the energy ranging from 60 to 200 mJ.

In order to measure the electrophysical characteristics, indium ohmic contacts were soldered to the por-Si film irradiated, and to the back surface of the sample. Before forming the ohmic contacts, short-term etching of the samples under investigation was carried out in the water HF solution (10 %) to remove the superficial oxidized por-Si layer. The samples intended for optical measurements were not subjected to such etching.

### Experimental results and discussion

The superficial thermo-electromotive force (thermo-emf) measurement after the partial removal of a por-Si layer showed  $n$ -conductivity of the samples exposed to laser radiation of their surface with  $\lambda = 355$  nm and an energy of 85 – 200 mJ and  $p$ -conductivity of the samples exposed to laser radiation with  $\lambda = 532$  nm. Thus, in the first case a  $p$ - $n$ -junction was formed. Because of this, further studies were carried out with the samples irradiated by the laser wavelength of 355 nm.

The etching in the water HF solution for 1 h led to the removal of the  $n$ -type layer.

Therefore, the  $p$ - $n$ -junction formed in the largest silicon crystallites of the por-Si film.

In order to investigate the microstructure features of the por-Si film, Raman scattering (RS) and photoluminescence (PL) were used for the samples irradiated by the laser wavelength of 355 nm with the impulse energy of 85 mJ and 200 mJ and for the unirradiated samples.

RS and PL in the por-Si film were excited by the argon laser emission with a wavelength of 488 nm. Excitation spectra were recorded using an U-1000 spectrometer (Jobin Ivon) in standard geometry, i. e., when the laser beam and the reflected one of diffused light were directed along a normal to the sample's surface.

RS spectra of the por-Si films for the samples irradiated and unirradiated by laser emission are shown in Fig. 1. For comparison, the figure also shows the spectrum of single-crystal silicon which was used as a substrate for preparation of the samples under consideration.

The first-order RS spectral line for the por-Si film which was not subjected to radiation has considerable broadening and is noticeably shifted to the low-frequency region relative to the frequency of  $521\text{ cm}^{-1}$  in comparison with the spectrum of single-crystal silicon (Fig. 1). It can be attributed to the effect of

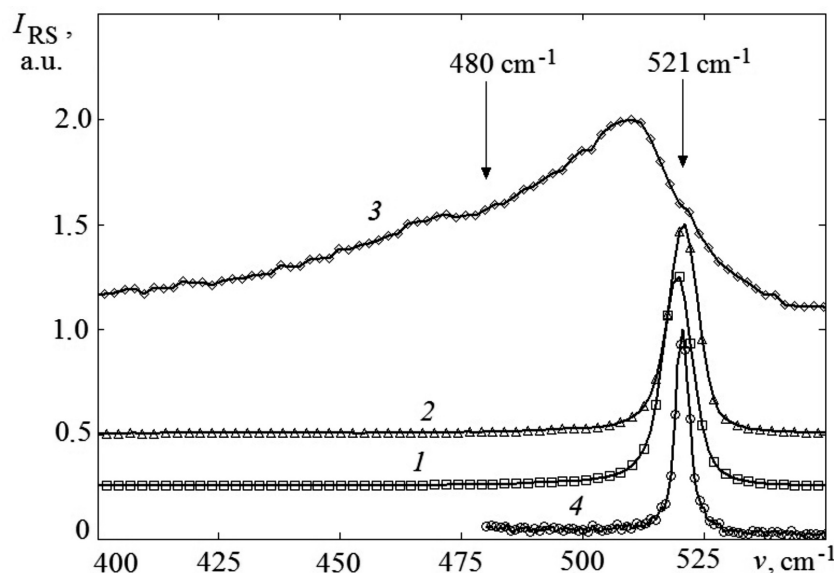


Fig. 1. RS spectra for por-Si films: exposed to laser radiation at a wavelength of 355 nm (1, 2) with  $E = 85$  mJ (1) and 200 mJ (2); the spectra for unirradiated (3) and for single-crystal silicon (4) samples are added for comparison





spatial restriction of phonons in ensembles of silicon crystallites with sizes of several nanometers [5, 6]. The considered RS curve also exhibits a wide band in the region of  $480 \text{ cm}^{-1}$  specific to the existence of an amorphous phase in por-Si films [5].

The average diameter of silicon crystallites in por-Si film before laser irradiation is 2.2 nm; it is estimated by the shift value and the broadening of the RS spectral line of the first order according to the technique presented in Ref. [6].

Laser irradiation at the wavelength of 355 nm with the energy of 85–200 mJ causes the sharp narrowing of the first-order RS line in the spectrum of the por-Si film and a decrease in the shift relative to the frequency of  $521 \text{ cm}^{-1}$  (see Fig. 1). The average diameters of silicon crystallites in por-Si film estimated according to technique [6] are 9.5 nm for the sample irradiated with the impulse energy of 85 mJ and 17.0 nm for that irradiated with 200 mJ. It follows from the analysis of RS spectra (see Fig. 1) that ablation of the por-Si film by the laser leads to disappearance of a wide spectral band in the region of  $480 \text{ cm}^{-1}$ .

The form of PL spectra for the samples laser-irradiated and unirradiated is typical for por-Si films (Fig. 2).

Laser radiation of a por-Si film's surface led to an essential decrease in PL intensity (Fig. 2) compared with the state of the initial

sample. Besides, there was no correlation between the sizes of silicon crystallites and the peak positions in PL spectra determined by the quantum-dimensional effect in the por-Si film. The maxima of spectral lines for samples with large sizes of silicon crystallites had to shift considerably to the long-wave region, however, it was not observed in our experiments. According to Ref. [7], a similar situation can take place in por-Si films when radiation-recombination processes considerably affect the superficial states of silicon crystallites. The decrease in PL intensity with laser energy growth can be connected with an increase in the concentration of defects on the surfaces of silicon crystallites which are the centers of nonradiative recombination.

To study the electrophysical processes in the investigated semiconductor structure with the  $p$ - $n$ -junction, the current-voltage and the capacitance-voltage characteristics were measured at room temperature.

The above-mentioned curves for the samples obtained under irradiation at energies ranging from  $E = 85 - 200 \text{ mJ}$  were identical in character. Because of this, only the characteristics of the sample obtained at  $E = 85 \text{ mJ}$  are discussed further. Measurements were taken by means of E7-20 digital measuring instrument. When measuring current-voltage and capacitance-voltage characteristics a negative voltage application to the por-Si at

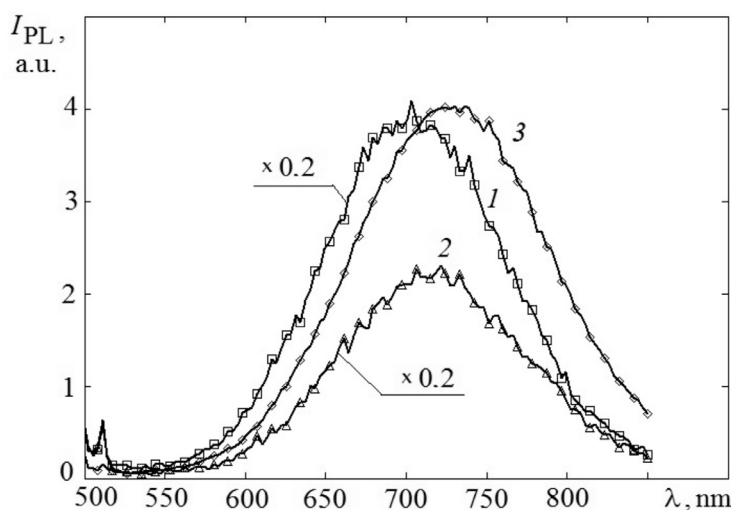


Fig. 2. PL spectra for por-Si films: exposed to laser radiation at a wavelength of 355 nm (1, 2) with  $E = 85 \text{ mJ}$  (1) and  $200 \text{ mJ}$  (2); unirradiated (3)

the contact corresponds to the forward bias.

Direct branches of the current-voltage curves on a double logarithmic scale (Fig. 3, *a*) can be divided into three regions of approximately linear dependences which can be presented by the power relationship

$$I \sim U^m \quad (1)$$

where  $I$  is the current,  $U$  is the voltage shift,  $m$  is the exponent characterizing an inclination of the respective straight line [8]. Such a dependence is used describing the current flow mechanisms within the model of space-charge-limited currents (SCL).

The known expression for a  $p$ - $n$ -junction holds for the first part of the direct branch of the current-voltage curve:

$$I \sim \exp(qU/nkT), \quad (2)$$

where  $q$  is the elementary charge;  $n$  is the non-ideality factor,  $k$  is the Boltzmann constant,  $T$  is the absolute temperature [9].

The value of the factor  $n$  is 1.7, therefore, the current flow corresponding to this part of the current-voltage characteristic is determined by recombination of carriers in the space charge region of the  $p$ - $n$ -junction.

The second part of the direct branch of the current-voltage characteristic is described by expression (1) and is explained within the SCL model by the trap square law as  $m = 2$  [8]. In the third part of the curve (Fig. 3), the condition  $1 < m < 2$  holds. Within the framework of the SCL model, this behavior can be explained by the depletion of the traps' level whose recharge

is determined by the process expressed by the second part of the curve. On the other hand, the third part of the straight branch of the current-voltage characteristic can be explained by the tunneling of charge carriers inside the por-Si layer between the traps' levels on the silicon crystallites surface through the  $\text{SiO}_x$  barriers. Such mechanism of the current flow for the forward bias, according to Ref. [10], can take place in structures with a  $p$ - $n$ -junction and por-Si film.

As for the reverse bias, the current-voltage characteristic has the form typical for the so-called "soft" breakdown (Fig. 3, *b*). This is usually explained by an avalanche breakdown involving a sufficiently large number of defects with deep energy levels [9].

The capacitance-voltage characteristic of the structure under study is shown in Fig. 4. It was measured in the frequency range between 1 kHz and 1 MHz. An increase in capacitance with decreasing frequency for forward and reverse biases indicates the presence of traps with deep energy levels and surface states on silicon crystallites in the por-Si film in the  $p$ -region of the semiconductor structure under study.

The high-frequency capacitance-voltage characteristic (1 MHz) in the region of positive values of  $U$ , represented in  $C^{-2}(U)$  coordinates, is linear (Fig. 4, *b*); hence, the  $p$ - $n$ -junction is sharp. A sufficiently large value of the diffusion potential of the  $p$ - $n$ -junction (1.87 V), determined from the characteristic in Fig. 4, *b*, can be explained by the effect of an incompletely removed por-Si surface layer

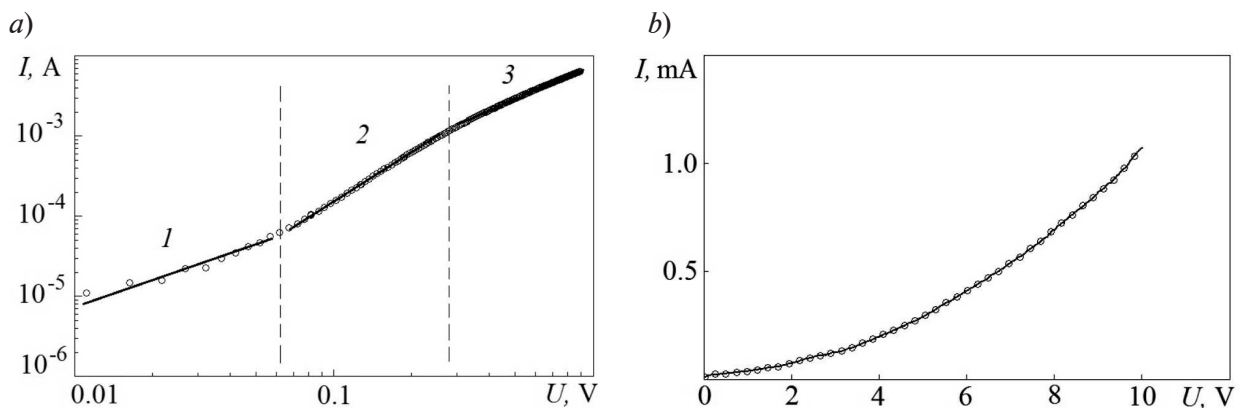


Fig. 3. Current-voltage characteristics of por-Si films at direct (*a*) and reverse (*b*) biases; the parts of the curve are numbered 1 to 3 for discussion

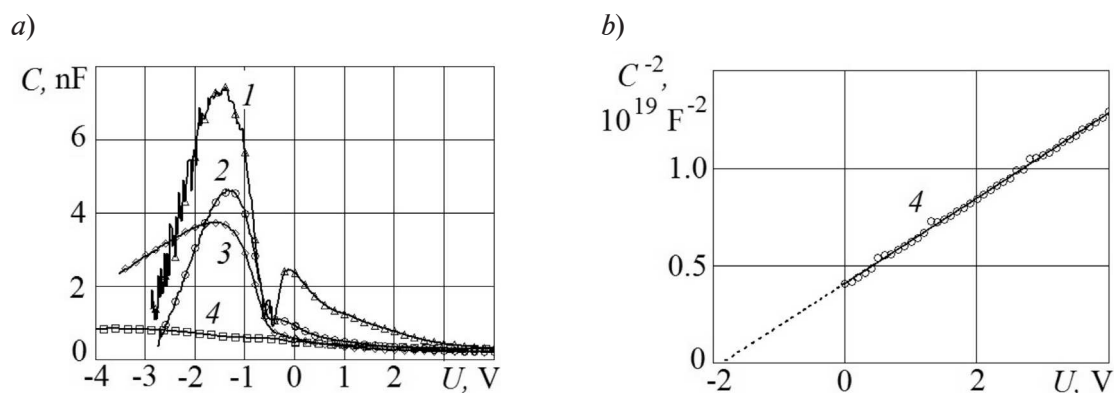


Fig. 4. Capacitance-voltage characteristics at various frequencies  $f$  of the measuring signal (a) and one of them in the coordinates of  $C^{-2}, U$  (b);  $f$ , kHz: 1 (1), 10 (2), 100 (3), 1000 (4)

oxidized as a result of laser radiation during the formation of the  $p$ - $n$ -junction. The impurity concentration in the base region of the  $p$ - $n$ -junction, determined from the slope of the characteristic in Fig. 4, b, was  $1.6 \cdot 10^{16} \text{ cm}^{-3}$ . This value practically coincides with that of the acceptor impurity in the initial silicon  $p$ -type plate on which the por-Si film was formed.

### Summary

Thus, irradiation of a por-Si film containing a phosphorus impurity with a single 18 ns laser pulse at  $\lambda = 355 \text{ nm}$  and with  $E = 85 - 200 \text{ mJ}$  results in the formation of a  $p$ - $n$ -junction within the largest silicon crystallites. As a result of laser irradiation, the microstructure of the por-Si film undergoes significant changes: its amorphized phase disappears, and only the largest silicon crystallites remain. Furthermore,

as the energy of the laser pulse increases, the silicon crystallites grow in size. Simultaneously, surface states are forming on the surfaces of the crystallites which are the centers of nonradiative recombination.

Perhaps, a partial recrystallization of the por-Si film occurs as a result of laser radiation. The resulting  $p$ - $n$ -junction is sharp. The mechanisms of current flow are complex in nature and are mainly determined by the processes of recombination and charge carrier generation involving deep energy levels in the space charge region.

The obtained results can be useful in the engineering of optical sensors and photovoltaic solar energy converters.

The work was supported by Ministry of Education and Science of Russian Federation (grant 3.9506.2017/BCH).

### REFERENCES

- [1] **T. Dzhafarov**, Porous silicon and solar cells, In: L. Canham (Ed.), Handbook of Porous Silicon, Springer International Publishing, Switzerland (2014) 501–511.
- [2] **J.P. Zheng, K.L. Jiao, W.P. Shen**, Highly sensitive photodetector using porous silicon, Appl. Phys. Lett. 61 (4) (1992) 459–461.
- [3] **N.N. Melnik, V.V. Tregulov, A.A. Krivushin**, Svoystva  $n$ - $p$  perhoda, sformirovannogo termicheskoy diffuziey v plenke poristogo kremniya [Properties of  $n$ - $p$ -junction formed by thermal diffusion in a porous silicon film], Sbornik trudov VI Vserossiyskoy molodezhnoy konferentsii po fundamentalnyim i innovatsionnyim voprosam sovremennoy fiziki, Moscow, FIAN (2015) 155.
- [4] **T.D. Dzhafarov**, Fotostimulirovannyye atomnyie protsessyi v poluprovodnikah [Photo-stimulated atomic processes in semiconductors], Energoatomizdat, Moscow, 1984.
- [5] **W.J. Salcedo, F.R. Fernandez, J.C. Rubimc**, Influence of laser excitation on Raman and photoluminescence spectra and FTIR study of porous silicon layers, Brazilian Journal of Physics. 29 (4) (1999) 751–755.
- [6] **M. Yang, D. Huang, P. Hao**, Study of the Raman peak shift and the linewidth of light-

emitting porous silicon, J. Appl. Phys. 75 (1) (1994) 651–653.

[7] **N.N. Melnik, V.V. Tregulov**, Photoluminescence and Raman studies of the structure of a thick porous silicon film, Bulletin of the Lebedev Physics Institute. 42 (3) (2015) 77–80.

[8] **M.A. Lampert, P. Mark**, Current injection in solids, Academic Press, New York and London, 1970.

[9] **S.M. Sze**, Physics of semiconductor devices, Second edition, A Wiley-Interscience Publication John Wiley & Sons, 1981.

[10] **V.V. Tregulov, V.A. Stepanov, V.G. Litvinov, A.V. Ermachikhin**, Specific features of current flow mechanisms in the semiconductor structure of a photoelectric converter with an  $n^+-p$ -junction and an antireflective porous silicon film, Technical Physics. 61 (11) (2016) 1694–1697.

*Received 03.10.2017, accepted 18.10.2017.*

#### THE AUTHORS

**TREGULOV Vadim V.**

*Ryazan State University named for S.A. Yesenin*  
40 Svobody St., Ryazan, 390000, Russian Federation.  
trww@yandex.ru

**STEPANOV Vladimir A.**

*Ryazan State University named for S.A. Yesenin*  
40 Svobody St., Ryazan, 390000, Russian Federation.  
stepanov@physicist.net

**MELNIK Nikolay N.**

*Lebedev Physical Institute of Russian Academy of Science*  
53 Leninsky Ave., Moscow, 119991, Russian Federation.  
melnik@lebedev.ru



## ELECTRET EFFECT IN BIODECOMPOSED POLYLACTIDE FILMS FILLED WITH NANOSCALE MAGNESIA

A.P. Platko<sup>1</sup>, Yu.I. Sotova<sup>1</sup>, Yu.A. Gorokhovatskiy<sup>1</sup>,  
E.A. Karulina<sup>1</sup>, M.F. Galikhanov<sup>2</sup>

<sup>1</sup> Herzen State Pedagogical University of Russia, St. Petersburg, Russian Federation;

<sup>2</sup> Kazan National Research Technological University, Kazan, Russian Federation

In the paper, the results of studies in the charge relaxation mechanism in polylactide films with nanoscale hydrophilic filler (magnesia) have been obtained using thermally stimulated depolarization current (TSDC) and thermally stimulated surface-potential decay (TSSPD) methods. The loading of the hydrophilic filler (magnesia) was shown to result in the polymer conductance reduction, i. e., in the improvement of the electret properties of the composite. The optimal content of magnesia (4%) responsible for the highest electret state stability in polylactide films was determined. The values of the effective frequency factor and the activation energy of the deep traps for the injected charge being inherent to the polymer matrix were estimated by regularization technique. The obtained results demonstrate the capability of making active (long time retaining the organoleptic properties of the products) and biodegradable (solving the problem of recycling) packaging materials based on composite polylactide films with magnesia as a filler.

**Key words:** polylactide; hydrophilous filler; biodecomposed film; electret state; charge-dipole complex

**Citation:** A.P. Platko, Yu.I. Sotova, Yu.A. Gorokhovatskiy, E.A. Karulina, M.F. Galikhanov, Electret effect in biodecomposed polylactide films filled with nanoscale magnesia, St. Petersburg State Polytechnical University Journal. Physics and Mathematics. 11(1) (2018) 19 – 24. DOI: 10.18721/JPM.11103

### Introduction

Synthetic polymers have found wide application as a packaging material for food products. Recycling these polymer materials after use in packaging is a pressing problem since incineration leads to release of toxic gases and decomposition in soil can take over hundreds of years.

One way of solving this problem is using biodegradable polymers. To date, the most promising material for this purpose is polylactide (PLA), a polymer whose monomer (lactide  $C_3H_4O_2$ ) is obtained from lactic acid. It has been established that if a stable electret state is formed in a polymer film, the packaging made of this material preserves the organoleptic properties of the products for a long time [1 – 3]. Such packaging is referred to as active [4, 5]. It is known that PLA's electret state is not sufficiently high in its initial form [6 – 8] but introducing various fillers, in particular, Aerosil  $SiO_2$ , into the polymer makes it possible to significantly improve the stability

of the electret state in PLA-based films [9].

It should be noted that Aerosil is rather expensive to produce, which in turn raises the cost of products packed in PLA films with the Aerosil filler. For this reason, it is of interest to investigate the effect of other fillers on the stability of the electret state in PLA-based composite films. In this study, magnesium oxide was chosen as the filler. It is a hydrophilic filler like Aerosil but its production is cheaper [10].

Thus, the purpose of this study is to establish the nature of the electret state in composite PLA-based films with magnesium oxide as a filler (PLA + MgO system).

### Experimental procedure

In this paper, we investigated PLA and PLA + MgO films, obtained by pressing in accordance with GOST 12019-66 at the Kazan National Research Technological University. The thickness of the films was 100–200  $\mu m$ , the mass fraction of magnesium oxide varied and amounted to 0 %, 2 %, 4 %, and 8 %.

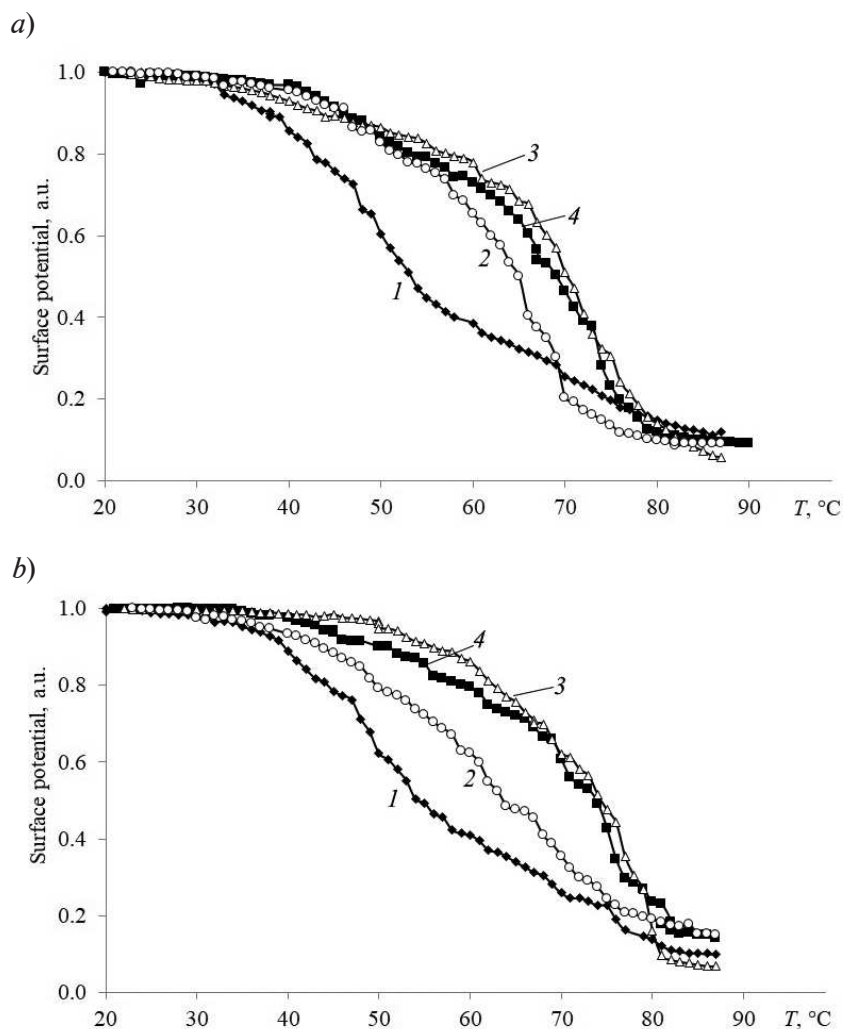


Fig. 1. TSSPD curves for films based on the initial PLA (1) and the PLA with filler (magnesium oxide) (2 – 4) for negatively (a) and positively (b) polarized corona electrode. The MgO concentrations, %: 2 (2), 4 (3), 8 (4)

The electret state in the films under investigation was achieved by exposing the film to a positive or negative corona discharge field for 5 min at room temperature. The stability and nature of the electret state were studied by methods of thermally stimulated depolarization currents (TSDC) and thermally stimulated surface potential decay (TSSPD).

The TSSPD method is based on recording the temperature dependence of the surface potential of samples under linear heating. The TSDC method is based on measuring the short-circuit current in samples under linear heating. (The electret state is formed in the samples in advance in both cases.)

Fig. 1 shows the TSSPD curves for PLA and (PLA + MgO)-based films with different filler contents, with the electret state induced by negative and positive corona charging.

It can be seen from the obtained curves that when the MgO filler is added, the stability of the electret state in composite PLA films increases and reaches its maximum at a mass fraction of MgO of 4% (curves 3 in Fig. 1). A further increase in filler concentration leads to a decrease in the stability of the electret state in composite PLA films with a hydrophilic nano-sized MgO filler (Fig. 2). The temperature stability of the electret state was estimated by processing the TSSPD curves



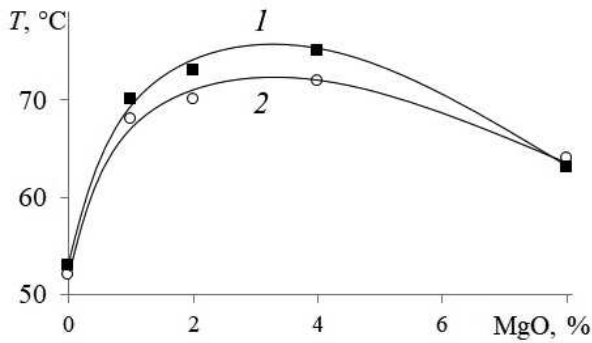


Fig. 2. Curves of temperature stability of the electret state (the temperature of the inflection point of the TSSPD curve) as a percentage of the MgO filler in composite PLA films; the curves were obtained with positive (1) and negative (2) corona discharges

(see Fig. 1): their temperature inflection points were determined.

For clarity, Fig. 3 shows a separate comparison of the TSSPD curves for composite PLA + 4 % MgO films with the electret state induced at different polarities of the corona electrodes.

It can be seen that the character of potential decay depends on the sign of the corona electrode polarity: a positively polarized electret state is more stable with positive polarity than with the negative one. This suggests that the decrease in

the surface potential is governed by the release of the charge captured under electretization from near-surface traps. Evidently, the energy depth of the traps is greater for positive than for negative charge carriers.

The increase in the stability of the electret state with the filler added can be attributed to the presence of so-called charge–dipole centers in the polymer. The latter are formed as a result of the interaction of water molecules with polymer chains, which, on the one hand, have a dipole moment (i.e., they are capable of participating in dipole polarization), and, on the other hand, serve as traps for charge carriers (and thus determine the volume conductivity of the film) [11]. Since magnesium oxide is a hydrophilic filler, it can capture some of the water molecules, thus leading to a decrease in the concentration of charge–dipole centers in composite PLA films compared to the initial PLA (without filler), and, as a consequence, to a decrease in conductivity and a respective increase in the stability of the electret state.

The non-monotonic dependence of the temperature stability of the electret state of composite polylactide films on the percentage of the MgO nanoscale hydrophilic filler can be explained by the presence of two competing bulk conductivity mechanisms. On the one hand, as mentioned above, bulk conductivity decreases with increasing filler concentra-

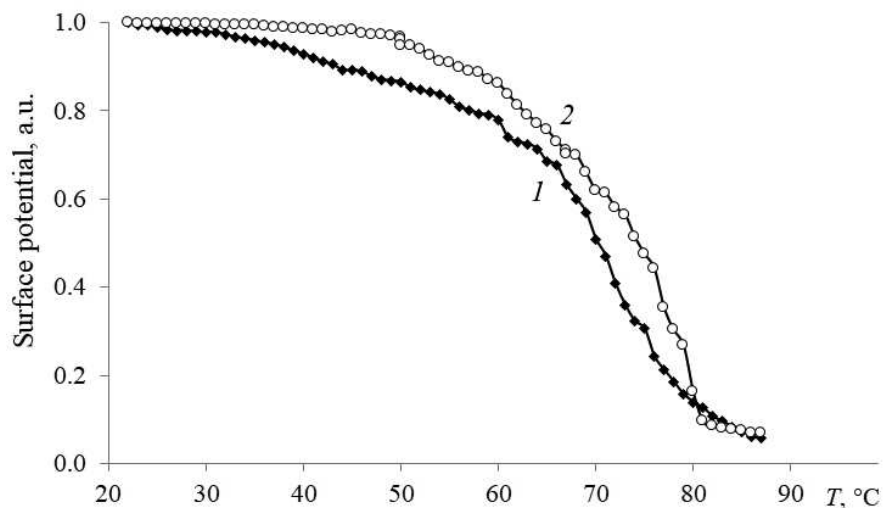


Fig. 3. TSSPD curves of composite PLA + 4 % MgO films obtained under negative (1) and positive (2) corona discharges



tion due to a decrease in the concentration of charge–dipole centers, which means that the stability of the electret state increases; on the other hand, bulk conductivity can increase due to increasing probability of conducting clusters forming over the filler particles, which, accordingly, should lead to a decrease in the stability of the electret state. Thus, there should be an optimal value of the MgO filler concentration in PLA-based films ensuring the greatest stability of the electret state in the films. In our case, the optimal concentration is 4 %.

Fig. 4 shows the TSDC curves of composite PLA + 4 % MgO films with the electret state induced by positive and negative corona discharges.

Two peaks are observed on the TSDC curves in composite PLA-based films. A low-temperature peak near 40 °C is associated with heterocharge relaxation (the orientation of charge-dipole centers in our model). The height of this peak, if compared with the data on the initial PLA films, is two orders of magnitude smaller [6]. This result agrees with the assumption that introducing a nanoscale hydrophilic MgO filler lowers the concentration of charge–dipole centers (the effect of MgO is similar to that of Aerosil SiO<sub>2</sub> described in the paper).

High-temperature peaks on the TSDC curves in composite PLA films correspond to homocharge relaxation. This suggests that these peaks are due to charge ejection from deep near-surface traps. The curves in Fig. 4 indicate that the depth (activation energy) of traps is less for negative charge carriers than for positive ones. This result is consistent with the TSSPD data. The calculated values of trap activation energy were  $W = 0.84 \pm 0.03$  eV for positive charge carriers and  $W = 0.76 \pm 0.03$  eV for negative ones (the frequency factor was equal to  $10^{11} \text{ s}^{-1}$  in both cases). Since the temperature position of the high-temperature peaks in composite PLA + 4 % MgO films coincides with the temperature position of similar peaks in the initial PLA films (see [6]), it can be concluded that the traps determining the potential stability of the electret state are inherent for the PLA polymer matrix.

The results obtained by TSDC in composite films based on PLA and MgO filler are similar to the TSDC dependences previously studied in composite PLA films filled with aerosil SiO<sub>2</sub> [6], the only difference being that the optimal (from the standpoint of the electret state stability) concentration was 2 % for the Aerosil filler, while for magnesium oxide this value is 4 %.

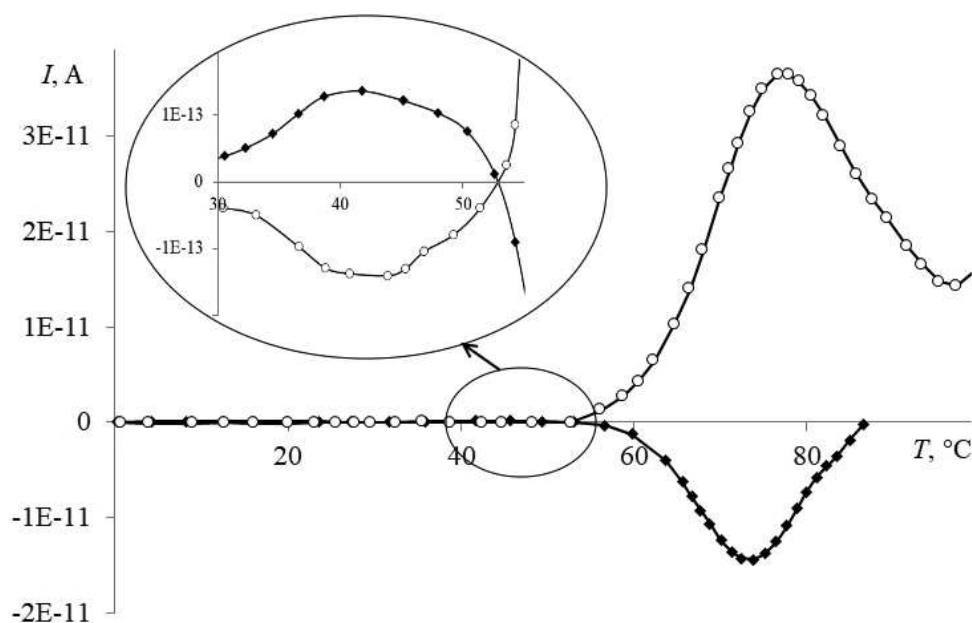


Fig. 4. TSDC curves in the corona electret system of a composite PLA + 4 % MgO film; the films were obtained under positive (1) and negative (2) corona discharges



### Conclusion

A hydrophilic nanosized MgO filler can be proposed as a cheaper alternative to the Aerosil

SiO<sub>2</sub> filler, improving the stability of the electret state in biodegradable PLA-based composite films used to create an active packaging material.

### REFERENCES

- [1] M.F. Galikhanov, A.N. Borisova, A.Yu. Krynitskaya, R.Ya. Deberdeyev, Vliyaniye aktivnogo upakovochного materiala na kachestvo moloka [Influence of active packaging material on milk quality], *Izvestiya vuzov. Pishchevaya tekhnologiya*. (2–3) (2005) 71–73.
- [2] M.F. Galikhanov, A.N. Borisova, R.Ya. Deberdeyev, Aktivniy upakovochный material dlya yablok [Active packaging material for apples], *Herald of Kazan Technological University*. (2) (2004) 163–167.
- [3] A. Sodergard, M. Stolt, Industrial production of high molecular weight poly(lactic acid), *Poly(Lactic Acid): Synthesis, Structures, Properties, Processing, and Applications*, edited by R. Auras, L.T. Lim, S.E.M. Selke, H. Tsuji. Hoboken, John Wiley & Sons, Inc., 2010.
- [4] D. Dainelli, N. Gontard, D. Spyropoulos, et al., Active and intelligent food packaging: legal aspects and safety concerns, *Trends in Food Science & Technology*. 19, Suppl. 1 (November) (2008) S103–S112.
- [5] A.Yu. Krynitskaya, A.N. Borisova, M.F. Galikhanov, M.A. Sysoeva, V.S. Gamayurova, Vliyaniye aktivnogo upakovochного materiala na razvitiye mikroorganizmov v pishchevykh produktakh [Influence of “active” packaging material on the development of microorganisms in foodstuffs], *Food industry*. (1) (2011) 27–29.
- [6] Yu.A. Gorokhovatskiy, M.F. Galikhanov, D.A. Ignatyeva, et al., Charge relaxation mechanisms in composite films based on polylactide, *Humanities and Science University Journal*. 27 (2017) 46–55.
- [7] A. Guzhova, T. Yovcheva, A. Viraneva, Study of polylactic acid corona electrets, *Bulgarian Chemical Communications*. 47 (Special Issue B) (2015) 115–120.
- [8] A.A. Guzhova, M.F. Galikhanov, Charge depth in polylactic acid electret filled with fine filler, *Bulgarian Chemical Communications*. 47 (Special Issue B) (2015) 103–108.
- [9] Yu.A. Gorokhovatskiy, M.F. Galikhanov, D.A. Ignatyeva, et al., Ways to increase the stability of the electret state in composite polylactide films, *Bulletin of Kazan University of Technology*. 20 (4) (2017) 27–30.
- [10] R.Kh. Khuziakhmetov, V.A. Khusnutdinov, R.S. Sayfullin, Poluchenie aktivnogo oksida magniya [Preparation of active magnesium oxide], *Postepy Tekhnologii Chemicznej Nieorganicznej: “CHEMTEX-93”*. Wroclaw (1993) 107–114.
- [11] Yu.A. Gorokhovatskiy, L.B. Aniskina, A.S. Viktorovich, et al., The manifestation of the spin-orbit interaction in the vibrational spectra of polyelectrolytes – fibrous and film electrets based on polypropylene and polyethylene, *Izvestia: Herzen University Journal of Humanities & Science*. (79) (2009) 47–61.

*Received 18.01.2018, accepted 24.01.2018.*

### THE AUTHORS

**PLATKO Anastasiya P.**

*Herzen State Pedagogical University of Russia*

48 Moyka Emb., St. Petersburg, 191186, Russian Federation

stewnstewn@gmail.com

**SOTOVA Yulia I.**

*Herzen State Pedagogical University of Russia*

48 Moyka Emb., St. Petersburg, 191186, Russian Federation

juliasotova1992@mail.ru

**GOROKHOVATSKIY Yuriy A.**

*Herzen State Pedagogical University of Russia*

48 Moyka Emb., St. Petersburg, 191186, Russian Federation

yurig@fromru.com

**KARULINA Elena A.**

*Herzen State Pedagogical University of Russia*

48 Moyka Emb., St. Petersburg, 191186, Russian Federation

karulina@mail.ru

**GALIKHANOV Mansur F.**

*Kazan National Research Technological University*

68 Karl Marx St., Kazan, 420015, Russian Federation

mgalikhanov@yandex.ru



# MÖSSBAUER EMISSION SPECTRA OF STANNUM DAUGHTER ISOTOPES MEASURED UNDER CONDITION OF A DYNAMIC RADIOACTIVE EQUILIBRIUM OF TELLURIUM PARENT ISOTOPES AND ANTIMONIUM DAUGHTER ONES

**N.N. Zhukov, A.V. Marchenko, K.B. Shakhovich**

Herzen State Pedagogical University of Russia, St. Petersburg, Russian Federation

The information on a valence and a coordination states of the  $^{119m}\text{Sn}$  daughter atoms formed in the cationic and anionic lattice sites of the crystalline lead telluride  $\text{PbTe}$  and the glassy arsenic telluride  $\text{As}_2\text{Te}_3$  from the  $^{119}\text{Sb}$  and  $^{119m}\text{Te}$  parent isotopes has been obtained using the emission Mössbauer spectroscopy with the  $^{119m}\text{Te}$  parent isotopes being in a dynamic radioactive equilibrium with the  $^{119}\text{Sb}$  daughter ones. It was found by calculation and experimentally that the proportion of various valent and coordinate states of tin atoms in the crystal and the glass depended on the preparation moment of Mössbauer sources. Moreover, the displacement of a part of the  $^{119}\text{Sb}$  daughter atoms from lattice sites of the  $^{119m}\text{Te}$  parent isotopes as a result of a radioactive decay was established when bringing into agreement with experimental data.

**Key words:** dynamic radioactive equilibrium; Mössbauer emission spectroscopy; isotope; telluride; lead; arsenic

**Citation:** N.N. Zhukov, A.V. Marchenko, K.B. Shakhovich, Mössbauer emission spectra of stannum daughter isotopes measured under condition of a dynamic radioactive equilibrium of tellurium parent isotopes and antimony daughter ones, St. Petersburg State Polytechnical University Journal. Physics and Mathematics. 11(1) (2018) 25 – 32. DOI: 10.18721/JPM.11104

## Introduction

Mössbauer emission spectroscopy on the  $^{119m}\text{Sn}$  tin isotope with parent  $^{119}\text{Sb}$  antimony and  $^{119m}\text{Te}$  tellurium nuclei is widely used to study the state of impurity atoms in crystalline lead chalcogenides and glassy chalcogenides of arsenic and germanium [1 – 11]. Depending on the chemical nature of the parent isotope, daughter tin atoms can stabilize either at chalcogen sublattice sites (if the  $^{119m}\text{Te}$  isotope is used) [2, 3, 5, 7, 8], or at sites not determined in advance (if the  $^{119}\text{Sb}$  isotope is used) [1, 4, 6 – 11].

In this paper we have measured the  $^{119m}\text{Sn}$  Mössbauer emission spectra for sources based on crystalline lead telluride  $\text{PbTe}$  and glassy arsenic telluride  $\text{As}_2\text{Te}_3$ , containing simultaneously parent  $^{119m}\text{Te}$  and  $^{119}\text{Sb}$  isotopes. The spectra allowed to obtain data on the state of parent impurity atoms of tellurium and antimony, and daughter impurity atoms of tin.

## Experimental samples and procedure

It follows from Fig. 1 that the decay of par-

ent  $^{119m}\text{Te}$  atoms occurs with the formation of radioactive daughter  $^{119}\text{Sb}$  nuclei. By the time dynamic equilibrium (the maximum concentration of the  $^{119}\text{Sb}$  isotope) is established, a mixture of radioactive atoms of tellurium (denoted as  $^{119m}\text{Te-1}$ ) and antimony (denoted as  $^{119}\text{Sb-1}$ ) is formed.

The fraction of  $^{119m}\text{Te-1}$  atoms in the initial content of  $^{119m}\text{Te}$  is 0.575, while the fraction of  $^{119}\text{Sb-1}$  atoms is 0.195. This mixture was fused with glassy arsenic telluride  $\text{As}_2\text{Te}_3$  or crystalline lead telluride  $\text{PbTe}$  in vacuum-sealed quartz tubes. The estimated concentration of impurity atoms did not exceed  $10^{17} \text{ cm}^{-3}$ . The  $\text{As}_2\text{Te}_3$  melt was air-quenched; the glassy state was assessed by such criteria as conchoidal fracture, the absence of lines on the X-ray powder patterns, the absence of inclusions and inhomogeneities on polished surfaces observed under an MIM-7 metallographic microscope and an MIK-1 IR microscope. The initial  $\text{PbTe}$  samples were *n*-type (with an excess of lead,  $n \approx 5 \cdot 10^{18} \text{ cm}^{-3}$ ) and *p*-type (with an excess of tellurium,  $p \approx 10^{18} \text{ cm}^{-3}$ ). The quantitative composition of glasses and crystals was moni-

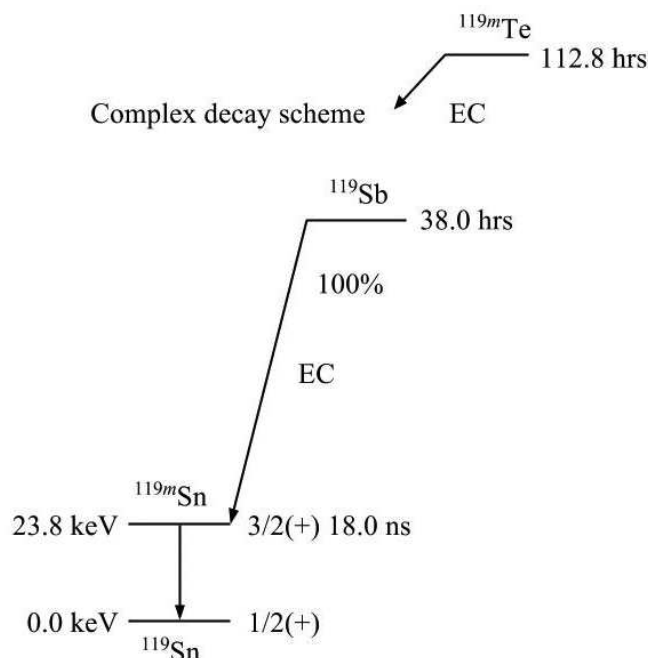
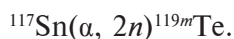


Fig. 1. Diagram of decay of parent  $^{119m}\text{Te}$  and  $^{119}\text{Sb}$  isotopes.

The decay periods and the energy released are indicated. The decay is accompanied by electron capture (EC)

tored by X-ray fluorescence analysis.

The  $^{119m}\text{Te}$  isotope was obtained by the reaction



The anion exchange procedure was used to separate the carrier-free  $^{119m}\text{Te}$  sample [5].

The  $^{119m}\text{Sn}$  Mössbauer spectra were measured with an SM-2201 spectrometer at a temperature of 80 K with calcium stannate  $\text{CaSnO}_3$  (tin density of 5 mg/cm<sup>2</sup>) as an absorber. The typical Mössbauer spectra of  $\text{PbTe} : (^{119}\text{Sb} + ^{119m}\text{Te})$  and  $\text{As}_2\text{Te}_3 : (^{119}\text{Sb} + ^{119m}\text{Te})$  samples are shown in the figures below.

A series of emission spectra of  $^{119m}\text{Sn}$  was recorded for each source with the acquisition lasting for 9.5 h in the interval from the end of sample alloying to 190.5 h. Evidently, parent  $^{119}\text{Sb}$ -1 atoms (the decay constant  $\lambda_{\text{Sb}} = 5.05 \cdot 10^{-6} \text{ s}^{-1}$ ) make the main contribution to the Mössbauer spectra of  $\text{PbTe} : (^{119}\text{Sb} + ^{119m}\text{Te})$  and  $\text{As}_2\text{Te}_3 : (^{119}\text{Sb} + ^{119m}\text{Te})$  samples in the initial period of measurements, whereas the intensity of the spectrum from parent  $^{119}\text{Sb}$ -2 atoms increases with the accumulation of second antimony  $^{119}\text{Sb}$ -2 formed during the decay of  $^{119m}\text{Te}$ -1 ( $\lambda_{\text{Te}} = 1.70 \cdot 10^{-6} \text{ s}^{-1}$ ).

## Experimental results and discussion

**Lead telluride.** The experimental Mössbauer spectra of the  $^{119m}\text{Sn}$  isotope for  $n\text{-PbTe} : (^{119}\text{Sb} + ^{119m}\text{Te})$  ( $n$ -type lead telluride) and  $p\text{-PbTe} : (^{119}\text{Sb} + ^{119m}\text{Te})$  ( $p$ -type lead telluride) samples are a superposition of two lines (Fig. 2).

One of these lines has an isomer shift of 2.31(2) mm/s; it is typical for isomer shifts of the  $^{119}\text{Sn}$  Mössbauer spectra of intermetallic tin compounds, and, accordingly, this line should be attributed to  $^{119m}\text{Sn}^0$  centers formed after the chain of decays



at tellurium sublattice sites (spectrum I).

The second line has an isomer shift of 3.42(2) mm/s; it corresponds to tin telluride and, consequently, this line can be attributed to divalent  $^{119m}\text{Sn}^{2+}$  centers formed after the decay of  $^{119}\text{Sb}$ -1 atoms at lead sublattice sites (spectrum II).

The intensity of the  $^{119m}\text{Sn}^0$  spectrum in the tellurium sublattice for the  $p$ -type sample increases with time that has elapsed since the synthesis of Mössbauer sources (this time variable shall be referred to as the source age

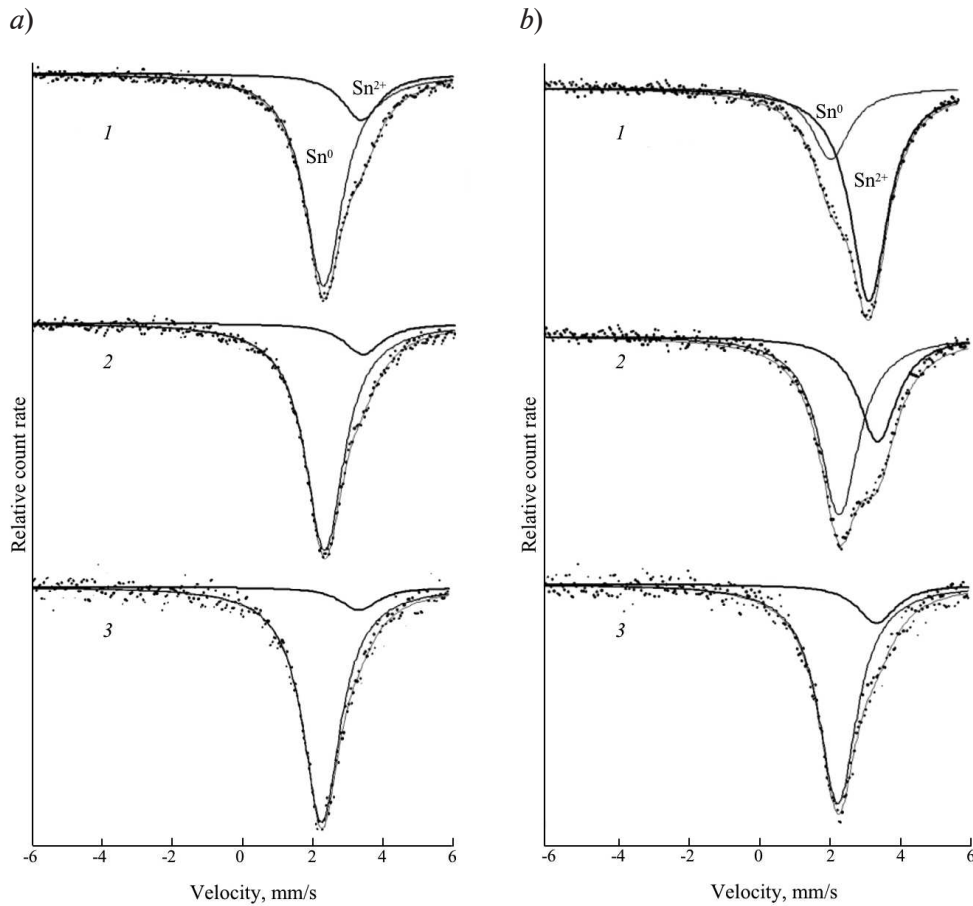


Fig. 2.  $^{119m}\text{Sn}$  Mössbauer emission spectra in  $n\text{-PbTe}$  (a) and  $p\text{-PbTe}$  (b). The spectra were obtained at 80 K in the time intervals of 0 – 9.5 h (1), 66.7 – 76.2 h (2) and 152.4 – 190.5 h (3) after the preparation of the Mössbauer source. Emission lines corresponding to the  $\text{Sn}^0$  and  $\text{Sn}^{2+}$  centers are shown.

from now on), while the ratio of the areas under the two lines varies only slightly for the  $n$ -type sample. Since tin impurity atoms in lead telluride are electrically inactive [4, 5], the differing behavior of the  $^{119m}\text{Sn}$  Mössbauer spectra for the hole and electron lead telluride samples needs an explanation.

To quantitatively describe the change in the structure of the  $^{119m}\text{Sn}$  Mössbauer spectra in lead telluride, the experimental ratios

$$P = \frac{SI}{SI + SII}$$

were calculated for different source age values (here  $SI$  and  $SII$  are the areas under the normalized Mössbauer spectra I and II, respectively).

The area  $S$  under the  $^{119m}\text{Sn}$  spectrum is

proportional to the concentration of antimony atoms  $N_{\text{Sb}}$  and the Mössbauer factor  $f$  in the corresponding sublattice:

$$S \sim f N_{\text{Sb}}.$$

Antimony atoms  $^{119}\text{Sb}$  are direct radioactive precursors of the  $^{119m}\text{Sn}$  isotope.

The dependence of the  $N_{\text{Sb}}$  concentration on the time  $t$  can be obtained from the balance equation:

$$N_{\text{Sb}} = \frac{\lambda_{\text{Te}}}{\lambda_{\text{Sb}} - \lambda_{\text{Te}}} N_{\text{Te}}^0 [\exp(-\lambda_{\text{Te}} t) - \exp(-\lambda_{\text{Sb}} t)] + N_{\text{Sb}}^0 \exp(-\lambda_{\text{Sb}} t),$$

where  $\lambda_{\text{Te}}$ ,  $\lambda_{\text{Sb}}$  are the decay constants of the corresponding parent isotopes;  $N_{\text{Te}}^0$ , and  $N_{\text{Sb}}^0$  are the concentrations of  $^{119m}\text{Te}$  and  $^{119}\text{Sb}$  atoms at the initial time; the subscript Te indicates



that the  $^{119m}\text{Te}$  concentration is taken in the same sublattice as Sb.

Since the  $N_{\text{Te}}^0$  concentration in the lead sublattice can be neglected, instead of expression (1) we obtain:

$$N_{\text{Sb in Pb}} = N_{\text{Sb in Pb}}^0 \exp(-\lambda_{\text{Sb}} t), \quad (2)$$

where  $N_{\text{Sb in Pb}}^0$  is the concentration of Sb-1 atoms at lead sites.

Similarly, we obtain for the tellurium sublattice:

$$N_{\text{Sb in Te}} = \frac{\lambda_{\text{Te}}}{\lambda_{\text{Sb}} - \lambda_{\text{Te}}} N_{\text{Te}}^0 [\exp(-\lambda_{\text{Te}} t) - \exp(-\lambda_{\text{Sb}} t)] + N_{\text{Sb}}^0 \exp(-\lambda_{\text{Sb}} t), \quad (3)$$

with the total concentration of Sb-1 determined as

$$N_{\text{Sb}}^0 = N_{\text{Sb in Pb}}^0 + N_{\text{Sb in Te}}^0.$$

Thus, the ratio of the areas under the normalized spectra can be written in the following form:

$$P = \left[ \frac{\lambda_{\text{Te}}}{\lambda_{\text{Sb}} - \lambda_{\text{Te}}} N_{\text{Te}}^0 [\exp(-\lambda_{\text{Te}} t) - \exp(-\lambda_{\text{Sb}} t)] + \right.$$

$$\left. + N_{\text{Sb in Te}}^0 \exp(-\lambda_{\text{Sb}} t) \right] \cdot f_{\text{Te}} \times \\ \times \left[ \frac{\lambda_{\text{Te}}}{\lambda_{\text{Sb}} - \lambda_{\text{Te}}} N_{\text{Te}}^0 [\exp(-\lambda_{\text{Te}} t) - \exp(-\lambda_{\text{Sb}} t)] + \right. \\ \left. + N_{\text{Sb in Te}}^0 \exp(-\lambda_{\text{Sb}} t) \right] \cdot f_{\text{Te}} + \\ \left. + N_{\text{Sb in Pb}}^0 \exp(-\lambda_{\text{Sb}} t) \cdot f_{\text{Pb}} \right]^{-1}. \quad (4)$$

Ratio (4) allows to extrapolate the curves in Fig. 3 to obtain the values

$$q = \frac{N_{\text{Sb in Te}}^0 f_{\text{Te}}}{N_{\text{Sb in Te}}^0 f_{\text{Te}} + N_{\text{Sb in Pb}}^0 f_{\text{Pb}}},$$

equal to 0.2 for  $p\text{-PbTe}$  and 0.8 for  $n\text{-PbTe}$ .

If we disregard the difference in the Mössbauer factors at tellurium sublattice sites  $f_{\text{Te}}$  and at lead sublattice sites  $f_{\text{Pb}}$  (which is valid at 80 K), then these quantities indicate the fraction of Sb-1 that got into the tellurium sublattice during synthesis. Sb-1 atoms in the

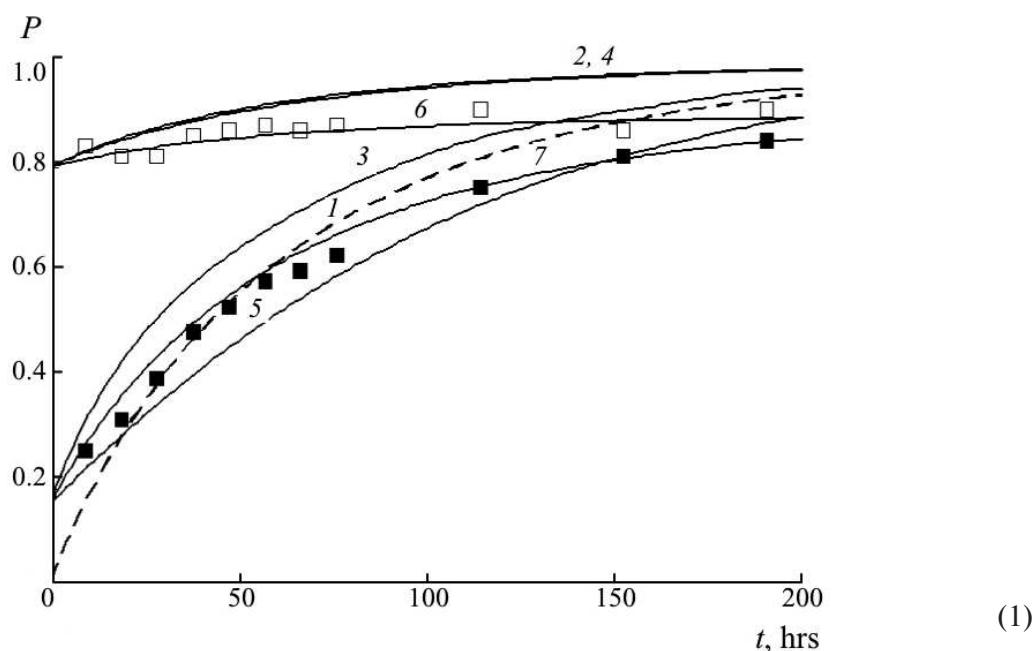


Fig. 3. Experimental (symbols) and calculated (curves 1–7) dependences of the ratio  $P$  on source ages for electron (shaded squares, curves 2, 4, 6) and hole (open squares, curves 3, 5, 7) of  $\text{PbTe}:(^{119}\text{Sb}+^{119m}\text{Te})$  samples; the calculated curves were obtained under different assumptions, for varying contents of  $^{119}\text{Sb}$  atoms in the lead sublattice (also curve 1) (see description in the text)



$n$ -PbTe sample (with an excess of lead atoms and tellurium vacancies) fill tellurium vacancies with a probability of about 0.8, while most of the antimony atoms in the  $p$ -PbTe sample appear at lead lattice sites.

The time dependences  $P(t)$  of the ratio of the areas for the electron and hole lead tellurides, calculated by formula (4) with the above distribution of Sb-1 over the sublattices and taking into account the value

$$m = \frac{N_{\text{Te}}^0}{N_{\text{Sb}}^0} = 2.949,$$

are shown in Fig. 3 together with the experimental values of  $P$ .

Curve 1, calculated with the assumption that all  $^{119}\text{Sb-1}$  atoms are located in the lead sublattice, and all  $^{119m}\text{Te-1}$  atoms in the tellurium sublattice, deviates significantly from the behavior of the experimental values for both hole and (in particular) electron lead telluride. With above assumption that part of  $^{119}\text{Sb-1}$  is displaced into the tellurium sublattice, the calculated  $P(t)$  curves are in satisfactory agreement with the experimental data for a small source age but yield overestimated values for the spectra measured a considerable time after source preparation (curves 2 and 3 in Fig. 3). The reasons for this discrepancy might be, firstly, the smaller value of the Mössbauer factor  $f_{\text{Te}}$  for the structural sites of tellurium in comparison with that for the lead sites ( $f_{\text{Pb}}$ ), and, secondly, the displacement of a part of the  $^{119}\text{Sb-2}$  atoms of the tellurium sublattice into the lead sublattice that can occur due to the recoil energy obtained by the daughter  $^{119}\text{Sb-2}$  atoms during radioactive decay of the parent  $^{119m}\text{Te-1}$  atoms [5].

Curves 4 and 5 in Fig. 3 show the behavior of  $P(t)$  calculated for the hole and electron lead tellurides under the assumption that  $f_{\text{Te}}/f_{\text{Pb}} = 0.5$ . This assumption significantly improves agreement with the experiment for the hole sample, but hardly changes the form of the  $P(t)$  curve for the electron sample. Consequently, the difference in the Mössbauer factors cannot explain the lower values of  $P(t)$  for the spectra of sources with an older age. In further calculations, it was assumed that  $f_{\text{Te}}/f_{\text{Pb}} = 0.5$ .

Curves 6 and 7 in Fig. 3 show the behav-

ior of  $P(t)$  calculated for the hole and electron lead tellurides under the assumption that some of the total population of  $^{119}\text{Sb-2}$  atoms (the fraction  $\alpha = 0.1$ ) is displaced into to the lead sublattice. In this case, ratio (4) can be transformed into

$$P = 1 - \alpha - (1 - q - \alpha) \times \left( m \frac{\lambda_{\text{Te}}}{\lambda_{\text{Sb}} - \lambda_{\text{Te}}} \{ \exp[(\lambda_{\text{Sb}} - \lambda_{\text{Te}})t] - 1 \} + 1 \right)^{-1} \quad (5)$$

A satisfactory agreement with the measured values of  $P$  is observed for both types of samples. This result also confirms the conclusion of Ref. [5] on the displacement of  $^{119}\text{Sb-2}$  atoms

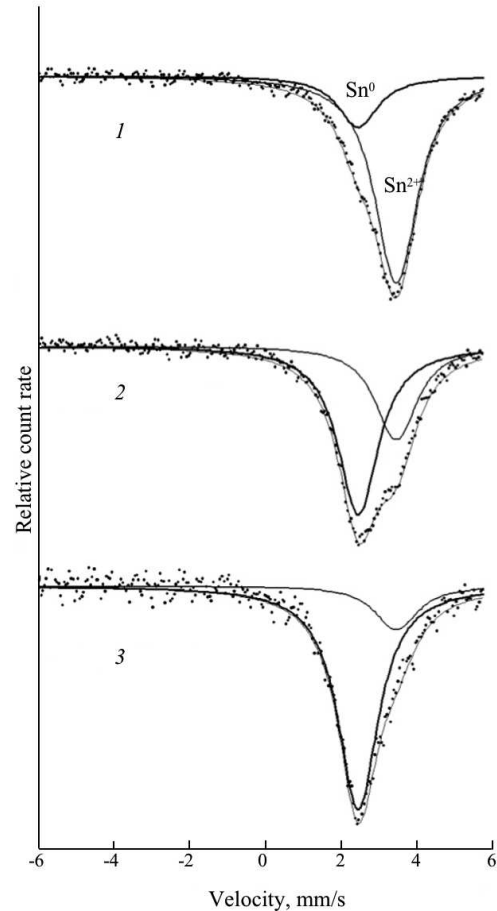


Fig. 4.  $^{119m}\text{Sn}$  Mössbauer emission spectra in a glassy  $\text{As}_2\text{Te}_3$ : ( $^{119}\text{Sb} + ^{119m}\text{Te}$ ) sample. The conditions in which the spectra were recorded and the notations are identical to those shown in Fig. 2. Emission lines corresponding to the  $\text{Sn}^0$  and  $\text{Sn}^{2+}$  centers are also shown

during the decay of the parent  $^{119m}\text{Te}$  isotopes.

**Arsenic telluride.** According to the data of Ref. [12], impurity tin atoms in glassy arsenic telluride  $\text{As}_2\text{Te}_3$  are electrically inactive (in accordance with the general principle that chalcogenide glassy semiconductors are unable to form solid solutions with dopants). The experimental Mössbauer spectra of the  $^{119m}\text{Sn}$  isotope in the  $\text{As}_2\text{Te}_3 : (^{119}\text{Sb} + ^{119m}\text{Te})$  alloy that we have obtained are a superposition of two lines (Fig. 4).

A less intense line for the spectrum measured in the time range of 0 – 19.05 h has an isomer shift of 2.61 (2) mm/s; it is close to the isomer shift of the  $^{119}\text{Sn}$  Mössbauer spectrum in the semimetallic compound of tin arsenide  $\text{SnAs}$  and, consequently, this line can be attributed to  $^{119m}\text{Sn}^0$  tin impurity centers formed after the decay of  $^{119m}\text{Te}$ -1 atoms at tellurium sublattice sites (spectrum I). The relative intensity of this line increases with the source age, which also indicates its origin from  $^{119m}\text{Te}$ -1 at tellurium structural sites.

The isomer shift of the line whose intensity decreases with the source age is 3.65 (2) mm/s; it is close to the isomer shift of the  $^{119}\text{Sn}$  Mössbauer spectrum for the  $\text{SnTe}$  compound

and, consequently, this line can be attributed to divalent  $^{119m}\text{Sn}^{2+}$  tin impurity centers formed after the decay of  $^{119}\text{Sb}$ -1 atoms in arsenic sites (spectrum II). Evidently, the relative intensity of the  $^{119m}\text{Sn}^0$  Mössbauer spectrum at tellurium sites increases with the source age.

To quantitatively describe the changes in the structure of the  $^{119m}\text{Sn}$  Mössbauer spectra shown in Fig. 4, we have calculated the dependences of the ratio

$$P = \frac{SI}{SI + SII}$$

on the age of the source  $(\text{As}, ^{119}\text{Sb})_2 ^{119m}\text{Te}_3$ .

The calculated  $P(t)$  dependences are shown in Fig. 5 together with the corresponding experimental values of  $P$ . If  $P$  is calculated under the assumption that  $^{119}\text{Sb}$ -1 atoms are located in arsenic sublattice sites, and the  $^{119}\text{Sb}$ -2 atoms in tellurium sublattice sites during Mössbauer spectra measurements, the calculation yields overestimated values of the  $P$  ratio. To fit these data, we should assume that a fraction of  $^{119m}\text{Te}$ -1 atoms ( $\alpha = 0.15(2)$ ) is displaced from tellurium structural sites into arsenic sublattice sites during the measurement of the spectra

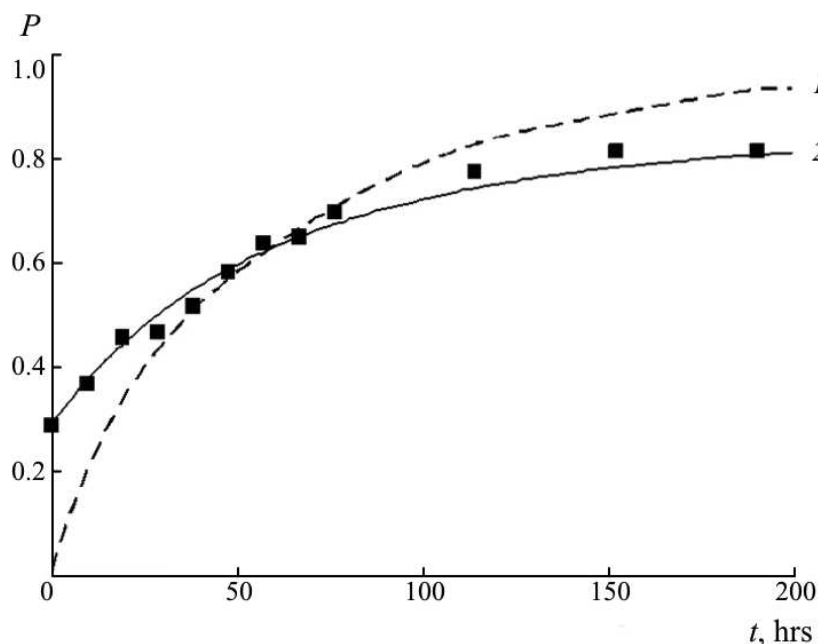


Fig. 5. Experimental (symbols) and calculated (curves 1, 2) dependences of the ratio  $P$  on the source age for samples of glassy  $\text{As}_2\text{Te}_3$  ( $^{119}\text{Sb} + ^{119m}\text{Te}$ ); the calculated curves were obtained under different assumptions, for varying contents of  $^{119}\text{Sb}$  atoms in the arsenic sublattice (see description in the text)



(this value is obtained by extrapolating the experimental  $P(t)$  dependence to  $t \rightarrow \infty$ ) (solid line 1 in Fig. 5). This displacement can occur due to the recoil energy obtained by the daughter  $^{119}\text{Sb}$ -2 atoms during the radioactive decay of  $^{119\text{m}}\text{Te}$ -1 atoms. In addition, the local environment of the formed  $^{119}\text{Sb}$ -2 atoms can be restructured during the lifetime of  $^{119}\text{Sb}$  (55 h).

### Conclusion

It is shown that data on the location of

antimony and tellurium atoms in the crystal lattice of lead telluride (or at the structural lattice sites of glassy arsenic telluride) and the valence state of tin daughter atoms formed from parent  $^{119}\text{Sb}$  atoms can be obtained from a series of Mössbauer emission spectra of a single  $^{119}\text{Sb} + ^{119\text{m}}\text{Te}$  source. We have also established that some of the  $^{119}\text{Sb}$  daughter atoms are displaced from the structural positions of the  $^{119\text{m}}\text{Te}$  parent atoms as a result of the decay of the latter.

### REFERENCES

- [1] F. Ambe, S. Ambe, H. Shoji, N. Saito, Mössbauer emission spectra of  $^{119}\text{Sn}$  after the EC decay of  $^{119}\text{Sb}$  in metals, oxides, and chalcogenides of antimony and tellurium, *J. Chem. Phys.* 60 (10) (1974) 3773–3778.
- [2] F. Ambe, S. Ambe, Mössbauer emission studies of defect  $^{119}\text{Sn}$ ,  $^{119}\text{Sb}$ , and  $^{119\text{m}}\text{Te}$  atoms after nuclear decays and reactions in  $\text{SnSb}$ ,  $\text{SnTe}$ , and  $\text{Sb}_2\text{Te}_3$ , *J. Chem. Phys.* 73(5) (1980) 2029–2036.
- [3] F. Ambe, S. Ambe, A site distribution study of dilute  $^{119}\text{Sb}$  and  $^{119\text{m}}\text{Te}$  on solidification of  $\text{SnTe}$  and  $\text{SnSb}$  by Mössbauer emission spectroscopy of  $^{119}\text{Sn}$ , *J. Chem. Phys.* 75 (5) (1981) 2463–2465.
- [4] V.F. Masterov, F.S. Nasredinov, S.A. Nemov, et al., Position of antimony impurity atoms in  $\text{PbTe}$  lattice determined by emission Mössbauer spectroscopy, *Semiconductors*. 31 (11) (1997) 1138–1139.
- [5] V.F. Masterov, S.I. Bondarevskii, F.S. Nasredinov, et al., Antistructural defects in  $\text{PbTe}$ -type semiconductors, *Semiconductors*. 33 (7) (1999) 710–711.
- [6] V.F. Masterov, F.S. Nasredinov, P.P. Seregin, et al., Determining the position of antimony impurity atoms in  $\text{PbS}$  by  $^{119}\text{Sb}(^{119\text{m}}\text{Sn})$  emission Mössbauer spectroscopy, *Semiconductors*. 33 (8) (1999) 836–837.
- [7] S.A. Nemov, P.P. Seregin, Yu.V. Kozhanova, N.P. Seregin, Two-electron tin centers formed in lead chalcogenides as a result of nuclear transmutations, *Semiconductors*. 37 (12) (2003) 1367–1372.
- [8] N.P. Seregin, P.P. Seregin, S.A. Nemov, A.Y. Yanvareva, Antistructural defects in lead chalcogenides, *J. Phys.: Condensed Matter*. 15 (44) (2003) 7591–7597.
- [9] G.A. Bordovsky, A.V. Marchenko, A.V. Zaiceva, et al., States of antimony and tin atoms in lead chalcogenides, *Semiconductors*. 45 (4) (2011) 427–430.
- [10] G.A. Bordovsky, A.V. Marchenko, N.I. Anisimova, et al., Two-electron tin centers with a negative correlation energy in lead sulfide, *Glass Physics and Chemistry*. 39 (2) (2013). 201–207.
- [11] A.V. Marchenko, A.V. Nikolayeva, P.P. Seregin, et al., The two-electron exchange between  $\text{U}^-$  tin centers in crystal and glass-like chalcogenide semiconductors, *Glass Physics and Chemistry*. 42 (2) (2016) 164–171.
- [12] G.A. Bordovsky, A.V. Marchenko, P.P. Seregin, et al., Two-electron tin centers formed in chalcogenide glasses as a result of nuclear transformations, *Glass Physics and Chemistry*. 36 (6) (2010) 652–656.

Received 19.01.2018, accepted 24.01.2018.

### THE AUTHORS

**ZHUKOV Nikolay N.**

*Herzen State Pedagogical University of Russia*

48 Moyka Emb., St. Petersburg, 191186, Russian Federation

nzhukov@herzen.spb.ru

**MARCHENKO Alla V.**

*Herzen State Pedagogical University of Russia*

48 Moyka Emb., St. Petersburg, 191186, Russian Federation

al7140@rambler.ru

**SHAKHOVICH Kirill B.**

*Herzen State Pedagogical University of Russia*

48 Moyka Emb., St. Petersburg, 191186, Russian Federation

shakhovichkirill@gmail.com



# SPECTRAL AND LUMINESCENT PROPERTIES OF DOPED FLUOROALUMINATE GLASSES PROMISING FOR OPTICAL TEMPERATURE SENSORS

V.A. Klinkov

Peter the Great St. Petersburg Polytechnic University, St. Petersburg, Russian Federation

Spectral and luminescent properties of  $\text{Er}^{3+}$ -doped fluoroaluminate glasses have been studied and presented in the paper. The subject of inquiry was  $98\text{MgCaSrBaYAl}_2\text{F}_{14}-2\text{Ba}(\text{PO}_3)_2$  glass, the  $\text{ErF}_3$  concentrations were of 0.1 – 1.0 mol. %. The optical absorption spectra were analyzed in the range from 190 to 1700 nm, and the nature of absorption bands was explained on a basis of the  $\text{Er}^{3+}$  ion energy diagram. The up-conversion spectra were measured at 77 and 300 K in the 500 – 700 nm range upon 975 nm laser excitation. The temperature dependences of FIR were calculated using the experimental data in a range of (77 – 300) K. Among the samples under investigation the 0.1%  $\text{ErF}_3$  one possessed the greatest response to temperature changes in the range of (77 – 300) K. The studied material was proved to be a candidate for realizing the optical temperature sensors.

**Key words:** optical temperature sensor; rare-earth ion; absorption spectrum; luminescence; fluoroaluminate glass

**Citation:** V.A. Klinkov, Spectral and luminescent properties of doped fluoroaluminate glasses promising for optical temperature sensors, St. Petersburg State Polytechnical University Journal. Physics and Mathematics. 11 (1) (2018) 33 – 40. DOI: 10.18721/JPM.11105

## Introduction

To date, numerous applied and fundamental have been aimed at synthesizing new glassy materials for the near and mid infrared (IR) ranges, since the currently available materials are limited. Vibrational-rotational absorption bands of most molecules and chemical compounds are located within these spectral ranges, making them detectable by IR spectroscopy [1].

The materials of the mid IR range include non-oxide glasses, in particular, fluoride and chalcogenide. The latter are characterized not only by a wider bandwidth of electromagnetic radiation in the IR region than quartz glasses, but also by lower optical losses (this was proved by theoretical studies) [2]. Optical fiber amplifiers and fiber lasers based on non-oxide glass doped with rare earth elements have a significant practical significance for telecommunication lines [3]. It is non-oxide glasses that have an important distinctive characteristic: their high-frequency boundary of the vibrational spectrum is substantially lower than that of oxide glasses; as a consequence, the probability of intracenter nonradiative processes decreases [4] and the quantum yield of the luminescence of

the dopants introduced into the glass matrix increases. In addition, laser electron transitions, which are quenched by thermal lattice vibrations of the glassy matrix in oxide glasses, can be achieved in non-oxide fluoride and chalcogenide glasses.

Non-oxide glasses doped with trivalent ions of rare earth elements are studied for potential applications in near and mid-IR lasers [4], fiber lasers [5], fiber amplifiers [6] and optical sensors [7, 8]. In particular, glasses doped with erbium ions ( $\text{Er}^{3+}$ ) were used to create optical fiber amplifiers for fiber optic communication lines and optical temperature sensors [9], operating on the principle of upconversion luminescence using the FIR (Fluorescence Intensity Ratio) technique; these devices are an alternative to quartz-based ones.

The main advantages of optical temperature detectors over classical contact methods of measurement is that they have a high temperature sensitivity and low inertia, small sizes, electromagnetic passivity and high noise immunity, and they can be used in extreme environmental conditions [10]. To date, the choice of a glassy matrix for optical temperature sensors remains an open problem, but it was established in [11] that the glassy matrix plays a key role in the

sensitivity of optical temperature sensors: the best results have been obtained for glassy systems with lower values of the high-frequency boundary of the vibrational spectrum.

Thus, from the standpoint of their luminescent properties (in particular, taking into account the phenomenon of upconversion luminescence), chalcogenide and fluoride glasses can be considered to be the most promising for creating optical temperature sensors.

The disadvantages of chalcogenide glasses include low chemical and thermal stability, toxicity, incompatibility with quartz glasses in terms of the refractive index ( $n > 2.2$ ) and the thermal parameters, complicated synthesis and low solubility of active impurities such as transition and rare earth elements.

Fluoride glasses allow introducing high concentrations of rare-earth dopants, have a refractive index close to quartz fiber ( $n \approx 1.5$ ), high thermal stability and a wide transparency range (from 0.25 to 8.00  $\mu\text{m}$ ), which makes them the best glassy materials for applications in active optical media for the mid-IR range.

The spectral and luminescent properties of fluoroaluminate  $98\text{MgCaSrBaYAl}_2\text{F}_{14}-2\text{Ba}(\text{PO}_3)_2$  glasses doped with erbium ions ( $\text{Er}^{3+}$ ) have been investigated in this study; the upconversion luminescence spectra obtained at temperatures of 77 and 300 K have been recorded and interpreted.

The intensity ratios of the fluorescence bands generated by energy transitions from the thermally coupled levels to the ground state were calculated on the basis of the experimental data for the temperature range of 77 – 300 K. According to the data available in the literature, the glasses of this composition with this dopant were not previously studied as sensitive elements for upconversion temperature sensors.

The composition of the glass was chosen taking into account the results obtained earlier in [12, 13]. In particular, glasses with the selected composition exhibit reduced crystallization ability, high homogeneity and minimum content of OH groups, as well as a wide pass-band up to 6.4  $\mu\text{m}$ .

### Experimental procedure

The glasses were synthesized in an SU-2000 crucible of for 1 h at temperatures of

Table

**Dopant contents in fluoride  
 $98\text{MgCaSrBaYAl}_2\text{F}_{14}-2\text{Ba}(\text{PO}_3)_2$   
glasses and sample notations**

$\text{Er}^{3+}$ content, mol %	Sample notation
0.1	0.1 % $\text{ErF}_3$
0.5	0.5 % $\text{ErF}_3$
1.0	1.0 % $\text{ErF}_3$

Note. The dopant was introduced into the glassy matrix through erbium fluoride  $\text{ErF}_3$  in excess of 100 mol%.

850 – 950 ° C, without stirring the glass melt, in an argon atmosphere. The glass was melted in an inert argon atmosphere to prevent impurities, particularly, water, iron and hydroxyl groups, from entering the melt from the surrounding air. Erbium fluoride was introduced in excess of 100 mol%. The glass samples obtained this way were cut into 1-mm-thick plane-parallel plates, ground and polished. Compositions and names of the glass samples are given in the Table.

The optical absorption spectra were recorded with a Lambda 900 spectrophotometer (Perkin-Elmer LLC, USA) at room temperature (300 K).

The pumping radiation source was a Ti:sapphire laser with a working wavelength  $\lambda = 975$  nm (the Spectra Physics Model 3900) operating in continuous mode. Luminescence spectra in the 450 – 900 nm range were recorded with a highly sensitive AvaSpec-2048 USB2 fiber-optic spectrometer, an Acton-300 monochromator and an ID-441 receiver (Acton Research Corporation). A GS21525 variable temperature cell holder with optical windows (Specac), paired with a diffusion pump, was used for low-temperature measurements.

### Results and discussion

Fig. 1 shows the optical absorption spectra of fluoroaluminate glass samples in the 190 – 1700 nm range. The bands observed in this range correspond to the  $4f^{11} \rightarrow 4f^{11}$  intraconfiguration transitions from the  $^4I_{15/2}$  ground state to the excited states of  $\text{Er}^{3+}$ , with the position of the maxima of these bands corresponding to the well-known Dicke diagram [14].



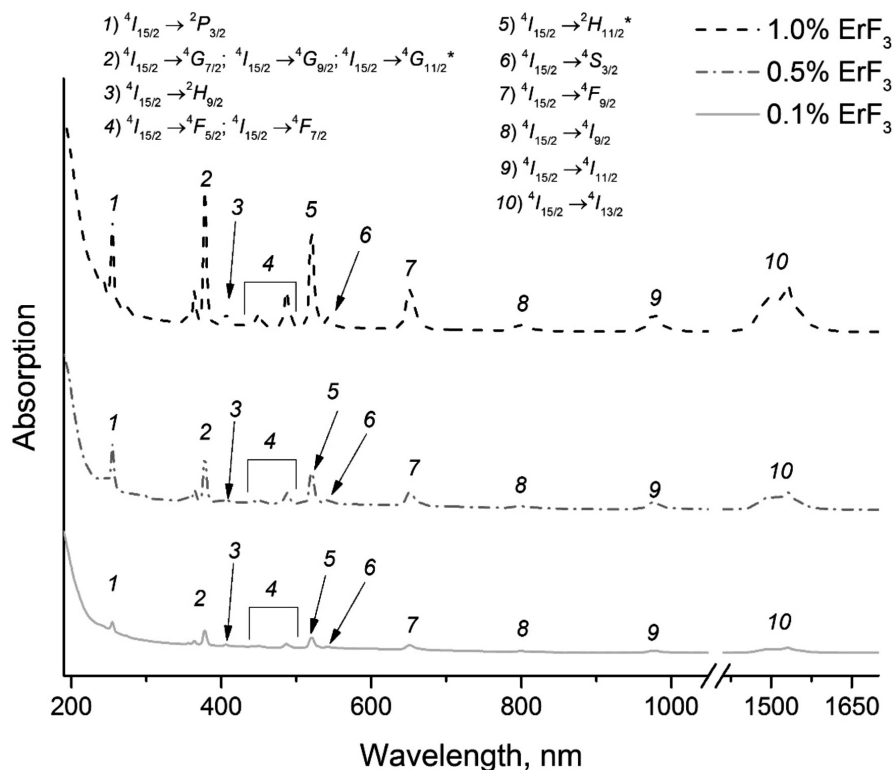


Fig. 1. Optical absorption spectra of fluoroaluminate glass samples of (0.1 – 1.0) %  $\text{ErF}_3$  in the 190 – 1700 nm range.

The asterisks mark the hypersensitive transitions  $^4I_{15/2} \rightarrow ^2H_{11/2}$  and  $^4I_{15/2} \rightarrow ^4G_{11/2}$

The most intense and wide absorption bands have maxima at about 378, 487, 521, 651, 976 and 1532 nm and correspond to transitions from the  $^4I_{15/2}$  ground state to the  $^4G_{11/2}$ ,  $^4F_{7/2}$ ,  $^2H_{11/2}$ ,  $^4F_{9/2}$ ,  $^4I_{11/2}$  and  $^4I_{13/2}$  levels, respectively. The positions of the absorption band maxima do not change with increasing dopant concentration and leads only to a relative increase in the absorption intensity, which may indirectly indicate a homogeneous distribution of the dopant.

To verify the agreement between the actual concentrations of the absorption centers ( $\text{Er}^{3+}$  ions) and the calculated values and to confirm the absence of dopant segregation in the glass [15], we have checked whether the Beer–Lambert–Bouguer law [16] was fulfilled for bands with the highest absorption coefficient values: 378, 521, 976 and 1532 nm (the positions of the maxima are indicated). The dependence of the absorption coefficients on the dopant concentration is shown in Fig. 2. The linear

dependence obtained confirms that this law is fulfilled and that the actual concentrations of

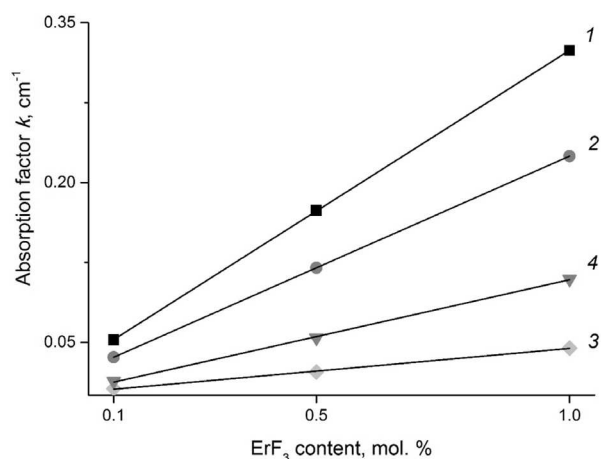


Fig. 2. Concentration dependences of the optical absorption coefficient for electron transitions at wavelengths of 378 nm (1), 521 nm (2), 976 nm (3) and 1532 nm (4) in fluoroaluminate glass samples activated by  $\text{Er}^{3+}$  ions



dopant ions agree with the calculated values.

The narrow and well-resolved absorption bands associated with the hypersensitive electron transitions  $^4I_{15/2} \rightarrow ^2H_{11/2}$  and  $^4I_{15/2} \rightarrow ^4G_{11/2}$  also indicate that the dopant distribution in the samples is homogeneous. Thus, analysis of the obtained optical absorption spectra showed that segregation effects are not observed

in the samples and there is no inhomogeneous broadening of the absorption bands. This indicates that an increase in the concentration of  $Er^{3+}$  ions does not lead to a disturbance of the glass structure and does not generate diverse local environments that  $Er^{3+}$  ions can occupy [17].

Fig. 3 shows the upconversion luminescence

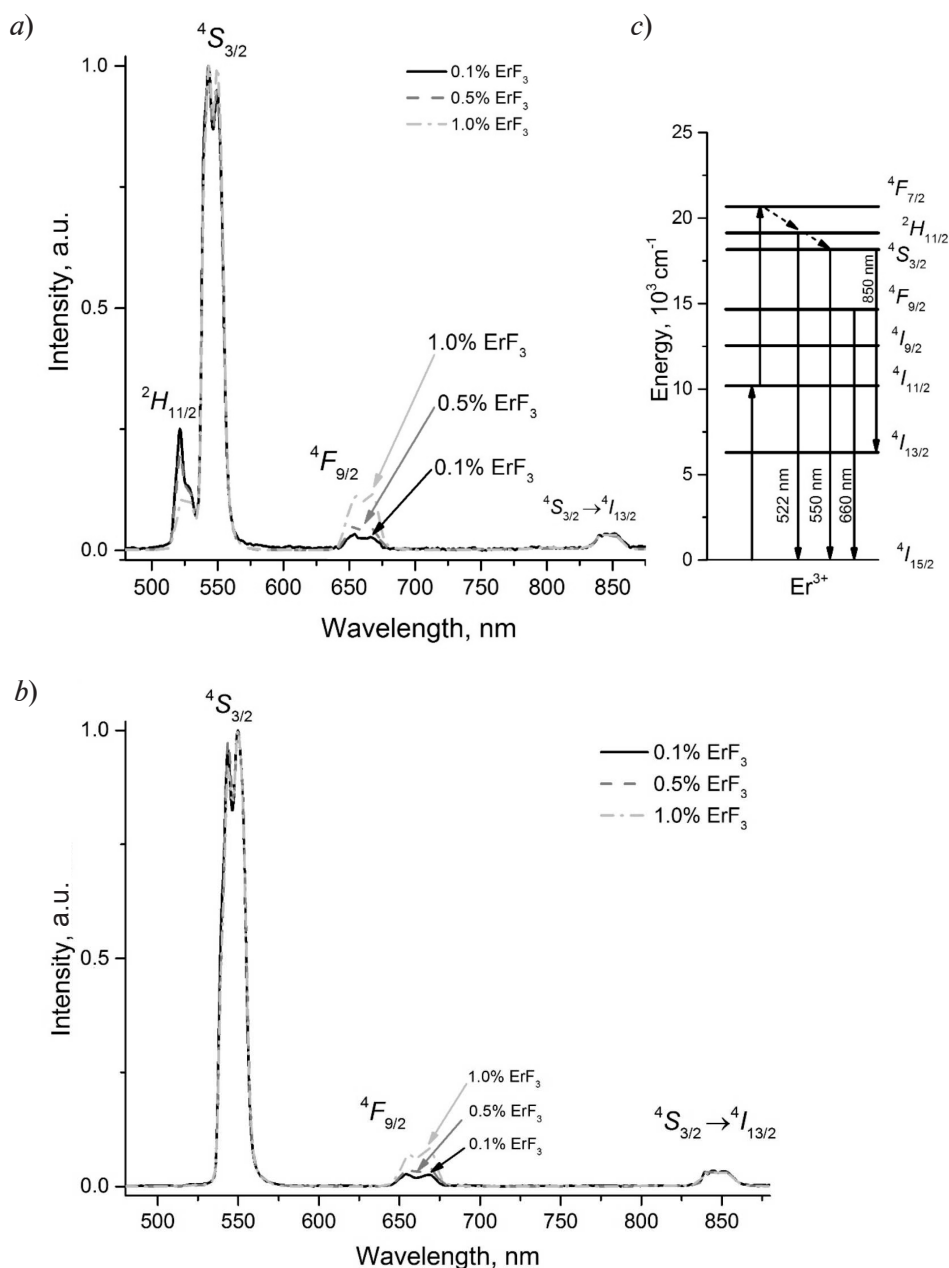


Fig. 3. Upconversion luminescence spectra of doped fluoroaluminate glass samples at 300 K (a) and 77 K (b); the luminescence intensities are normalized to the maximum intensity of each spectrum; the energy level diagram of the  $Er^{3+}$  ion and the excitation energy transfer mechanism (c) are given



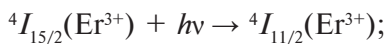
spectra of doped fluoroaluminate glass samples in the 450 – 900 nm range obtained by excitation with coherent radiation from a Ti:sapphire laser at a wavelength  $\lambda = 975$  nm operating in continuous mode at temperatures of 300 and 77 K.

Let us consider the luminescence spectra obtained at 300 K (Fig. 3, *a*). The spectra include three groups of bands: with emission maxima around 522 and 550 nm in the green region, around 660 nm in the red region and around 850 nm in the near IR region.

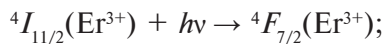
The first group of bands is due to electron transitions from the  $^2H_{11/2}$  (522 nm) and  $^4S_{3/2}$  (550 nm) levels to the  $^4I_{15/2}$  ground state. These levels are populated from the upper  $^2F_{7/2}$  level by a mechanism of excitation energy transfer [13]. The energy level diagram of the  $\text{Er}^{3+}$  ion and the excitation energy transfer mechanism under pumping by laser radiation at a wavelength  $\lambda = 975$  nm are shown in Fig. 3, *c*.

Let us consider the mechanism of excitation energy transfer in more detail. The mechanism includes ground state absorption (GSA), excited state absorption (ESA), and the exchange interaction. In view of these phenomena, the population of the  $^4F_{7/2}$  level can occur by the following scheme:

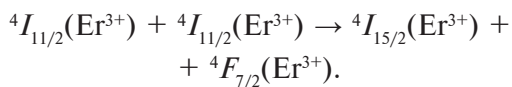
ground state absorption by the reaction



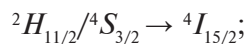
excited state absorption by the reaction



exchange interaction by reaction

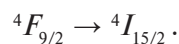


Next, non-radiative relaxation occurs from the  $^4F_{7/2}$  level to the levels  $^4H_{11/2}$  and  $^4S_{3/2}$ , and then a radiative transition to the ground state occurs by the scheme



while the luminescence peaks are positioned at wavelengths of about 522 and 550 nm, respectively.

The red luminescence band (660 nm) is associated with an electron transition



The population of the  $^4F_{9/2}$  level occurs with the participation of the energy levels  $^4F_{7/2}$ ,  $^4H_{11/2}$  and  $^4S_{3/2}$  above it through a non-radiative relaxation process. Due to the multistage nature of the population mechanism, the  $^4F_{9/2}$  level is far less populated than the levels  $^4H_{11/2}$  and  $^4S_{3/2}$ , which leads to a significantly lower relative intensity of the luminescence band with a maximum at about 660 nm.

The third luminescence band in the 850 nm region is due to the  $^4S_{3/2} \rightarrow ^4I_{13/2}$  electron transition. The presence of this band is important because in this case the transition is not from the excited state to the ground state but from the excited state to the non-ground state below it. The probability of this process is rather low, and the value of the high-frequency boundary of the vibrational spectrum of the glassy matrix is a factor considerably affecting the  $^4S_{3/2} \rightarrow ^4I_{13/2}$  transition. Notably, this band is found mainly in non-oxide glasses, in particular, in fluoride glasses [18].

Let us analyze the upconversion luminescence spectra obtained at a temperature of 77 K (Fig. 3, *b*). The same as at room temperature, three groups of bands can be observed on the spectra. The spectral positions of the luminescence band maxima are completely identical at 300 and 77 K. However, a significant decrease is observed in the intensity of the luminescence peak around 522 nm for all concentrations of the dopant. This phenomenon confirms the thermal nature of the population of the  $^2H_{11/2}$  energy level. At room temperature, the  $^2H_{11/2}$  level is thermally populated from the  $^4S_{3/2}$  level, but as the temperature decreases to 77 K, the energy of thermal quanta and consequently the probability that the  $^2H_{11/2}$  level is populated decrease as well. This can explain the significant decrease in the relative intensity of the luminescence band around 522 nm at  $T = 77$  K.

Going back to the luminescence spectra at 300 K (see Fig. 3, *a*), we can see that the spectrum of the 1.0 %  $\text{ErF}_3$  sample has the lowest value of the relative intensity of the luminescence peak caused by the  $^2H_{11/2} \rightarrow ^4I_{15/2}$  transition (522 nm) and the highest value for the  $^4F_{9/2} \rightarrow ^4I_{15/2}$  transition (660 nm). Notice that the maximum relative intensity of the 660-nm

band was observed in the spectrum of this sample both at room temperature and at 77 K.

A consistent explanation for these facts is as follows. An increase in the dopant concentration leads to a decrease in the average distance between optically active ions and an increased probability of their exchange interaction, which affects the increase in the population of the  $^4F_{9/2}$  level and a decrease in the relative population of the  $^2H_{11/2}$  level. The invariable relative intensity of the  $^4S_{3/2} \rightarrow ^4I_{13/2}$  transition (850 nm) indicates that the change in the  $Er^{3+}$  ion concentration does not lead to a change in the  $^4S_{3/2}$  level population mechanism.

Let us consider the characteristics of the energy levels  $^2H_{11/2}$  and  $^4S_{3/2}$  in more detail. According to the data obtained from the optical absorption spectra, the energy gap  $\Delta E$  between these levels is about  $770 \text{ cm}^{-1}$ . Due to such a low value (much less than  $2000 \text{ cm}^{-1}$ ) for glasses doped with  $Er^{3+}$  ions, the relative population of the  $^4H_{11/2}$  and  $^4S_{3/2}$  levels depends on temperature [19]. Besides, since  $\Delta E$  exceeds the energy of thermal quanta (about  $210 \text{ cm}^{-1}$ ) at room temperature, the luminescence bands from two energy levels do not overlap. As a result, the upper  $^2H_{11/2}$  level has a smaller population of optically active ions than the  $^4S_{3/2}$  level; thus, the  $^2H_{11/2}$  and  $^4S_{3/2}$  levels turn out to be thermally coupled, and their relative populations obey the Boltzmann distribution [19].

This phenomenon is used to develop optical temperature sensors based on the FIR (Fluorescence Intensity Ratio) technique [20] requiring for the temperature dependence of the intensity ratio of the thermally coupled levels to be proportional to the relative population of the  $^2H_{11/2}$  and  $^4S_{3/2}$  levels [21]:

$$\text{FIR} = \frac{I_H}{I_S} = \frac{g_H \sigma_H \omega_H}{g_S \sigma_S \omega_S} \exp\left(-\frac{\Delta E}{k_B T}\right) = C \exp\left(-\frac{\Delta E}{k_B T}\right), \quad (1)$$

where  $I_H, I_S$  are the intensities of the luminescence peaks associated with the  $^2H_{11/2} \rightarrow ^4I_{15/2}$  and  $^4S_{3/2} \rightarrow ^4I_{15/2}$  transitions, respectively; the parameters  $\sigma_H, \sigma_S, \omega_H, \omega_S$  are the emission cross-sections and frequencies of the luminescent transitions  $^2H_{11/2} \rightarrow ^4I_{15/2}$  and  $^4S_{3/2} \rightarrow ^4I_{15/2}$ ;  $g_H, g_S$  are the degeneracy factors of the  $^2H_{11/2}$  and  $^4S_{3/2}$

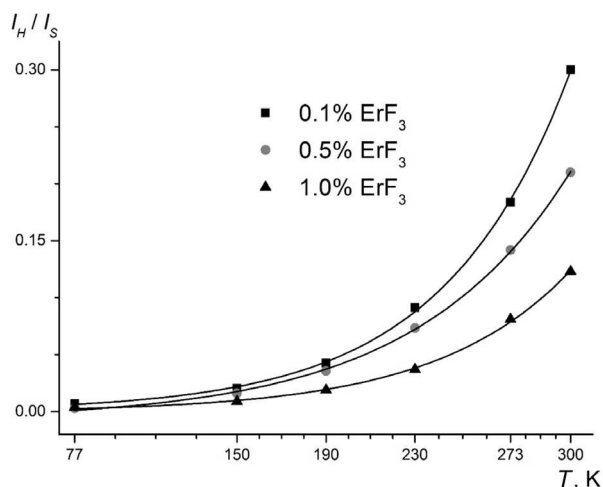


Fig. 4. Experimental FIR ( $I_H / I_S$ ) results (symbols) for fluoroaluminate glass samples with different concentrations of the dopant  $Er^{3+}$ . The solid lines correspond to the exponential approximation by formula (1)

levels;  $k_B$  is the Boltzmann constant, and  $T$  is the temperature.

To obtain the temperature dependences for FIR of the samples under consideration, we have measured the upconversion luminescence in the temperature range of  $77 - 300 \text{ K}$ . The experimental data obtained are shown in Fig. 4. We should note that the temperature dependence of the ratio of fluorescence peaks (FIR) is in agreement with the theoretical one and has an exponential character. It can be also seen that FIR increases with increasing temperature for all the samples, indicating an increase in sensitivity. The sample with the lowest  $Er^{3+}$  content, 0.1 %  $ErF_3$ , has exhibited the highest FIR values in the investigated temperature range, possibly due to a lower probability of exchange interactions of optically active ions and radiation reabsorption, which modify the mechanism of population of the  $^2H_{11/2}$  and  $^4S_{3/2}$  levels [11].

The obtained results indicate that the sample with the lowest content of  $Er^{3+}$  ions was the most sensitive to temperature changes of all samples with the concentrations of the  $ErF_3$  dopant ranging from 0.1 to 1.0 mol%.

## Conclusion

We have studied the spectral and lumines-



cent properties of fluoroaluminate glasses of the composition  $98\text{MgCaSrBaYAl}_2\text{F}_{14}-2\text{Ba}(\text{PO}_3)_2$ , doped with the  $\text{Er}^{3+}$  ions with variable dopant content. Analysis of the optical absorption spectra of the glasses revealed no effects of dopant segregation and no inhomogeneous broadening of the spectral bands in the samples under consideration. The Beer–Lambert–Bouguer law was found to be fulfilled for the most intense absorption bands.

We have obtained the upconversion luminescence spectra at temperatures of 77 and 300 K, and proposed a mechanism for the transfer of excitation energy, explaining the nature of the observed luminescence bands in the visible and near-infrared regions of the spectrum, based on analysis of the energy level diagram of the  $\text{Er}^{3+}$  ion. The key factor governing the emergence of these bands is the population of the  $^4F_{7/2}$  energy level, which may occur in two ways: through exchange interaction and through absorption of electromagnetic radiation energy from the excited state.

We have established the influence of the concentration of dopant ions on the relative intensity of the band with a maximum of about 660 nm corresponding to the  $^4F_{9/2} \rightarrow ^4I_{15/2}$  electronic transition. The relative intensity growth in this band with an increase in the dopant concentration can be attributed to increasing probability of exchange interaction between optically active ions due to a decrease in the average distance between  $\text{Er}^{3+}$  ions.

The intensity ratio of the upconversion luminescence bands with maxima around 522 nm and 550 nm in the temperature range of 77–300 K were analyzed using the FIR technique. These bands correspond to transitions from the thermally coupled energy levels  $^2H_{11/2}$  and  $^4S_{3/2}$  to the ground state  $^4I_{15/2}$ . The obtained

temperature dependences of the ratio of the fluorescence intensity peaks indicate the exponential character of the relative population of the  $^2H_{11/2}$  and  $^4S_{3/2}$  levels. We have additionally found that the FIR value increased and reached its maximum value at 300 K with increasing temperature for all the samples examined. We have also established that the FIR response decreases with an increase in the  $\text{Er}^{3+}$  ion concentration at the same temperature, which may be associated with an increasing probability of exchange interactions between optically active ions and with radiation reabsorption; these factors lead to a modification of the process of population of the  $^2H_{11/2}$  and  $^4S_{3/2}$  levels.

The results of this study indicate that it is possible to use activated fluoroaluminate glasses of the composition we have investigated as a material for creating a sensitive element in optical temperature sensors based on the FIR technique.

Of all the samples examined, the one with the minimal  $\text{Er}^{3+}$  ion content (0.1%) was the most sensitive to temperature changes in the temperature range of 77–300 K.

Potential use of fluoroaluminate glasses of the investigated composition in the region of high temperatures (up to 600 K) and the reaction of the samples to such temperature changes require further study.

### Acknowledgment

The author expresses his most sincere gratitude to V.A. Assev, associate professor of the ITMO University, for assistance in conducting luminescence measurements, and to A.V. Semench, associate professor of the Polytechnic University for fruitful discussion of the results.

### REFERENCES

- [1] M.J. Thorpe, K.D. Moll, R.J. Jones, et al., Broadband cavity ringdown spectroscopy for sensitive and rapid molecular detection, *Science*. 311 (5767) (2006) 1595–1599.
- [2] G.F. West, W. Höfle, Spectral attenuation of fluoride glass fibers, *J. Non-Cryst. Solids*. 213–214 (1997) 189–192.
- [3] M.A. Khamis, K. Ennser, Design of highly efficient  $\text{Pr}^{3+}$ -doped chalcogenide fiber laser, *IEEE Photonics Technology Letters*. 29 (18) (2017) 1580–1583.
- [4] H. Chen, F. Chen, T. Wei, et al.,  $\text{Ho}^{3+}$ -doped fluorophosphate glasses sensitized by  $\text{Yb}^{3+}$  for efficient 2  $\mu\text{m}$  laser applications, *Opt. Commun.* 321 (2014) 183–188.
- [5] M.C. Paul, S. Bysakh, Sh. Das, et al., Recent developments in rare-earths doped nano-engineered glass based optical fibers for high power fiber lasers, *Trans. Ind. Ceram. Soc.* 75 (4) (2016) 195–208.
- [6] G. Tang, Z. Yang, L. Luo, W. Chen,  $\text{Dy}^{3+}$ -

doped chalcogenide glass for 1.3- $\mu\text{m}$  optical fiber amplifiers, *J. Mater. Res.* 23 (4) (2008) 954–961.

[7] **J. Fu, M. Kobayashi, S. Sugimoto, J.M. Parker**,  $\text{Eu}^{3+}$ -activated heavy scintillating glasses, *Mater. Res. Bull.* 43 (6) (2008) 1502–1508.

[8] **M. Haouari, A. Maaoui, N. Saad, A. Bulou**, Optical temperature sensing using green emissions of  $\text{Er}^{3+}$  doped fluoro-tellurite glass, *Sensors and Actuators, A: Physical*. 261 (2017) 235–242.

[9] **Z.P. Cai, Hue-Yin Xu, S.L. Yang, et al.**, Micrometer-sized point temperature sensor in  $\text{Er}$ :  $\text{ZBLALiP}$ , *Proc. SPIE*. 4919 (20 Sept.) (2002) 501–507.

[10] **C.D.S. Brites, P.P. Lima, N.J.O. Silva, et al.**, Thermometry at the nanoscale, *Nanoscale*. 4 (2014) 4799–4829.

[11] **S.F. León-Luis, U.R. Rodríguez-Mendoza, P. Haro-González, et al.**, Role of the host matrix on the thermal sensitivity of the  $\text{Er}^{3+}$  luminescence in optical temperature sensors, *Sensors and Actuators. B: Chemical*. 174 (2012) 176–186.

[12] **S.A. Sirotkin, D.S. Sysoev, T.V. Bocharova, et al.**, Spectroscopic properties of the glass of fluoroaluminate systems with small additives of barium metaphosphate activated with the ions of rare-earth elements, *Glass Phys. Chem.* 41 (3) (2015) 265–271.

[13] **V.A. Klinkov, A.V. Semench, E.A. Tsimerman**, Advanced materials for fiber communication systems, Internet of Things, Smart Spaces, and Next Generation Networks and Systems, 17<sup>th</sup> Intern. Conf., Russia, St. Petersburg,

Aug. 28 –30, 2017. *Proc.*, Springer, Pp. 184–195.

[14] **G.H. Dieke, R.A. Satten**, Spectra and energy levels of rare earth ions in crystals, *Am. J. Phys.* 38 (3) (1970) 399–400.

[15] **A.V. Dmitryuk, G.O. Karapetyan, L.V. Maksimov**, Phenomenon of activator segregation and its spectroscopic consequences, *J. Appl. Spectroscopy*. 22 (1) (1975) 119–141.

[16] **G.S. Landsberg**, *Optika [Optics]*, Moscow, Nauka, 1976.

[17] **A.V. Malov, M.O. Marychev, P.A. Ryabochkina, et al.**, Spektroskopicheskiye i strukturnyye svoystva kristallov kaltsiy-niobiy-galliyevogo granata, aktivirovannykh ionami  $\text{Er}^{3+}$  [Spectroscopic and structural properties of  $\text{Er}^{3+}$ -doped calcium-niobium-gallium garnet crystals], *Vestnik Nizhegorodskogo universiteta im. N.I. Lobachevskogo*. (6) (2008) 46–52.

[18] **T. Catunda, L.A.O. Nunes, A. Florez, et al.**, Spectroscopic properties and upconversion mechanisms in  $\text{Er}^{3+}$ -doped fluorindate glasses, *Phys. Rev. B*. 53 (10) (1996) 6065–6070.

[19] **E. Maurice, G. Baxter, G. Monnom, et al.**, Thermalization effects between upper levels of green fluorescence in  $\text{Er}$ -doped silica fibers, *Opt. Lett.* 19 (13) (1994) 990–992.

[20] **V.K. Rai**, Temperature sensors and optical sensors, *Appl. Phys. B*. 88 (2) (2007) 297–303.

[21] **V.K. Rai, S.B. Rai**, A comparative study of FIR and FL based temperature sensing schemes: an example of  $\text{Pr}^{3+}$ , *Appl. Phys. B*. 87 (2) (2007) 323–325.

*Received 19.01.2018, accepted 24.01.2018.*

#### THE AUTHOR

**KLINKOV Victor A.**

*Peter the Great St. Petersburg Polytechnic University*

29 Politechnicheskaya St., St. Petersburg, 195251, Russian Federation

klinkovvictor@yandex.ru



## SIMULATION OF HIGH-SPEED CAVITATING FLOWS IN CHANNELS

**I.I. Isaenko<sup>1</sup>, A.V. Makhnov<sup>1</sup>, E.M. Smirnov<sup>1</sup>, A.A. Schmidt<sup>2</sup>**

<sup>1</sup>Peter the Great St. Petersburg Polytechnic University, St. Petersburg, Russian Federation;

<sup>2</sup>Ioffe Institute of the Russian Academy of Science, St. Petersburg, Russian Federation

Cavitation is a process of vapour and gas bubbles formation in a liquid flow. It occurs when a flow pressure drops below a certain level depending on liquid's physical properties and its temperature. One of the important factors of cavitation is the presence of unsolved microscopic bubbles filled with gas and/or vapour in real liquids. These bubbles, or nucleation sites, evolve under pressure drops that are sufficient for evaporation of surrounding liquid.

A model of cavitating flows based on Euler – Lagrange description of multiphase medium has been developed. It took into account heterogeneous nature of cavitation bubbles formation. The Rayleigh – Plesset equation along with interphase mass and energy transfer equations were used to simulate bubbles evolution. The developed model provides qualitatively accurate prediction of cavity shape and its borders position in comparison with the experimental data.

**Key words:** high-speed flow; cavitation; Rayleigh–Plesset equation; multiphase medium

**Citation:** I.I. Isaenko, A.V. Makhnov, E.M. Smirnov, A.A. Schmidt, Simulation of high-speed cavitating flows in channels, St. Petersburg Polytechnical State University Journal. Physics and Mathematics. 11 (1) (2018) 41 – 49. DOI: 10.18721/JPM.11106

### Introduction

Cavitation, i.e., the formation of cavities (bubbles or caverns) filled with vapor or vapor-gas mixture in a liquid is a fundamental problem that is the focus of constant interest in connection with the developing theory of multiphase media with its vast array of applications [1]. The phenomenon of cavitation occurs when pressure drops below a certain level depending on the properties of the liquid and its temperature [2 – 6]. Microscopic inclusions (such as bubbles and solid particles), i.e., nucleation sites or cavitation nuclei, that may be present in the liquid play a major role in this.

As pressure increases in the cavitating medium, cavities (bubbles) collapse, generating shock waves and high-velocity cumulative jets that cause cavitation-induced erosion.

Cavitation is a widespread phenomenon, which is why cavitation research has a great practical importance. Studies on the subject

cover a diverse range of issues from physiology (for example, blood boiling with a decrease in pressure [1]) to design of power and transport equipment (water turbines, pumps, propellers, valves, etc.) [3 – 4, 7] and technologies using the effects of energy release in liquids [2, 8 – 9].

The erosion accompanying the evolving cavitation can greatly affect the functioning of the corresponding devices, decreasing their productivity and even causing them to break down. Therefore, erosion research is also of great interest in fundamental and applied research.

It should be noted that experimental study of cavitation is incredibly difficult due to the extreme values of cavitation parameters and different spatio-temporal scales of the processes under consideration. Because of this, mathematical modeling becomes a promising and effective tool for studying cavitation [7 – 9].

This paper is devoted to the analysis of one possible approach to mathematical simulation of cavitation.

### Mathematical model of cavitating fluid flows

The Euler/Euler and Euler/Lagrange representations [10] are the two main approaches to flow simulation in multiphase media.

In the first case, the heterogeneous medium under consideration is replaced by a quasi-homogeneous mixture with continuous distributions of densities, velocities, pressures, and other phase parameters. Both phases (carrier liquid and bubbles) in this model occupy the entire volume of the mixture, and the concept of phase volume fraction is introduced, allowing to determine the effective densities of the components of a quasi-homogeneous mixture and to use a system of Navier – Stokes equations for computing cavitation flows.

However, these models typically do not account for the physics of evolution of the bubbles formed during cavitation, which can be a crucial factor in some cases.

Within the second approach, the motion of the carrier phase is governed by the equations of dynamics of a continuous medium, and the Lagrange approach based on introducing a set of test particles is used for describing the motion of dispersed phase (in particular, bubbles). The computation of flows in a multiphase medium includes the following stages:

solving the carrier phase equations (Euler stage);

solving the equations of test particle motion in accordance with the flow field of the carrier phase obtained in the previous stage (the Lagrange stage equations);

solving the interphase transport equations to take into account the effect of the dispersed phase on the carrier;

refining the flow field of the carrier phase taking into account the effect of the dispersed phase (a new time step within the Euler stage).

The second approach involves considerable computational costs but allows to compute the dynamics of each test particle (bubble) individually, and also to take into account the fact that the particle size distribution is non-uniform, in contrast with the Euler/Euler model that averages the particles' behavior. This advantage is the reason why developing Euler/Lagrange methods seems to be the most expedient.

The motion of the carrier phase at the Euler stage is described by a system of Navier – Stokes equations:

$$\begin{aligned}\frac{\partial \rho}{\partial t} + \nabla \cdot (\rho \mathbf{V}) &= 0; \\ \frac{\partial (\rho \mathbf{V})}{\partial t} + \nabla \cdot (\rho \mathbf{V} \mathbf{V}) &= -\nabla P + \frac{\partial \tau_{ij}}{\partial x_j}; \\ \frac{\partial}{\partial t} (\alpha_v \rho_v) + \nabla \cdot (\alpha_v \rho_v \mathbf{V}) &= S_v - S_l,\end{aligned}\quad (1)$$

where  $\rho$ , kg/m<sup>3</sup> is the mixture density;  $\rho = \rho_l \alpha_l + \rho_v \alpha_v$ , ( $\alpha$  is the volume fraction of matter, the indices  $l$  and  $v$  refer to liquid and vapor, respectively);  $\mathbf{V}$ , m/s, is the velocity vector;  $P$ , Pa, is the pressure;  $S$ , kg/m<sup>3</sup>·s, are the source terms (distribution densities of mass sources, the indices  $l$  and  $v$  also refer to liquid and vapor, respectively);  $\tau_{ij}$  are the stress tensor components.

The motion of bubbles in the velocity field at the Lagrange stage is computed with or without mass forces:

$$\frac{d\mathbf{X}}{dt} = \mathbf{F}, \quad (2)$$

where  $\mathbf{X} = [x; y; z]$ ,  $\mathbf{F} = [V_x; V_y; V_z]$  ( $V_i$  are the velocity components).

Next, a system of equations based on the laws of conservation of mass and energy is solved:

$$\frac{d}{dt} \left( \frac{4}{3} \pi R_B^3 \rho_v \right) = 4 \pi R_B^2 \dot{m}, \quad (3)$$

$$\begin{aligned}\frac{d}{dt} \left( \frac{4}{3} \pi R_B^3 \rho_v U_B \right) &= \\ &= -P_B \frac{d}{dt} \left( \frac{4}{3} \pi R_B^3 \right) - 4 \pi R_B^2 U_{12},\end{aligned}\quad (4)$$

where  $R_B$  is the radius of a cavitation bubble;  $m$  is the mass;  $U_B$  is the internal energy of a cavitation bubble;  $P_B$ , Pa, is the vapor pressure in a cavitation bubble;  $U_{12}$  is the energy flux through the interface.

System (3), (4) can be transformed to the following form, suitable for directly determining the parameters of the vapor inside the bubble [9, 19]:





$$\frac{dP_B}{dt} = P_B \left( \frac{1}{T_B} \frac{dT_B}{dt} - \frac{3}{R_B} \left[ \frac{dR_B}{dt} - \frac{\eta_{ac} T_B}{P_B} \frac{\sqrt{r_v}}{\sqrt{2\pi}} \left( \frac{P_s(T_l)}{\sqrt{T_l}} - \frac{P_B}{\sqrt{T_B}} \right) \right] \right); \quad (5)$$

$$\frac{dT_B}{dt} = -3 \frac{T_B}{R_B P_B} \left[ (\gamma - 1) \left( P_B + \frac{2\Sigma}{R_B} \right) \frac{dR_B}{dt} + \eta_{ac} P_s(T_l) (T_B - T_l) \sqrt{\frac{r_v}{2\pi T_l}} \right], \quad (6)$$

where  $P_s$ , Pa, is the saturated vapor pressure;  $T_l$ ,  $T_B$ , K, are the temperatures of liquid and gas in the bubble, respectively;  $\eta_{ac}$  is the accommodation coefficient;  $r_v$  is the specific gas constant;  $\Sigma$ , N/m, is the coefficient of surface tension;  $\gamma$  is the adiabatic exponent of gas.

The accommodation coefficient  $\eta_{ac}$  is equal to 0.04 for water, the specific gas constant  $r_v = P_v / \rho_v T_v M_v$  ( $T_v$  is the vapor temperature,  $M_v$  is the molar mass of the gas in the bubble), the adiabatic exponent of gas  $\gamma = 1.4$ .

Eqs. (5) and (6) are supplemented by the equation for the dynamics of radial motion of a bubble in the Rayleigh – Plesset form [11, 12]:

$$R_B \frac{d^2 R_B}{dt^2} + \frac{3}{2} \left( \frac{dR_B}{dt} \right)^2 = \frac{1}{\rho_l} \left( P_B - P_\infty - \frac{4\mu}{R_B} \frac{dR_B}{dt} - \frac{2\Sigma}{R_B} \right), \quad (7)$$

where  $P_\infty$ , Pa, is the external flow pressure;  $\mu$ , Pa·s, is the dynamic viscosity.

This equation describes the growth and collapse of a spherically symmetric vapor bubble taking into account the inertia in the radial motion of the surrounding liquid, the difference between internal and external pressures ( $P_B - P_\infty$ ), and viscosity and surface tension. The processes of gas diffusion have not been described in our study.

#### Approaches to describing the emerging cavitation

Most models of cavitation flows use the Euler/Euler description of a two-phase medium.

They can be based on barotropic equations of the state of the medium [18], thermodynamic relations [17] or the coupling equations between the source terms  $S$  responsible for interphase mass transfer and the dynamics of bubble growth and collapse [16, 17]. The problem of flow past a NACA-66 airfoil was considered in [13, 14, 16], with experimental data provided in [15].

A number of cavitation models based on thermodynamic relations for phase transitions were proposed in [17]. The simplest of these models is based on the assumption of phase equilibrium and the number of cavitation nuclei sufficient to neglect the metastable state time, which is valid for simple flows. The study also considers some more complex differential models that take into account metastability, heat transfer during phase transitions, presence of bubbles of undissolved gas and other factors. Models using the Euler/Euler description give qualitatively similar distributions of the vapor fraction and are adequate for predicting the size of the cavities. However, these models do not take into account the physics of vaporization and condensation, since they assume that vapor is formed only when the saturation pressure is reached (the volume fraction of gas bubbles in the mixture is assumed to be sufficient to neglect the delay in the phase transition). Another disadvantage of this approach is that the simulation results depend on the values of empirical parameters included in the equations; because of this, they have to be additionally adjusted [16, 17].

In recent years, various research groups have performed computations of cavitation flows using the Euler/Lagrange description. In Ref. [19], a cavitation cloud was computed using the Lagrange method for modeling the dynamics of discrete bubbles. The carrier phase is represented by a quasi-homogeneous mixture with a variable continuous density distribution satisfying the laws of conservation of mass and momentum. The growth and collapse of bubbles was simulated using the Keller – Herring equation (a modification of the Rayleigh – Plesset equation). The volume fraction of vapor was computed from the data on the location of bubbles and their sizes, a Gaussian distribution function was used to

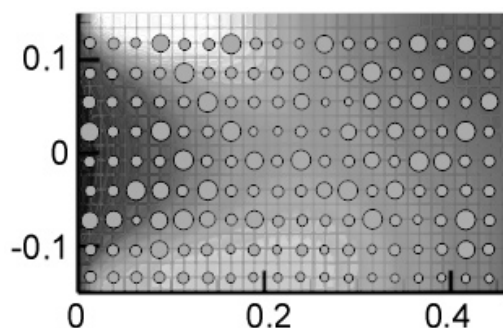


Fig. 1. Computational scheme for the distribution of test bubbles in the field of the carrier medium based on the experimental data of [4]

convert the discrete distribution of bubbles in the volume to a continuous density field of the mixture.

These studies used the data on the microparticles (microbubbles) observed in liquids, serving as nucleation sites. According to the experimental data of Ref. [4], one cubic meter of distilled water contains about  $10^{11}$  –  $10^{12}$  nucleation sites, and their characteristic radii lie in the range from 1 to 6  $\mu\text{m}$  (Fig. 1). The presence of these sites ensures that heterogeneous nucleation evolves and cavitation bubbles develop [20]. The basis for the developing cavitation nuclei are the particles or surface inhomogeneities whose sizes (radii) exceed the critical value  $R_{cr}$ , determined from the Laplace relation:

$$R_{cr} = \frac{2\Sigma}{P_s - P_l}, \quad (8)$$

where the indices  $s$  and  $l$  refer, respectively, to saturated vapor pressure and pressure in the liquid flow.

In this study we have used a technique for computing cavitation flows based on the Euler/Lagrange description of a two-phase medium and a simplified model of heterogeneous nucleation in which only vapor bubbles present in the liquid act as vaporization centers (other factors, such as air bubbles, solid impurities and surface roughness were not taken into account).

#### The Euler/Lagrange algorithm for computation of cavitating media flow

Each time step within the Euler stage of the algorithm involves determining the velocity and pressure fields of the carrier medium, used as input data for the Lagrange stage. At the first step, the computational domain is filled with test bubbles (see Fig. 1).

The initial distribution of bubbles in the liquid in this study is given in accordance with the experimental data from [4]. The size distribution of nucleation sites is replaced by a piecewise constant function;  $N_B$  is the number of nuclei with a radius  $R_B$  (Fig. 2).

The Lagrange stage of the algorithm

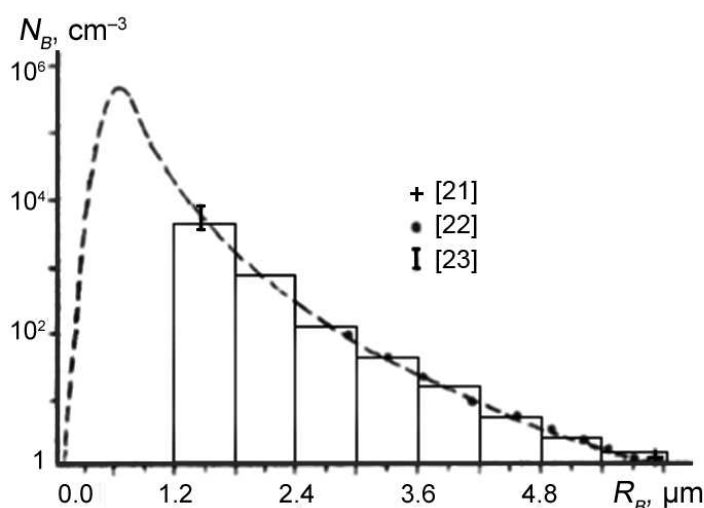


Fig. 2. Approximation of the spectrum of nucleation sites (dashed line) by a piecewise constant function (solid lines)



involves computing the motion and the change in the size of the test bubbles. In this case, the fields of the carrier phase are interpolated according to the scheme shown in Fig. 3, *a* to determine the parameters in the location of the bubble. The growth of test bubbles is described by system of equations (5) – (7).

After all available test bubbles have been processed, the volume fraction of vapor is computed taking into account the number of bubbles in each control volume and the numerical density (the probability of finding the bubbles) is computed for bubbles of a given type per unit volume (reference volume). The scheme used translates the values from bubble locations to the nearest nodes of the auxiliary computational grid (Fig. 3, *b*). This approach ensures that the field of the vapor volume fraction is continuous. The density field is adjusted with respect to the obtained values of the vapor volume fraction; next, adjustments for taking into account the law of conservation of mass are introduced, and a transition to the Euler stage is made for a new physical time step.

When bubbles move and grow, they can interact with each other and merge. The merging and break-off of bubbles is not taken into account in our study. Instead, a conditional boundary, determined by the value of the vapor volume fraction  $\alpha_v$ , is introduced between bubble cavitation and cavity modes. In

the latter case, Euler/Euler description can be used in the region where cavitation is deemed to be well-developed (with high  $\alpha_v$  values) and the internal parameters of the bubbles are fixed. Such a hybrid model preserves the advantages of the Lagrange description of the dynamics of discrete bubbles in cases of bubbly cavitation and allows to avoid time-consuming computations of the parameters of each bubble in regions with well-developed cavitation.

The assumptions introduced make it possible to simplify the implementation of the method, since that way, it is no longer necessary to simulate cavity collapse and the merging of individual bubbles, keeping their number constant. In this case, the cavity is represented by an artificial dense ‘cloud’ of cavitation bubbles.

### Testing the model

The following problems have been considered in simulating the cavitation process:

1. Evolution of a single bubble with sinusoidal oscillations of fluid pressure (acoustic cavitation):

$$P(t) = P_0 + (P_{\max} - |P_{\min}|) \sin(2\pi t/t_{\text{per}}), \quad (9)$$

where  $P_0$ ,  $P_{\max}$ ,  $P_{\min}$  are the mean, maximum and minimum pressures;  $t_{\text{per}}$  is the period of pressure oscillations.

2. The flow in a narrow channel of variable cross-section (Fig. 4); the channel considered

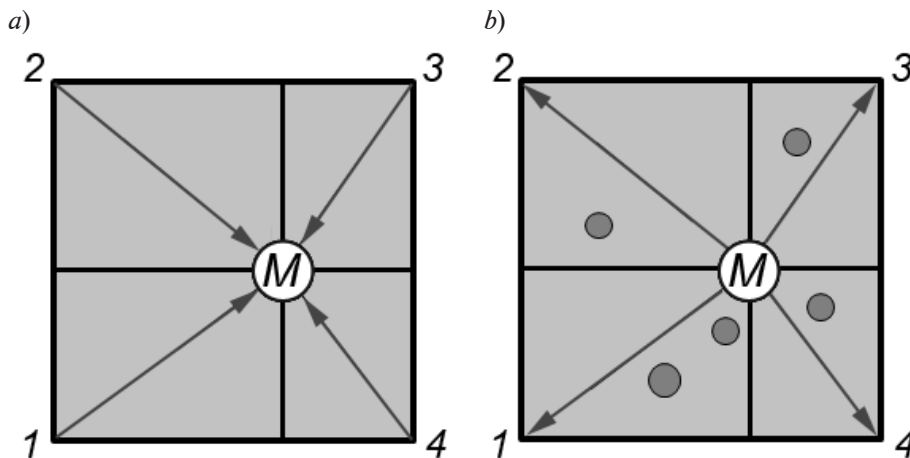


Fig. 3. Schematic explaining the connection between the Lagrange and the Euler stages of the computational algorithm:

*a* is the interpolation of hydrodynamic variables from grid nodes 1 – 4 to the location of bubble *M*,  
*b* is the transfer of information about the vapor fraction to grid nodes 1 – 4

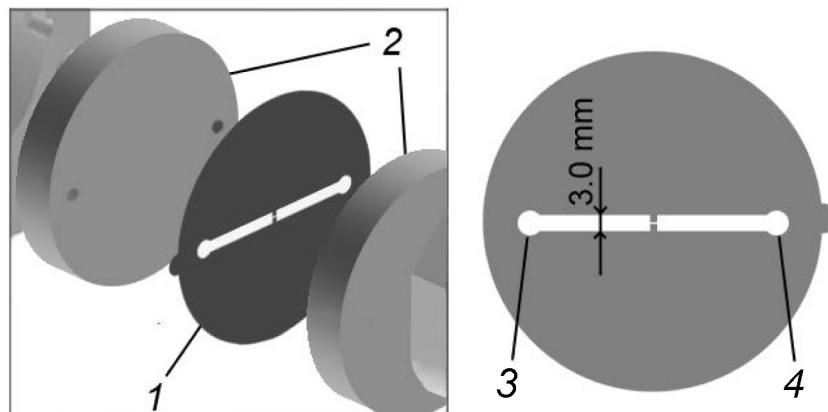


Fig. 4. Experimental setup for simulating the flow in the injector [7]: plate with a channel 1, windows for supply and discharge of liquid 2, channel inlet 3, input pressure  $P_{in} = 300$  atm, channel outlet 4, outlet pressure  $P_{out} = 52$  atm

is the same as the one described in [7].

Applying the Euler/Lagrange description involves a number of difficulties in this case. One of them is the problem of spatial scales: the characteristic sizes of the computational cells are comparable to the sizes of the cavitation bubbles, so it is necessary either to introduce additional coarsened grids or to construct special schemes for taking into account the effect of bubble distribution. The number of bubbles per unit volume may be less than one for the scales considered; the quantity should then express the probability of finding a bubble

in a given (control) volume.

We have carried out the Euler stage of numerical solution using solvers that are part of the OpenFOAM computing environment; the Lagrange stage was carried out using a specially developed software module.

The curves in Fig. 5 illustrate the growth of a single bubble with an initial radius  $R_B = 2 \mu\text{m}$  at an amplitude of pressure fluctuations  $\Delta P = 200$  atm and at different temperatures of the medium. It can be seen that the collapsing bubbles resume growth at the time of the second pressure drop. The differences in temperatures

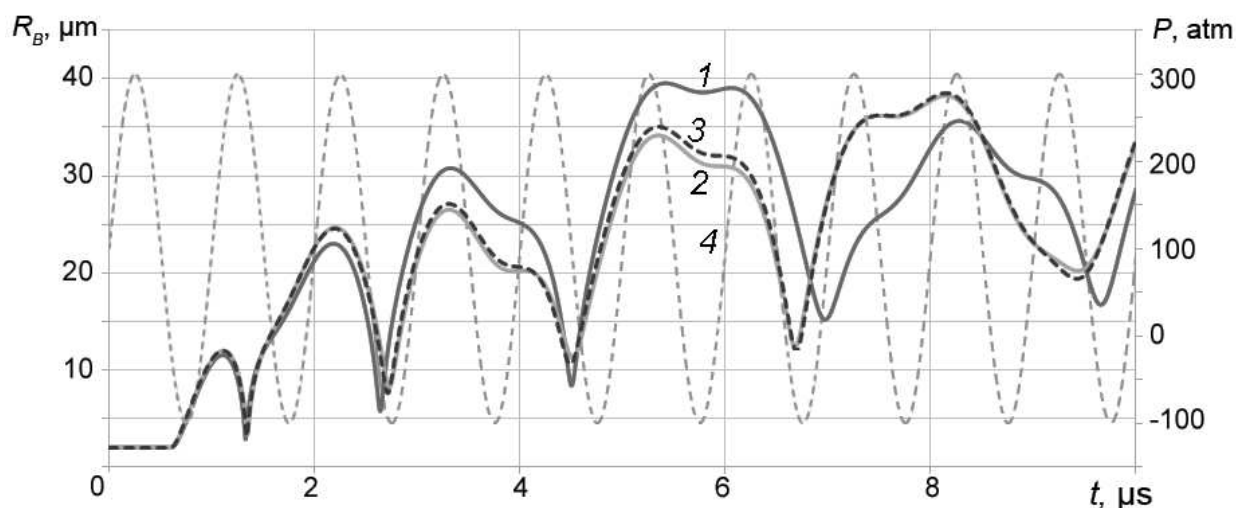


Fig. 5. Growth dynamics of a single bubble at different temperatures of the medium, °C: 30 (curve 1), 60 (2), 90 (3); the variations in the pressure of the medium are given (curve 4). The initial bubble radius is  $2 \mu\text{m}$



of the carrier medium have a pronounced effect if we compare the computational data at temperatures of 30 °C and above 60 °C. Bubbles start to grow earlier at higher temperatures, so respectively, they gain relatively larger mass and inertia, and their collapse occurs with a delay. For this reason, growth then also resumes with a delay, and as a result, the bubbles in the more heated liquid grow to a smaller volume than at a temperature of 30 °C at the time of the third increase in pressure. Further dynamics is governed by two main factors: the inertia of the bubble and the fluctuations in the external pressure. Notice that this effect is not observed in the computations with the single Rayleigh – Plesset equation: the bubble disappears after the first period of pressure recovery.

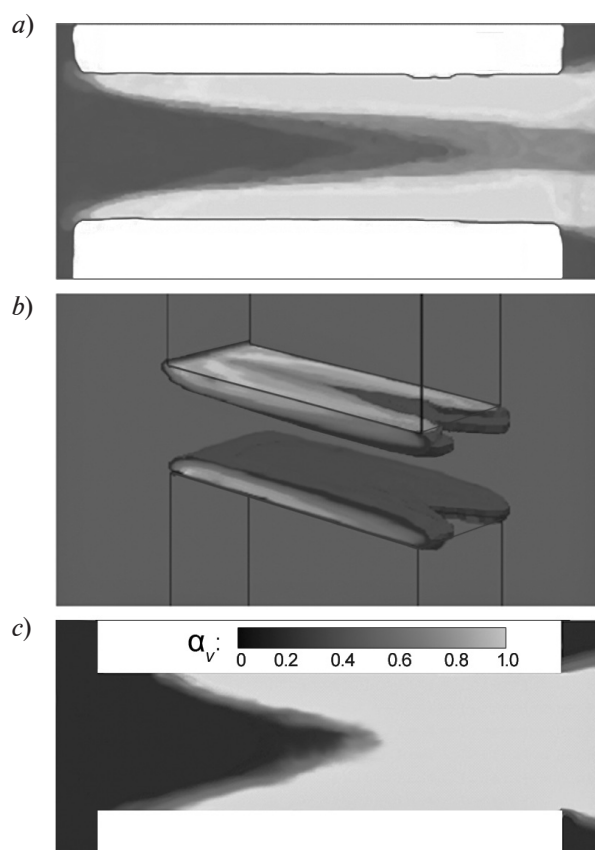


Fig. 6. Cavity shapes obtained experimentally (a) and from the computations (b, c).

Experimental data [7] are given for the time when the cavity extended beyond the channel ( $t = 60 \mu\text{s}$ ),  $T = 326 \text{ K}$ ,  $P_{out} = 52 \text{ atm}$ . The results of model flow computations were obtained in accordance with the Euler/Euler (b) and Lagrange/Euler (c) descriptions

Thus, it is more important to take into account the change in internal parameters at the stage of bubble collapse than at the stage of growth, where, according to our results, the dynamic behavior of the process does not significantly depend on the model used for describing it.

The conclusions drawn about the applicability of various equations of bubble dynamics allow to compile a scheme for computing more complex problems of cavitation flows. The changes in the internal parameters of the bubble can be neglected in the computations during the initial expansion of bubbles and the formation of cavities, because taking these parameters into account does not make a significant contribution to bubble growth dynamics at this stage.

Thus, the following states of the test bubble have been considered within the framework of this model:

- cavitation nucleus;
- primary growth of the bubble;
- part of the cavity region;
- collapsing bubble;

bubble ceasing to exist either as a result of collapse, collision with the wall or extending beyond the computational domain.

Fig. 6 shows a comparison of the obtained distribution of the volume fraction of vapor at time  $t = 60 \mu\text{s}$  with the results of computations using the cavitatingFoam solver and with the averaged experimental data presented in [7]. Even though the results obtained by the Euler/Lagrange method of simulating the test bubble dynamics turn out to be somewhat overestimated, they are closer to the averaged experimental results [7]. In both cases, the cavity extends beyond the narrow part of the channel. The vaporization rate is underestimated in the computations by the Euler/Euler approach due to the peculiarities of the model.

## Conclusion

In this paper, we have formulated a model of cavitation flow including the evolution of cavitation bubbles. We have used the Euler/Lagrange description of the medium taking into account a heterogeneous mechanism of bubble formation. Bubble growth and collapse



were simulated using the Rayleigh–Plesset equation and the equations of interphase mass and energy transfer determining the internal parameters of the bubbles.

The developed model ensures qualitative agreement of the cavity's shape and the position of its trailing boundary with the experimental observations.

## REFERENCES

- [1] **I.S. Pearsall**, Cavitation. UK: Mills and Boon, 1972.
- [2] **V.K. Kedrinskiy**, Gidrodinamika vzryva. Eksperiment i modeli [Explosion hydrodynamics. Experiment and models], Novosibirsk, the RAS Siberian Branch, 2000.
- [3] **Ya.E. Geguzin**, Puzyri [Bubbles], Moscow, Nauka, 1985.
- [4] **A.D. Pernik**, Problemy kavitatsii [Cavitation problems], Leningrad, Sudostroyeniye, 1966.
- [5] **R.T. Knapp, J.W. Daily, F.G. Hammitt**, Cavitation, McGraw-Hill, 1970.
- [6] **J.-P. Franc, J.-M. Michel**, Fundamentals of cavitation, Dordrecht, Kluwer Academic Publishers, 2004.
- [7] **R. Skoda, U. Iben, A. Morozov, et al.**, Numerical simulation of collapse induced shock dynamics for the prediction of the geometry, pressure and temperature impact on the cavitation erosion in microchannels, WIMRC 3rd International Cavitation Forum, 2011, University of Warwick, UK.
- [8] **N.V. Petrov, A.A. Schmidt**, Effect of a bubble nucleation model on cavitating flow structure in rarefaction wave, Shock Waves. 27 (4) (2017) 635–639.
- [9] **N.V. Petrov, A.A. Schmidt**, Multiphase phenomena in underwater explosion, Exp. Therm. Fluid Sci. 60 (2015) 367–373.
- [10] **A. Sokolichin, G. Eigenberger, A. Lapin, A. Lübert**, Dynamic numerical simulation of gas-liquid two-phase flows: Euler/Euler versus Euler/Lagrange, Chemical Eng. Science. 52 (4) (1997) 611–626.
- [11] **Lord Rayleigh**, VIII. On the pressure developed in a liquid during the collapse of a spherical cavity, Philosophical Magazine, Ser. 6. 34 (200) (1917) 94–98.
- [12] **M. Plesset, A. Prosperetti**, Bubble dynamics and cavitation, Ann. Rev. Fluid Mech. 9 (1977) 145–185.
- [13] **S. Frikha, O. Coutier-Delgosha, J.A. Astolfi**, Influence of the cavitation model on the simulation of cloud cavitation on 2D foil section, Int. Journal of Rotating Machinery. 2008 (2008), ID 146234, 12 p.
- [14] **A.A. Gavrilov, A.A. Dekterev, K.A. Finnikov**, Modelirovaniye kavitatsionnykh techeniy s ispolzovaniyem RANS podkhoda [Cavity flows simulation using RANS approach], Proceedings of the 4-th Russian National Conf. on Heat Exchange (RNCH-4), Moscow, 5 (2006) 241–244.
- [15] **Y. Shen, P. Dimotakis**, The influence of surface cavitation on hydrodynamic forces, Proceedings of the 22nd American Towing Tank Conference, St. John's, Canada, August (1989) 44–53.
- [16] **F. Bakir, R. Rey, A.G. Gerber, et al.**, Numerical and experimental investigations of the cavitating behavior of an inducer, International Journal of Rotating Machinery. 10 (1) (2004) 15–25.
- [17] **U. Iben**, Modeling of cavitation; Systems Analysis, Modeling and Simulation (SAMS). 42 (2002) 1283–1307.
- [18] **D.P. Schmidt, C.J. Rutland, M.L. Corradini**, A fully compressible, two-dimensional model of small, high-speed, cavitating nozzles, Atomization and Sprays. 9 (3) (1999) 255–276.
- [19] **J. Ma, C.-T. Hsiao, G.L. Chahine**, Shared-memory parallelization for two-way coupled Euler–Lagrange modeling of cavitating bubbly flows, J. Fluids Engineering. 137 (4) (2015) 121106–1–121106–8.
- [20] **E.Yu. Kumzerova, A.A. Schmidt**, Numerical simulation of homogeneous nucleation and bubble dynamics in a depressurized liquid, Proc. 4th International Conference on Multiphase Flow. New Orleans (2001).
- [21] **M. Strasberg**, Undissolved air in cavitation nuclei, Cavitation in Hydrodynamics. London: National Phys. Lab., 1956.
- [22] **F.G. Hammitt, A. Koller, O. Ahmed, et al.**, Cavitation threshold and superheat in various fluids, Proc. of Conference on Cavitation. Edinburg, September 3–5 (1974) 341–354.
- [23] **A.S. Besov, V.K. Kedrinskii, E.I. Pal'chikov**, Izucheniye nachalnoy stadii kavitatsii s pomoshchyu difraktsionnoy opticheskoy metodiki [Studying of initial stage of cavitation using diffraction-optic method], Tech. Phys. Letters. 10 (4) 1984. 240–244.

*Received 29.09.2017, accepted 09.11.2017.*



## THE AUTHORS

**ISAENKO Iliya I.**

*Peter the Great St. Petersburg Polytechnic University*  
29 Politechnicheskaya St., St. Petersburg, 195251, Russian Federation  
a906nn@gmail.com

**MAKHNOV Andrey V.**

*Peter the Great St. Petersburg Polytechnic University*  
29 Politechnicheskaya St., St. Petersburg, 195251, Russian Federation  
a\_makhnov@mail.ru

**SMIRNOV Evgeniy M.**

*Peter the Great St. Petersburg Polytechnic University*  
29 Politechnicheskaya St., St. Petersburg, 195251, Russian Federation  
smirnov\_em@spbstu.ru

**SCHMIDT Alexander A.**

*Ioffe Institute of RAS, Peter the Great St. Petersburg Polytechnic University*  
26 Politechnicheskaya St., St. Petersburg, 194021, Russian Federation  
alexander.schmidt@mail.ioffe.ru



## THE CONCEPT OF BUILDING A WIRELESS OPTICAL COMMUNICATION NETWORK BETWEEN SURFACE SHIPS

E.G. Chulyaeva<sup>1</sup>, S.N. Kuznetsov<sup>2</sup>, B.I. Ognev<sup>2</sup>

<sup>1</sup>Joint-stock company «Plasma», Ryazan, Russian Federation

<sup>2</sup>JSC «Mostcom», Ryazan, Russian Federation

The problem of organization of a wireless optical multi-node network (MANET) between surface ships has been considered. This type of connection can be an alternative to the classical radio message. The advantages of optical communication are faster data transmission, high security and immunity to interference. The goal of the work is creation of computer model of such communication network, a choice of an algorithm of the organization of logical network infrastructure and determination of the main technical requirements to optical communication terminals. The software “The emulator of a wireless optical network” was developed for simulation of the network of the moving surface ships. For the organization of a communication network the well-known algorithms of discrete mathematics (such as the Kruskal algorithm) were used. The simulation of the network was carried out; technical requirements to optical communication terminals as an element of the specified network were formulated.

**Key words:** wireless optical communication; free space optics; optical communication terminal; MANET

**Citation:** E.G. Chulyaeva, S.N. Kuznetsov, B.I. Ognev, The concept of building a wireless optical communication network between surface ships, St. Petersburg Polytechnical State University Journal. Physics and Mathematics. 11 (1) (2018) 50 – 55. DOI: 10.18721/JPM.11107

### Introduction

There is currently a growing need for increasing the throughput of communication channels, including optical lines [1 – 8]; increasing the data transmission rate over communication lines is also important for design of communication systems between surface ships.

High-speed communication is needed not only between the ships, but also in communication between the ships and the shore and between the ships and aircraft for solving a wide array of problems, from aerial reconnaissance to the operation of communication systems in radio silence or with an increased level of interference (for example, electronic warfare). The quality of radio communications that are traditional in this segment does not meet the modern requirements to the data transmission rate.

On the other hand, high-speed microwave transmission over the water surface is complicated both by the conditions for propagation of radio signals over the conducting surface and by large angular deviations of the ship (motion and

maneuvering) relative to the angular sizes of directivity diagrams.

For these reasons, wireless optical communication is virtually the only solution to the problem of high-speed communication between surface ships. However, it is scarcely used at present due to some properties of this type of transmission and peculiarities of its applications.

In this paper, we consider the concept of constructing a wireless optical communication network between surface ships, starting from requirements for optical communication terminals, and dealing with algorithms for organizing a logical network infrastructure.

### Problem statement

The main requirement for wireless optical communication is direct visibility between transceivers (optical communication terminals (OCT)). Line-of-sight range is substantially limited due to the curvature of the Earth's surface. For example, for an OCT installed at a height of 20 m, the line-of-sight distance is no more than 16 km.



Relatively small divergence angles of transmitter radiation and small viewing angles of OCT receivers significantly complicate the organization of a wireless optical communication channel between surface ships. As for transmitters, the requirement for narrow angular diagrams is due to the need to increase the margin for enhancing the optical power budget of a communication line. Reducing the viewing angles of receivers is necessary for minimizing their exposure to external radiation. The advantages of narrow angular diagrams of OCT transceivers are that adjacent OCTs practically do not affect each other and signal detection out of beam range is impossible (the communication channels are secure). The disadvantage of narrow diagrams is that additional instruments (such as charge-coupled devices (CCDs)) have to be introduced for searching, capturing and tracking subscribers while establishing and maintaining an optical communication channel.

Simultaneous requirements of wide coverage angles of the communication system and narrow viewing angles of the OCT entail using an optical beacon or a panoramic lighting system that allows each OCT to find all possible subscribers in the visible horizon.

In addition, while OCTs can be guided to each other manually for stationary applications (if they are fixed on a fairly steady support), CCD systems are absolutely necessary for moving and maneuvering surface ships.

Finding methods for deploying wireless optical communication networks is another major problem that needs to be addressed. These networks can consist of several mobile objects, with several point-to-point links with other objects organized on each of them. Due to the mobility of the objects to be connected and several directions of communication at each site, they have to be organized into a mobile dynamic (or ad-hoc) network, called MANET (Mobile Ad hoc NETWORK) [9].

### Possible solutions of the problem

Based on the above-described equipment requirements, wireless optical communication devices should be used as OCTs, automatically searching for subscribers and capturing them (identification and establishing communication)

in a wide angular sector of the horizon (testing the ship's maneuvers) and with an elevation angle of at least  $\pm 30^\circ$  (the ship's motion). Additionally, the subscriber has to be tracked in these conditions.

From the standpoint of organizing communication, the OCT control system of each ship should be able to determine the optimal configuration of communication directions and the operation mode of the ports connected to each OCT at each moment. In order to perform these tasks, the control system should have information about the location and spatial orientation of the ship's principal axis. Determining the optimal network configuration in MANET is a fairly complex problem [9, 10], and solving it considerably depends on the scenarios of application. For example, Ref. [9] considers the general case of configuring the network for use on various terrestrial terrain types, with aerial mobile objects and various types of communication (RF modules such as Bluetooth and Wi-Fi serve for data transmission in the VHF range).

Organizing wireless optical communication between sea ships is greatly simplified in the case under consideration because the dimensions of the connectivity domain are known (up to 20 km) and there is certain direct visibility between the ships.

The following procedures are necessary as a basic option of solving the task of building a network:

- determining all possible communication lines between the ships (based on the information on their location and orientation);

- constructing an optimal (spanning) tree of links between the ships;

- assigning the remaining available links as backup or parallel communication channels.

Based on possible scenarios, the above-mentioned link tree can be constructed not only with complete information about the location and orientation of the ship (which is not always available), but also using two other options:

- 1) based on a pre-designated central node (for example, a flagship);

- 2) by parallel construction of separate communication channels between adjacent ships, gradually integrating them into a common network.

Kruskal's, Prim's and Borůvka's algorithms are well-known methods of discrete mathematics that can be used for constructing the above-described spanning tree [11 – 14].

### Simulation of the network configuration

The “Emulator of a wireless optical network” software was developed to simulate a network of mobile ships.

This software allows to arrange several ships on a plane with a given number of OCTs on each ship, specifying the position and orientation of each ship

The basic element in the model is a surface ship where optical communication terminals are installed, with working angles whose axes are pointing in opposite directions. The term ‘working angles’ here refers to horizontal fields of view containing directions on which communication can be established (including all three phases of communication: search, capture, tracking). A geometric model explaining the location of the ships with OCTS and working angles is shown schematically in Fig. 1.

According to the proposed model, each ship as a network object is characterized by the number of OCTs and their working angles.

This model assumes that it is possible to construct a graph of possible links between the ships by specifying their number, location and orientation.

Fig. 2 shows eight ships located on the simulation plane, with the OCT viewing angles and all possible communication links indicated.

Evidently, the set of possible connections between the ship is quite large. Constructing a spanning tree by Kruskal's algorithm (based on the complete data on the location and orientation of the ship) was carried out according to the flow chart shown in Fig. 3. The algorithm was modified for searching for a fail-safe edge. When analyzing each communication link, i.e., each candidate for connection to the network, not only a single node belonging to the network's connectivity component (‘security’), but also an edge equipped with free OCTs was taken into account

This algorithm was applied to building a communication network (Fig. 4).

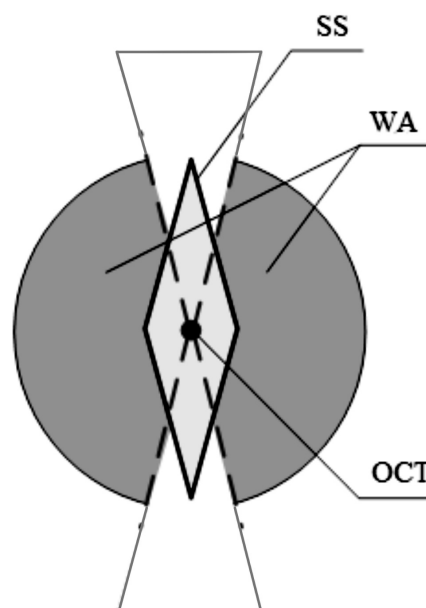


Fig. 1. Geometric model explaining the location of a surface ship (SS) with an optical communication terminal (OCT) and working angles (WAs)

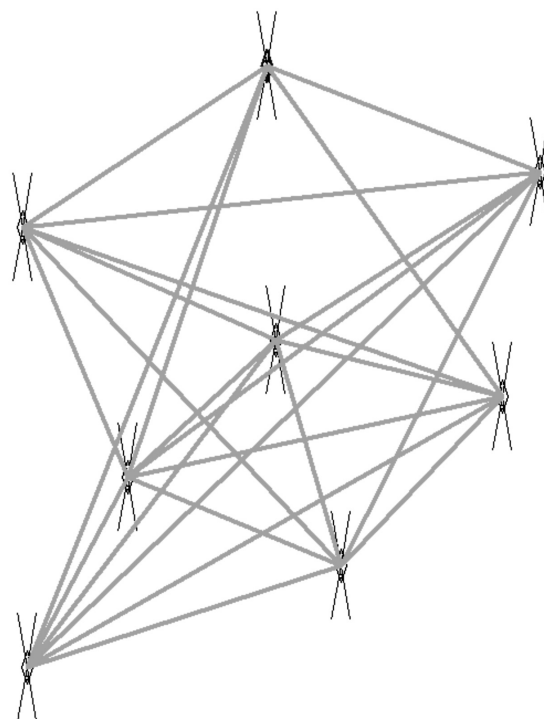


Fig. 2. Eight surface ships on the simulation plane of the “Emulator of a wireless optical network” software; OCT viewing angles and all possible communication links are shown

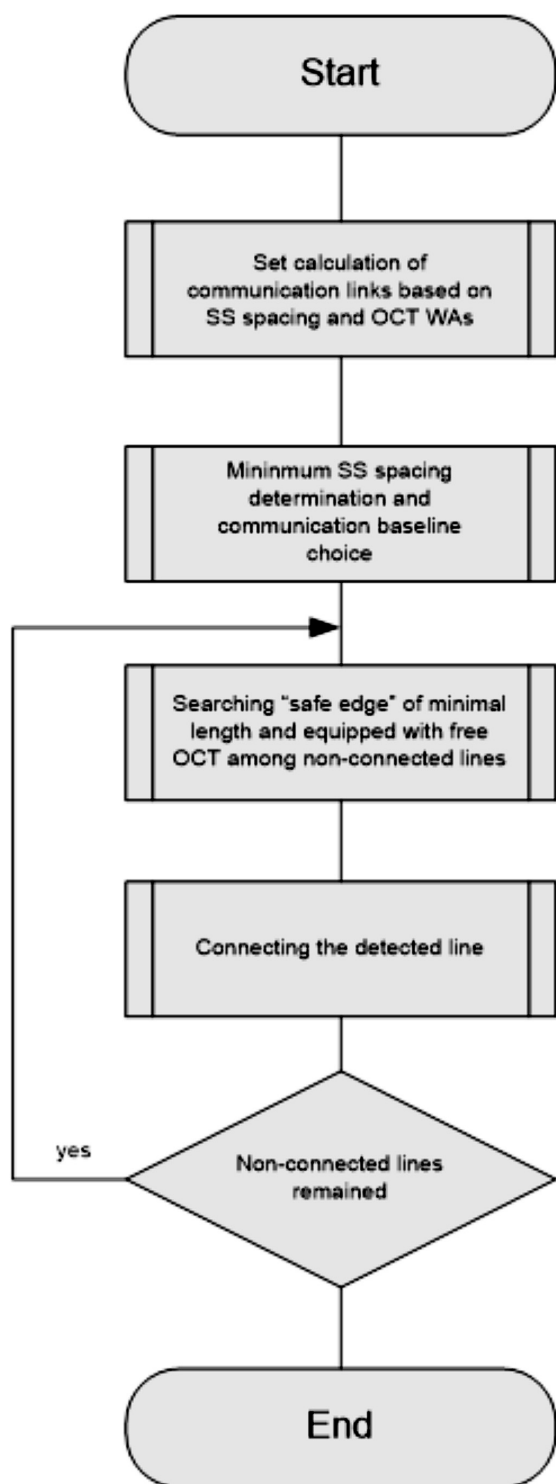


Fig. 3. Kruskal's algorithm for constructing a spanning tree of ship communication on the simulation plane of the EWON software; the algorithm is modified for searching for a safe edge

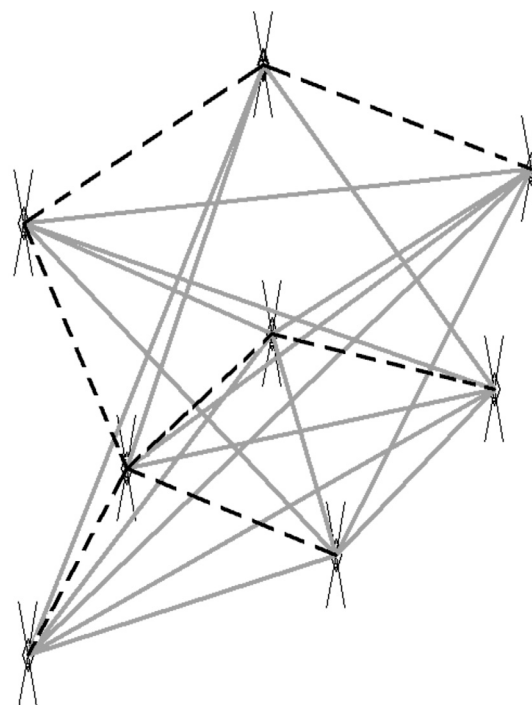


Fig. 4. A spanning tree of ship communication, obtained by Kruskal's algorithm (see Fig. 3); the main communication links are shown in dashed lines

Running Prim's and Borůvka's algorithms for the other two scenarios of building a communication network yields the same spanning tree (see Fig. 4). Unused links may remain in the spanning tree but it may still be possible to implement them (their number is what matters). The remaining possible communication links can be distributed with two purposes:

- for redundancy of already established communication links (parallel connections), integrating them into a single communication channel with load balancing;

- for organizing workarounds (unused loops) in order to improve the reliability of the network as a whole.

Thus, simulation of the communication network has confirmed that it is possible to create a wireless optical communication network between arbitrarily arranged surface ships taking into account their location and use of optical communication terminals that have finite working angles.

Based on the properties of the OCT and the methods of communication we have considered, we can formulate the main technical requirements for implementing the proposed network:

in search mode, panoramic lighting of the ship should be provided so that it can be found by its subscribers (the OCTs installed on other ships);

automatic guidance of the OCT should be developed in the tracking mode (after communication is established), compensating for all types of ship motion;

a central control unit (CCU) is required for all OCTs installed on one ship for the purpose of network configuration, routing, redundancy of communication lines and balancing of data

streams, as well as exchange of service information about the network status with the CCUs of other ships and integration with the local ship network.

## Conclusion

In this paper, we have considered the problems of organizing a wireless optical multi-node communication network between surface ships. We have found the algorithms for organizing the communication network in three possible scenarios; these algorithms produce one configuration of a communication spanning tree. We have formulated the requirements for the technical means providing this communication network.

## REFERENCES

- [1] Yu. Li, N. Pappas, V. Angelakis, M. Pioro, Yu. Di, Optimization of free space optical wireless network for cellular backhauling, *IEEE Journal on Selected Areas in Communications*. 33 (2) (2015) 1841–1854.
- [2] X. Rong, Y. Won-Hyuk, K. Young-Chon, Reconfigurable routing protocol for free space optical sensor networks, *Sensors*. 12 (4) (2012) 4824–4845.
- [3] M. Khalighi, M. Uysal, Survey on free space optical communication: A communication theory perspective, *IEEE Communications Surveys & Tutorials*. 10 (2) (2014) 1–22.
- [4] H. Zhou, A. Babaei, S. Mao, P. Agrawal, Algebraic connectivity of degree constrained spanning trees for FSO networks, *IEEE ICC*, 9–13 June. Budapest, Hungary (2013) 5991–5996.
- [5] D.M. Forin, G. Incerti, G.M.T. Beleffi, et al., Free space optical technologies, In: *Trends in Telecommunications Technologies*, Ch. 13, Ed. Ch.J. Bouras, Intech (2010) 257–296.
- [6] A.G. Alkholidi, K.S. Altowij, Free space optical communications: Theory and practices, In: *Contemporary Issues in Wireless Communications*, Ch. 5, Ed. M. Khatib, InTech (2014) 159–212.
- [7] V.S. Gurov, V.S. Zorkin, E.Yu. Gomozkova, et al., *Informatsionnyye lazernyye tekhnologii v promyshlennosti i sistemakh svyazi* [Informational laser technologies in industry and communications systems], Ryazan, Ryazan. State Radioeng. Un-ty, 2016.
- [8] V.S. Gurov, V.Yu. Mishin, E.G. Chulyayeva, *Lazernyye informatsionnyye tekhnologii* [Informational laser technologies], Lambert Academie Publishing, 2017.
- [9] A. Dwivedi, P. Harshavardhana, P.G. Velez, D.J. Tebben, Dynamic topology optimization for assuring connectivity in multihop mobile optical wireless communications networks, *Johns Hopkins Apl. Technical Digest*. 30 (2) (2011) 151–167.
- [10] H. Kaushal, G. Kaddoum, Free space optical communication: challenges and mitigation techniques, *IEEE Communications Surveys & Tutorials*. 19 (1) (2017) 57–96.
- [11] A.I. Belousov, S.B. Tkachev, *Diskretnaya matematika* [Discrete mathematics], Moscow, MSTU, 2006.
- [12] D. Cheriton, R.E. Tarjan, Finding minimum spanning trees, *SIAM Journal on Computing*. 5 (4) (1976) 724–741.
- [13] D. Eppstein, Spanning trees and spanners, *Handbook of Computational Geometry* (1999) 425–461.
- [14] M. Mareš, Two linear time algorithms for MST on minor closed graph classes, *Archivum mathematicum*. 40 (3) (2004) 315–320.

*Received 24.10.2017, accepted 06.11.2017.*

## THE AUTHORS

**CHULYAEVA Elena G.**

*Joint-stock company "Plasma"*

24 Tsiolkovskogo St., Ryazan, 390000, Russian Federation.  
grp@plasmalabs.ru



**KUZNETSOV Sergey N.**

*JSC "Mostcom"*

6 Frunze St., Ryazan, 390046, Russian Federation.

ksn@mocckom.ru

**OGNEV Boris I.**

*JSC "Mostcom"*

6 Frunze St., Ryazan, 390046, Russian Federation.

develop@mocckom.ru



## THE VORTEX STRUCTURE FORMATION AROUND A CIRCULAR CYLINDER PLACED ON A VERTICAL HEATED PLATE

**Yu.S. Chumakov, A.M. Levchenya, H. Malah**

Peter the Great St. Petersburg Polytechnic University, St. Petersburg, Russian Federation

The interaction process analysis and results of numerical simulation of a free-convection boundary layer developing around a circular cylinder placed on a vertical heated plate are presented. The cylinder axis is directed normally to the plate. The numerical model is based on the Navier–Stokes and the energy balance equations. The assumed system of equations is solved using the Boussinesq approximation. It is shown that the presence of a three-dimensional obstacle (cylinder) on the plate results in the formation of a complex vortex structure both upstream and downstream of the cylinder. In particular, a horseshoe vortex formed upstream of it is similar to vortex formation that has been observed in forced convection heat transfer by many researchers. In this paper, the tentative results of the study of the complex three-dimensional vortical structure in conditions of free-convection and its influence on the heat transfer are presented.

**Key words:** numerical modeling; natural convection heat transfer; vortex structure; horseshoe vortex system; heat transfer coefficient

**Citation:** Yu.S. Chumakov, A.M. Levchenya, H. Malah, The vortex structure formation around a circular cylinder placed on a vertical heated plate, St. Petersburg Polytechnical State University Journal. Physics and Mathematics. 11 (1) (2018) 56 – 66. DOI: 10.18721/JPM.11108

### Introduction

The past two decades have seen an increased interest in the flows arising when the boundary layer interacts with different obstacles on the surface along which these flows develop. Flow over an obstacle initiates an adverse pressure gradient causing the separation of the boundary layer. The formation of a rather complex vortex structure and, primarily, the formation of the so-called horseshoe vortex (HSV) is typical for these flows [1].

This type of flows includes forced convection flows arising in the wing/body junction of aircraft, in endwall regions of turbine cascades, in different heat exchange units of complex geometry. The increased pressure region in these flows is stretched along the entire height of the obstacle over which the external flow is incoming, so the separation of the boundary layer and the emerging HSV are very intense. A review of numerous experimental studies that were carried out before the 21st century and dedicated to HSV forms in forced convection flows is presented in [2], and studies of the last fifteen years are briefly reviewed in a recent experimental work [3].

Developing vortex structures obviously have

a noticeable effect on exchange processes in the flow, and, if there is a temperature difference between the flow and the streamlined surface, can contribute to significant non-uniformities of local heat transfer. There is a whole class of heat exchange devices where heat exchange occurs under free-convection conditions. For example, one of the models of such heat exchangers can be represented, as a vertical heated plate with a free-convection boundary layer developing along it. Various devices whose temperature is equal to or different from the surface temperature can be mounted on the plate. A strong pressure gradient in the narrow region where the free-convection boundary layer approaches the obstacle leads to separation of the boundary layer. Thus, it can be assumed that, similar to forced convection flow, a complex vortex structure containing a horseshoe-shaped vortex can develop on the plate in the vicinity of the leading edge of the obstacle. The behavior of the flow in this case is determined not only by the intensity of the separation, but also by buoyancy forces acting on the heated flow pushed away from the plate.

The current research in the field of computational fluid dynamics is focused on using numerical simulation techniques for



computing essentially three-dimensional flows with horseshoe vortex structures in forced convection boundary layers (see, for example, Refs. [4, 5]). Successful computation of heat transfer in devices with flow of a free-convection boundary layer over an obstacle largely depends on accurately reproducing the complex dynamic structure of vortex formations both directly in the region where the obstacles approach the surface and in their wake. It should be borne in mind that the flow itself arises from a locally acting body force and is not affected by incoming flow. Unfortunately, we have been unable to uncover any experimental or computational studies on horseshoe vortices in free-convection flow. Ref. [6] is dedicated to analysis of unsteady free convection near a vertical surface under local perturbation due to a small cubic obstacle mounted on the wall. The authors established that the presence of a cylinder immersed in a free-convection boundary layer intensifies heat transfer.

In this paper, we present the results of numerical simulation of a three-dimensional free-convection flow occurring near a vertical heated plate with a circular cylinder placed on it; the axis of the cylinder is directed normally to the surface.

### Problem definition

A laminar flow of a viscous incompressible fluid was considered in the Boussinesq approximation in the vicinity of a circular cylinder mounted on a rectangular vertical plane surface (referred to as a plate from now on). The plate was heated relative to the medium that filled the external environment. The air near the plate moved up under the action of a buoyancy force emerging in the gravitational field and formed a free-convection boundary layer along the plate. The surfaces of the plate and the cylinder served as the boundaries of the computational domain; conjugate heat transfer was not simulated. Two parameters of the problem changed in the process of variant (parametric) computations: the temperature of the cylinder and its height.

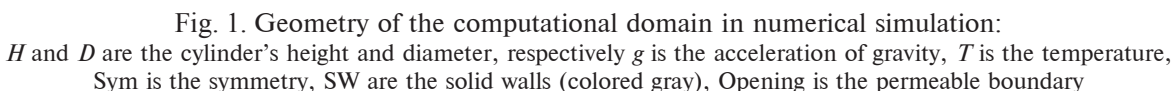
The goal of the study was to analyze the influence of cylinder heating on the structure of three-dimensional free-convection flow near the junction of the cylinder and the plate, and

also to compare the characteristics of the flow and the heat transfer in cases when the cylinder was completely immersed in the boundary layer and when the cylinder height exceeded the thickness of the boundary layer.

Fig. 1 shows a schematic of the computational domain and the coordinate system, as well as the boundary conditions (described below). The origin of the coordinate system is located 0.8 m from the trailing edge of the plate and coincides with the center of the base of the cylinder, the  $X$  axis corresponds to the horizontal direction, the  $Y$  axis to the vertical one (in the direction of flow), and the  $Z$  axis is perpendicular to the plate.

The diameter of the cylinder  $D = 0.02$  m. The computational domain was a parallelepiped with the height of  $120D$ , the width of  $25D$  and the thickness of  $10D$ . All computations were performed with artificial symmetrization of the flow in a plane parallel to the action of gravity, which divides the cylinder in half along its axis. The distance from the cylinder axis to the bottom boundary of the computational domain is  $50D$ , and  $70D$  to the top boundary (see Fig. 1). The height of the cylinder removed (cut off) from the computational domain varies in the simulations (the specific values are given in Table 1).

The boundary conditions are shown in Fig. 1 and were formulated as follows. Surfaces of the plate and the cylinder were solid walls (colored gray) with the no-slip condition imposed. The temperature of the plate was  $60^\circ\text{C}$  for all variants computed, and the surface temperature of the cylinder was set according to Table 1. The no-slip condition was also imposed on the bottom and top boundaries of the domain, with the temperature equal to the surrounding medium temperature of  $20^\circ\text{C}$ . The symmetry conditions were imposed on the plane separating the cylinder in half along its axis, parallel to its outer boundary. The symmetry condition was also imposed in the  $10D$ -long sections before and after the plate (in the vertical direction), ensuring impermeability and zero shear in these regions. The boundary parallel to the plate was permeable: the flow could move through it, both inward ejected by the boundary layer (in this case the temperature of the flowing air was  $20^\circ\text{C}$ ), and outward,



Body-fitted computational grids were used for numerical simulation. The grids were more refined near solid surfaces and in the entire vicinity of the obstacle to improve the resolution quality of horseshoe vortex structures. The grid was clustered to solid walls with a clustering

factor of 1.05. Block-structured grids consisting of quadrilaterals with rectangular cells were constructed in the plane of the plate away from the obstacle. A grid block in the vicinity of the cylinder was a *C*-grid in the form of a ‘screw-nut’ enclosing the cylinder (Fig. 2). Additional grid blocks between the refined grid in the

### Configurations and heating modes considered

Computational variant	Dimensionless cylinder height (H/D)	Cylinder surface temperature, °C
B-1-60	1	60
B-1-120	1	120
B-5-60	5	60
B-5-120	5	120

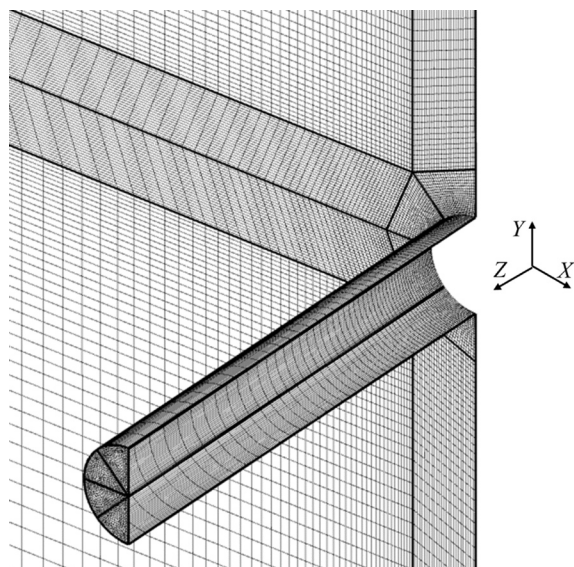


Fig. 2. Fragment of the computational grid near the cylinder

vicinity of the cylinder and a coarser outer region served to smooth the shape and equalize the size of the cells. Such a configuration of the subdomains was chosen to ensure efficient refinement of the grid in the region that interested us without forming strongly skewed or stretched cells, which could occur if a single grid structure was used for the entire computational domain. The resulting grid in the plane of the plate consisted of approximately 50,000 cells. The grid was clustered in the  $YZ$  plane in the vicinity of the cylinder in such a way that the cell size in the region where the horseshoe vortex developed was 50 times smaller than the diameter  $D$  of the cylinder. In the direction normal to the plate, the grid consisted of 73 cells with clustering to the plate and to the trailing edge of the cylinder. Three-dimensional grids were obtained by translating the original grid in the direction normal to the plate. The size of a near-wall cell was  $0.014D$ , and 31 cells fell inside the boundary layer unperturbed by the cylinder. The cell size in the inner block inside the region where the HSV developed was  $0.014 - 0.040D$ . The cell sizes did not exceed  $0.3D$  in any direction throughout the computational domain. The dimension of the resulting three-dimensional grid was about 3.6 million cells.

The commercial package ANSYS FLUENT

16.2 [7] was used for computations in the study. The solution of the Navier – Stokes and the energy equations was obtained using a coupled algorithm. The discretization of the governing equations was carried out with a second order of accuracy for all spatial derivatives.

The difficulties arising in simulation of free-convection flows are primarily due to relatively small velocities of motion and having to simultaneously solve the equations of motion and energy, which makes the numerical model less stable than in simulation of forced convection. The small inertia of the flow and the close relationship between the equations of motion and energy entail performing a larger number of iterations to obtain a converged solution in the computations. The number of iterations in our computations ranged from 1350 to 1600, and the balance accuracy was up to  $10^{-6}$ .

## Results and analysis

As a result of the computations, we have obtained steady-state solutions for the four variants listed in Table 1. The results in the vicinity of the cylinder mounted on the plate are of particular interest. The presence of this cylinder completely broke down the incoming flow and turned a two-dimensional free-convection boundary layer into three-dimensional flow, which ultimately had a significant effect on heat transfer.

The structure of the flow in case of forced convection is generally governed by the parameters of the incoming flow, while heat exchange within the model of an incompressible fluid has no effect on the flow field. At the same time, the flow under free convection is generated by the action of the buoyancy force whose intensity depends on the local temperature difference. To assess the effect of the cylinder on the breakdown of the incoming two-dimensional free-convection boundary layer and the resulting development of an extensive region of a three-dimensional vortex flow, it seems expedient to start analyzing the results by determining the boundaries of the temperature inhomogeneity in the vicinity of the cylinder. To this end, a 2 % thickness of the region with temperature non-uniformities was determined for each computational vari-

Table 2

The results of estimating the width of the perturbation region

Computational variant	Width of the perturbation region ( $X/D$ )
B-1-60	2.25
B-1-120	2.25
B-5-60	2.50
B-5-120	2.40

ant in different longitudinal cross-sections  $YZ$  ( $X = \text{const}$  is chosen), referred to as the near-wall region from now on. This thickness, denoted as  $\delta$  below, is the coordinate in the  $YZ$  plane where the local temperature differs from the temperature at the outer boundary of the computational domain by 2 %.

By comparing the results obtained with the corresponding thickness of the unperturbed boundary layer, we determined the extent of the region where the cylinder had an influence on the two-dimensional boundary layer.

Table 2, in particular, lists the dimensions of the region of the cylinder's influence at the level of the horizontal line  $Y = 0$ , along the  $X$  axis from the surface of the cylinder.

It follows from Table 2 that an increase in the surface temperature of a short cylinder did not affect the width of the perturbation region of the temperature field (variants B-1-60 and B-1-120) but reduced the size of this region in case of a long cylinder (B-5-60, B -5-120). We should also note that increasing the height of the cylinder resulted in an expansion of the perturbation region, regardless of cylinder heating.

Fig. 3 shows comparisons of the 2% thicknesses of the unperturbed two-dimensional boundary layer with their magnitude in the presence of an obstacle (the cylinder) along the plate on the symmetry line ( $X = 0$ ). Notably, the maximum computed thickness of the temperature boundary layer developing on the vertical heated plate without an obstacle is approximately 0.022 – 0.025 m.

Analysis of the curves in Fig. 3 reveals the following:

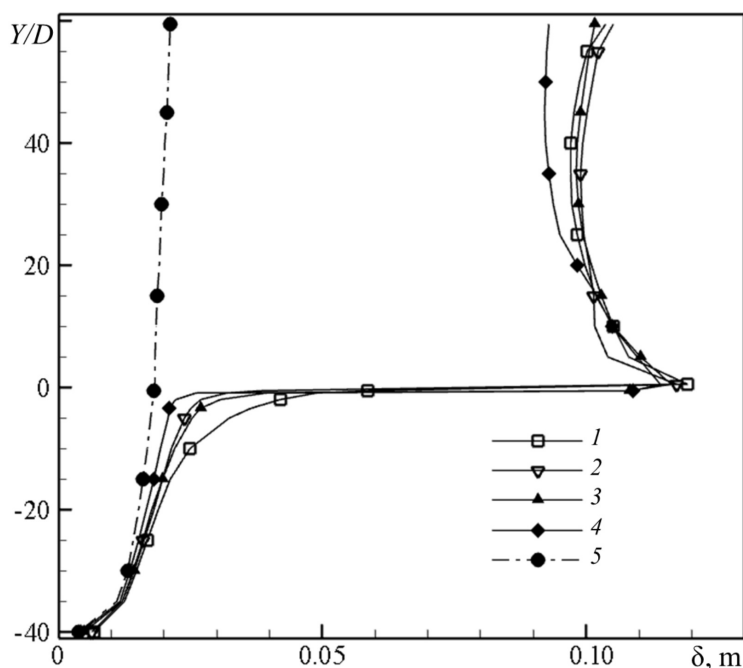


Fig. 3. Distributions of the 2 % thickness of the near-wall region  $\delta$  as a function of the  $Y/D$  coordinate, obtained for different variants: B-1-60 (1), B-1-120 (2), B-5-60 (3), B-5-120 (4) (see Table 1); the distribution in the absence of the cylinder (5) is also shown



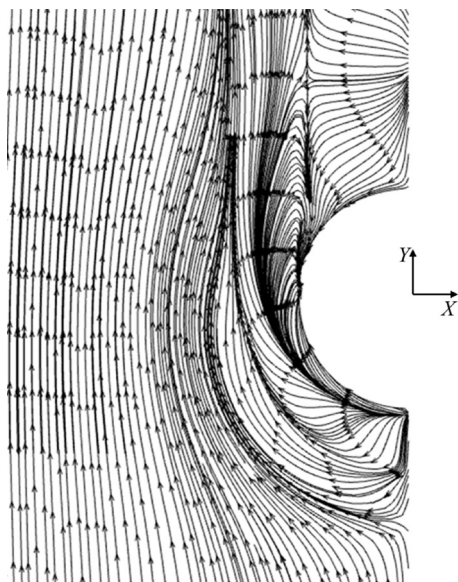


Fig. 4. Surface streamlines on the plate for variant B-1-60 (see Table 1)

the effect of the obstacle spread rather far upstream; the influence of the cylinder on the thickness of the wall layer was already noticeable at a distance  $Y/D = -35$ , and this influence was greater in case of a short cylinder;

increasing the temperature of the cylinder slightly reduced the degree of influence on the upstream flow;

the thicknesses of the wall layer in the region downstream of the cylinder were practically the same for all variants except variant B-5-120, for which some decrease in thickness was observed. The reason for this behavior was possibly that a long heated cylinder extending beyond the wall layer initiated its own free-convection flow, thus affecting the flow near the surface.

Let us analyze in more detail the flow field in the region of juncture of the cylinder and the plate.

The surface streamlines on the plate near

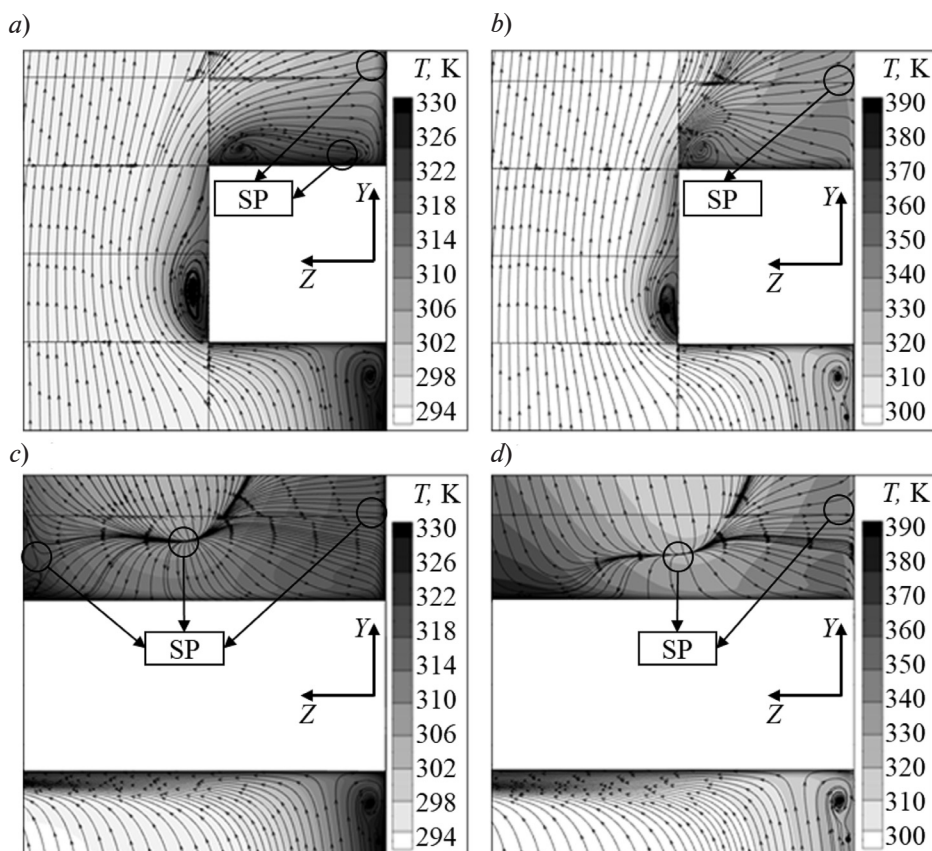


Fig. 5. Volume streamlines and temperature contours (as shades of gray) in the symmetry plane  $YZ$  for computational variants B-1-60 (a), B-1-120 (b), B-5-60 (c), B-5-120 (d) (see Table 1); SP are singular points



the cylinder for variant B-1-60 are shown in Fig. 4. This can be regarded as a picture of the vortex structures developed, allowing to identify the line of separation of the boundary layer upstream of the cylinder, with horseshoe vortices inside the line encircling the obstacle. Traces of the corner vortex developing in front of the cylinder and the development of the entire structure in the wake of the obstacle are visible near the cylinder.

Fragments of streamlines with the temperature fields (as shades of gray) are shown in Fig. 5 in the plane of symmetry  $YZ$  ( $X = 0$ ). Comparing different modes allows analyzing the effect of the height of the cylinder and its overheating relative to the medium on the dimensions of the HSV. Vortices can be detected in the corner of the junction of the cylinder and the plate in each figure: the primary (more intense) and secondary (weak) HSV; the secondary vortex was located upstream of the primary one, formed as a result of separation of the free-convection boundary layer along the plate. The HSV sizes were similar for all computational variants. A vortex developed in the trailing edge of the cylinder is visible for the cases of flow around a short cylinder (Fig. 5, *a, b*). Its axis shifted upstream (towards the cylinder) as its surface temperature increased. A complex vortex structure was formed downstream of the obstacle: for a short cylinder, this was a concentrated vortex (recirculation bubble). The swirling flows inside the vortices stirred and diffused the heated air, changing the heat transfer on the surface of the plate and the cylinder mounted on it.

Several singular points (SP in Fig. 5) were present in the cylinder's wake for all four cases considered, allowing to draw an analogy with a tornado [8]. These singularities drew the fluid particles upstream, along the plate, shifting downstream as the surface temperature of the cylinder and its height increased. Fig. 6 shows tornado-shaped vortices for variant B-5-120. When the height of the cylinder increased and its surface temperature decreased, the base of the vortex funnel moved away from the cylinder's symmetry plane along the  $x$  axis.

The primary and secondary horseshoe vortices merged together and formed a single

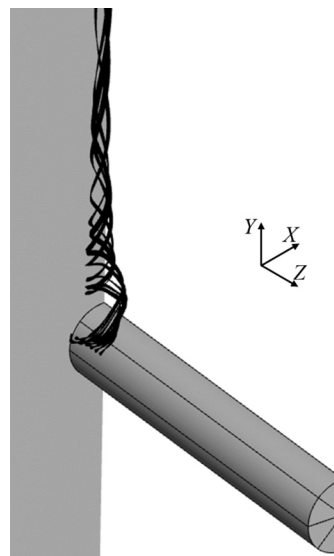


Fig. 6. Streamlines in the trailing edge of the cylinder (variant B-5-120)

structure that slowly moved towards the cylinder, and ultimately contributed to the development of the HSV system [9] (Fig. 7).

A  $Q$ -criterion [10] was used to visualize three-dimensional vortex structures in Fig. 7; this criterion is defined as follows:

$$Q = \frac{1}{2}(\Omega_{ij}\Omega_{ij} - S_{ij}S_{ij}), \quad (2)$$

where  $\Omega_{ij}$  and  $S_{ij}$  are the antisymmetric and symmetric parts of the second invariant of the velocity gradient tensor, respectively.

According to [10], vortex structures can be found in regions where  $Q > 0$ , when the local rotation speed exceeds the strain rate. Comparing the distributions of the  $Q$ -criterion near the surface of the cylinder and in the region of the junction of the cylinder and the plate for each computational variant (Fig. 7) yields data on the topology and intensity of the vortex structures.

We should note that the HSV systems that developed in the computations with coinciding cylinder heights were identical in shape but had different sizes of the leg of the primary HSV and different intensities, while an increase in the  $Q$ -criterion was observed over the entire height of the cylinder for the fourth variant. Regardless of the height of the cylinder, as its temperature increased, the isosurface of the

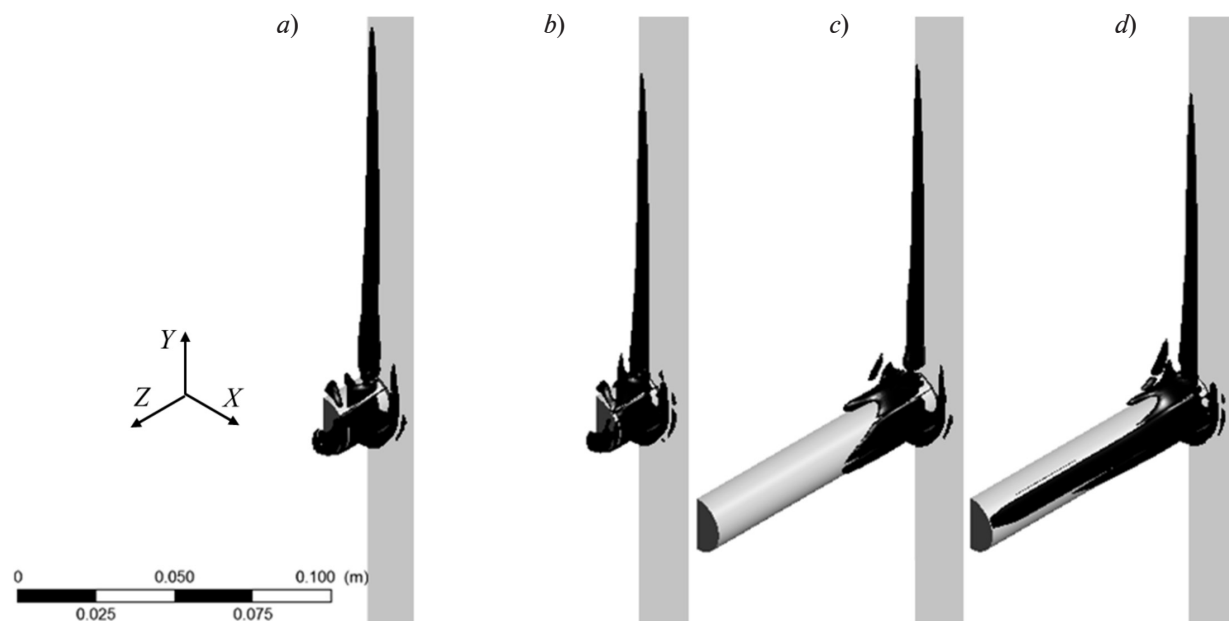


Fig. 7. Visualization of the vortex flow structure around the cylinder using the  $Q$ -criterion isosurfaces for variants B-1-60 (a), B-1-120 (b), B-5-60 (c), B-5-120 (d)

$Q$ -criterion stretched along the entire height of the cylinder, covering its lateral surface completely, corresponding to intensification of the vortex structures. The legs of the primary HSV in the cylinder's wake reduced in size with an increase in surface temperature of the cylinder and in its height.

A brief analysis of the flow in the vicinity of the junction of the cylinder and the plate and in the wake of the cylinder indicates the formation of a very complex vortex structure contributing to intense mixing of cold and hot air, which undoubtedly had a significant effect on heat exchange in this region. To analyze the effect on heat transfer of three-dimensional vortex flow, it is convenient to use the heat transfer coefficient  $\alpha$ , which is defined as follows:

$$\alpha = q / \Delta T,$$

where  $q$  is the heat flux from the wall,  $\Delta T$  is temperature difference between the wall and the external environment.

The distributions of the heat transfer coefficient along the polygonal line made by intersection of the symmetry plane and the solid walls are shown for all computational variants in Fig. 8. The figure consists of three separate

spatially related graphs, each of them showing one or two families of curves.

The lower graph shows two families of curves. The first is the distribution of the quantity  $\alpha$  ( $Y/D$ ) along the section of the plate under the cylinder (upstream of it); the vertical axis of the graph serves as the coordinate axis, and the  $\alpha$  values are plotted horizontally. These distributions coincide for different computational variants, while the value of  $\alpha$  decreases monotonically as the boundary layer develops on the plate, right up to the region directly in front of the cylinder ( $Y/D > -1$ ) where a horseshoe vortex is formed and monotonicity is violated.

It should be noted that the distributions of the heat transfer coefficient obtained in the computations for the region upstream of the cylinder and away from it (i.e., in the region of the unperturbed free-convection boundary layer) are consistent with the data available in the literature. The criterial relation between the local Nusselt number and the local Grashof number has the form of a power function with an exponent close to the value of  $1/4$ , standard for laminar flow near a vertical heated plate [11].

The second family of curves on the lower

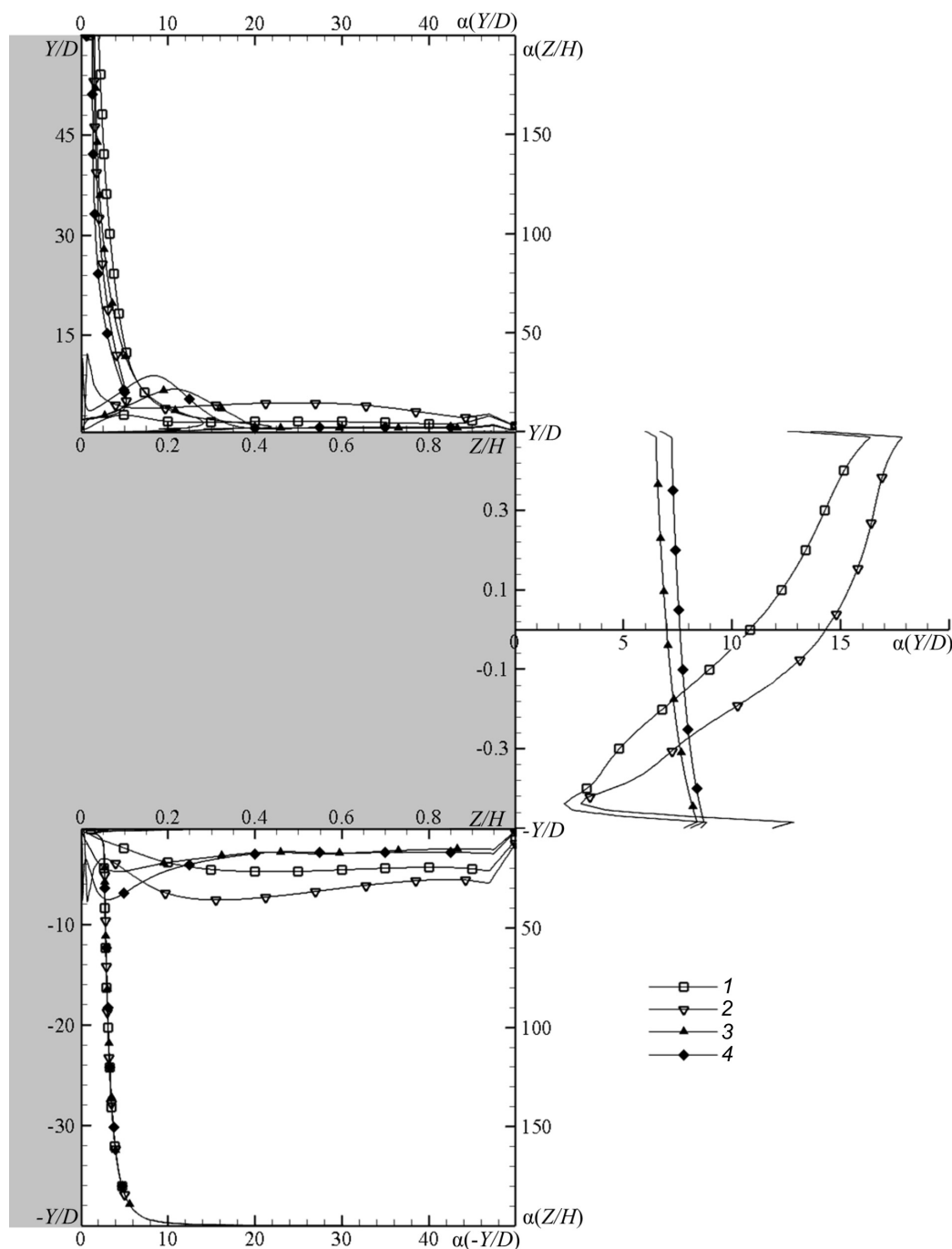


Fig. 8. Distributions of the heat transfer coefficient  $\alpha$  along the line of intersection of the symmetry plane ( $YZ$ ) and solid surfaces for computational variants B-1-60 (a), B-1-120 (b), B-5-60 (c), B-5-120 (d) (see Table 1)

graph corresponds to the distribution of the heat transfer coefficient along the height of the cylinder, along its leading edge: the coordinate axes change places in accordance with the spatial orientation. The heat transfer coefficient

on the lateral surface of the cylinder virtually does not change along the cylinder, while the average level of the coefficient  $\alpha$  for a short cylinder slightly increases with increasing surface temperature.



We should note that an increase in the surface temperature leads to a pronounced nonmonotonic change in the coefficient  $\alpha$  in the vicinity of the junction of the cylinder and the plate for cylinders of different heights. This circumstance is of course due to intense development of the vortex structure in this region. Similar behavior of the heat transfer coefficient is also characteristic for the distribution of  $\alpha$  along the trailing edge of the cylinder (see the upper graph, the dependences  $\alpha(Y/D)$ ).

The graph in the middle shows the distributions of the value of  $\alpha$  along the diameter of the upper edge of the cylinder. A general tendency to an increase in the heat transfer coefficient can be observed with an increase in the surface temperature of the cylinder. However, while the coefficient  $\alpha$  is practically constant for a long cylinder, the heat transfer coefficient increases several times in the downstream direction for a short cylinder completely immersed in the boundary layer. The distributions of the heat transfer coefficient in the region in the cylinder's wake, along the surface of the plate (the upper graph, the dependence  $\alpha(Z/H)$ ), are similar for different variants, exhibiting a slow, almost monotonic decrease in heat transfer with increasing distance away from the cylinder. The values of  $\alpha$  decrease with an increase in both the surface temperature of the cylinder and in its height.

## Conclusion

The results of numerical simulation of the interaction of a free-convection boundary layer with a three-dimensional obstacle (cylinder) allow us to draw the following conclusions:

the assumption that a complex vortex structure with a horseshoe vortex develops in the leading edge of a cylinder located on a vertical plate was confirmed for the case of free-convection flow;

the height of the cylinder has a significant effect on the formation of the vortex zone if it is commensurable with the thickness of the boundary layer;

cylinder overheating compared to the plate temperature has little effect on the upstream flow, but has a marked effect on the flow downstream of the cylinder;

the effect of cylinder overheating is apparently even more pronounced if the height of the cylinder exceeds the thickness of the boundary layer, since in this case the cylinder is an independent source of a free-convection flow, which can significantly affect the downstream flow under certain conditions;

finally, (this, perhaps, is the most important practical conclusion), the heat exchange of the plate (together with the cylinder) with the surrounding air is largely governed by the vortex structure of the flow near the plate, and, consequently, successful computation of the heat exchange largely depends on the accuracy of predicting the dynamic structure of the flow.

## REFERENCES

- [1] C.D. Anderson, S.P. Lynch, Time resolved stereo-PIV measurements of the horseshoe vortex system in a low aspect ratio pin-fin array, AIAA Propulsion and Energy Forum. Orlando, FL, USA (2015) 3733.
- [2] F. Ballio, C. Bettoni, S. Franzetti, A survey of time-averaged characteristics of laminar and turbulent horseshoe vortices, ASME Journal of Fluids Engineering. 120 (2) (1998) 233–242.
- [3] N. Apsilidis, P. Diplas, C.L. Dancy, P. Bouratsis, Time-resolved flow dynamics and Reynolds number effects at a wall-cylinder junction, Journal of Fluid Mechanics. 776 (2015) 475–511.
- [4] M.R. Visbal, Structure of laminar juncture flows, AIAA Journal. 29 (8) (1991) 1273–1282.
- [5] A.M. Levchenya, Chislennoye modelirovaniye trekhmernogo potoka, obteyushchego krugovoy tsilindr v oblasti yego sochleneniya s gladkoy stenкой [Numerical simulation of a 3D flow around a circular cylinder in its overlapping area with a smooth wall], In: Vserossiyskiy seminar po aerogidrodinamike, posvyashchennyy 90-letiyu so dnya rozhdeniya S.V. Vallandera: izbrannyye trudy vserossiyskogo seminar [The All-Russian seminar on aerodynamics on the occasion of 90<sup>th</sup> anniversary of S.V. Vallander: Selecta from The All-Russian seminar], St. Petersburg, SPbSU (2008) 64–69.
- [6] G. Polidori, J. Padet, Flow visualization and free convection heat transfer at the junction of short cylinders mounted on a heated wall, Journal of Flow Visualization and Image Processing. 10 (2003) 13–26.
- [7] ANSYS Academic Research Mechanical, Release 16.2, Help System, Fluent Theory Guide,

ANSYS, Inc. 2015.

[8] **G. Kirkil, G. Constantinescu**, Effects of cylinder Reynolds number on the turbulent horseshoe vortex system and near wake of a surface-mounted circular cylinder, *Physics of Fluids*. 27 (7) (2015) 075102.

[9] **J.V.S. Tala, S. Russeil, D. Bougeard, J.L. Harion**, Investigation of the flow characteristics in a multirow finned-tube heat exchanger model by means of PIV measurements, *Experimental Thermal*

*and Fluid Science*. 50 (2013) 45–53.

[10] **J.C.R. Hunt, A.A. Wray, P. Moin**, Eddies, stream, and convergence zones in turbulent flows, *Center for Turbulence Research Report (CTR-S88)*. (1988) 193–208.

[11] **V.A. Kuzmitskii, Yu.S. Chumakov**, Analysis of characteristics of flow under conditions of laminar-to-turbulent transition in a free-convection boundary layer, *High Temperature*. 37(2) (1999) 247–253.

*Received 06.11.2017, accepted 05.12.2017.*

#### THE AUTHORS

**CHUMAKOV Yuri S.**

*Peter the Great St. Petersburg Polytechnic University*

29 Politechnicheskaya St., St. Petersburg, 195251, Russian Federation  
chymakov@yahoo.com

**LEVCHENYA Alexander M.**

*Peter the Great St. Petersburg Polytechnic University*

29 Politechnicheskaya St., St. Petersburg, 195251, Russian Federation  
levchenya\_am@spbstu.ru

**MALAH Hamid**

*Peter the Great St. Petersburg Polytechnic University*

29 Politechnicheskaya St., St. Petersburg, 195251, Russian Federation  
hamid.malah@gmail.com

## ON SIMULATION OF CLUSTER FORMATION PROCESS UNDER WATER VAPOR SPHERICAL EXPANSION INTO VACUUM

**N.Yu. Bykov**

Peter the Great St. Petersburg Polytechnic University, St. Petersburg, Russian Federation

The calculation of a water vapor outflow into vacuum has been performed using the direct simulation Monte Carlo with taking into account a condensation process. Two cluster-formation models were employed for simulation. The former is based on a kinetic approach, the latter is based on conclusions drawn from the modified classical nucleation theory. The analysis of physical adequacy of models and features of their program implementation was carried out. The simulation of spherical vapor expansion from an evaporating surface was performed over a range of Knudsen numbers corresponding to transient and near-continual flow regimes. The influence of a condensation process on gasdynamic flow parameters was analyzed. The effect of freezing of cluster mole-fractions when receding from the evaporating source was demonstrated.

**Key words:** direct simulation Monte Carlo; condensation; water cluster; transient flow regime

**Citation:** N.Yu. Bykov, On simulation of cluster formation process under water vapor spherical expansion into vacuum, St. Petersburg Polytechnical State University Journal. Physics and Mathematics. 11 (1) (2018) 37 – 49. DOI: 10.18721/JPM.11109

### Introduction

The processes of condensation of water vapor in expanding flows are widespread in nature and technology. Natural phenomena include atmospheric events such as water clusters developing in gas flows making up the near-nucleus atmosphere of comets [1]. Technical applications concern the processes of condensation of water vapor in nozzles and jets [2], for example, in spacecraft engines working at high altitudes [3].

Depending on the characteristic Knudsen number ( $Kn = \lambda/D$ , where  $\lambda$  is the mean free path of molecules, and  $D$  is the characteristic flow dimension), the outflow of vapor into vacuum is rarefied at the periphery of the jet or in the entire flow region. The direct simulation Monte Carlo method (DSMC) is traditionally used to calculate rarefied flows [4].

The interest towards modeling the formation and growth of clusters in rarefied flows by the DSMC method started in the early

2000s in connection with the rapidly evolving vacuum technologies for deposition of various coatings, including laser ablation technologies. These flows were calculated by kinetic models [5 – 8], where probabilities of particle association in mutual collisions were cluster size functions (equal to unity in the simplest case), and the monomolecular cluster decay was simulated by the formula of the Rice – Ramsperger – Kassel (RRK) theory. The studies gave a detailed description of the first stage of cluster formation (dimerization) and implemented the RRK formula for monomolecular decay algorithmically. The method of direct statistical modeling of flows with condensation processes based on the kinetic model was further developed in [9], where the probabilities of the association processes were obtained using the molecular dynamics (MD) approaches, and also in [10], which offered an exact algorithm for implementing the RRK formula for monomolecular decay for the DSMC method. It was found in all of these studies that the rates



of the forward process of particle association and the reverse process of decay were not related to each other. Ref. [11] proposed a condensation model where the probabilities of cluster growth/decay were obtained from the data on the rates of forward and reverse reactions of the corresponding processes. The rate constants of the forward and reverse reactions are related by the equilibrium constants which are assumed to be known. Distinctive aspects of [11] are the original expressions for the probability of monomolecular cluster decay (coinciding with the RRK theory in a particular case) and the probability of dimer formation in a three-particle collision of monomers. This kinetic model [11] was used for obtaining the key results of this paper.

Another group of studies [12, 13] described performing DSMC calculations of water vapor condensation in a rarefied far field of a jet engine plume. These papers used classical nucleation theory (CNT), with conclusions adapted for the DSMC algorithm.

The intention to employ CNT for practical calculations seems well-grounded. First of all, the theory's conclusions have long been used to describe flows with condensation. The required thermodynamic parameters (vapor pressure and temperature, supersaturation degree, nucleation rate and critical cluster size) can be calculated within the framework of DSMC. Secondly, simulation of the cluster growth process, starting from the formation of a critical nucleus, has its computational advantages, eliminating the need to spend the computational time on simulating the formation of subcritical clusters, including the formation of a dimer in triple recombination of monomers.

However, CNT also has its known drawbacks, as it uses the concept of surface tension for small clusters and predicts the size of the critical cluster to be less than unity for high values of vapor supersaturation. Refs. [12, 13] ignored the effect of the release of binding energy during particle association, and, consequently, failed to take into account the effect of increasing internal temperature of the cluster accompanying this process; the implementation of the algorithm for the case of high supersaturation was not clarified as well.

To eliminate these shortcomings of CNT, it

was proposed in [14] to use modified classical nucleation theory (MCNT). Within the MCNT model, there is no need to involve the concept of surface tension [15], and the size of the critical cluster for high supersaturation values is equal to unity. This latter circumstance entails making additional assumptions in the algorithmic implementation of the model. The MCNT model was implemented for the spatially homogeneous case of condensation of copper vapor [16]. However, a direct comparison of the calculation results obtained for the same flows using both models (based on the kinetic and the MCNT approach) has not been carried out. Additionally, comprehensive analysis of the algorithmic possibilities of implementing the MCNT model has not been performed for the DSMC method.

One of the goals of this study was to compare the results of calculations (we calculated the size distributions of the resulting clusters and the coordinate distributions of gasdynamic parameters) using the two models (kinetic and MCNT) with one object as an example.

The paper also discusses the specifics of algorithmic implementation of the MCNT approach and the parameters of the MCNT model for which these calculated results are close to the ones obtained by the kinetic approach.

The object chosen for study in the paper was a steady one-dimensional flow of water vapor from an evaporating spherical surface. Simulation of the expansion of non-reacting gas from the surface of a sphere into vacuum was performed in [17, 18]. These studies considered the effect of the degree of rarefaction on gas dynamics of the flow, analyzed the peculiarities of formation of the Knudsen layer near the surface of the sphere and the relaxation of translational degrees of freedom.

Ref. [19] calculated the parameters of clusters in the region  $X < 5R$  ( $X$  is the radial coordinate,  $R$  is the radius of the sphere) and of the vapor at the sonic line during the expansion of water vapor from a spherical source. A simplified condensation model was used for the calculations: in particular, the probabilities of particle association were assumed to be equal to unity during clustering reactions, and the evaporation process was simulated by the RRK



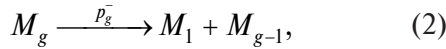
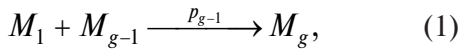
theory. A significant mass fraction of clusters (up to 19%) was observed within the flow field for the model parameters used in [19], and the condensation process was confirmed to have a considerable effect on the parameters of the sonic line.

Other goals of this paper were to carry out a series of calculations for flow from a spherical source using a refined condensation model proposed in [11], to study the effect of the clustering process on the parameters of vapor flow and to study the parameters of the forming clusters.

### Model of cluster formation

According to the data given in [11], a water cluster  $M_g$  is characterized by the number of monomers  $g$ , the number of surface monomers  $g_0$ , the mass  $m_g$ , the diameter  $d_g$ , the translational velocity  $v_g$ , the internal energy  $E_{int,g}$ , the number of rotational ( $\zeta_{r,g}$ ) and vibrational ( $Z_{v,g}$ ) degrees of freedom and the energy of evaporation of one monomer from the surface  $\varepsilon_g$ .

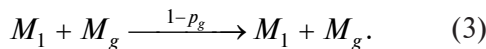
The following association/decay reactions are considered for clusters of size  $g > 2$ :



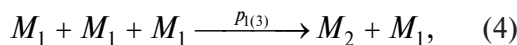
where  $p_{g-1}$ ,  $p_g^-$  are the probabilities of association and decay, respectively.

Reaction (1) describes the attachment of a monomer to a cluster in a binary collision, reaction (2) describes the unimolecular decay of the cluster. The unimolecular decay time of the cluster is of the order of  $1/\nu_0$ , where  $\nu_0$  is the characteristic vibrational frequency of the monomers in the cluster. The forward process (1) is characterized by the rate constant  $K_{g-1}$ , the inverse process (2) is characterized by the rate constant  $K_g^-$ .

An elastic collision between a monomer and a cluster occurs with the probability  $1-p_g$ :

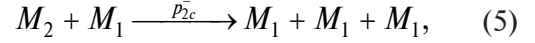


Within the framework of the model under consideration, water dimers are formed as a result of three-particle collisions:



where  $p_{1(3)}$  is the respective probability.

The reverse reaction occurs by the scheme:



where  $p_{2c}^-$  is the probability of collision decay.

Let us denote the rates of the forward (4) and the reverse (5) reactions by  $K_{1(3)}$  and  $K_{2c}^-$ , respectively.

### Model based on the modified classical nucleation theory

The specifics of the MCNT-based model is that the size of the critical cluster  $g_*$  and the nucleation rate  $J$ , which are functions of thermophysical parameters, have to be calculated in each computational cell.

Within the MCNT model, the nucleation rate is determined as follows [2, 15]:

$$J = 1 / \sum_{g=2}^{\infty} R_g^{-1}, \quad R_g = K_{g-1} n_1 n_{g-1}^e, \quad (6)$$

where  $n_g$  is the concentration of  $g$ -mers;  $K_{g-1}$  are the rate constants of processes (1) and (4) for  $g > 2$  (for the case when water dimers form through reaction (4),  $K_1 = K_{1(3)} n_1$ ); the superscript  $e$  denotes the equilibrium concentration,  $n_1^e = n_1$ .

A given degree of supersaturation  $S$  corresponds to a certain critical cluster size  $g_*$  [2, 15]. The critical size in the range  $S < S_{\min}$  is equal to the critical size determined according to classical nucleation theory (CNT) [2]; this size is equal to the coordination number  $N_c$  in the range  $S_{\min} < S < S_{\max}$ , while for the case  $S > S_{\max}$   $g_* = 1$ . The  $S_{\max}$  and  $S_{\min}$  values were determined in [14, 15]. The critical cluster size has to be found for determining the value of  $J$ , since clusters of near-critical size make the main contribution to the sum in expression (6).

After the values of  $J$  and  $g_*$  have been determined, the computational algorithm based on the MCNT approach is reduced to injecting clusters into a cell at a rate  $J$ . Determining the size of the injected clusters is the first distinctive feature of the MCNT-based algorithm. In [12, 13] clusters of critical size  $g_*$  were injected into the cell. Injecting clusters of size  $g_* > 2$  into a cell leads to a reduction of the real size distribution of the clusters. In this case it is assumed that

the concentrations of subcritical clusters in the cell correspond to the equilibrium distribution. In this situation, additional simulation of the distribution of subcritical clusters has to be carried out within the framework of the DSMC method (this problem was not considered in [12, 13]) and changes have to be made to the computational algorithm. On the other hand, with  $S \gg 1$ ,  $g_* = 1$  within the MCNT approach (classical nucleation theory predicts that  $g_* < 1$  for this case). There is no point in injecting monomers into the cell. Since the growth rates of clusters of any size within CNT are equal to the nucleation rates  $J$  [2], it is possible to inject clusters of near-critical or subcritical size  $g_a$  into the cell [14]. Choosing  $g_a = 2$  for the size of the cluster is optimal, since, on the one hand, the distribution of the clusters by size (starting with the dimer) should be reproduced in any cell, and on the other hand, this solves the problem of injecting clusters with  $S \gg 1$ . This is exactly the approach used in our study.

The second distinctive feature of the MCNT-based algorithm is that the reactions of growth of  $g_a$ -sized clusters (during the association of a monomer and a cluster of size  $(g_a - 1)$ ) and of their decay are excluded from the computational algorithm, as both processes are included in the nucleation rate  $J$  [2].

The third distinctive feature of the computational algorithm based on MCNT is that the vapor temperature has to be determined for performing Monte Carlo simulations of the evaporation process. In the standard case, it is not necessary to determine the macroscopic parameters at each time step for the purpose simulating the collisions and motions of molecules by the DSMC method. Models based on MCNT or CNT are single-temperature, i.e., they assume that the translational and internal temperatures of monomers and clusters are equal. Since clustering leads to release of latent condensation heat into the flow, this approach implies using a single temperature to determine the rate constants of growth and decay of clusters. This can be either the translational monomer temperature  $T_1$ , or the temperature  $T_{tot}$ , averaged over the translational and internal energies of the particles in the cell [11]. On the one hand, however, if  $n_1 \gg n_g$ , the averaged temperature  $T_{tot}$  is close to the translational

monomer temperature  $T_1$ , and, the same as  $T_1$ , it does not reflect the real internal energy of the individual cluster  $g$ . On the other hand, the implementation of the algorithm using the  $T_{tot}$  quantity means that the changes that are incorrect from a physical standpoint have to be introduced to the main collision module of the program, since the number of collisions in a cell depends on temperature. In view of these circumstances, we have used the monomer temperature  $T_1$  to determine the reaction rates in this study.

We should note that it is possible to implement a mixed algorithm (this option is also considered in this paper) where dimers are injected into the flow field according to the MCNT algorithm, and the subsequent process of cluster evaporation is considered in a manner similar to the kinetic approach (the probability of a monomer evaporating from a cluster depends on the internal temperature of the individual cluster). However, this computational model cannot be accepted as correct from the standpoint of basic CNT.

### The kinetic approach to constructing the model

The kinetic approach involves no additional assumptions about the size of the clusters injected into the computational cell or about the calculation of the nucleation rate. Clustering starts with the formation of dimers by reaction (4).

The probabilities of the reactions occurring in case of known rate constants are determined using the Total Collision Energy model (TCE) [4, 20, 21]. This model is based on the assumption that the corresponding probabilities can be given in the form

$$p = L \frac{(E_{tot} - \varepsilon)^{Y + \zeta_{tot}/2 - 1}}{E_{tot}^{\zeta_{tot}/2 - 1}}, \quad (7)$$

where  $E_{tot}$  is the total energy;  $\zeta_{tot}$  is the total number of degrees of freedom;  $\varepsilon$  is the activation energy;  $L$ ,  $Y$  are the constants depending on the parameters of the model of elastic collisions of particles and the parameters of the rate constants of reactions.

To determine the parameters  $L$  and  $Y$  in expression (7), the reaction rate constants should be given in the Arrhenius form:



$$K = AT^B \exp(-\varepsilon/kT)$$

( $k$  is the Boltzmann constant); the constants  $A$ ,  $B$  and the activation energy  $\varepsilon$  are assumed to be known.

The kinetic model notably lacks the drawbacks of the MCNT model as it does not require either determining the macroscopic temperature in the cell or making additional assumptions about the size of the clusters injected into the cell and their parameters.

### Problem statement

The goal of this study is in calculating spherical steady-state expansion of water vapor from the surface of a sphere of radius  $R$  into vacuum. The calculation was performed using the direct simulation Monte Carlo method taking into account the process of vapor condensation in the volume.

The problem under consideration is one-dimensional, with a single radial coordinate  $X$ . However, implementing the DSMC method involves simulating all three components of particle velocity: the radial one  $v_x$  and the two components perpendicular to it,  $v_\theta$  and  $v_\phi$ . The source temperature  $T_0$  is assumed to be constant. Only monomers (molecules) of water evaporate from the surface. Evaporation is described by the Hertz – Knudsen law according to which the flux  $F^+$  of evaporating molecules is equal to

$$F^+ = n_0 v_0 / 4,$$

where  $n_0$  is the concentration of saturated vapor (corresponding to the equilibrium pressure determined by  $T_0$ );  $v_0$  is the average thermal velocity of the evaporating particles;

$$v_0 = (8kT_0/\pi m_1)^{1/2}$$

( $m_1$  is the monomer mass).

The equilibrium vapor pressure  $p_0(T)$  is determined in the same way as in [22]. The remaining parameters of water vapor correspond to those given in [23]. It is assumed that the distribution function for water molecules leaving the surface is semi-Maxwellian [19].

The vibrational degrees of freedom of the evaporating water molecules are assumed to be frozen for the range of source temperatures under consideration [24]. The internal energy of

the monomers leaving the surface is equal to the rotational energy

$$E_{int,1} = (\zeta_{r,1} / 2) k T_0.$$

The Larsen – Borgnakke model [4] is used for simulating the energy exchange between the translational and internal degrees of freedom. The probability of energy exchange between the rotational and translational degrees of freedom of water molecules in mutual collisions is taken equal to unity. The probabilities of energy exchange between the translational and internal degrees of freedom in monomer-cluster collisions are taken equal to 0.1 [10]. The formation of clusters in the flow field occurs according to the above-described condensation model. The reaction rate constants and the parameters of the collision models are taken from [25].

The molecules and clusters reaching the outer boundary of the region were excluded from the calculations (hypersonic boundary condition). The particles crossing the source boundary in the opposite direction were also excluded (the condition of total condensation on the surface).

The gas-dynamic flow pattern in the considered statement is determined by the Knudsen numbers

$$Kn = \lambda_0 / D = \lambda_0 / (2R),$$

where  $\lambda_0$  is the mean free path of the water molecules, corresponding to the parameters  $n_0$  and  $T_0$ ;  $D$  is the diameter of the sphere диаметр сферы, the characteristic reaction rates are given by (1), (2), (4), (5).

Calculation variants and the values of the determining parameters are listed in Table 1.

The calculations were performed by the DSCM method with a collision scheme without a time counter [4], using the developed software package at the Polytechnic RSC Tornado cluster of the Polytechnic University Supercomputer Center.

### Calculation results and discussion

Fig. 1 shows the simulation results, including data on the dynamics of the normalized values



Table 1

**Variants of calculation of spherical steady-state expansion  
of water vapor into vacuum**

Number	Model basis	Condensation taken into account	Knudsen number
1	—	—	$10^{-4}$
2	KA	+	$10^{-4}$
3	—	—	$10^{-2}$
4	KA	+	$10^{-2}$
5	MCNT	+	$10^{-4}$
6	MCNT + KA (for evaporation)	+	$10^{-4}$

Notes. 1. The source temperature was the same for all variants:  $T_0 = 350$  K.  
2. The Knudsen number  $Kn = \lambda_0/(2R)$ , where  $\lambda_0$  is the mean free path,  $R$  is the radius of the sphere.

Abbreviations: MCNT stands for modified classical nucleation theory, KA stands for kinetic approach.

of the concentration, velocity, and temperature of the vapor in the flow field. The vapor density decreases with distance from the surface, asymptotically tending to zero, while the gas velocity increases (Fig. 1, *a*). In case of outflow into a continuous medium ( $Kn = 0$ ), the velocity tends to its thermodynamic limit of steady-state expansion

$$u = (2 / (\gamma - 1))^{1/2} a_0,$$

where  $\gamma$  is the adiabatic exponent;  $a_0$  is the sound velocity determined from the temperature  $T_0$  [26].

In case of collisionless expansion ( $Kn \rightarrow \infty$ ), the vapor velocity tends to the thermal velocity determined from the equilibrium vapor temperature on the surface [27]:

$$u_{\max} = v_0.$$

The heat content of the vapor drops to zero for continuous-medium flow [26].

The temperature of the gas in case of free-molecular flow drops to the value [27]:

$$T / T_0 = 1 - 8 / (3\pi)$$

(Fig. 1, *b*).

The decrease in the degree of flow rarefaction (a decrease in the Knudsen number) leads to a greater number of collisions between particles and a more efficient conversion of ther-

mal energy into the energy of directed motion of particles. As a result, the gas velocity for a more dense flow regime ( $Kn = 10^{-4}$ ) increases with respect to the more rarefied flow ( $Kn = 10^{-2}$ ), while the density and the temperature decrease with distance from the source.

Notably, the result indicates that increasing the Knudsen number leads to a violation of the equilibrium between the translational and the internal degrees of freedom [17, 18]. The difference between the corresponding temperature components in the considered region is insignificant for  $Kn = 10^{-4}$ . However, the difference between the components becomes substantial even for Knudsen numbers of the order of 0.01.

Taking condensation into account in the calculations leads to two effects:

the release of energy from latent condensation heat into the flow. Within the model under consideration, the binding energy is released into internal degrees of freedom of clusters of size  $g > 2$  (see reaction (1)), as well as into translational and internal degrees of freedom of monomers and dimers under triple recombination of monomers during reaction (4);

a natural decrease of monomers during the formation and growth of clusters in the flow.

In view of the above-discussed factors, the condensation process contributes to an

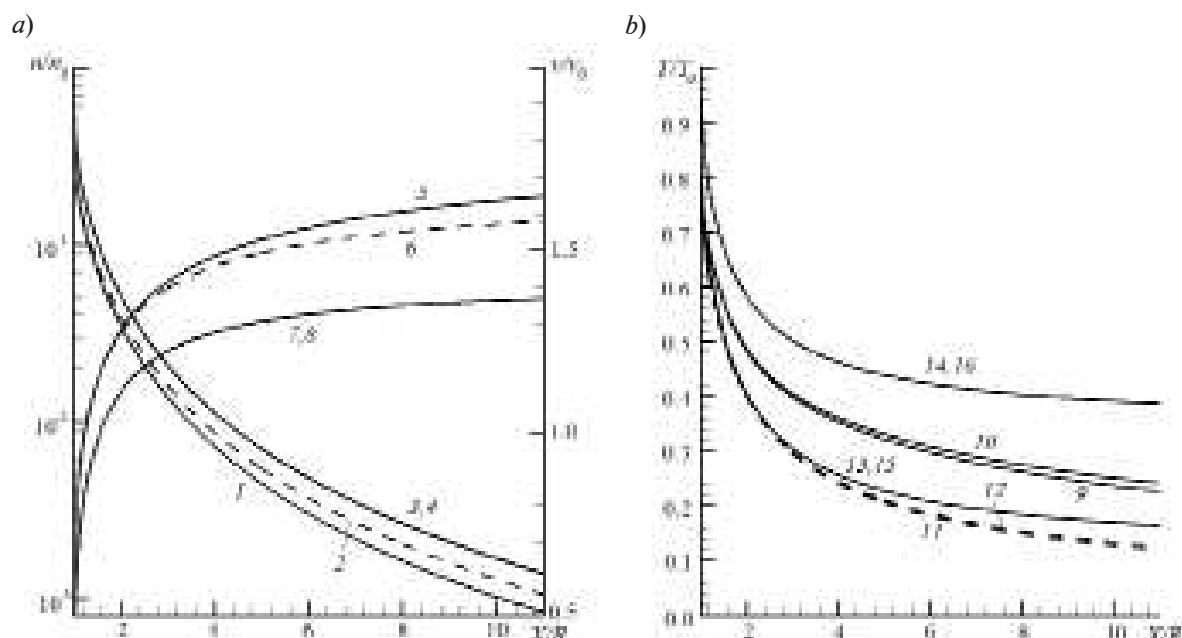


Fig. 1. Calculated density (curves 1 – 4) and velocity (5 – 8) distributions (a), and temperatures (b) of monomer vapor. Temperatures of translational (9, 11, 13, 15) and internal (10, 12, 14, 16) degrees of freedom are given. The calculations were performed with and without clustering taken into account (curves (1, 3, 5, 7, 9, 10, 13, 14) and (2, 4, 6, 8, 11, 12, 15, 16), respectively).  
 $Kn = 10^{-4}$  (1, 2, 5, 6, 9 – 12) and  $10^{-2}$  (3, 4, 7, 8, 13 – 16)

increase in the velocity and the temperature and to a faster decrease in the density of vapor in the flow. This effect can be clearly seen in Fig. 1 for the calculation variant ( $Kn = 10^{-4}$ ), for which the volume fraction of clusters is 5.4 %. The volume fraction of clusters in the flow for the Knudsen number 0.01 is less than 0.2 % and the condensation process has no effect on the gas dynamics of the flow.

The effect of clustering on the density and velocity distributions on the evaporating surface

is insignificant even for values of  $Kn = 10^{-4}$  (see Fig. 1). For example, the parameters of vapor on the sonic line differ by less than 3 % for the calculation variants with and without clustering taken into account (Table 2). The effect of the condensation process on the parameters of the sonic line turned out to be weaker compared with the results obtained in [19]. The distance of the sonic line from the evaporating surface in the variants with and without condensation is  $48.8\lambda_0$  and  $48.8\lambda_0$ , re-

Table 2

**Results of calculation of vapor parameters on the sonic line**

Variant number	Condensation taken into account	$n/n_0$	$T/T_0$	Reverse flow fraction, %
1	–	0.316	0.793	19.3
2	+	0.307	0.803	19.5

Note. The Knudsen number for the results given was  $Kn = 10^{-4}$ .

The numbers of the variants correspond to those in Table 1.

Notations:  $n/n_0$  is the normalized concentration of vapor,  $T/T_0$  is the normalized temperature of vapor.



spectively (for  $Kn = 10^{-4}$ ). The effect of condensation on the flow parameters (especially on the temperature) increases with increasing distance from the surface.

A feature of this class of rarefied flows is its translational nonequilibrium, which increases with increasing Knudsen number. The regions of translational nonequilibrium (i.e., the regions where the components  $T_x$ ,  $T_\theta$ ,  $T_\phi$  of the translational temperature  $T_r$  are different) for any Knudsen number are found directly near the evaporating surface (a Knudsen layer with a thickness on the order of several mean free paths of molecules) and at some distance from the surface when the local mean free path of particles becomes large with respect to the characteristic flow size [18]. The data in Fig. 2, *a* show the dimensions of the Knudsen layer at the surface. The two following conditions have to be simultaneously fulfilled to determine the size of the layer [18, 19]:

$$\frac{|T_x - T_\theta|}{T} \cdot 100\% < 3\%;$$

$$\frac{|T_r - T_{int}|}{T} \cdot 100\% < 3\%,$$

where  $T_{int}$  is the temperature of the internal degrees of freedom

The resulting layer thickness is  $40\lambda_0$  and practically does not depend on taking into account the condensation process.

In case of collisionless expansion, the entire flow region is the zone of translational nonequilibrium [27]. The difference between the temperature components  $T_x$  and  $T_\theta = T_\phi$  is also observed in the larger flow region for the calculation variant with  $Kn = 10^{-2}$  (Fig. 2, *b*), and only in the far-field of the jet for the case  $Kn = 10^{-4}$ . As a result, taking into account the condensation process has no noticeable effect on the degree of flow nonequilibrium.

The presence of nonequilibrium regions (with respect to translational and internal degrees of freedom) argues in favor of choosing the kinetic approach as the calculation method, since it does not involve calculating the vapor temperature for determining the rates of the reactions under consideration.

A case in point is the calculation of the flow using the MCNT approach, with condensation taken into account. Fig. 3 shows the calculated data for the changes in the degree of

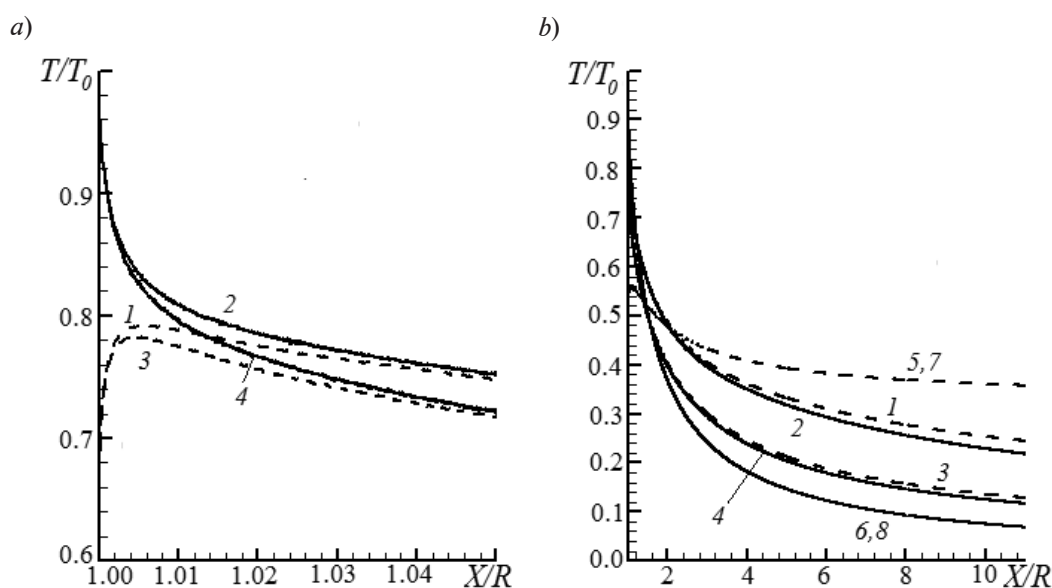


Fig. 2. Translational nonequilibrium near the surface of the sphere (*a*) and in the flow field (*b*). Data are given for the temperature components  $T_x$  (1, 3, 5, 7);  $T_\theta$ ,  $T_\phi$  (2, 4, 6, 8) at the values  $Kn = 10^{-4}$  (1 – 4) and  $10^{-2}$  (5 – 8). The calculations were carried out with (1, 2, 5, 6) and without (3, 4, 7, 8) clustering processes taken into account

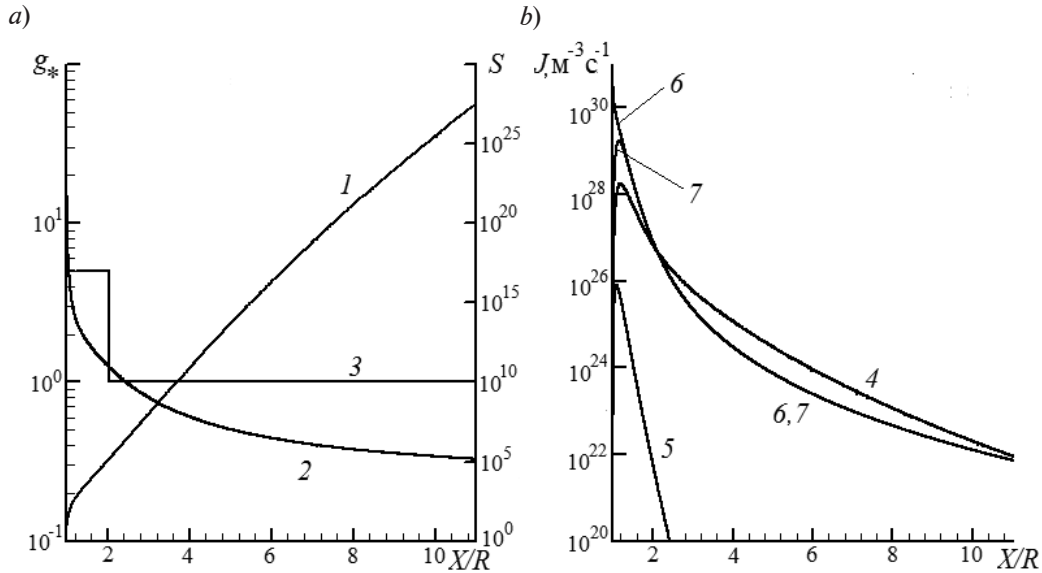


Fig. 3. Dependences of the supersaturation degree  $S$  (1), the critical cluster size  $g_*$  (2, 3) (a), the nucleation rates (4, 5, 7) and  $K_1$  (6) (b) versus the Knudsen numbers  $Kn = 10^{-4}$  (MCNT model). The values of  $g_*$  (curves 2 and 3 are the CNT and MCNT-based estimates, respectively),  $J_{clas}$  (4),  $J_K$  (5) and the calculated value of  $J$  (7) are given

supersaturation, the critical cluster size, and the nucleation rates as a function of the coordinate obtained for calculation variant 5 (the MCNT-based variant taking clustering into account, see Table 1). The degree of vapor supersaturation is small at the surface of the source where  $1.00 < X/R < 1.05$  (see Fig. 3,a), the size of the critical cluster  $g_* \gg 1$  and coincides for combined application of CNT and MCNT. The degree of supersaturation rapidly increases with distance from the source, and the critical size of the clusters decreases as a consequence. For this case, CNT predicts values of the degree of supersaturation to be less than unity as soon as distances of the order of one radius from the source are reached.

The MCNT approach predicts  $g_* = N_c$  at distances  $1.05 < X/R < 1.90$  (curve 3 in Fig. 3, a) from the source surface. The quantity  $g_*$  becomes equal to unity with further increase in the  $X/R$  coordinate.

The nucleation rates corresponding to the considered variants are shown in Fig. 3, b. The size of the critical cluster is fairly large directly at the surface of the source for low values of the equilibrium concentration  $n_{g^*}$ , predetermining low nucleation rates. The nucleation rate calculated by formula (1) for

MCNT coincides with the dimerization rate for triple collisions of monomers. The nucleation rate  $J_{clas}$ , calculated by the CNT formula [2], and the velocity  $J_K = J_{clas}/S$  with the Courtney correction differ significantly from the  $J$  values obtained within the MCNT model.

The behavior of clusters obtained by the calculation based on the kinetic approach is characterized by rather intense evaporation, and the maximum cluster size achieved in these calculations is limited to fourteen monomers. According to the calculations based on the MCNT, the clusters evaporate at a temperature equal to the translational temperature of the monomer vapor. The cluster growth rate turns out to be significantly higher than the evaporation rate. As a result, the number of clusters with the sizes  $g \gg 1$  varies little with increasing  $g$ .

Fig. 4 also shows the data for calculation variant 6 (see Table 1), where the injection of critical clusters into a cell was based on the MCNT model, and the evaporation in each cluster depended on its individual internal temperature (the same as with the kinetic approach). Apparently, using this approach brings the results substantially closer to those obtained based on the kinetic model.

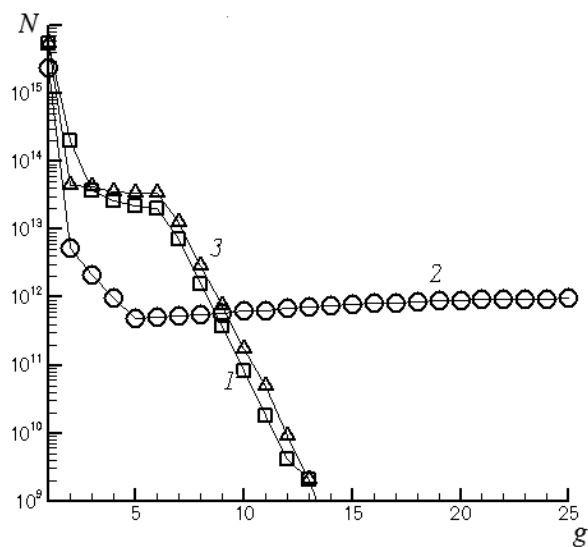


Fig. 4. Size distributions of clusters in the flow field, obtained from the calculation variants 2 (curve 1), 5 (2) and 6 (3)

The coordinate distributions of the density and the mole fraction of the clusters are shown in Fig. 5 for the Knudsen number  $10^{-4}$ . Dimers ( $g = 2$ ) form in the immediate vicinity of the source surface. The peaks on the distributions 5-mers ( $g = 5$ ) are shifted away from

the surface. The distance from the distribution maximum to the source increases with increasing cluster size. Fig. 5, *b* shows the coordinate distributions of the mole fraction of the clusters with the sizes  $g = 2, 3$  and 5. The presented results indicate freezing of the mole fractions starting with a certain coordinate depending on the cluster size. Since the nucleation rate  $J$  is low near the surface, the dimer concentrations at the surface, obtained by direct statistical simulation based on MCNT, are small compared to the concentrations obtained based on the kinetic approach, and the maximum of the dimer distribution is shifted away from the surface by  $0.25R$ .

The concentrations of the 5-mers in the greater part of the flow turn out to be substantially smaller than similar concentrations obtained using the kinetic approach. In case of variant 6 (MCNT model, with evaporation considered in accordance with the kinetic approach), the distributions of dimer and 5-mer concentrations turn out to be closer to the results of the calculations based on the kinetic approach (variant 5), however, the data do not coincide.

We should note that the results obtained

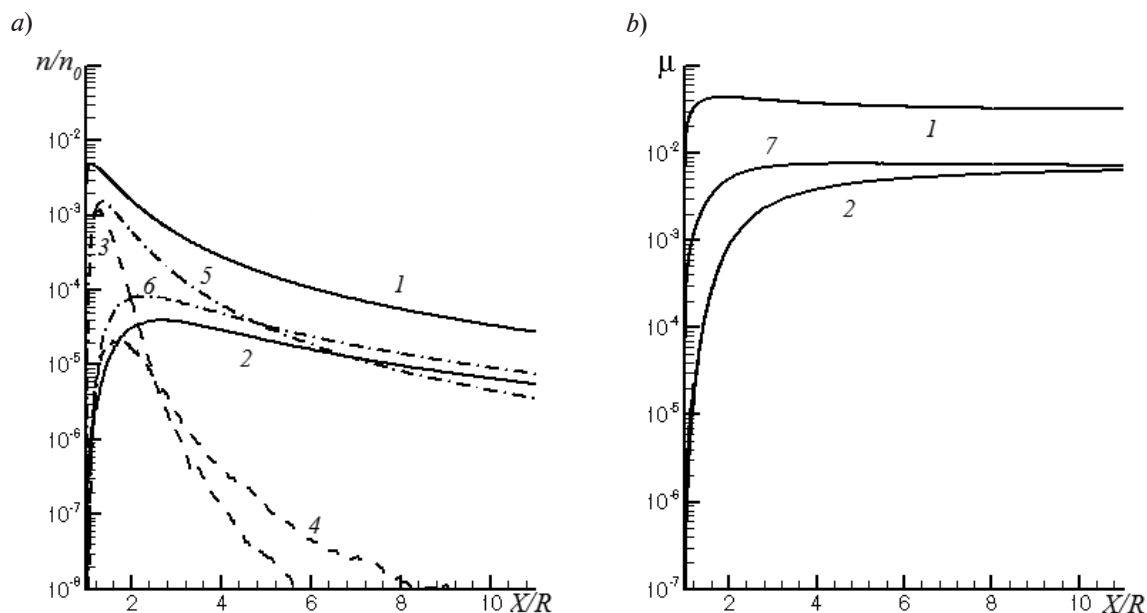


Fig. 5. Distributions of concentration (a) and mole fraction (b) of clusters along the radial coordinate for clusters with different sizes  $g$ . The calculations are based on the kinetic approach (1, 2, 7), on MCNT (3, 4) and on variant 6 (5, 6);  $g = 2$  (1, 3, 5), 3 (7) and 5 (2, 4, 6).  
Knudsen number  $\text{Kn} = 10^{-4}$

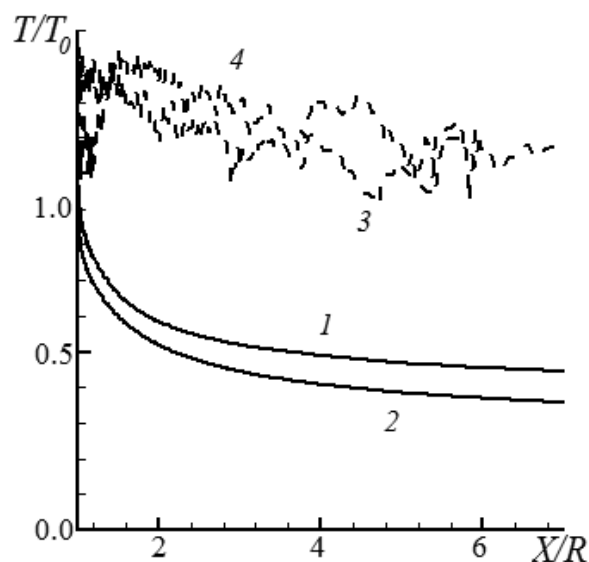


Fig. 6. Distributions of the internal temperature of particles along the radial coordinate for clusters of two sizes: dimers (curves 1, 3) and trimers (2, 4). Calculations are based on the kinetic approach (1, 2) and on MCNT (3, 4)

using the model [11] differ from those in [19]. Size distributions of clusters have a maximum corresponding to the dimer size.

The translational velocities of the growing clusters coincide with the monomer velocity for the calculation variant with  $Kn = 10^{-4}$ . The internal temperatures of the clusters are shown in Fig. 6. These temperatures of dimers and trimers are above the translational temperature because latent condensation heat is released into the flow during cluster growth. The growth is accompanied by evaporation of clusters, during which the binding energy is absorbed. The evaporation rate of each cluster within the model based on the kinetic approach depends on its own internal temperature and this rate proves to be comparable with the growth rate. As a result, the evaporation process leads to a moderate difference in the translational and internal temperatures of the clusters and a limited maximum cluster size (see Fig. 4). The evaporation rate for the MCNT model is governed by the translational temperature of the monomers. The growth process plays the principal role within the MCNT-based approach. The evaporation of clusters, which reduces their

internal energy, has a rate that is small compared to their growth rate. As a result, growth of large clusters ( $g \gg 1$ ) is observed, and the energy that is released during this process is accumulated in internal degrees of freedom. The internal temperature of the clusters obtained in the calculations based on the MCNT model is higher than the internal temperatures of the clusters predicted by the kinetic model of condensation (see Fig. 6).

### Conclusion

We have carried out a calculation of expansion of water vapor into vacuum from the surface of a spherical source by direct statistical modeling, taking into account cluster growth in the flow field. Two models of the clustering process were used for the calculations:

one based on the conclusions of the modified classical nucleation theory;

and one based on the kinetic approach.

One of the main drawbacks of MCNT is that the model based on it is single-temperature. It is impossible to correctly describe the processes of evaporation of monomers from clusters within this approach. Implementing the model through a computational algorithm is complex and additional assumptions have to be introduced. The calculated main characteristics of clustering (the spatial distribution of the cluster concentration, the size distribution of clusters in the flow field) obtained using the MCNT model differ significantly from those obtained by the model based on the kinetic approach.

The kinetic model is free of all drawbacks of the MCNT model. This approach allows to obtain the probabilities of cluster growth/evaporation as functions of individual parameters of colliding/decaying particles, which is in full agreement with the DSMC method. The temperature of vapor in a cell does not need to be determined for simulating the condensation process. From a methodological standpoint, using a model based on the kinetic approach is justified.

Calculations of condensation of water vapor expanding from a spherical surface into vacuum based on the kinetic model in near-continuous and transient Knudsen regimes indicate that the condensation process does not

affect the parameters of gas-dynamic flow at clustering degrees less than 1 %. The degree of clustering becomes noticeable (5.4 %) in near-continuous regimes ( $Kn = 10^{-4}$ ). In this case, the release of latent heat of condensation into the flow leads to a faster growth of gas velocity and temperature and to a drop in gas density. The clustering process has a particularly strong effect on the distribution of translational and internal temperatures of the vapor. However, even for the calculation variant corresponding to  $Kn = 10^{-4}$ , the condensation process does not significantly affect the parameters of the sonic line, the size of the Knudsen layer, and the degree of translational nonequilibrium compared to the calculation results obtained

without taking into account the condensation process. The maximal concentration of clusters in the flow field corresponds to size of a dimer.

The study has described the effect of the mole fractions of clusters ‘freezing’ as they move away from the surface of the source. For larger clusters, the effect is observed at large distances from the evaporated surface. The rates and translational temperatures of the clusters formed in the flow prove to be close to the corresponding parameters of the monomers. The release of binding energy in the process of particle association leads to higher values of internal temperatures of the clusters compared to the internal temperature of the monomers.

## REFERENCES

- [1] **J.F. Crifo**, Water clusters in the coma of comet Halley and their effect on the gas density, temperature, and velocity, *Icarus*. 84 (2) (1990) 414–446.
- [2] **L.E. Sternin**, *Osnovy gazodinamiki dvukhfaznykh techeniy v soplakh* [Fundamentals of gas dynamics of two-phase flows in the nozzles]. Mashinostroyeniye, Moscow, 1974.
- [3] **Yu.V. Platov, B.P. Filippov, A.I. Semenov**, Condensation of combustion products in the exhaust plumes of rocket engines in the upper atmosphere, *Geomagnetism and Aeronomy*. 51 (4) (2011) 550–556.
- [4] **G.A. Bird**, *Molecular gas dynamics and the direct simulation of gas flows*, Clarenton Press, Oxford, 1994.
- [5] **B. Briehe, H.M. Urbassek**, Monte Carlo simulation of growth and decay processes in a cluster aggregation source, *J. Vac. Sci. Technol. A*. 17 (1) (1999) 256–265.
- [6] **M.I. Zeifman, B.J. Garrison, L.V. Zhigilei**, Combined molecular dynamics direct simulation Monte Carlo computation study of laser ablation plume evolution, *J. Appl. Phys.* 92 (4) (2002) 2181–2193.
- [7] **N.Yu. Bykov, G.A. Lukyanov**, Direct simulation Monte Carlo of pulsed laser ablation of metals with clusterization processes in vapor, *Thermophysics and Aeromechanics*. 13 (4) (2006) 569–582.
- [8] **T.E. Itina, K. Gouriet, L.V. Zhigilei, et al.**, Mechanisms of small clusters production by short and ultra-short pulse laser ablation, *Appl. Surf. Sci.* 253 (19) (2007) 7656–7661.
- [9] **Z. Li, J. Zhong, D.A. Levin, B.J. Garrison**, Development of homogeneous water condensation models using molecular dynamics, *AIAA Journal*. 47 (5) (2009) 1241–1251.
- [10] **R. Jansen, I. Wysong, S. Gimelshein, et al.**, Nonequilibrium numerical model of homogeneous condensation in argon and water vapor expansions, *J. Chem. Phys.* 132 (24) (2010) 244105.
- [11] **N.Yu. Bykov, Yu.E. Gorbachev**, Mathematical models of water nucleation process for the Direct Simulation Monte Carlo method, *Applied Mathematics and Computation*. 296 (1 March) (2017) 215–232.
- [12] **J. Zhong, M.I. Zeifman, S.F. Gimelshein, D.A. Levin**, Modeling of homogeneous condensation in supersonic plumes with the DSMC method, *AIAA Paper* (2004), 42<sup>nd</sup> Aerospace Sciences Meeting, Jan. 5 – 8, Reno, Nevada, 2004-0166.
- [13] **J. Zhong, M.I. Zeifman, S.F. Gimelshein, D.A. Levin**, Direct simulation Monte Carlo modeling of homogeneous condensation in supersonic plumes, *AIAA Journal*. 43 (8) (2005) 1784–1796.
- [14] **N.Y. Bykov, Y.E. Gorbachev**, Direct statistical simulation of the processes of clusters formation in the gas phase: classical approach with cluster size correction, *High Temperature*. 53 (2) (2015) 291–300.
- [15] **D.I. Zhukhovitskii**, Size-corrected theory of homogeneous nucleation, *J. Chem. Phys.* 101 (6) (1994) 5076–5080.
- [16] **N.Y. Bykov, Y.E. Gorbachev**, Comparative analysis of condensation models within DSMC, *AIP Conference Proceedings*. 1628 (1) (2014) 139–147.
- [17] **N.M. Bulgakova, M.Yu. Plotnikov, A.K. Rebrov**, Modeling steady-state gas expansion from a spherical surface into a vacuum, *Fluid Dynamics*. 32 (6) (1997) 137–143.
- [18] **G.A. Lukyanov, Gr.O. Khanlarov**, Stationary water vapor expansion from a spherical surface into vacuum, *Thermophysics and Aeromechanics*. 7 (4) (2000) 511–521.



- [19] **N.Yu. Bykov**, Modelling of condensation at spherical expansion of water vapor into vacuum, *Thermophysics and Aeromechanics*. 2009. 16 (2) (2009) 189–199.
- [20] **G.A. Bird**, Simulation of multi-dimensional and chemically reacting flows, In: *Rarefied Gas Dynamics*, ed. by R. Campargue, Commissariat a Lenergie Atomique, Paris, 1 (1979) 365–388.
- [21] **S.F. Gimelshein, N.E. Gimelshein, D.A. Levin, et al.**, On the use of chemical reaction rates with discrete internal energies in the direct simulation Monte Carlo method, *Physics of Fluids*. 16 (7) (2004) 2442–2451.
- [22] **N. Goldman, R.S. Fellers, C. Leforestier, R.J. Saykally**, Water dimers in the atmosphere: Equilibrium constant for water dimerization from the VRT (ASP-W) potential surface, *J. Phys. Chem. A*. 105 (3) (2001) 515–519.
- [23] **J. Wolk, R. Strey**, Homogeneous nucleation of  $H_2O$  and  $D_2O$  in comparison: the isotope effect, *J. Phys. Chem. B*. 105 (47) (2005) 11683–11701.
- [24] **X. Xu, W. Goddard**, Bonding properties of water dimer: a comparative study of density functional theories, *J. Phys. Chem. A*. 108 (12) (2004) 2305–2313.
- [25] **N.Y. Bykov, Y.E. Gorbachev, V.V. Zakharov**, Simulation of small cluster formation in water vapor plumes, *AIP Conference Proceedings*, 1786 (1) (2016) 050001-1–050001-8.
- [26] **G.G. Cherniy**, *Gazovaya dinamika* [Gas dynamics], Nauka, Moscow, 1988.
- [27] **Yu.A. Koshmarov, Yu.A. Ryzhov**, *Prikladnaya dinamika razrezhennogo gaza* [Applied rarefied gas dynamics], Mashinostroyeniye, Moscow, 1977.

*Received 30.11.2017, accepted 08.02.2018.*

#### THE AUTHOR

**BYKOV Nikolay Yu.**

*Peter the Great St. Petersburg Polytechnic University*

29 Politechnicheskaya St., St. Petersburg, 195251, Russian Federation

nbykov2006@yandex.ru



## POROSITY AND SURFACE MORPHOLOGY OF LEAD SELENIDE – TIN SELENIDE LAYERS ON SILICON SUBSTRATES: X-RAY DIFFRACTION STUDIES

**A.I. Mamontov<sup>1</sup>, A.P. Petrakov<sup>2</sup>, S.P. Zimin<sup>3</sup>**

<sup>1</sup>Vyatka State Humanities University, Kirov, Russian Federation;

<sup>2</sup>Syktyvkar State University Named after Pitirim Sorokin, Syktyvkar, Russian Federation;

<sup>3</sup>P.G. Demidov Yaroslavl State University, Yaroslavl, Russian Federation

In the paper, the surface porosity and morphology of  $\text{Pb}_{0.97}\text{Sn}_{0.03}\text{Se}$  films on silicon substrates subjected to anodic electrochemical etching in the Tompkins-Johnson's electrolyte at a current density of  $1 \text{ mA/cm}^2$  have been studied using X-ray reflectometry. To reduce the difference in lattice parameters of a growing film, buffer  $\text{CaF}_2$  layer (about 2 nm thick) and buffer PbSe one (about 400 nm thick) were used. The averaged thickness of re-precipitated near-surface selenium layer was determined to be 45 nm. The X-ray experimental results showed qualitative agreement with electron-microscopical data. It was established by high-resolution X-ray diffraction methods that macroporous structure with transverse and longitudinal porous projections of sizes 47 and 82 nm (relatively) was forming in electrochemical etching. The angle of porous tilt with the surface normal was found to be 34.5 degrees. The applicability of high-resolution X-ray methods to nondestructive investigation of porous structure was shown.

**Key words:** anodizing; porosity; total external reflection method; electrochemical etching; lead-tin selenide

**Citation:** A.I. Mamontov, A.P. Petrakov, S.P. Zimin, Porosity and surface morphology of lead selenide – tin selenide layers on silicon substrates: X-ray diffraction studies, St. Petersburg Polytechnical State University Journal. Physics and Mathematics. 11 (1) (2018) 67 – 74. DOI: 10.18721/JPM.11110

### Introduction

Porous semiconductor materials now attract a great deal of attention due to their unique properties and potential applications. The processes of pore formation are actively studied in elemental semiconductors (silicon and germanium), in binary and ternary materials  $\text{A}^3\text{B}^5$ ,  $\text{A}^2\text{B}^6$  [1 – 3, etc.]. Lead chalcogenides (PbTe, PbSe, PbS and solid solutions based on them) that belong to the group of narrow-band semiconductors  $\text{A}^4\text{B}^6$  are traditionally widely used in thermoelectric devices, optoelectronics devices of the IR range, solar cells, etc. Pore formation in these materials can lead to effective modification of structural, electrical and optical properties [4 – 7, etc.]. At the same time, it is extremely important to obtain data on the

surface morphology, the structure of porous objects, the size of the pores and the magnitude of porosity. For example, it was established in [7] that the processes of pore formation in lead selenide and tin selenide films are accompanied by a significant reprecipitation of selenium on the walls of pores and on the surface.

The goal of this study has been to determine the pore and surface parameters of porous  $\text{Pb}_{0.97}\text{Sn}_{0.03}\text{Se}$  films on silicon substrates using high-resolution X-ray methods. The presented results continue the studies published in [7].

### Experimental procedure

Film samples of  $\text{Pb}_{0.97}\text{Sn}_{0.03}\text{Se}/\text{PbSe}/\text{CaF}_2/\text{Si}(111)$  with a total thickness of  $4.5 \text{ }\mu\text{m}$  were grown by molecular beam epitaxy on a single-crystal Si(111) substrate. The size of the sub-

strate's mosaic blocks, determined by high-resolution X-ray diffraction [8], was approximately 30  $\mu\text{m}$ . Thin buffer layers of  $\text{CaF}_2$  (about 2 nm thick) and  $\text{PbSe}$  (about 400 nm) were used to reduce the discrepancy between the lattice parameter of the growing film ( $a_1 = 0.615$  nm) and of the substrate ( $a_2 = 0.543$  nm), as well as to reduce mechanical stresses in the ternary solid solution.

Pore formation in the near-surface layer of lead selenide – tin selenide was carried out in a vertical electrochemical cell with a platinum upper cathode at a current density of 1 mA/cm<sup>2</sup> for 10 min. The etching was done in the Tompkins and Johnson solution: 40 ml of glycerin, 10 ml of  $\text{HNO}_3$ , 10 ml of glacial acetic acid. The technology and basic properties of the porous structure of the obtained samples are described in [7].

High-resolution X-ray diffractometry and X-ray reflectometry studies were carried out using a DRON-UM1 X-ray powder diffractometer. The radiation of  $\text{CuK}_{\alpha 1}$  ( $\lambda K_{\alpha 1} = 1.5405$  Å,  $\lambda K_{\alpha 2} = 1.5443$  Å) was formed by a slit monochromator made of single-crystal silicon with a triple reflection (111) and vertical and horizontal collimator exit slits with the width of 2.0 mm and 0.1 mm, respectively.

The diffraction scheme was assembled with a goniometer allowing to register the angular deviation in three-crystal geometry with an accuracy of 0.1 arcsec. (Fig. 1, *a*). A planar  $\text{Si}(111)$  crystal analyzer was placed between the sample and the detector.

Data on the properties of the samples and their surfaces were obtained from the dependence of the detected intensity on the rotation angles of the sample and the analyzer. The method makes it possible to determine the interplanar spacings of epitaxial structures, as well as the pore parameters in porous materials. Scattering by a rough surface or scattering caused by defects can be separated from scattering by a perfect crystal.

The method of X-ray reflectometry, based on measuring the reflectivity of X-ray radiation in the angular region of total external reflection (TER), was also used in the study. A slit with the width  $S_2 = 0.25$  mm was placed in front of the detector for reflectometry measurements (Fig. 1, *b*).

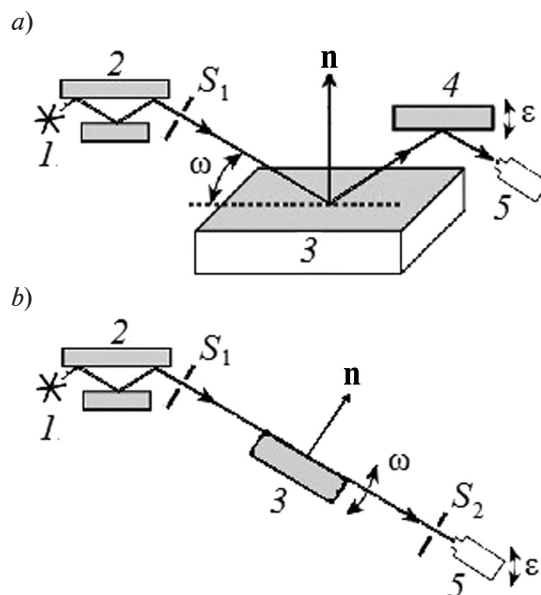


Fig. 1. Three-crystal diffraction (*a*) and reflectometric (*b*) schemes of X-ray imaging methods:

source of X-ray radiation 1, monochromator 2, sample 3, analyzer 4, detector 5;  $\mathbf{n}$  is the normal to the surface;  $S_1$ ,  $S_2$  are the slits; the notations for the angles are explained in the text

### Processing and discussion of the results

The structural features of porous layers of  $\text{Pb}_{0.97}\text{Sn}_{0.03}\text{Se}$  were studied by high-resolution three-crystal X-ray diffractometry (TCXRD). For this purpose, contours of equal diffuse scattering intensity were plotted on the X-ray patterns taken by the analyzer in scanning mode at different positions of the sample crystal [9]. The contours of equal intensity (Fig. 2) were constructed in inverse space according to the formulae:

$$q_z = (2\pi\varepsilon \cdot \cos \theta_B) / \lambda, \quad (1)$$

$$q_x = [2\pi(2\omega - \varepsilon)\sin\theta_B] / \lambda, \quad (2)$$

where  $\varepsilon$  and  $\omega$  are, respectively, the angles by which the analyzer and the sample deviate from the Bragg angle;  $\theta_B$  is the Bragg angle;  $\lambda$  is the X-ray wavelength.

The system had the following resolution:  $\Delta q_z = 0.1(\mu\text{m})^{-1}$ ,  $\Delta q_x = 0.2(\mu\text{m})^{-1}$ .

Sufficiently perfect crystals are typically obtained through growing layers of lead selenide – tin selenide by molecular-beam epitaxy.

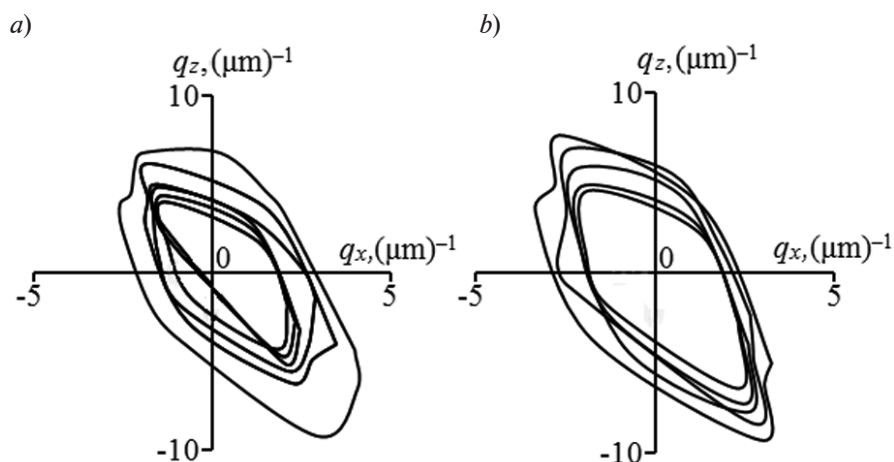


Fig. 2. Equal intensity contours around the (111) reciprocal lattice site for the  $\text{Pb}_{0.97}\text{Sn}_{0.03}\text{Se}/\text{PbSe}/\text{CaF}_2/\text{Si}(111)$  structure obtained by TCXRD for the initial (a) and the porous (b) surface

However, because of the mismatch between the lattice parameters of the substrate and the buffer layer and the parameters of the structure under consideration, caused by the difference in the linear thermal expansion coefficients of the materials of the multilayer system, penetrating dislocations and point defects evolve in the epitaxial film. In addition, the substrate initially had a small lattice deviation from the surface, amounting to approximately 1 – 2 degrees. This led to a slight tilt of the lattice and the grown film.

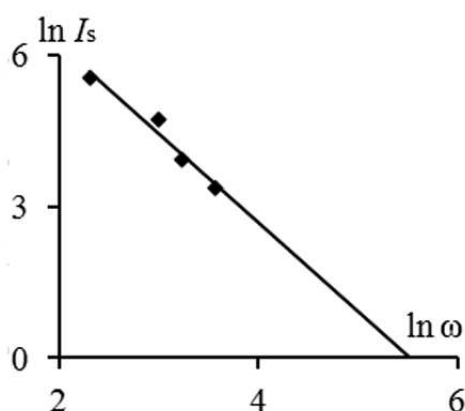


Fig. 3. Linear anamorphosis of the angular dependence of the diffuse scattering peak intensity for the initial  $\text{Pb}_{0.97}\text{Sn}_{0.03}\text{Se}/\text{PbSe}/\text{CaF}_2/\text{Si}(111)$  system; the dependence was obtained by the TCXRD method;  $\omega$  is the angle of rotation of the sample (see Fig. 1, a)

Fig. 3 shows the dependence of the diffuse scattering intensity  $I_s$  on the TCXRD curves on the sample rotation angle  $\omega$  (on a double logarithmic scale). It can be seen that the intensity decreases by the  $\omega$ - $b$  law. The parameter  $b$  was sought by determining the tilt of the curve

$$\ln I_s = f(\ln \omega);$$

it was found to be equal to 1.8.

This value of the parameter indicates that X-ray radiation is scattered mainly by dislocations [8]. The physical nature and the role of dislocations in such systems (lead chalcogenide films on a silicon substrate) are described in detail in [10].

The contours around the (111) reciprocal lattice site are shaped as a tilted oval (see Fig. 2) with indented edges, which corresponds to diffuse scattering by small defects of trigonal symmetry [11]. The shape of the contours becomes more characteristic for diffuse scattering on small defects after anodizing. Pores are typically the main defects formed during anodizing; for this reason, it seems logical to assume that the diffraction pattern in porous  $\text{Pb}_{0.97}\text{Sn}_{0.03}\text{Se}$  films is primarily governed by X-ray scattering by pores.

SEM micrographs images of porous film cleavage are shown in Fig. 4. The surfaces of the films exhibit a fairly homogeneous structure (region I). After the electrochemical etching process, a porous layer with a thickness of

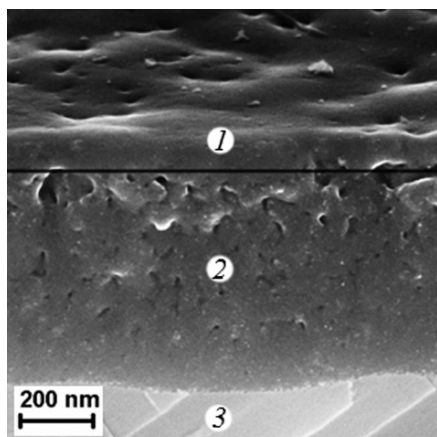


Fig. 4. Micrographs of cleavage of porous lead selenide – tin selenide film; regions of reprecipitated selenium (1), the porous structure (2), and the unchanged region (3) are shown

about 700 nm (region 2) was formed, and the surface of the sample gained a complex morphology. Notably, a near-surface layer about 50 nm thick (region 1 of the cleavage) had no pronounced pores and was, apparently, a layer of precipitated selenium-based products of electrochemical reactions. This is confirmed by backscattering of electrons at a voltage of 10 kV [7]. An estimate of the geometric porosity (the ratio of the pore area to the total area) over a series of cleavage images showed that the porosity was non-uniform in thickness and varied from 37 % in the upper part to 18 % in

the lower part of the porous  $\text{Pb}_{0.97}\text{Sn}_{0.03}\text{Se}$  layer under consideration.

Electrochemical anodizing in  $\text{Pb}_{0.97}\text{Sn}_{0.03}\text{Se}$  crystals generated pores shaped as parallelepipeds with blurred boundaries [7]. The average pore dimensions along the surface ( $l_x$ ) and perpendicular to it ( $l_z$ ) can be estimated from the half-width of the diffuse scattering peaks obtained by rotating the sample crystal at a fixed angular position of the crystal analyzer ( $\omega$  scan) and ( $\theta/2\theta$ ) scans (Fig. 5):

$$l_x \approx \lambda / (2\Delta\theta \cdot \sin\theta_B), \quad (3)$$

$$l_z \approx \lambda / (2\Delta\theta_z \cdot \cos\theta_B), \quad (4)$$

where  $\Delta\theta$ ,  $\Delta\theta_z$  are the widths of the diffuse scattering peak on the TCXRD curves taken in the  $\omega$  and ( $\theta/2\theta$ ) scanning modes, respectively (the rotation step of the analyzer is twice as large as that of the sample in the latter of these modes).

The pores are not actually parallelepiped-shaped vertical cavities; they have kinks and are tilted at an angle to the surface of the film [7], which leads to a decrease in average pore sizes over depth. The average angle  $\xi$  of pore tilt to the normal of the sample surface can be estimated from the angular position of the diffuse peak on the X-ray patterns taken while rotating the sample crystal at a fixed angular position of the analyzer crystal (see Fig. 5):

$$\text{tg}\xi = q_{x0} / q_{z0}, \quad (5)$$

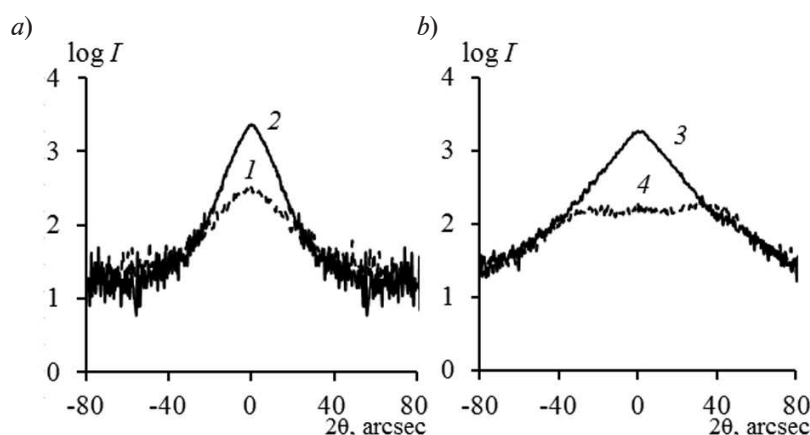


Fig. 5. Diffuse scattering intensities (TCXRD curves) recorded for porous lead selenide – tin selenide in the ( $\theta/2\theta$ ) (a) and  $\omega$  (b) scanning modes; curves 1 and 2 were obtained for the initial and the porous surface, respectively; curves 3 and 4 were obtained for the values of the angle  $\varepsilon = 0$  and  $-30^\circ$ , respectively



where  $q_{x0}$  and  $q_{z0}$  are the coordinates of the diffuse peak on the TCXRD cross-sections.

The value of the tilt angle  $\xi$  allows to estimate the average values of the transverse ( $d$ ) and longitudinal ( $l_l$ ) pore sizes (perpendicular to and along the surface normal) [8]:

$$d \approx l_x \sin \xi, \quad (6)$$

$$l_l \approx l_z / \sin \xi, \quad (7)$$

where  $l_x$ ,  $l_z$  are the average pore sizes along the surface and over the layer depth.

With a current density of 1 mA/cm<sup>2</sup> and anodizing time of 10 min, the transverse and longitudinal pore projections were 47 and 82 nm, respectively. The average tilt angle of the pores from the normal to the surface was 34.5 degrees. This value is close to the angle of 35 degrees, determined for the propagation of pores in lead telluride films [5] and the corresponding pore formation in the crystallographic direction (110). Interestingly, the longitudinal sizes of the pores turned out to be less than the total thickness of the porous layer, which, apparently, indicates the that through pores broke down into several segments.

Fig. 6 shows the normalized experimental integral curves obtained by X-ray reflectometry before and after electrolytic etching. The depth of X-ray penetration into the sample was minimal and expressed by the extinction length

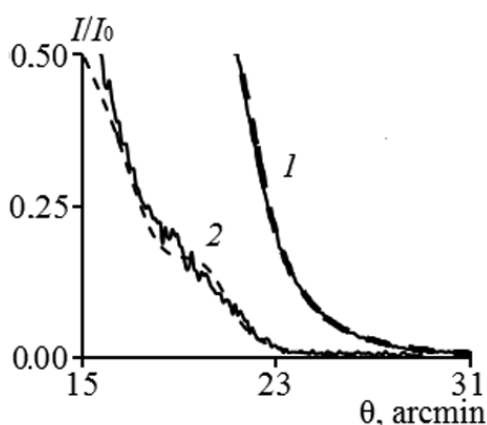


Fig. 6. Experimental (solid lines) and theoretical (dashed lines) curves obtained by X-ray reflectometry for the initial (1) and the porous (2) surface;  $\chi^2 = 0.32$  (1) and 2.34 (2)

determined by the polarization coefficient  $\chi$  within the Bragg reflection. The extinction length for a lead selenide single crystal was about 380 nm.

The value of the critical angle on the curves obtained by reflectometry allows to calculate the degree of porosity  $P$  for homogeneous systems, that is, the ratio of the pore volume to the sample volume in percent [12, 13]:

$$P = 1 - (\theta_{ca} / \theta_{ci})^2, \quad (8)$$

where  $\theta_{ci}$  and  $\theta_{ca}$  are the critical angles on the diffraction curves before and after anodizing, respectively.

The main factors affecting the change in the shape of the diffraction curve are the surface microgeometry and the presence of inhomogeneities in the near-surface region of the sample. The critical angle  $\theta_c$  was determined from the angular position of the point with an intensity equal to half the height in the region of diminishing intensity. A significant decrease in the  $\theta_c$  value after anodizing treatment is explained by the increase in the degree of X-ray absorption as a result of the emergence of pores. The degree of porosity was 44 %.

We should note that the extinction length was almost half the thickness of the anodized region (700 nm judging by the image of the cleavage, see Fig. 4) and the degree of porosity was calculated only for the upper region of the porous sample. An additional porous layer of selenium was located on the surface of the porous  $\text{Pb}_{0.97}\text{Sn}_{0.03}\text{Se}$  layer in the case under consideration.

Importantly, the critical angles used to determine the porosity depend on the polarization coefficient of the substance, while a part of the near-surface layer about 50 nm thick (1/6th – 1/7th part of the surface) was made up of deposited reaction products. For comparison, the critical angle for a perfect selenium single crystal ( $0.281^\circ$ ) was less than that for a lead selenide crystal ( $0.367^\circ$ ). Since the thickness of the selenium layer was 14–17 % of the region under consideration, it is obvious that the influence of this layer on the X-ray reflectometry curves cannot be neglected. As a result, the porosity values in lead-tin selenide, obtained by formula (8), turned out to be overestimated compared to the geometric porosity



value in the upper region of the porous layer. For this reason, the next stage of the study involved the analysis of X-ray reflectometry data for a porous system within the framework of a two-layer model.

A theoretical plot is usually constructed from X-ray reflectometry data to determine the structural parameters of the surface under consideration (see the dashed curves in Fig. 6), achieving a high degree of convergence with the experimental reflectometry curve [14, 15]. An analysis scheme with Parratt's recursion relations for calculating the  $R_n$  amplitude of mirror reflection of X-rays from  $n$  layers of a given structure is used to construct the theoretical curve [15]:

$$R_n = \frac{r_n + R_{n-1} \exp(2\pi D_n k_n / \lambda)}{1 + r_n R_{n-1} \exp(2\pi D_n k_n / \lambda)}, \quad (9)$$

$$k_n = \sin^2 \theta + \chi_n, \quad (10)$$

where  $\theta$  is the incidence angle of X-rays;  $\chi_n$  is the polarizability of the material of the  $n$ th layer (in the first approximation it is proportional to the electron density in this material);  $D_n$  is the thickness of the layer.

The amplitudes  $r_n$  of reflection from the boundary of each individual layer are determined by the Fresnel coefficients  $k_n$ :

$$r_n = \frac{k_{n+1} - k_n}{k_{n+1} + k_n} \exp \left[ -0,5 \left( \frac{2\pi}{\lambda} k_n \sigma_n \right)^2 \right], \quad (11)$$

where  $\sigma_n$  is the roughness of the layer.

The thickness  $D_n$  and the roughness  $\sigma_n$  of the layers were fitted in modeling the theoretical reflectometry curve. The parameters of the  $\text{Pb}_{0.97}\text{Sn}_{0.03}\text{Se}$  surface, obtained by minimizing the functional  $\chi^2$ , are shown in the table. For initial films, we have a fairly flat surface with distinctive triangular nanotraces, typically several nanometers high [5]. The calculated density  $\rho$  for the initial surface in the model turned out to be slightly less than that of the lead selenide single crystal. After electrochemical etching, the density of lead-tin selenide decreased by 32 %, compared with tabular values for lead selenide (8.3 g/cm<sup>3</sup>). The porosity value of 32 %, found from the density change, is in good agreement with the averaged geometric porosity in the upper half of the porous  $\text{Pb}_{0.97}\text{Sn}_{0.03}\text{Se}$  layer. A thin surface layer, presumably consisting of selenium, was discovered for anodized films (tabular density values of various modifications of selenium are in the range of 4.3–4.8 g/cm<sup>3</sup>) with a thickness of about 45 nm, which corresponds to the estimates acquired by scanning electron microscopy. The  $\sigma_2$  value for the second layer is the roughness of the boundaries between the layers.

## Conclusion

Thus, the methods of reflectometry and high-resolution X-ray diffraction proved to be effective tools for determining the porosity value and the pore parameters of  $\text{Pb}_{0.97}\text{Sn}_{0.03}\text{Se}$

Table

Simulation results of  $\text{Pb}_{0.97}\text{Sn}_{0.03}\text{Se}$  layers

Surface (convergence $\chi^2$ )	$D_n, \text{\AA}$		$\sigma_n, \text{\AA}$		$\rho_n, \text{g/cm}^3$	
	$n = 1$	$n = 2$	$n = 1$	$n = 2$	$n = 1$	$n = 2$
Initial (0.32)	—	—	43	—	7.8	—
Porous (2.34)	450	—	350	50	4.4	5.7

Notations:  $D_n$ ,  $\sigma_n$ ,  $\rho_n$  are the thickness, the roughness and the density of the  $n$ -th layer.

Notes: 1. The porous surface consists of the near-surface layer and the porous layer itself.

2. The scattering of X-rays by the substrate and the initial non-porous layer was not taken into account in the simulations.





films. We have established that a macroporous structure with transverse pore projections of 47 nm and longitudinal pore projections of 82 nm formed under electrochemical treatment in a Tompkins-Johnson electrolyte at a current density of 1 mA/cm<sup>2</sup>. We have found the averaged thickness of the near-surface selenium layer to be 45 nm, which had a significant effect on the porosity value determined by reflectometry. A qualitative agreement has been obtained between the results of X-ray and SEM studies. We have demonstrated the possibilities of using high-resolution X-ray methods for

nondestructive investigation of the structure of porous materials.

### Acknowledgment

The authors are grateful to H. Zogg (ETH Zurich) for providing the PbSnSe/PbSe/CaF<sub>2</sub>/Si(111) films for the studies, and to E.Yu. Buchin (deputy director of the Yaroslavl branch of the Ioffe Institute) for assistance in carrying out anodic treatment.

The study was carried out with the partial financial support of RFBR (grant 13-02-00381).

### REFERENCES

- [1] Properties of porous silicon, Ed. by L. Canham, Malvern, DERA, 1997.
- [2] A. Cojocaru, M. Leisner, J. Carstensen, H. Föll, Comparison of currentline pore growth in *n*-type InP and in *n*-type Si, *Phys. Stat. Sol. (c)*. 8 (6) (2011) 1779–1782.
- [3] I.M. Tiginyanu, E. Monaico, V.V. Ursaki, et al., Fabrication and photoluminescence properties of porous CdSe, *Appl. Phys. Lett.* 86 (6) (2005) 063115.
- [4] S.P. Zimin, E.A. Bogoyavlenskaya, E.Yu. Buchin, et al., Formation of porous nanostructured lead telluride films by anodic electrochemical etching method, *Semicond. Sci. Technol.* 24 (10) (2009) 105008(1)–105008(6).
- [5] S.P. Zimin, V.M. Vasin, E.S. Gorlachev, et al., Fabrication and study of porous PbTe layers on silicon substrates, *Phys. Stat. Sol. (c)*. 8 (6) (2011) 1801–1804.
- [6] S.P. Zimin, V.M. Vasin, E.S. Gorlachev, et al., Investigations of PbSe porous layers by scanning electron microscopy, *Phys. Stat. Sol. (c)*. 8 (6) (2011) 1918–1922.
- [7] S.P. Zimin, E.S. Gorlachev, F.O. Skok, V.V. Naumov, Investigations of the pore formation in the lead selenide films using glacial acetic acid- and nitric acid-based electrolyte, *Nanoscale Research Letters*. 7 (1) (2012) 338.
- [8] V.A. Bushuyev, A.P. Petrakov, Influence of laser annealing on the structure of the surface layers of ion-implanted silicon by X-ray diffractometry, *Physics of the Solid State*. 35 (2) (1993) 355–364.
- [9] A.A. Lomov, D.Yu. Prokhorov, R.M. Imamov, et al., Characterization of porous InP (001) layers by triple-crystal X-ray diffractometry, *Crystallography Reports*. 51 (5) (2006) 754–760.
- [10] H. Zogg, C. Maissen, S. Blunier, et al., Thermal-mismatch strain relaxation mechanisms in heteroepitaxial lead chalcogenide layers on Si substrates, *Semicond. Sci. and Technol.* 8(1S) (1993) S337–S341.
- [11] M.A. Krivoglaz, *Difraktsiya rentgenovskikh luchey i neytronov v neidealnykh kristallakh* [Diffraction of X-rays and neutrons in imperfect crystals], Kiev, Naukova Dumka, 1983.
- [12] A.P. Petrakov, *Issledovaniye pripoverkhnostnykh sloev veshchestv rentgenovskimi metodami difraktsii, reflektometrii i fazovogo kontrasta* [Studies of near-surface substance layers by X-ray diffraction, reflectometry and phase contrast techniques], Syktyvkar, Izd-vo Syktyvskarskogo un-ta, 2007.
- [13] A.P. Petrakov, D.V. Sadovnikov, *Rentgenovskaya reflektometriya poverkhnostey monokristallov, nanokompozitnykh i okisnykh plenok* [X-ray reflectometry of monocrystalline surfaces, nanocomposite and oxide films], *Vestnik Komi NTs UrO RAN.* (9) (2006) 7–9.
- [14] S.N. Yakunin, E.M. Pashaev, A.A. Zaytsev, et al., Si/Si<sub>1-x</sub>Ge<sub>x</sub> superlattice structure from X-ray-scattering data, *Russian Microelectronics*. 34 (4) (2005) 242–251.
- [15] M.A. Chuev, I.A. Subbotin, E.M. Pashaev, et al., Phase relations in analysis of glancing incidence X-ray rocking curves from superlattices, *JETP Letters*. 85 (1) (2007) 17–22.

Received 01.11.2017, accepted 21.11.2017.

### THE AUTHORS

MAMONTOV Alexander I.

Vyatka State Humanities University

26 Krasnoarmeyskaya St., Kirov, Kirov region, Volga Federal district, 610002, Russian Federation.  
snowchek@mail.ru

**PETRAKOV Anatoliy P.**

*Syktyvkar State University Named after Pitirim Sorokin*

55 Oktyabrskiy Ave., Syktyvkar, Republic of Komi, 167001, Russian Federation.

petrakov@syktsu.ru

**ZIMIN Sergey P.**

*P.G. Demidof Yaroslavl State University*

14 Sovetskaya St., Yaroslavl, 150000, Russian Federation.

zimin@uniyar.ac.ru



## MORPHOLOGY OF DRIED NANOGE FILMS OF BACTERIAL CELLULOSE IMPREGNATED WITH THE SILVER NITRATE SOLUTION

A.K. Khripunov<sup>1</sup>, T.P. Stepanova<sup>1</sup>, N.N. Saprykina<sup>1</sup>, E.P. Astapenko<sup>1</sup>,  
D.P. Romanov<sup>2</sup>, A.A. Tkachenko<sup>3</sup>, V.M. Kapralova<sup>4</sup>

<sup>1</sup> Institute of Macromolecular Compounds of Russian Academy of Sciences,  
St. Petersburg, Russian Federation;

<sup>2</sup>I.V. Grebenshchikov Institute of Silicate Chemistry of Russian Academy of Sciences,  
St. Petersburg, Russian Federation;

<sup>3</sup> St. Petersburg State University, St. Petersburg, Russian Federation;

<sup>4</sup> Peter the Great St. Petersburg Polytechnic University,  
St. Petersburg, Russian Federation

A comparative study of dried nanogel films of the *Gluconacetobacter xylinus* cellulose (GXC) in native and disintegrated forms treated with AgNO<sub>3</sub> solution has been carried out by means of SEM and XRD. The supermolecular structure of samples studied was shown to be 3D network of nanostrips formed with oriented macrofibrils in which amorphous and crystalline regions alternate. XRD patterns of the GXC dry films, pre-treated with AgNO<sub>3</sub> aqueous solution, demonstrate both residual AgNO<sub>3</sub> and reduced Ag<sup>0</sup>, the latter positioned in longwise direction of morphologic structure elements. The XRD and SEM studies of dried GXC films disintegrated in 1 % AgNO<sub>3</sub> aqueous solution showed the presence of reduced Ag<sup>0</sup> in the form of nanoparticles 10 – 50 nm in diameter located in the free volume of the GXC 3D network nearby structural elements.

**Keywords:** nanogel film; bacterial cellulose; SEM; XRD

**Citation:** A.K. Khripunov, T.P. Stepanova, N.N. Saprykina, E.P. Astapenko, D.P. Romanov, A.A. Tkachenko, V.M. Kapralova, Morphology of dried nanogel films of bacterial cellulose impregnated with the silver nitrate solution, St. Petersburg State Polytechnical University Journal. Physics and Mathematics. 11(1) (2018) 75 – 81. DOI: 10.18721/JPM.11111

### Introduction

The *Gluconacetobacter xylinus* cellulose (GXC) has been heavily studied in the past decade due to its numerous practical applications. Pure sugars and a variety of sugar-containing wastes can serve as potential carbon sources increasing the yield and reducing the costs of this product [1, 2]. However, few publications can be found on the morphology of GXC nanogel films (NGFs) [3] that show great promise, primarily, for their applications in medicine (for example, as wound dressings saturated with various medications), where it is important to gain an understanding of the interaction of silver-based antiseptic with the elements of the supermolecular structure of GXC films [4, 5].

The goal of this work was a comparative study of the morphology of native GXC and its disintegrated form, pretreated with a silver nitrate solution.

### Experimental procedure

**Sample preparation.** Biosynthesis of GXC NGF was described previously in [1, 4]. After cells were removed by the conventional method of boiling in a 1 % sodium hydroxide solution and thorough washing with distilled water, the obtained GXC NGF was stored after sterilization in hermetically sealed containers at a constant temperature of +5 °C until use.

To determine the molecular weight by viscometry, a dry GXC film was dissolved in cadoxen (a cadmium oxide complex in an aqueous solution of ethylenediamine) to obtain molecularly dispersed solutions [6]. The molecular weight of GXC was found to be 3.89·10<sup>5</sup> Da.

The *Gluconacetobacter xylinus* cellulose film obtained by biosynthesis was dehydrated with a press, removing up to 95% of water. The film was then placed in a 1 % AgNO<sub>3</sub> solution for

about 12 h. The film saturated with this solution was secured in toroidal clamps and dried at room temperature.

The initial native GXC film was disintegrated by adding some distilled water and 100 ml of a 1 % aqueous solution of  $\text{AgNO}_3$  (the total volume of the solution was 310 ml). The reaction vessel was a 2-liter blender (JTC, Omniblend 1, model TM-767) with a blade rotation rate of 15,000 rpm. Disintegration was carried out in three stages, each lasting 5 min, with 30-minute breaks to cool the colloidal suspension to room temperature. The gel film of disintegrated GXC was dried in the same clamps as the native one. The resulting dry samples were then studied SEM and X-ray diffraction.

**X-ray diffraction.** A DRON-3M X-ray diffractometer was used to study the dried initial and disintegrated films.  $\text{Cu}_{K\alpha}$ -radiation was used.

**Scanning electron microscopy (SEM).** The GXC films were examined with a scanning

electron microscope (Supra 55VP, Zeiss, Germany). A 15–20 nm-thick platinum layer was deposited on the samples to maintain the electrically conductive properties of the samples, to eliminate interference caused by accumulation of the surface charge during scanning and to increase contrast. This layer was deposited by cathode sputtering with a turbo-pumped sputter coater (Quorum-150, UK). The samples were then glued to the microscope stage with a double-sided electrically conductive tape. Surface morphology was studied using the secondary electron (SE2) mode.

**Energy dispersive X-ray microanalysis (EDXMA).** The elemental composition of the samples and the composition of the individual phases were determined using an INCA Energy microanalysis system with an X-Max-80 detector (Oxford Instruments, UK), completed with a Supra 55VP microscope. To identify the phases in the sample, spectra were recorded both from the sample's entire surface and from its individual points.

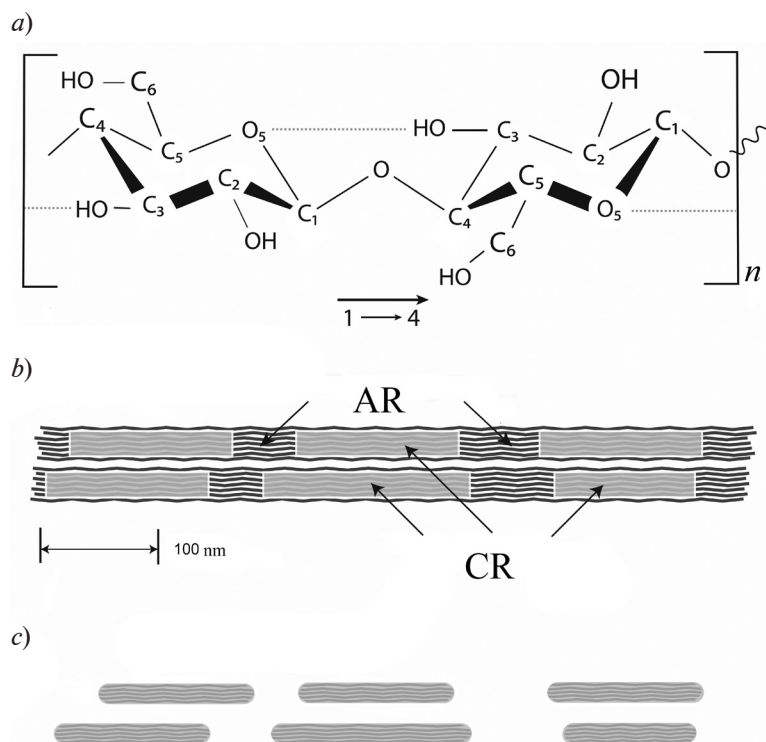


Fig. 1. Schematics of the structure of a monocellulose macromolecule (a), fragment of a macrofibril strip in one of the hypothetical configurations of crystalline (CR) and amorphous (AR) regions (b) and single GXC nanocrystals after dissolution of disordered regions by acid hydrolysis (c).

The arrow indicates the direction of the  $\text{C}_1 - \text{C}_4$  bond (a)

### Experimental results and discussion

Cellulose macromolecules whose monomer unit is cellobiose tend to be mutually ordered due to intra- and intermolecular hydrogen bonds [7 – 11]. The data obtained by XRD analysis, SEM and TEM indicate that the formation of the spatial morphological structure of GXC NGF involves the formation of microfibrils (consisting of about seven orientationally ordered cellulose macromolecules); these microfibrils then become ordered into macrofibrils; the

latter form ordered strips with nanochannels between them.

Due to conformational disorder in the attachment of cellobiose units during biosynthesis, microfibrils consist of alternating crystallites and amorphous regions that microfibril packaging requires to ensure flexibility in the spatial morphological structure of cellulose. Fig. 1 shows the known [8] scheme of the structure of a monomeric unit of a cellulose macromolecule, a strip and single GXC crystallites.

Fig. 2. shows XRD patterns of native and

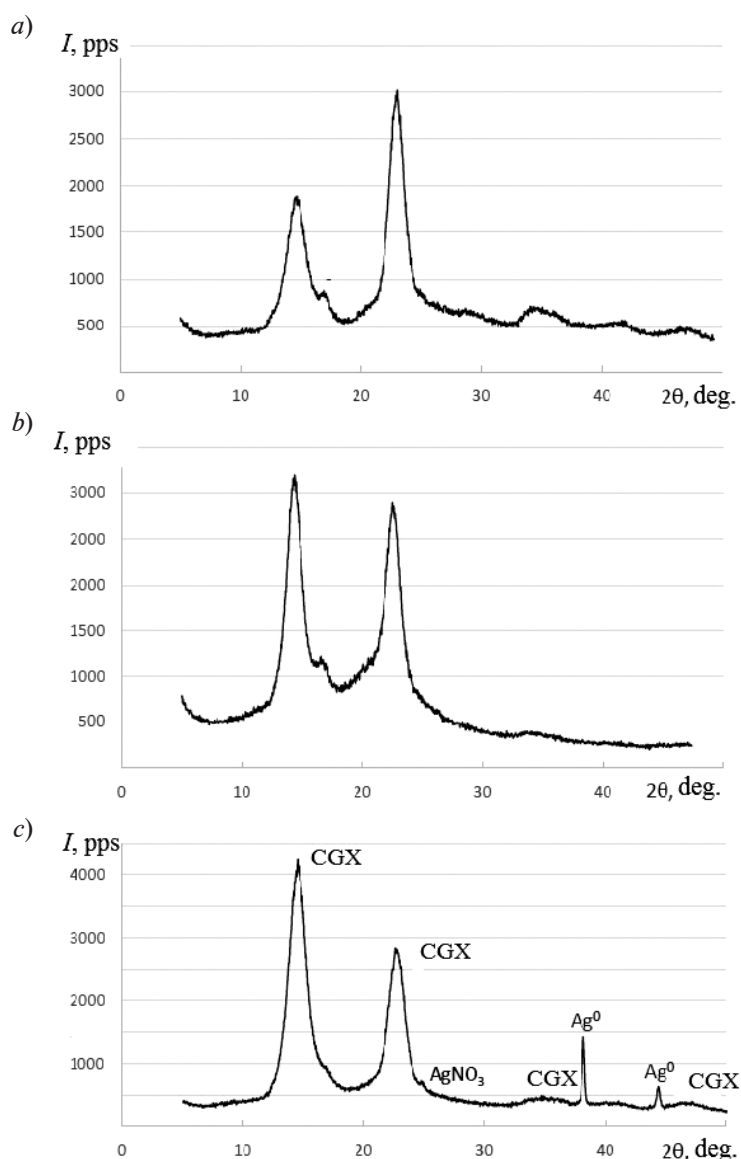


Fig. 2. XRD patterns of GXC films:  
initial native (a), more morphologically ordered disintegrated (b),  
treated with an  $\text{AgNO}_3$  solution during disintegration (c)

Table 1

Results of energy-dispersive analysis of GXC samples treated with a 1%  $\text{AgNO}_3$  solution

GXC film	Chemical composition, at%				Ag/N
	C	N	O	Ag	
Native	72.0	0.3	26.0	1.7	5.7
Disintegrated	54.5	5.5	30.0	10.0	1.8

disintegrated GXC films. Three main X-ray scattering peaks can be observed in both cases, localized at  $2\theta$  values equal to  $15.0^\circ$ ,  $16.6^\circ$  and  $22.4^\circ$ , which indicates that the morphological structure of cellulose is preserved after the disintegration of the GXC film. The width of the peaks confirms that GXC is partially crystalline. The first intensity peak is narrower and higher (Fig. 2, *b*), which indicates an increased degree of orientational order in the crystalline objects after the disintegration

of the GXC film and proves (as discussed in [7]) that constant stoichiometry is preserved in colloids in aqueous suspensions. The XRD pattern in Fig. 2, *c* shows the regions indicating the presence of silver ( $\text{Ag}^0$ ) and silver nitrate ( $\text{AgNO}_3$ ) nanoparticles in the native and disintegrated GXC films (disintegration was carried out in the presence of a silver solution). This composition is confirmed by the data of elemental microanalysis (see Table 1) used to obtain averaged comparative results of the

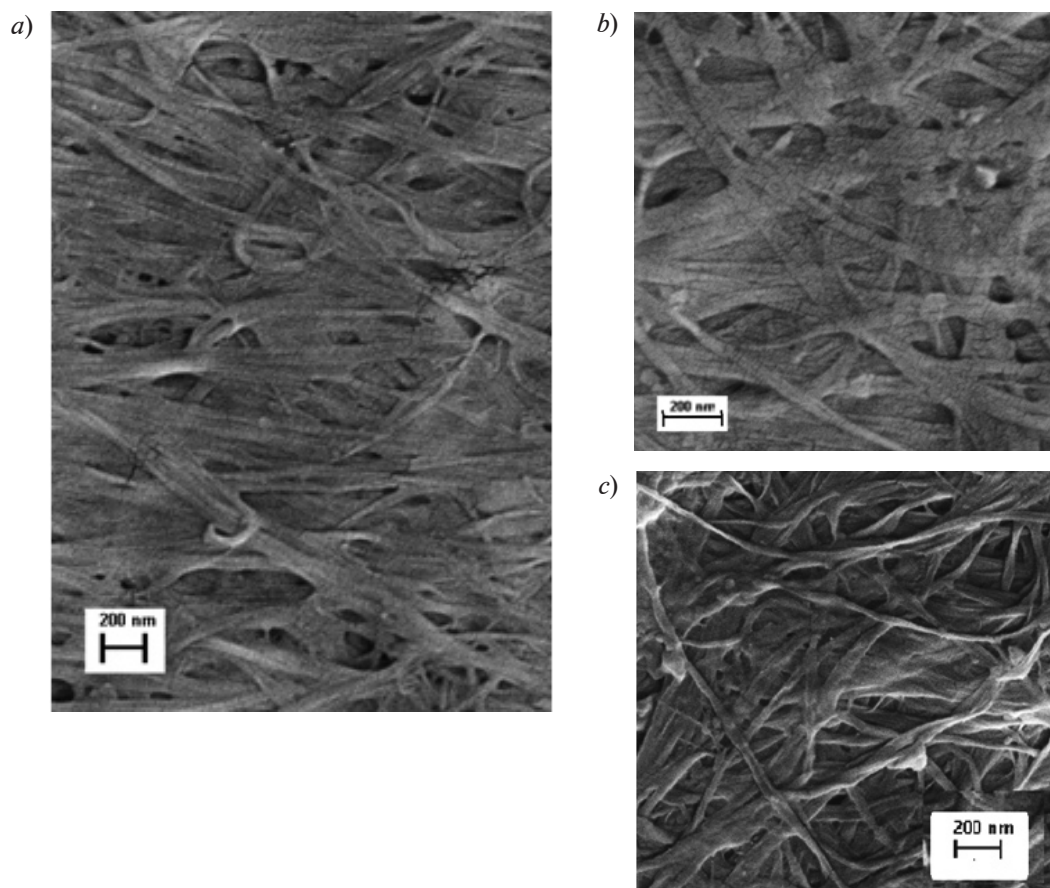


Fig. 3. Micrographs of dried films of native (*a*, *b*) and disintegrated (*c*) GXC obtained by SEM magnified 50,000 (*a*, *c*) and 130,000 (*b*) times



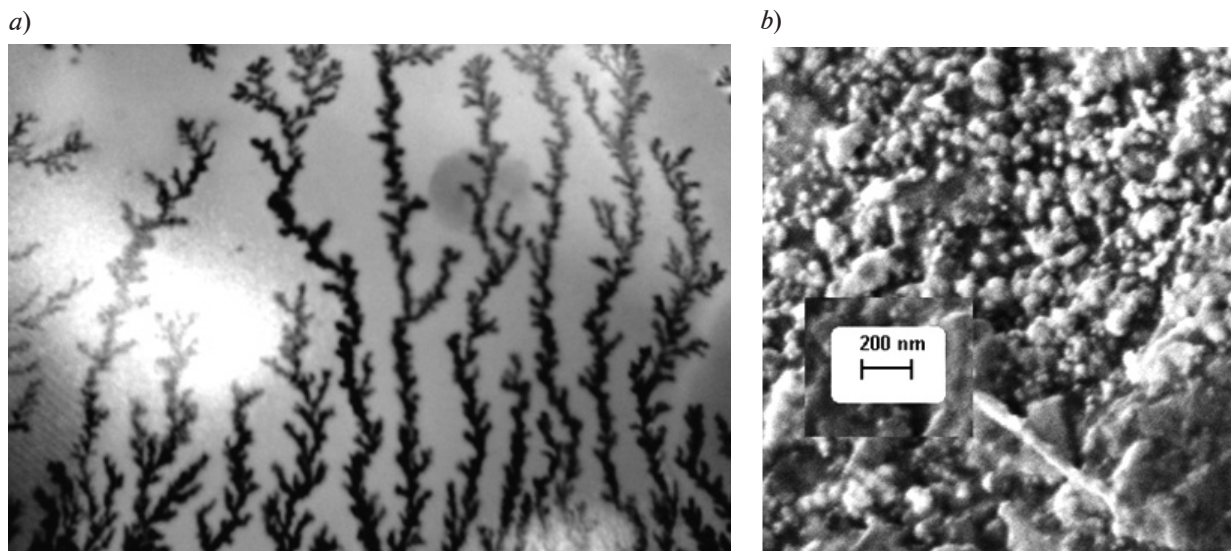


Fig. 4. A photograph (a) and a micrograph obtained by SEM (b) of a dried native GXC film pretreated with a 1 %  $\text{AgNO}_3$  solution. Magnification by 1.5 (a) and 50,000 (b) times. Dendrites of reduced silver in the photograph visualize the elements of the supermolecular structure of the sample

content of chemical elements in native and disintegrated GXC films treated with a 1%  $\text{AgNO}_3$  solution.

Fig. 3 shows micrographs of native and disintegrated GXC films obtained by SEM at different magnifications. Characteristic fibril strip structures are visible in Fig. 3, a; alternating crystallite (with the size of about 10 nm) and amorphous regions can be observed in microfibrils at a higher magnification (Fig. 3, b). Such objects of disintegration of GXC films as individual broken strips and chaotically located single macrofibrils are clearly visible in micrographs in Fig. 3, c.

Fig. 4 shows a photograph and a micrograph of a dried native GXC film pretreated with a 1 %  $\text{AgNO}_3$  solution. Dendrites of reduced silver visualizing the elements of the morphological nanostrip structure of GXC can be observed on the surface of the film (Fig. 4, a). Both dendrites and silver nanoparticles (30 – 80 nm) filling the space between the strips are visible on the micrograph (Fig. 4, b).

The situation is different for dried films of aqueous suspensions of disintegrated GXC obtained by introducing a 1%  $\text{AgNO}_3$  solution into the blender during disintegration of GXC. Fig. 5 shows a micrograph of such films, where  $\text{Ag}^0$  nanoparticles 10 – 50 nm in size, located

in the cavities of the network formed by fragments of disintegrated GXC strips, can be observed to develop. It should be noted that silver nanoparticles form near the elements of the morphological structure of GXC.

The obtained results indicate that both  $\text{Ag}^0$  nanoparticles and  $\text{AgNO}_3$  salt are contained in

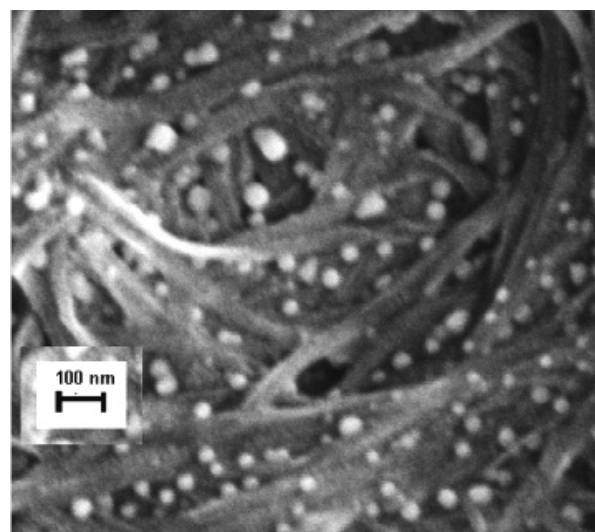


Fig. 5. A micrograph of a GXC film of treated with a 1 %  $\text{AgNO}_3$  solution in the process of disintegration. The micrograph was obtained by SEM with a magnification by 100,000 times

samples of dried GXC films treated with a 1 %  $\text{AgNO}_3$  solution. The films samples have varying nanoparticle contents. However, it is obvious that the supermolecular structure of GXC is capable of reducing silver atoms from its salt and lead to the appearance of either dendrites from silver atoms in the native GXC or to the formation of isolated silver nanoparticles during the disintegration of GXC in the presence of  $\text{AgNO}_3$  solution.

This indicates that chemisorption interactions exist in the cellulose, making it capable of reducing silver atoms near the elements of the morphological structure. Such a result gives further insight into the properties of GXC, for which previously only molecular interactions were known, namely, intra- and intermolecular hydrogen bonds, as well as van der Waals bonds.

### Conclusions

We have used scanning electron microscopy and X-ray diffraction analysis to study the effect of mechanical disintegration on the morphology of a native film of *Gluconacetobacter xylinus*

cellulose (GXC) and found that

the morphological structure characteristic for GXC is preserved in the disintegrated films; however, there is a certain change in the orientational order, and a background amorphous phase forms from the disintegrated elements;

silver ( $\text{Ag}^0$ ) nanoparticles and residual silver nitrate are present in the films of native and disintegrated GXC treated with a solution of silver nitrate;

dendrites are formed from reduced silver in dried and solution-treated films of the initial native GXC, which are visible to the naked eye and visualize the morphological structure of GXC;

silver nanoparticles with a predominant size of 10–50 nm, located in the cavities of the GXC network near the structural elements were found in dried GXC films disintegrated in the presence of a 1 % silver nitrate solution.

The chemisorption interactions capable of reducing atomic silver from its salt were discovered in the supramolecular structure of GXC.

### REFERENCES

- [1] Yu.G. Baklagina, A.K. Khripunov, A.A. Tkachenko, et al., Sorption properties of gel films of bacterial cellulose, Russian Journal of Applied Chemistry. 78 (7) (2005) 1176–1181.
- [2] A.A. Jozala, L.C. de Lancastre-Novaes, A.M. Lopes, et al., Bacterial nanocellulose production and application: a 10-year overview, Appl. Microbiol. Biotechnol. 100 (5) (2016) 2063–2072.
- [3] N.S. Thompson, J.A. Carlson, H.M. Kaustinen, K.I. Uhlin, Tunnel structures in *Acetobacter xylinum*, Int. J. Biol. Macromol. 10 (2) (1988) 126–127.
- [4] V.A. Popov, Ranevyy protsess: nanobiotehnologii optimizatsii [Wound process: optimization nanobiotechnologies], St. Petersburg, SpetsLit, 2013.
- [5] A.K. Khripunov, T.P. Stepanova, E.V. Antonenkova, et al., O nekotorykh svoystvakh vody v nano-gel-plenkakh tsellyulozy *Gluconacetobacter xylinus* [On some properties of water in the nanogel films of *Gluconacetobacter xylinus* cellulose], High Technologies, Economics, Industry, Collection of Sci. Articles, Ed. A.P. Kudinov, St. Petersburg, Polytechn. Univ. Publ. House, 2-1 (2013) 261–262.
- [6] L.S. Bolotnikova, T.I. Samsonova, Zavisimost mezhdu molekulyarnym vesom i kharakteristicheskoy vyazkostyu tsellyulozy v rastvorakh kadmiiy etilen diaminovogo kompleksa. [A correlation between a molecular weight and the viscosity of cellulose in the solutions of cadmium ethylene diamine complex], Polymer Sci. 6 (3) (1964) 533–537.
- [7] A.K. Khripunov, T.P. Stepanova, A.A. Tkachenko, et al., Dielectric properties and microstructure of the disintegrated nanogel films of bacterial cellulose, St. Petersburg Polytechnical University Journal: Physics and Mathematics. 10 (2) (2017) 45–57.
- [8] R.J. Moon, A. Martini, J. Nairn, et al., Cellulose nanomaterials review: structure, properties and nanocomposites, Chem. Soc. Rev. 40 (7) (2011) 3941–3944.
- [9] R.M. Brown, Jr. The biosynthesis of cellulose, Journ. Mol. Sci., A. Pure Appl. Chem. 1996. A 33 (10) (1996) 1345–1373.
- [10] T. Kondo, M. Nojiri, Yu. Hishikawa, et al., Biodirected epitaxial nanodeposition of polymers on oriented macromolecular templates, Proc. of Nat. Acad. Sci. (PNAS). 99 (22) (2002) 14008–14013.
- [11] T.A. Babushkina, T.P. Klimova, E.V. Shtykova, et al., Study of gel films of *Acetobacter*



xylinum cellulose and its modified samples by  $^1\text{H}$  NMR, crioporometry and small-angle X-ray scattering, Crystallograpy Reports. 55 (2) (2010) 344–349.

*Received 12.12.2017, accepted 14.12.2017.*

#### THE AUTHORS

**KHRIPUNOV Albert K.**

*Institute of Macromolecular Compounds RAS*

31 Bolshoy Ave. V.O., St. Petersburg, 199004, Russian Federation  
xelmie@mail.macro.ru

**STEPANOVA Tamara P.**

*Institute of Macromolecular Compounds RAS*

31 Bolshoy Ave. V.O., St. Petersburg, 199004, Russian Federation  
t\_stepanova2005@mail.ru

**SAPRYKINA Nataliya N.**

*Institute of Macromolecular Compounds RAS*

31 Bolshoy Ave. V.O., St. Petersburg, 199004, Russian Federation  
saprykina@hq.macro.ru

**ASTAPENKO Ella P.**

*Institute of Macromolecular Compounds RAS*

31 Bolshoy Ave. V.O., St. Petersburg, 199004, Russian Federation  
imc@hq.macro.ru

**ROMANOV Dmitriy P.**

*I.V. Grebenshchikov Institute of Silicate Chemistry*

2 Makarova Emb., St. Petersburg, 199034, Russian Federation  
ichsran@isc.nw.ru

**TKACHENKO Albina A.**

*St. Petersburg State University*

7-9 Universitetskaya Emb., St. Petersburg, 199034, Russian Federation  
albina.tkachenko@mail.ru

**KAPRALOVA Victoria M.**

*Peter the Great St. Petersburg Polytechnic University*

29 Politechnicheskaya St., St. Petersburg, 195251, Russian Federation  
kapralova2006@yandex.ru

## DARK MATTER SEARCHES AT THE LARGE HADRON COLLIDER

**A.E. Basalaev, Yu.G. Naryshkin**

Petersburg Nuclear Physics Institute of National Research Center “Kurchatov Institute”,  
Gatchina, Russian Federation

One of the promising lines of investigation at the Large Hadron Collider (LHC) is a search for dark matter particles. Despite a large body of evidence for dark matter existence, its nature remains unknown. The leading hypothesis is that dark matter consists of weakly interacting massive particles. Collider searches for such particles are most sensitive in the case of spin-dependent interactions, and for the low masses of dark matter particles in the case of spin-independent interactions. The strategies of dark matter searches at the LHC are described, and upper limits on dark matter-nucleon cross-sections based on the experimental data collected in 2015 and 2016 by the ATLAS and CMS collaborations are presented in comparison with the results of other experiments. In conclusion, the perspectives of further searches of dark matter at the LHC are discussed.

**Key words:** dark matter; LHC; ATLAS; CMS; WIMP; dark matter associative production; mono- $X$

**Citation:** A.E. Basalaev, Yu.G. Naryshkin, Dark matter searches at the Large Hadron Collider, St. Petersburg Polytechnical State University Journal. Physics and Mathematics. 11 (1) (2018) 82 – 93. DOI: 10.18721/JPM.11112

### Introduction

One of the major challenges for the experiments at the Large Hadron Collider located at the European Center for Nuclear Research (CERN, Switzerland) is the search for dark matter particles. Dutch astronomer Jacobus Kapteyn was the first to hypothesize in 1922 that such a substance exists, based on the results of studying rotational velocities of galaxies [1]. The term “dark matter” gained wide circulation after the publication of Fritz Zwicky’s works [2].

Some of the current astrophysical observations indicate the existence of dark matter. These include the study of the rotational velocities of galaxies [3], gravitational lensing [4], the structure of the Bullet cluster [5], etc. The theory of primary nucleosynthesis predicts that the distribution of chemical elements in the universe is in good agreement with the observed baryon matter [6]; this implies that the nature of dark matter is non-baryonic. Analysis of the distribution of irregularities in the cos-

mic microwave background also points to the presence of non-baryonic dark matter [7].

Massive astrophysical compact halo objects (MACHOs) are regarded as potential dark matter formations. Studies of gravitational microlensing [8, 9] exclude the contribution from these objects with masses in the range from  $0.6 \cdot 10^{-7}$  to  $15 M_{\odot}$  ( $M_{\odot}$  is the mass of the Sun) as possible dark matter formations. According to recent estimates, dark matter comprises about 26.8 % of the total mass-energy of the Universe, while the fraction of baryonic matter does not exceed 5 % [10].

Even though a substantial amount of indirect evidence that dark matter exists has been accumulated, it has not yet proved possible to establish its nature. Attempts to construct modified gravity theories were made to explain this phenomenon but they all faced significant difficulties in interpreting all the available experimental data [11]. To date, the main hypothesis is that dark matter consists of weakly interacting massive particles (WIMPs) [12], which interact with matter only through gravity





and some kind of weak interaction.

Dark matter particles appear in some extensions of the Standard Model. For example, the neutralino (Lightest Supersymmetric Particle, LSP) is one of the possible dark matter particles in the minimal supersymmetric extension of the Standard Model [13]. Sterile neutrinos [14] and axions [15] are also considered as candidates for dark matter particles. A detailed review of the particles suitable for the role of dark matter objects can be found in [16].

At the present time, various experiments are under way to find dark matter particles. These are direct, indirect and collider experiments.

The effects of dark matter particles interacting with target nuclei are studied in experiments on direct search for dark matter particles [17 – 19]. A detailed review of direct experiments can be found in [20]. Typically, such studies are performed in laboratories located deep underground (to reduce background radiation), for example, at the Gran Sasso National Laboratory (Italy).

Indirect experiments on searching for dark matter particles study the effects associated with annihilation of dark matter particles and antiparticles, with a particle and an antiparticle of the Standard model (for example, electron-positron or proton-antiproton pairs) forming as a result [21, 22]. The ratio of the number of particles to the number of antiparticles is measured in these experiments as a function of energy. Comparing the measured spectra with the computation results obtained for radiation from known cosmic objects allows to draw conclusions about the existence of dark matter. Another branch of indirect experiments is measuring the gamma radiation flux; if the measured value exceeds the expected one, it indicates the annihilation of particles with antiparticles of dark matter [23].

The third type, collider experiments, are concerned with searching for dark matter particles produced as a result of annihilation of the quarks and antiquarks. The search for such particles is performed by detecting deviations of the experimental spectra from the predictions of the Standard Model.

To date, some studies have obtained confirmations that dark matter particles might exist. For example, the DAMA experiment [24]

studied the scattering of dark matter particles by target nuclei. For this purpose, the spectrum of recoil nuclei was measured for several years. It is assumed that our galaxy is in a cloud of dark matter. Since the Sun moves at a speed of 220 km/s relative to the center of the galaxy, and the Earth, revolving around the Sun at a speed of 30 km/s, moves at different speeds relative to the center of the galaxy in different time periods, the frequency of dark matter particle interactions with the target nuclei is different. As a result of the observations, annual modulations of the signal from scattering of particles by nuclei were found at a level of 9.3 standard deviations, which can be explained by the scattering of dark matter particles by the target nuclei.

Another experiment, AMS-02, involved measuring the energy spectra of cosmic positrons and antiprotons. The data of these measurements differ from the computational results describing the interaction of cosmic rays with the interstellar medium but are in good agreement with the models predicting the existence of dark matter particles with a mass of 1 TeV.

Nevertheless, in order to draw definitive conclusions about the existence of dark matter particles, it is necessary to exclude the contribution of radiation from additional sources such as pulsars. The energy spectrum of positrons in the high-energy region above 1 TeV should be studied for this purpose, which in turn requires more data expected to be obtained by 2025.

This paper presents a review of the studies on the search for dark matter particles (WIMPs) carried out by the ATLAS and CMS collaborations at the Large Hadron Collider in 2015–2016 with the energy of proton-proton interactions  $\sqrt{s} = 13$  TeV.

### Collider experiments

The first collider searches for dark matter particles were performed at the Tevatron accelerator of the Fermi Laboratory in proton-antiproton interactions in the CDF [25] and DØ [26] experiments with the energy  $\sqrt{s} = 1,96$  TeV.

The CDF experiment involved analysis of the data on associative production of dark matter particles and the  $t$ -quark. As a result, the upper limits established for the cross-section

for the production of dark matter particles were 0.5 pb (picobarn) for the masses of dark matter particles in the range of 0 – 150 GeV/c<sup>2</sup>.

In the DIII experiment, data were analyzed with the goal of finding a light gauge boson, the so-called ‘dark photon’  $\gamma_D$ , which is predicted by the minimal supersymmetric extension of the Standard Model (MSSM). Data analysis did not reveal the dark photon  $\gamma_D$  but helped establish the limits for its production cross-section.

Since the start of experiments at the Large Hadron Collider, the searches for dark matter particles of dark matter have been going in several directions. Collider experiments study the production of dark matter particles as a result of annihilation of quarks and antiquarks, but the dark matter particles themselves are not caught by the detector. In view of this, events producing these particles can only be detected for processes where additional particles are generated. For example, a force-carrying particle is formed in the so-called mono- $X$  channel during annihilation of a quark and an antiquark, which then breaks up into dark matter particles. Before the quark and the antiquark annihilate, one of them emits either a photon ( $\gamma$ ), a  $Z$  or  $W$  boson, or a gluon, which can be registered by the detector. The Feynman diagram for emission of a gluon in the initial state, followed by the formation of a jet, is shown in Fig. 1, *a*.

Associative production of dark matter particles (Fig. 1, *b*) is accompanied with the production of  $b\bar{b}$  или  $t\bar{t}$  pairs of quarks with subsequent formation of hadronic jets. A Higgs boson can form in the associative production of dark matter particles, instead of a pair of quarks.

Another option is directly searching for a force carrier mediating the interactions between the Standard Model and the dark matter particles, by recording its decay to particles of the Standard Model (Fig. 1, *c*).

So-called model-independent analysis using effective field theory [27] or simplified models [28] is used to interpret the experiments at the LHC. It is assumed that dark matter particles are Dirac fermions.

Effective field theory describes the point interaction of two particles (a quark and an an-

tiquark), with the subsequent production of a dark matter particle and an antiparticle. There are two parameters in this description of the field: the mass of the dark matter particle (antiparticle), and the parameter

$$\Lambda^2 = M^2 / (g_\chi \cdot g_q),$$

where  $M$  is the mass of the mediator (force carrier);  $g_\chi$  and  $g_q$  are the coupling constants between the mediator and the dark matter particles and quarks, respectively. This parameter characterizes the strength of the interaction between the Standard Model and the dark matter particles.

This approach is valid only if the mass of the mediator is greater than the momentum transferred, i.e.,  $M \gg Q$ . Since collision energy at the Large Hadron Collider has been increased to 13 TeV, this condition is often violated, and effective field theory has very limited applications at present; for this reason, simplified models in which this condition does not have to be fulfilled are used.

Simplified models consider a dark matter particle (and an antiparticle), as well as the mediator of the interactions between the Stan-

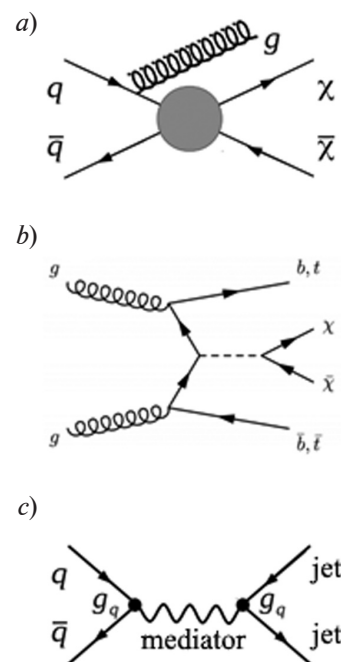


Fig. 1. Feynman diagrams for production of dark matter particles at the Large Hadron Collider: mono- $X$  channel *a*, associative birth *b*, search for a mediator+ particle *c*





Standard Model and the dark matter particles. The masses of the dark matter particles  $m_\chi$  and of the mediator  $m_\eta$  are given as parameters. The lifetime  $\Gamma$  (the decay width) of the mediator and its coupling constants with the Standard Model and dark matter particles ( $g_q$  and  $g_\chi$ ) are also used as parameters. Thus, the simplified model involves five parameters.

Data analysis is performed in the so-called signal region where the contribution of signal events is the greatest compared to the background. This region is selected based on the procedure for optimizing the selection of useful events. Both signal and background events obtained by the Monte Carlo simulations are used for optimization. The contribution of background processes, including the processes of the Standard Model, can be estimated by different methods based both on Monte Carlo simulations and on experimental data. Methods for estimating the background via the experimental data are used when Monte Carlo simulation cannot yield reliable estimates because the event generator is insufficiently accurate in describing the process and there are additional uncertainties related both to the description of the experimental setup and the response function of the detector. Such estimates typically have large systematic uncertainties. The MadGraph event generator is used to simulate the production of dark matter particles [29]. Different types of mediators are considered in simplified models: vector, axial-vector, scalar and pseudo+scalar, with different sets of coupling constants and in a wide range of particle masses [30]. Criteria of statistical significance are used for the final choice of the signal region, i.e., the one with the maximum contribution of signal events. The measured spectra are compared with the spectra of background processes in this region.

### Searches in the mono- $X$ channel

As stated above, an additional  $Z$  ( $W$ ) boson, a photon or a jet is detected in the mono- $X$  during the search for dark matter particles [31 – 33]. For example, a  $Z$  boson is produced in the mono- $Z$  process; it can be detected by its decay to an electron and a positron, a muon and an anti-muon, or a quark-antiquark pair with

the formation of two jets. The main background process in this case is the production of two  $Z$  bosons ( $ZZ$ ), one of them decaying to detectable particles (electrons, muons or hadrons), and the second into neutrinos. It is impossible to separate the signal and background processes of the production of a  $Z$  boson pair by means of kinematic variables. The contribution of this process in the signal region was estimated by Monte Carlo simulation. The contribution of the second largest process that is the simultaneous production of a  $W$  and a  $Z$  boson was estimated by a method based on using experimental data. The contribution from other background processes is much less than those mentioned above and was estimated using other methods based on experimental data.

Fig. 2, *a* shows the measured spectrum of the missing transverse energy  $E_T^{\text{miss}}$  for the mono- $Z$  process after the final selection of events in the signal region, obtained for the integral luminosity of  $36.1 \text{ (fb)}^{-1}$  in the ATLAS experiment. Events with  $E_T^{\text{miss}} > 90 \text{ GeV}$  were considered to reduce the background contribution from the production of  $Z$  bosons with jets. As can be seen from Fig. 2, the experimental spectra are in good agreement with the estimates of background events within statistical and systematic errors. The dashed line indicates the result of signal simulation for a dark matter particle with a mass  $m_\chi = 100 \text{ GeV}$  and a mediator with a mass  $m_{\text{med}} = 500 \text{ GeV}$ , scaled with a coefficient of 0.27. Fig. 2, *b* shows the restrictions on the mass of a dark matter particle as a function of the mediator mass during the decay of the  $Z$  boson to a pair of electrons or muons, obtained in the ATLAS experiment by analyzing the data for the axial-vector model of the mediator and the coupling constants equal to  $g_q = 2.5$  and  $g_\chi = 1.0$ . The range of particle masses falling inside the solid line was excluded [31]. Similar results were obtained in the CMS experiment [34]. The search for dark matter in mono- $X$  processes with the emission of  $W$  or  $Z$  bosons in the initial state with decay to hadrons is discussed in [35].

### Associative production of dark matter particles

Associative production means that one or two particles are additionally produced along with dark matter particles. For example, the

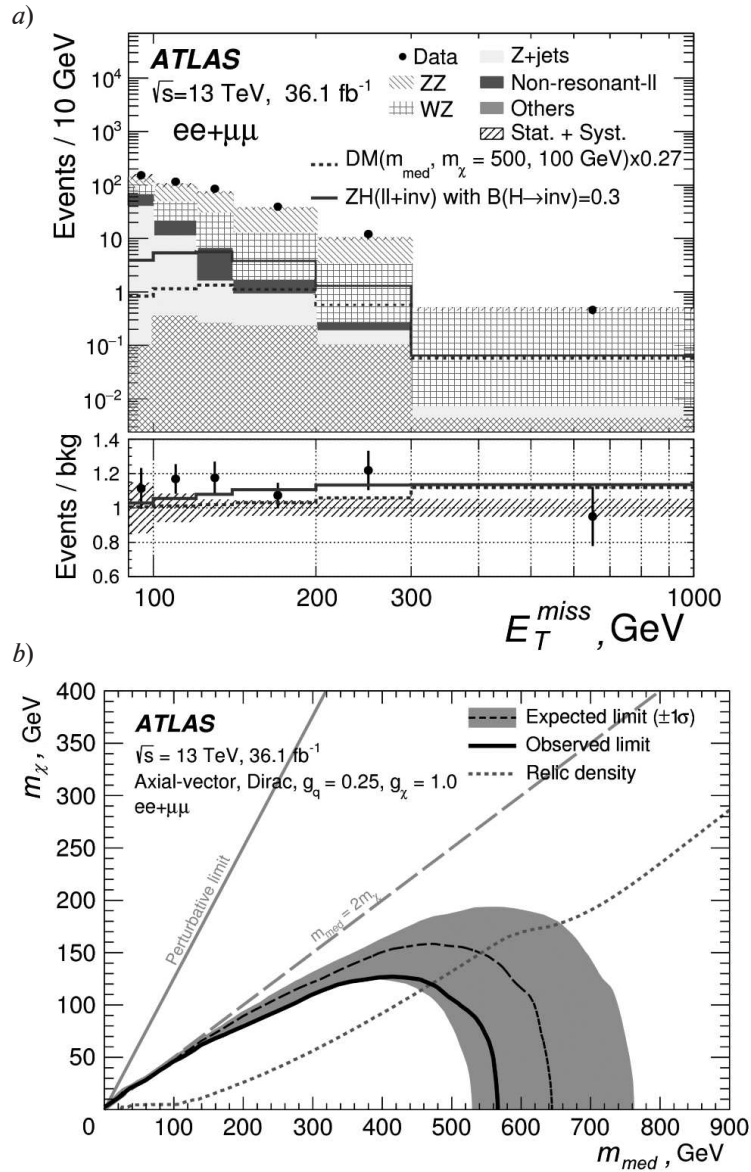


Fig. 2. Results of the search for dark matter particles of the mono- $Z$  process (the ATLAS experiment,  $\sqrt{s} = 13$  TeV):  $a$  are the distributions over the missing transverse energy  $E_T^{\text{miss}}$  for the combined  $ee$  and  $\mu\mu$  channels;  $b$  are the expected and observed limits for the masses of the mediator and the dark matter particle.

the black dots in (a) indicate the data, histograms show the results of the estimation of various background processes, diagonal hatching indicates the full systematic error, the dotted line indicates the simulation results of the signal events for  $m_\chi = 100$  GeV and  $m_{\text{med}} = 500$  GeV

production of a scalar or pseudo-scalar mediator that decays to dark matter particles is accompanied by the production of  $b\bar{b}$  or  $t\bar{t}$  quark pairs, with subsequent jet hadronization (see Fig. 1,  $b$ ). In this case, the presence of two  $b$  or  $t$  quark jets is a mandatory condition for selecting signal events. The main background

processes are the following:

the production of a  $Z$  boson and two jets, followed by the decay of the  $Z$  boson to two neutrinos;

processes with the production of  $b\bar{b}$  and  $t\bar{t}$  quark pairs.

Fig. 3 shows the upper limits for the cross-

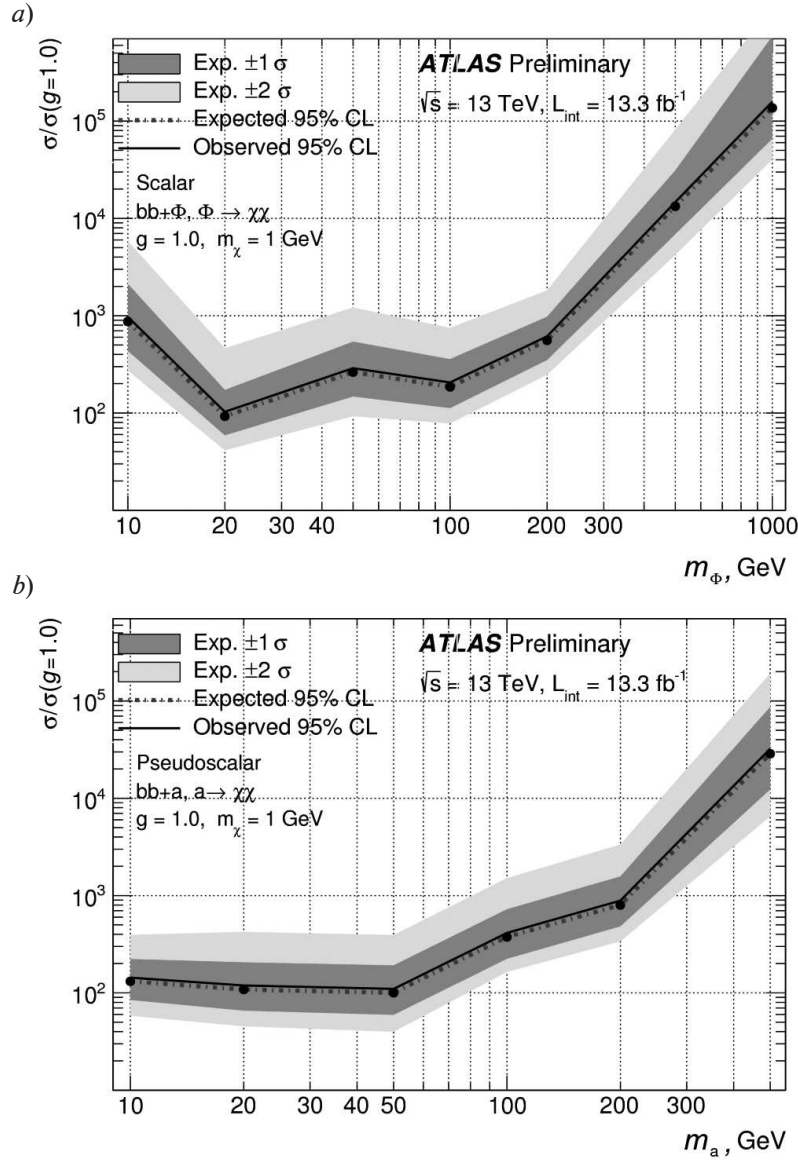


Fig. 3. The expected and observed limits (confidence interval 95 %) for the cross-sections of the production of dark matter particles, depending on the mediator mass, for the cases of scalar (a) and pseudoscalar (b) mediators.

The computations were performed for the mass of a dark matter particle equal to 1 GeV;  $g_q = g_\chi = 1.0$ . The data of 2015 – 2016 were analyzed; the integrated luminosity was  $13.3 \text{ (fb)}^{-1}$  for an energy in the center-of-mass system  $\sqrt{s} = 13 \text{ TeV}$  [36]

section of the production of dark matter particles in the mass range from 10 GeV to 1 TeV, obtained in the ATLAS experiment [36], for the case of a scalar mediator with masses in the range of 10 – 1000 GeV and for a pseudoscalar interaction carrier with masses in the range of 10 – 400 GeV, depending on the mass of the dark matter particle, with the coupling constant  $g_q = 1$ . The results were obtained by analysis of

the 2015 – 2016 data at an integrated luminosity of  $36.1 \text{ (fb)}^{-1}$ .

Other options of associative production of dark matter particles are also explored. For example, some extensions of the Standard Model predict the production of a heavy vector boson  $Z'$ , with subsequent decay to dark matter particles [37], or into two Higgs bosons: a light neutral  $h$  and a CP-odd pseudo-scalar neutral

$A^0$  followed by the decay of  $A^0$  to dark matter particles,  $A^0 \rightarrow \chi\chi$  [38]. Dark matter particles can also be produced in the decay of a heavy CP-even neutral Higgs boson  $H$  [38].

### Search for the mediator

The mediator of the interaction between the

Standard Model and the dark matter particles, for example, quarks with the formation of jets in the final state. Notably, direct searches for the mediator are possible only in collider experiments. There are different models for the interaction mediator, for example, a heavy

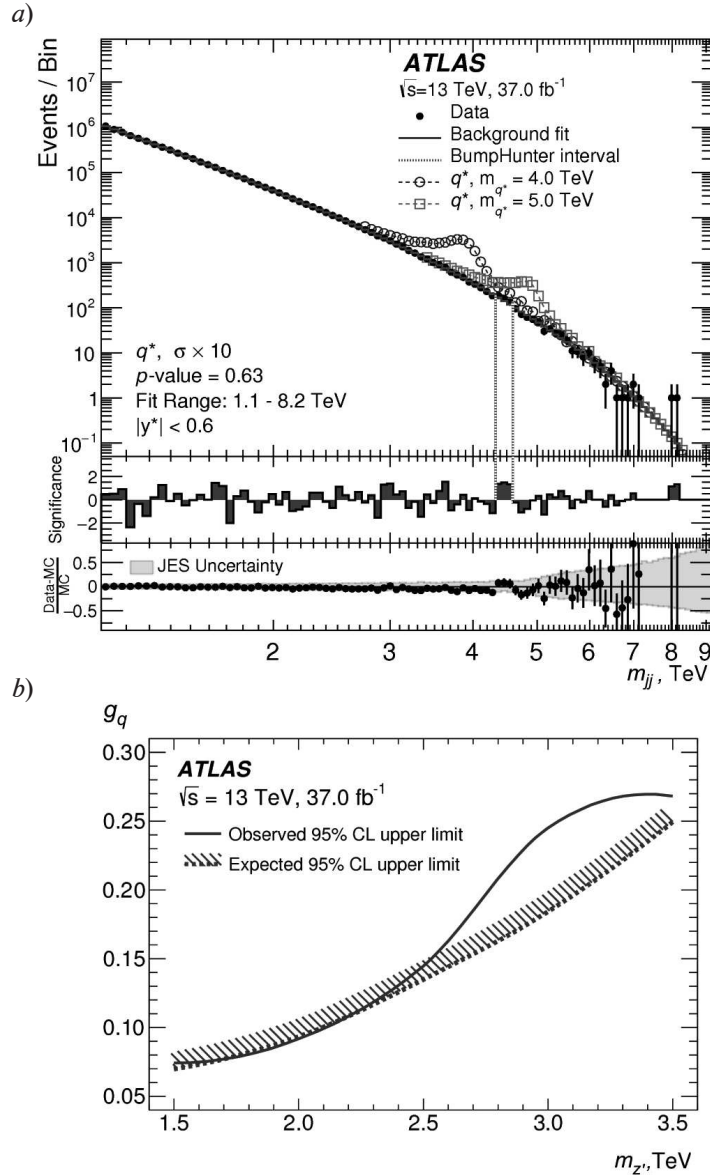


Fig. 4. Results of the studies on the direct search for a dark matter mediator (the ATLAS experiment for two-jet events): a are the spectra for invariant mass for the data, the background and the signal events; b are the obtained limits (confidence interval 95 %) for the constant  $g_q$  depending on the mass of the intermediate particle (the model of the  $Z'$  mediator is described in [41])

The bottom part of Fig. 4, a shows a comparison of the experiment with Monte Carlo simulation results; the solid bar is the systematic error





vector leptophobic boson  $Z'$ , which has either a small coupling constant with leptons [39], scalar or pseudo-scalar particles, or a colored scalar mediator [40]. Fig. 4, *a* shows the distribution over the invariant mass  $m_{jj}$  for two jets, obtained in the ATLAS experiment [41]. The circles in the figure indicate the results of simulation of signal events for mediators with masses of 4 and 5 GeV. The solid curve indicates the result of approximating the background distribution.

It can be seen from the figure that the data are in good agreement with the predictions of the Standard Model for the region considered.

The obtained limits for the value of the coupling constant between the mediator and the Standard model particles depending on the mediator mass  $m_{Z'}$  are shown in Fig. 4, *b*. The cross-section for a fixed mass increases with increasing  $g_q$ , and thus the range of values on the left and above the curve is excluded.

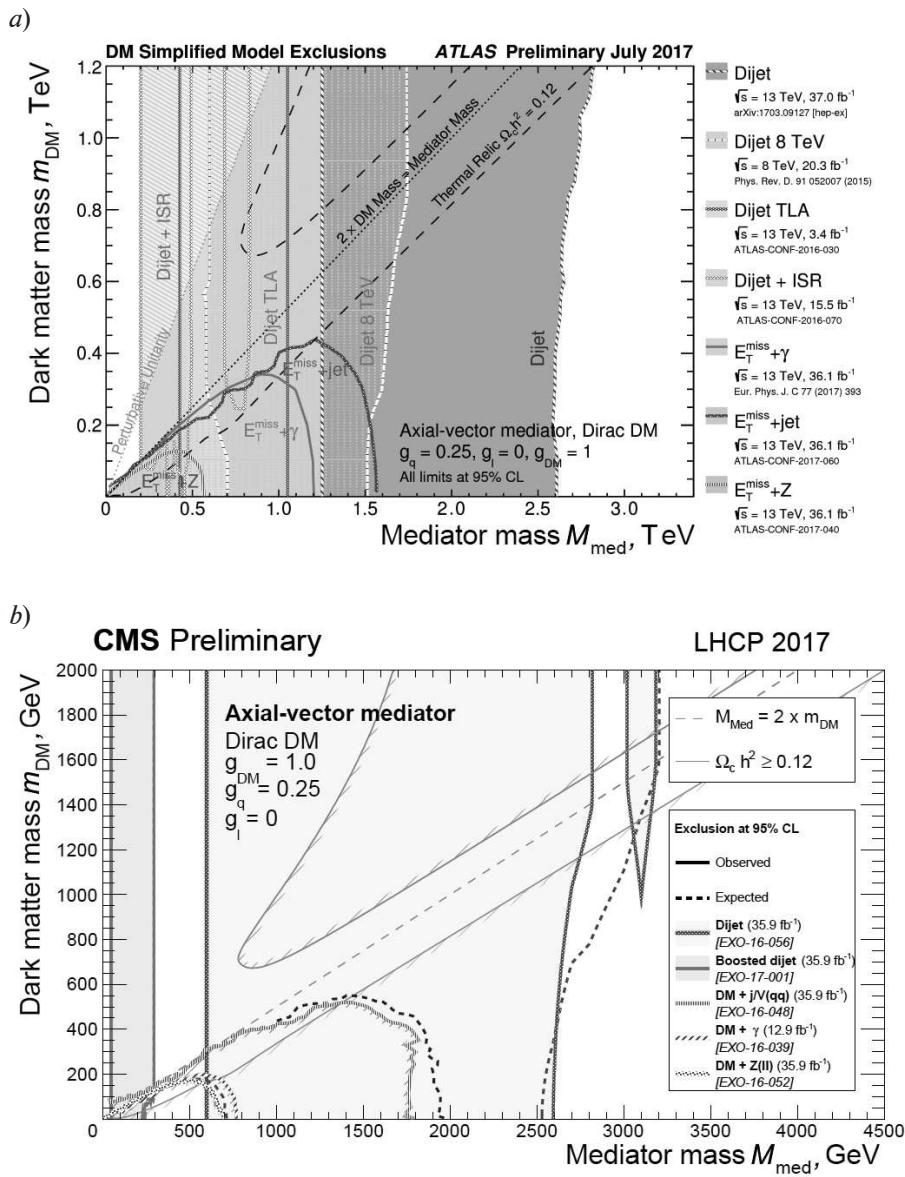


Fig. 5. Limits for dark matter particle masses depending on the mediator mass, obtained in the ATLAS (*a*) and CMS (*b*) experiments.

The coupling constants between the mediator and dark matter particles  $g_\chi = 1.00$  and between the mediator and quarks  $g_q = 0.25$  were used in the computations (the same for all types of quarks and for the axial-vector mediator)

### The results of collider experiments and discussion

The limits for the masses of dark matter particles and the axial-vector mediator obtained in the ATLAS and CMS experiments for the mono- $X$  processes, the associative production of dark matter particles and the

searches for the mediator particle are shown in Fig. 5 with the coupling constant between the mediator and the Standard model particles  $g_q = 0.25$  and between the mediator and the dark matter particles  $g_\chi = 1.00$ . It follows from the data given that the strongest restrictions on the mediator mass are obtained in analysis of

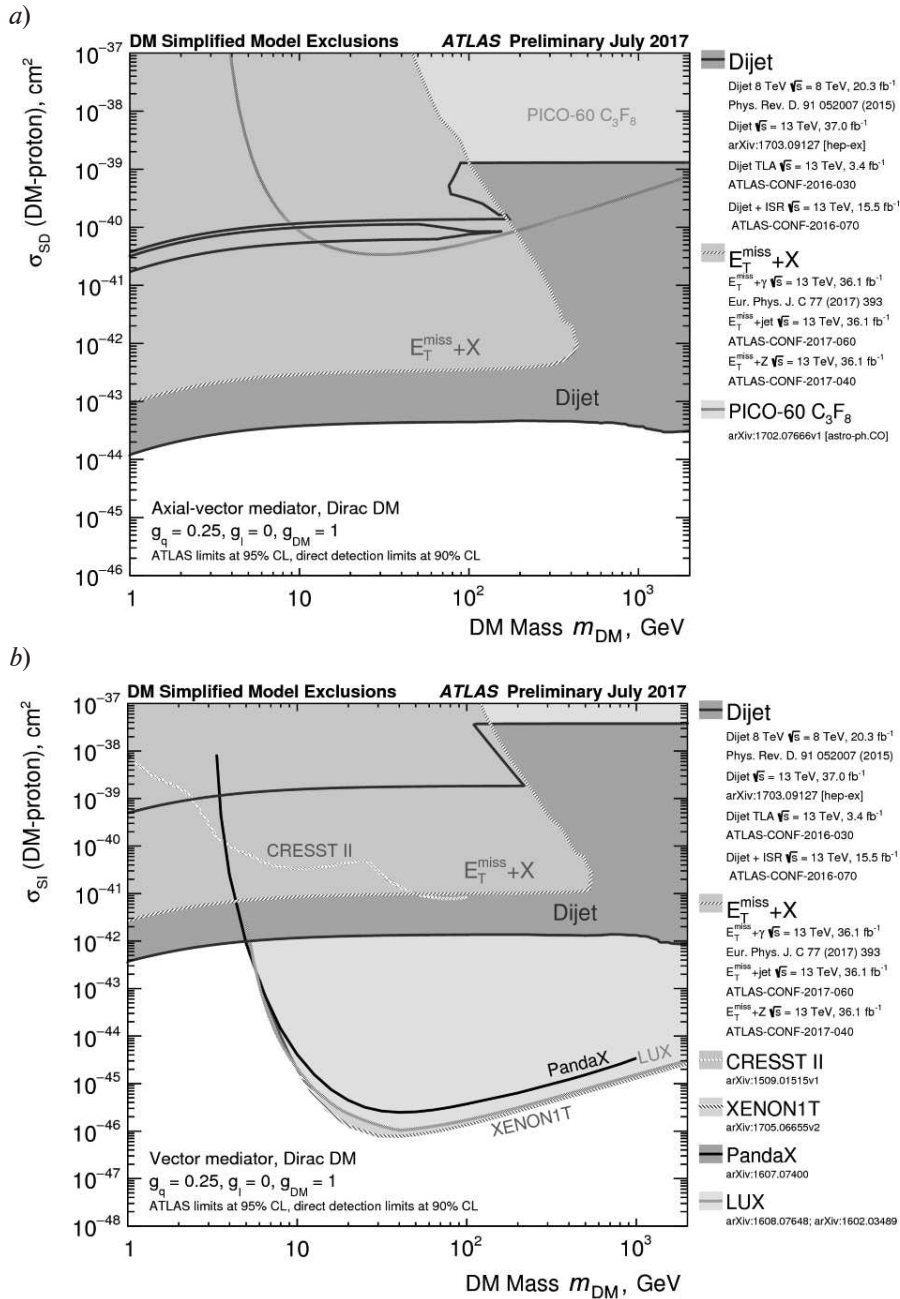


Fig. 6. Comparison of the results obtained in the ATLAS experiment with the results of direct measurements for spin-dependent (a) and spin-independent (b) cross-sections. Comparison with the experiments of the PICO (a) and CRESST, XENON1T, LUX and PandaX (b) experiments





two-jet events.

Fig. 6 shows the comparison of the results obtained at the LHC in the ATLAS experiment with the results of direct search experiments. Both spin-dependent and spin-independent interactions have been compared. The figure shows the upper limits for the cross-sections of the interaction of dark matter particles as a function of their mass, obtained in the ATLAS experiment by analysis of two-jet events: [41 – 44] and in the mono- $X$  channel [31 – 33], including a comparison with the results of direct search experiments: CRESST [45], XENON1T [46], PICO [47], LUX [48] and PandaX [49]. It follows from Fig. 6 that collider experiments are more sensitive than direct searches for dark matter particles (PICO, LUX) in case of spin-dependent interactions. The results of direct search experiments with spin-dependent interactions (PandaX) are more sensitive for dark matter particle masses above 6 GeV.

### Conclusion

To date, numerous studies have been conducted to search for dark matter particles in different channels in the ATLAS and CMS experiments at the Large Hadron Collider. Model-independent analysis was used to interpret the results, with different hypotheses for the mediator (vector, axial-vector, scalar and pseudoscalar). A wide range of possible masses from 10 GeV to 1 TeV was analyzed for both dark matter particles and the mediator. No deviations from the predictions of the Standard Model were discovered, with upper limits found for the cross-sections for the production of dark matter particles and for the masses of

dark matter particles, depending on the force carrier mass. The obtained limits for the cross-sections were compared with the results of direct search experiments for spin-dependent and spin-independent interactions: CRESST, XENON1T, PICO, LUX, and PandaX. The upper limits established for the cross-sections of the production of dark matter particles in experiments at the Large Hadron Collider for the case of spin-dependent interaction turned out to be lower than for direct measurement experiments; in other words, the experiments at the collider were more sensitive. At the same time, the experiments conducted at the Large Hadron Collider for spin-independent cross sections make it possible to analyze the range of masses of dark matter particles less than 6 GeV, and this option is not available in direct measurements.

It is expected that a data corresponding to an integrated luminosity of about  $120 \text{ (fb)}^{-1}$  will be accumulated during the second period of data collection at the Large Hadron Collider. That is 4 times higher than the current integral luminosity used for the results presented. It is proposed to use, among other models, an extension of the Standard Model including an additional doublet of the Higgs bosons, the 2HDM model, to interpret the data [50]. In addition to the limits for the cross-sections depending on the mass of dark matter particles and the mediator, it is proposed to establish limits for the model parameters, for example, the ratio of the vacuum means of two Higgs fields  $\tan\beta$  and the mixing angle  $\alpha$ .

This study was supported by a Russian Foundation for Basic Research grant no. 16-02-00015.

### REFERENCES

- [1] J.C. Kapteyn, First attempt at a theory of the arrangement and motion of the sidereal system, *Astrophysical Journal*. 55 (1922) 302–327.
- [2] F. Zwicky, Die Rotverschiebung von extragalaktischen Nebeln, *Helvetica Physica Acta*. 6 (1933) 110–127.
- [3] V.C. Rubin, N. Thonnard, W.K.Jr. Ford, Extended rotation curves of high-luminosity spiral galaxies. IV – Systematic dynamical properties, SA through SC, *The Astrophysical Journal Letters*. 225 (1978) L107–L111.
- [4] A.N. Taylor, S. Dye1, T.J. Broadhurst, N. Benitez, E. van Kampen, Gravitational lens magnification and the mass of Abell 1689, *The Astrophysical Journal*. 501 (2) (1998) 539–553.
- [5] M. Markevitch, A.H. Gonzalez, D. Clowe, et al., Direct constraints on the dark matter self-interaction cross-section from the merging galaxy cluster 1E0657-56, *The Astrophysical Journal*. 606 (2) (2003) 819–824.
- [6] C. Patrignani, K. Agashe, G. Aielli, et al. (Particle Data Group), Big-Bang nucleosynthesis, *Chinese Physics C*. 40 (10) (2016) 380.
- [7] L. Canetti, M. Drewes, M. Shaposhnikov, Matter and antimatter in the universe, *New Journal*

of Physics. 14 (9) (2012) 095012.

[8] **P. Tisserand, L. Le Guillou, C. Afonso, et al.**, Limits on the Macho content of the Galactic Halo from the EROS-2 survey of the Magellanic Clouds, *Astronomy and Astrophysics*. 469 (2) (2007) 387–404.

[9] **D.S. Graff, K. Freese**, Analysis of a Hubble Space telescope search for Red Dwarfs: Limits on baryonic matter in the galactic halo, *The Astrophysical Journal*. 456 (1) (1996) L49.

[10] **P.A.R. Ade, N. Aghanim, M.I.R. Alves, et al.** (Planck Collaboration), Planck 2013 results. I. Overview of products and scientific results, *Astronomy and Astrophysics*. 571 (2014) A1.

[11] **M. Milgrom**, A modification of the Newtonian dynamics as a possible alternative to the hidden mass hypothesis, *The Astrophysical Journal* 270 (1983) 365–370.

[12] **M. Kamionkowski**, WIMP and Axion dark matter. Rezhim dostupa: <https://arxiv.org/pdf/hep-ph/9710467>.

[13] **H. Baer, X. Tata**, Weak scale supersymmetry: from superfields to scattering events, Cambridge University Press, Cambridge, 2006.

[14] **S. Dodelson, L.M. Widrow**, Sterile-neutrinos as dark matter, *Physical Review Letters*. 72 (1) (1994) 17–20.

[15] **R. Holman, G. Lazarides, Q. Shafi**, Axions and the dark matter of the universe. *Physical Review D*. 27 (4) (1983) 995.

[16] **J.L. Feng**, Dark matter candidates from particle physics and methods of detection, *Annual Review of Astronomy and Astrophysics*. 48 (1) (2010) 495–545.

[17] **R. Bernabei, P. Belli, A. Bussolotti, et al.**, The DAMA/LIBRA apparatus, 17, *Nuclear Instruments and Methods in Physics Research A*. 592 (3) (2008) 297–315.

[18] **E. Aprile, J. Aalbers, F. Agostini et al.**, First dark matter search results from the XENON1T experiment. Rezhim dostupa: <https://arxiv.org/pdf/1705.06655>.

[19] **J.H. Davis, C. McCabe, C. Boehm**, Quantifying the evidence for dark matter in CoGeNT data, *Journal of Cosmology and Astroparticle Physics*. 2014 (08) (2014) 014.

[20] **V.A. Ryabov, V.A. Tsarev, A.M. Tskhovrebov**, The search for dark matter particles, *Physics-Uspekhi*. 51 (11) (2008) 1091–1121.

[21] **M. Aguilar, M. Alberti, G. Alpat, et al.** (AMS Collaboration), First result from the Alpha magnetic spectrometer on the International space station: precision measurement of the positron fraction in primary cosmic rays of 0.5–350 GeV, *Physical Review Letters*. 110 (14) (2013) 141102.

[22] **M. Casolino, N. De Simone, D. Bongue,**

**et al.**, Two years of flight of the Pamela experiment: results and perspectives. <https://arxiv.org/pdf/0810.4980>, (2008).

[23] **M. Ackermann, M. Ajello, A. Albert A., et al.** (Fermi-LAT Collaboration), The Fermi Galactic center GeV excess and implications for dark matter, *The Astrophysical Journal*. 840 (1) (2017) 43.

[24] **R. Bernabei, P. Belli, F. Cappella, et al.** (DAMA-LIBRA Collaboration), Model independent result on possible diurnal effect in DAMA/LIBRA-phase 1, *The European Physical Journal. C*. 74 (3) (2014) 2827.

[25] **T. Aaltonen, B. Alvarez Gonzalez, S. Amerio, et al.** (CDF Collaboration), Search for a dark matter candidate produced in association with a single top quark in  $pp$  collisions at  $\sqrt{s} = 1.96$  TeV, *Physical Review Letters*, 108 (20) (2012) 201802.

[26] **V.M. Abazov, B. Abbott, M. Abolins, et al.** (D0 Collaboration), Search for dark photons from supersymmetric hidden valleys, *Physical Review Letters*. 103 (8) (2009) 081802.

[27] **S. Liem, G. Bertone, F. Calore, et al.**, Effective field theory of dark matter: a global analysis, *Journal of High Energy Physics*. 2016 (9) (2016) 077.

[28] **D. Alves, N. Arkani-Hamed, S. Arora, et al.**, Simplified models for LHC new physics searches, *Journal of Physics. G*. 39 (2012) 105005.

[29] **J. Alwall, R. Frederix, S. Frixione, et al.**, The automated computation of tree-level and next-to-leading order differential cross sections, and their matching to parton shower simulations, *Journal of High Energy Physics*. 2014 (7) (2014) 079.

[30] **A. Albert, M. Backovic, A. Boveia, et al.**, Recommendations of the LHC dark matter working group: Comparing LHC searches for heavy mediators of dark matter production in visible and invisible decay channels, Rezhim dostupa: <https://arxiv.org/pdf/1703.05703>.

[31] **M. Aaboud, G. Aad, B. Abbott, et al.** (ATLAS Collaboration), Search for an invisibly decaying Higgs boson or dark matter candidates produced in association with a  $Z$  boson in  $pp$  collisions at  $\sqrt{s} = 13$  TeV with the ATLAS detector. <http://cds.cern.ch/record/2273610/files/ATLAS-CONF-2017-040.pdf>.

[32] **M. Aaboud, G. Aad, B. Abbott, et al.** (ATLAS Collaboration), Search for dark matter at  $\sqrt{s} = 13$  TeV in final states containing an energetic photon and large missing transverse momentum with the ATLAS detector, *The European Physical Journal. C*. 77 (6) (2017) 393.

[33] **M. Aaboud, G. Aad, B. Abbott, et al.**, Search for dark matter and other new phenomena in events with an energetic jet and large missing transverse momentum using the ATLAS detector,



<http://cds.cern.ch/record/2273876/files/ATLAS-CONF-2017-060.pdf>.

[34] A. Sirunyan, A. Tumasyan, W. Adam et al., Search for dark matter, invisible Higgs boson decays, and large extra dimensions in the  $Z \rightarrow ll + E_T^{\text{miss}}$  final state using 2016 data. Rezhim dostupa: <http://inspirehep.net/record/1599663/files/EXO-16-052-pas.pdf>.

[35] M. Aaboud, G. Aad, B. Abbott, et al. (ATLAS Collaboration), Search for dark matter produced in association with a hadronically decaying vector boson in  $pp$  collisions at  $\sqrt{s} = 13$  TeV with the ATLAS detector, Physics Letters B. 763 (2016) 251–268.

[36] M. Aaboud, G. Aad, B. Abbott, et al., Search for dark matter production associated with bottom quarks with 13.3 fb $^{-1}$  of  $pp$  collisions at  $\sqrt{s} = 13$  TeV with the ATLAS detector at the LHC. Rezhim dostupa: <http://cds.cern.ch/record/2206279/files/ATLAS-CONF-2016-086.pdf>.

[37] A. Alves, A. Berlin, S. Profumo, F.S. Queiroz, Dark matter complementarity and the  $Z'$  portal, Phys. Rev. D. 92 (8) (2015) 083004.

[38] M. Aaboud, G. Aad, B. Abbott, et al., Search for dark matter in association with a Higgs boson decaying to two photons at  $\sqrt{s} = 13$  TeV with the ATLAS detector. Rezhim dostupa: <https://arxiv.org/pdf/1706.03948>.

[39] M.R. Buckley, D. Hooper, J.L. Rosner, A leptophobic  $Z'$  and dark matter from grand unification, Physics Letters. B. 703 (2011) 343–347.

[40] P. Ko, A. Natale, M. Park, H. Yokoya, Simplified DM models with the full SM gauge symmetry: the case of  $t$ -channel colored scalar mediators, Journal of High Energy Physics. 2017 (1) (2017) 086.

[41] M. Aaboud, G. Aad, B. Abbott, et al., Search for new phenomena in dijet events using 37 fb $^{-1}$  of  $pp$  collision data collected at  $\sqrt{s} = 13$  TeV with the ATLAS detector. Rezhim dostupa: <https://arxiv.org/pdf/1703.09127>.

[42] G. Aad, B. Abbott, J. Abdallah, et al. (ATLAS Collaboration), Search for new phenomena in the dijet mass distribution using  $pp$  collision data at  $\sqrt{s} = 8$  TeV with the ATLAS detector, Physical Review. D. 91 (5) (2015) 052007.

[43] G. Aad, B. Abbott, J. Abdallah, et al. (ATLAS Collaboration), Search for light dijet resonances with the ATLAS detector using a Trigger-object level analysis in LHC  $pp$  collisions at  $\sqrt{s} = 13$  TeV. Rezhim dostupa: <http://inspirehep.net/record/1470774/files/ATLAS-CONF-2016-030.pdf>.

[44] G. Aad, B. Abbott, J. Abdallah, et al. (ATLAS Collaboration), Search for new light resonances decaying to jet pairs and produced in association with a photon or a jet in proton-proton collisions at  $\sqrt{s} = 13$  TeV with the ATLAS detector. <http://inspirehep.net/record/1480050/files/ATLAS-CONF-2016-070.pdf>.

[45] G. Angloher, A. Bento, C. Bucci, et al. (CRESST Collaboration), Results on light dark matter particles with a low-threshold CRESST-II detector, The European Physical Journal. C. 76 (1) (2016) 25.

[46] E. Aprile, J. Aalbers, F. Agostini, et al. (XENON Collaboration), First dark matter search results from the XENON1T experiment. <https://arxiv.org/pdf/1705.06655>.

[47] C. Amole, M. Ardid, I.J. Arnquist, et al. (PICO Collaboration), Dark matter search results from the PICO-60C $_3$ F $_8$  bubble chamber, Physical Review Letters. 118 (25) (2017) 251301.

[48] D.S. Akerib, S. Alsum, H.M. Araujo, et al. (LUX Collaboration), Results from a search for dark matter in the complete LUX exposure, Physical Review Letters. 118 (2) (2017) 021303.

[49] A. Tan, M. Xiao, X. Cui, et al. (PandaX-II Collaboration), Dark matter results from first 98.7 days of data from the PandaX-II experiment, Physical Review Letters. 117 (12) (2016) 121303.

[50] N. Craig, J. Galloway, S. Thomas, Searching for signs of the second Higgs doublet. Rezhim dostupa: <https://arxiv.org/pdf/1305.2424>.

Received 02.10.2017, accepted 06.12.2017.

#### THE AUTHORS

**BASALAEV Artyom E.**

*Petersburg Nuclear Physics Institute of National Research Center “Kurchatov Institute”*  
Orlova Roscha, Gatchina,  
188300, Leningrad Oblast, Russian Federation  
[artem.basalaev@cern.ch](mailto:artem.basalaev@cern.ch)

**NARYSHKIN Yuriy G.**

*Petersburg Nuclear Physics Institute of National Research Center “Kurchatov Institute”*  
Orlova Roscha, Gatchina, 188300, Leningrad Oblast, Russian Federation  
[yury.naryshkin@cern.ch](mailto:yury.naryshkin@cern.ch)

## ELECTROMAGNETIC WAVE PROPAGATION IN THE THREE-LAYER FERRITE-DIELECTRIC-FERRITE STRUCTURE

**A.S. Cherepanov**

Peter the Great St. Petersburg Polytechnic University, St. Petersburg, Russian Federation

A problem of wave propagation in a rectangular waveguide containing a three-layer ferrite-dielectric-ferrite (FDF) structure has been considered in the paper. The calculation of a free-space FDF structure usually runs into difficulties. The proposed approach has been made it possible to obtain a rigorous solution for the waveguide modes for which there is no dependence of electromagnetic fields on a coordinate directed along a magnetizing magnetic field. It is the main mode of the FDF structure that governs principal properties of a phased array. The obtained relationships were shown to describe the modes' behavior for a free-space FDF waveguide. The dependences of the mode propagation constants on the magnetizing magnetic field were calculated, electromagnetic field structures of the main and the higher modes were found. The optimal structure parameters were determined. They are optimal when the controllability of the FDF structure by a constant magnetic field is maximal.

**Key words:** ferrite; waveguide; antenna; dielectric structure; magnetizing magnetic field

**Citation:** A.S. Cherepanov, Electromagnetic wave propagation in the three-layer ferrite-dielectric structure, St. Petersburg State Polytechnical University Journal. Physics and Mathematics. 11 (1) (2018) 115 – 121. DOI: 10.18721/JPM.11113

### Introduction

To date, fabricating phased antenna arrays with optimal technical parameters and low cost remains an important problem. One possible solution is using electrically controlled ferrite-dielectric-ferrite (FDF) structures to construct integrated phased array antennas (IPAA) [1 – 3]. Such antenna arrays have a simple design, so they can be manufactured by integrated technology methods, which considerably reduces the production costs.

An FDF structure is an open waveguide operating with multimode operation. Electrodynamics analysis of such a structure is complicated because the waveguide is open (unshielded) and contains magnetized ferrite which is a non-reciprocal medium. For these reasons, the analysis can be performed only approximately.

Finding a strict dispersion equation describing the properties of at least the basic type of waves in such a waveguide is an interesting task (it is the properties of the main mode of waves in the FDF that determine the most impor-

tant characteristics of the IPAA). This allows to gain a better understanding of the physical properties of the proposed structure and to optimize the antenna.

In this paper, we have considered a three-layer FDF structure in a closed rectangular waveguide. It is known that the distribution of electromagnetic waves in such waveguides can be described rigorously in a number of cases [4, 5]. Below we are going to prove that for a high dielectric constant of a dielectric plate in an FDF structure, the electromagnetic field outside this structure decreases quite rapidly, so that the presence of the walls near the waveguide has virtually no effect on the main mode.

### Problem statement and solution

Let us consider the problem of a rectangular waveguide with two ferrite plates and a dielectric plate located between them (Fig. 1). The external bias magnetic field is directed along the  $z$  axis (the ferrite plates are magnetized in the opposite direction).

The magnetic permeability tensor of ferrite is written in the form

$$\hat{\mu} = \begin{bmatrix} \mu & i\mu_a & 0 \\ -i\mu_a & \mu & 0 \\ 0 & 0 & \mu_{\parallel} \end{bmatrix},$$

where  $i$  is the imaginary unit,  $\mu$ ,  $\mu_a$ ,  $\mu_{\parallel}$  are the components of the magnetic permeability tensor [4, 7, 8].

It was established in [4] that if the fields do not depend on the  $z$  coordinate, only the electric field components  $E_x$  and  $E_y$  remain nonzero in a rectangular waveguide. The component  $E_z$  in the ferrite satisfies the equation

$$\frac{d^2 E_z}{dx^2} + v_f^2 E_z = 0, \quad (1)$$

where  $v_f^2 = k^2 \varepsilon_f \mu_{\perp} - \beta^2$  ( $k$  is the wavenumber of the empty space,  $\varepsilon_f$  is the dielectric permittivity of the ferrite,  $\beta$  is the sought-for constant of wave propagation in the waveguide;

$$\mu_{\perp} = \frac{\mu^2 - \mu_a^2}{\mu}.$$

The components of the magnetic field in ferrite can be found using the following relations [4]:

$$H_x = \frac{1}{k\mu_{\perp}} \left( \beta E_z - \frac{\mu_a}{\mu} \frac{dE_z}{dx} \right), \quad (2)$$

$$H_y = \frac{j}{k\mu_{\perp}} \left( \beta \frac{\mu_a}{\mu} E_z - \frac{dE_z}{dx} \right). \quad (3)$$

Relations (1) – (3) describe the fields of regions II and IV (ferrite plates). Similar relations are also satisfied for region III (dielectric), and for regions I and V (air).

The only difference is the change in material parameters. For example, instead of the quantity  $v_f^2$ , the quantity

$$v_d^2 = k^2 \varepsilon_d - \beta^2$$

can be written for the dielectric, where  $\varepsilon_d$  is the dielectric permittivity of region III.

In the air-filled regions I and V,  $v_0^2 = k^2 - \beta^2$  instead of  $v_f^2$ . Similarly, the form of relations (2) and (3) changes in these regions.

We can write the solution of Eq. (1) for all five regions and apply the boundary conditions to them: that the component  $E_z$  be equal to zero on the side walls and that the tangential components of the fields ( $E_x$  and  $H_y$ ) be continuous at the interface between the regions.

In view of the above, we can write the fields for the waveguide regions I – V (see Fig. 1):

$$I. E_z = A \sin(v_0 x),$$

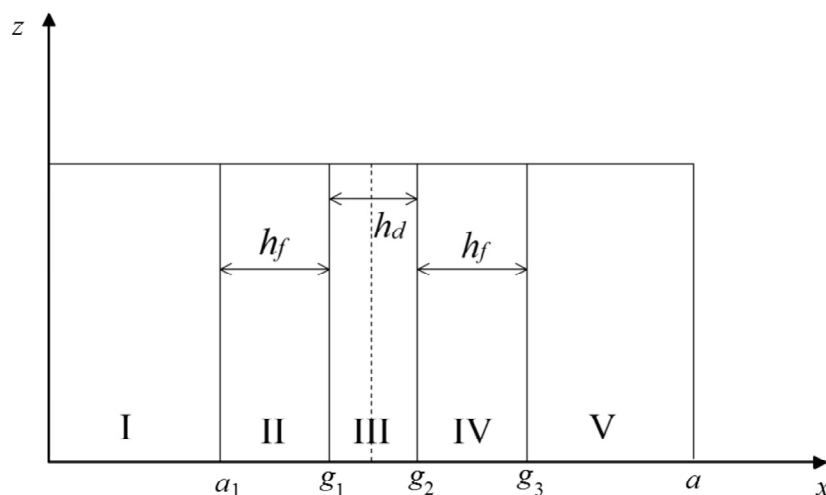


Fig. 1. Schematic representation of the FDF structure in a rectangular waveguide:  $a$  is the waveguide width;  $a_1$ ,  $g_1 - g_3$  are the other geometric parameters;  $h_f$ ,  $h_d$  are the widths of ferrite (II, IV) and dielectric (III) plates, respectively; regions I, V are filled with air; the external magnetic field is directed along the  $z$  axis





$$\text{II. } E_z = B \sin[v_f(x - a_1)] + C \cos[v_f(x - a_1)],$$

$$\text{III. } E_z = D \sin[v_d(x - a_1 - h_f)] + E \cos[v_d(x - a_1 - h_f)],$$

$$\text{IV. } E_z = F \sin[v_f(x - a_1 - h_f - h_d)] + G \cos[v_f(x - a_1 - h_f - h_d)],$$

$$\text{V. } E_z = I \sin[v_0(a - x)].$$

The boundary conditions on the side walls have already been taken into account here.

As a result, we obtain a homogeneous system of linear equations of the eighth order with unknown coefficients  $A, B, C, D, E, F, G, I$ . A non-trivial solution of this system exists only if its determinant is equal to zero:

$$\det \hat{Z} = \begin{vmatrix} z_{AA} & 0 & z_{AC} & 0 & 0 & 0 & 0 & 0 \\ z_{BA} & z_{BB} & z_{BC} & 0 & 0 & 0 & 0 & 0 \\ 0 & z_{CB} & z_{CC} & 0 & z_{CE} & 0 & 0 & 0 \\ 0 & z_{DB} & z_{DC} & z_{DD} & 0 & 0 & 0 & 0 \\ 0 & 0 & 0 & z_{ED} & z_{EE} & 0 & z_{EG} & 0 \\ 0 & 0 & 0 & z_{FD} & z_{FE} & z_{FF} & z_{FG} & 0 \\ 0 & 0 & 0 & 0 & 0 & z_{GF} & z_{GG} & z_{GI} \\ 0 & 0 & 0 & 0 & 0 & z_{IF} & z_{IG} & z_{II} \end{vmatrix} = 0. \quad (4)$$

Thus, we have obtained a dispersion equation that allows to find the propagation constants for the modes of the three-layer waveguide, first and foremost, for the main mode. The resulting equation is rigorous, that is, the accuracy of the solution is determined only by the accuracy of the procedure for calculating its roots.

The nonzero elements of the matrix  $\hat{Z}$  are given below:

$$z_{AA} = \sin(v_0 a_1), \quad z_{AC} = -1;$$

$$z_{BA} = -v_0 \cos(v_0 a_1), \quad z_{BB} = v_f / \mu_\perp,$$

$$z_{BC} = -\beta \mu_a / \mu \mu_\perp;$$

$$z_{CB} = \sin(v_f h_f), \quad z_{CC} = \cos(v_f h_f), \quad z_{CE} = -1;$$

$$z_{DB} = \frac{1}{\mu_\perp} \left[ \frac{\beta \mu_a}{\mu} \sin(v_f h_f) - v_f \cos(v_f h_f) \right],$$

$$z_{DC} = \frac{1}{\mu_\perp} \left[ \frac{\beta \mu_a}{\mu} \cos(v_f h_f) - v_f \cos(v_f h_f) \right],$$

$$z_{DD} = v_d;$$

$$z_{ED} = \sin(v_d h_d), \quad z_{EE} = \cos(v_d h_d), \quad z_{EG} = -1;$$

$$z_{FD} = v_d \cos(v_d h_d), \quad z_{FE} = -v_d \sin(v_d h_d),$$

$$z_{FF} = -v_f / \mu_\perp, \quad z_{FG} = \beta \mu_a / \mu \mu_\perp.$$

$$z_{GF} = \sin(v_f h_f), \quad z_{GG} = \cos(v_f h_f),$$

$$z_{GI} = -\sin(v_0 a_1);$$

$$z_{IF} = \frac{1}{\mu_\perp} \left[ -\frac{\beta \mu_a}{\mu} \sin(v_f h_f) - v_f \cos(v_f h_f) \right],$$

$$z_{IG} = \frac{1}{\mu_\perp} \left[ -\frac{\beta \mu_a}{\mu} \cos(v_f h_f) + v_f \cos(v_f h_f) \right],$$

$$z_{II} = -v_0 \cos(v_0 a_1).$$

### Investigation of the waveguide modes of the FDF structure

By solving dispersion equation (4), we can obtain the dependence of the propagation constant  $\beta$  on the off-diagonal term of the tensor  $\hat{\mu}$  (i.e., in fact, on the bias magnetic field), as well as on other parameters. Then, if we use the data of [4 – 6, 2, 3], we can find the structure of the fields for each mode. A combination of parameters of the FDF structure making it possible to create a workable IPAA was proposed and experimentally tested in [6]. However, no conclusions could be drawn as to whether this combination of parameters was optimal. It is possible to carry out such an investigation now that we have obtained an analytical solution for the main mode of an FDF waveguide.

FDF waveguides whose parameters are given in Table 1 were considered in Ref. [6].

Fig. 2 shows the dependence of the deceleration  $q = \beta / k$  for two modes of the FDF waveguide, obtained using the parameters from Table 1, on the magnitude of the off-diagonal term  $\mu_a$  of the tensor  $\hat{\mu}$  (the remaining elements of the tensor are assumed to be equal to unity). The result corresponds to that obtained in [6].

Fig. 3 shows the dependence of the controllability of the FDF waveguide

$$\Delta q = (\beta_{\max} - \beta_{\min}) / k$$



Table 1

Parameters of the FDF waveguides used in [6]

$ka$	$h_f / a$	$h_d / a$	$\varepsilon_f$	$\varepsilon_d$
4.82	0.097	0.042	12	40

Notations:  $h_f$ ,  $h_d$  are the widths of the ferrite and dielectric plates, respectively;  $\varepsilon_f$ ,  $\varepsilon_d$  are their dielectric permeabilities;  $k$  is the wavenumber of the empty space;  $a$  is the width of the rectangular waveguide.

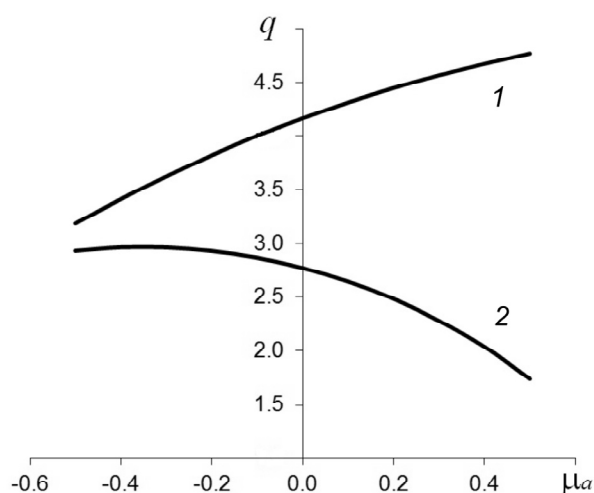


Fig. 2. Dependence of the deceleration  $q = \beta / k$  of the main (1) and second (2) modes of the FDF waveguide on the magnitude of the off-diagonal term  $\mu_a$  of the tensor  $\hat{\mu}$ ; parameters from Table 1 were used

on the thickness  $h_f / a$  of ferrite plates. The remaining parameters were assumed to be the same as before (see Table 1).

It can be seen from Fig. 3 that controllability  $\Delta q$  increases with increasing plate thickness but the growth rate drops sharply for thickness values  $h_f / a > 0.1$ . This is because ferrite effectively interacts with the electromagnetic wave only in the regions where the polarization of the magnetic field is close to circular, while the field's magnitude must be large enough. These regions are located near the dielectric plate. When thick ferrite plates are used, regions with a small magnetic field are involved. Therefore, a large increase in controllability is not achieved. A large amount of ferrite in the FDF waveguide leads to an increase in the waveguide's losses, as well as an increase in its

weight. Therefore, it is expedient to choose the plate thickness by the inequality  $h_f / a < 0.1$ . The value given in [6] seems valid.

Let us now investigate the dependence of controllability  $\Delta q$  on the thickness  $h_d$  of the dielectric. Fig. 4 shows the dependence of  $\Delta q$  on  $h_d / a$  (the other parameters are taken from Table 1). It can be seen from the graph that there is an optimal thickness value ensuring maximum controllability for the dielectric.

The physical meaning of the presence of a dielectric plate in an FDF waveguide is that it 'absorbs' the electromagnetic field so that the energy propagates along the waveguide inside the plate and in close proximity to it, i.e., where the ferrite is located. This is what provides good controllability. If the dielectric is too thick, the field is concentrated in it, and the ferrite has a small magnitude of the electromagnetic field, resulting in decreased controllability. If the dielectric is too thin, it cannot concentrate the field, a lot of energy propagates outside the ferrite, and controllability decreases as well.

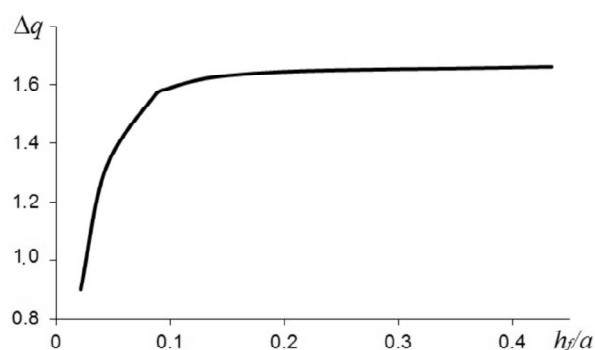


Fig. 3. Dependence of the controllability  $\Delta q = (\beta_{\max} - \beta_{\min}) / k$  of the FDF waveguide on the normalized thickness  $h_f / a$  of ferrite plates; parameters from Table 1 were used

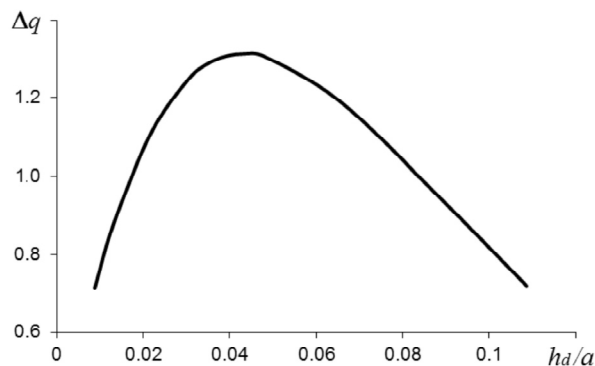


Fig. 4. Dependence of controllability  $\Delta q$  on the normalized thickness  $h_d/a$  of the dielectric; parameters from Table 1 were used

Fig. 5 shows the dependences of the normalized component of the electric field  $E_z$  on the coordinate  $x/a$  for the main and the second mode. It can be seen that the electromagnetic wave of the main mode is concentrated mainly in the FDF structure and decreases exponentially outside it. Therefore, the presence of side walls should not significantly affect the propagation constant of this mode. This is confirmed by direct calculation (the results are given in Table 2).

It can be seen from the data in Table 2 that deceleration remains constant to three decimal places with a change in the waveguide

width  $a$ . It follows then that narrow walls of the waveguide can be ‘continued to infinity’, that is, removed completely. Wide walls can also be removed, since the electric field on them does not have a tangential component and the boundary conditions are not violated. We obtain an open waveguide where we can accurately calculate the propagation constant of the main mode. The structure of the field is known in the region between the wide walls. Outside these wide walls, the field can be reconstructed, since tangential components of the magnetic field on these walls are known.

Thus, the problem of calculating the main mode for an open FDF structure has actually been solved.

The second mode decreases much slower outside the FDF structure, so a larger waveguide width  $a$  should be taken to calculate it accurately.

Fig. 6 shows the graphs of the structure of magnetic fields for the demagnetized state ( $\mu_a = 0$ ) and for the maximum values of magnetization ( $\mu_a = \pm 0.5$ ). The fields are normalized by  $H_{y\max}$  with  $\mu_a = 0$ . It can be seen that magnetic fields in ferrite are larger if  $\mu_a = -0.5$  than if  $\mu_a = 0.5$ . In addition, the polarization of the magnetic field in ferrite plates is close to circular for  $\mu_a = -0.5$ , while for  $\mu_a = 0.5$ , the field in ferrite, especially in

Table 2

Set of parameters used and the result of the calculation of deceleration of electromagnetic waves propagating in the FDF structure

Parameter	Notation	Unit	Value
Width ferrite dielectric	$h_f$	cm	0.224
	$h_d$		0.096
Off-diagonal term of the tensor of magnetic permeability of ferrite [7, 8]	$\mu_a$	—	+ 0.5
Dielectric constant ferrite dielectric	$\varepsilon_f$	—	12
	$\varepsilon_d$		40
Microwave frequency	$f$	GHz	10
Waveguide width	$a$	cm	2.3; 3.0; 4.0; 5.0
The obtained value of deceleration $q = \beta / k$ is 4.774 for all given parameter values			

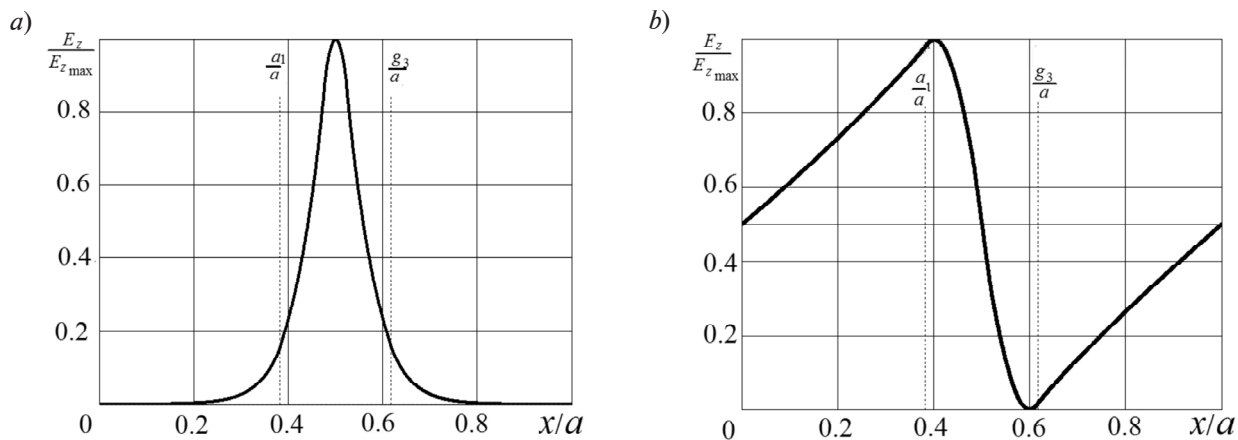


Fig. 5. Dependences of the normalized component of the electric field  $E_z$  on the normalized coordinate  $x$  for the main (a) and the second (b) mode.

The geometric parameters correspond to those shown in Fig. 1

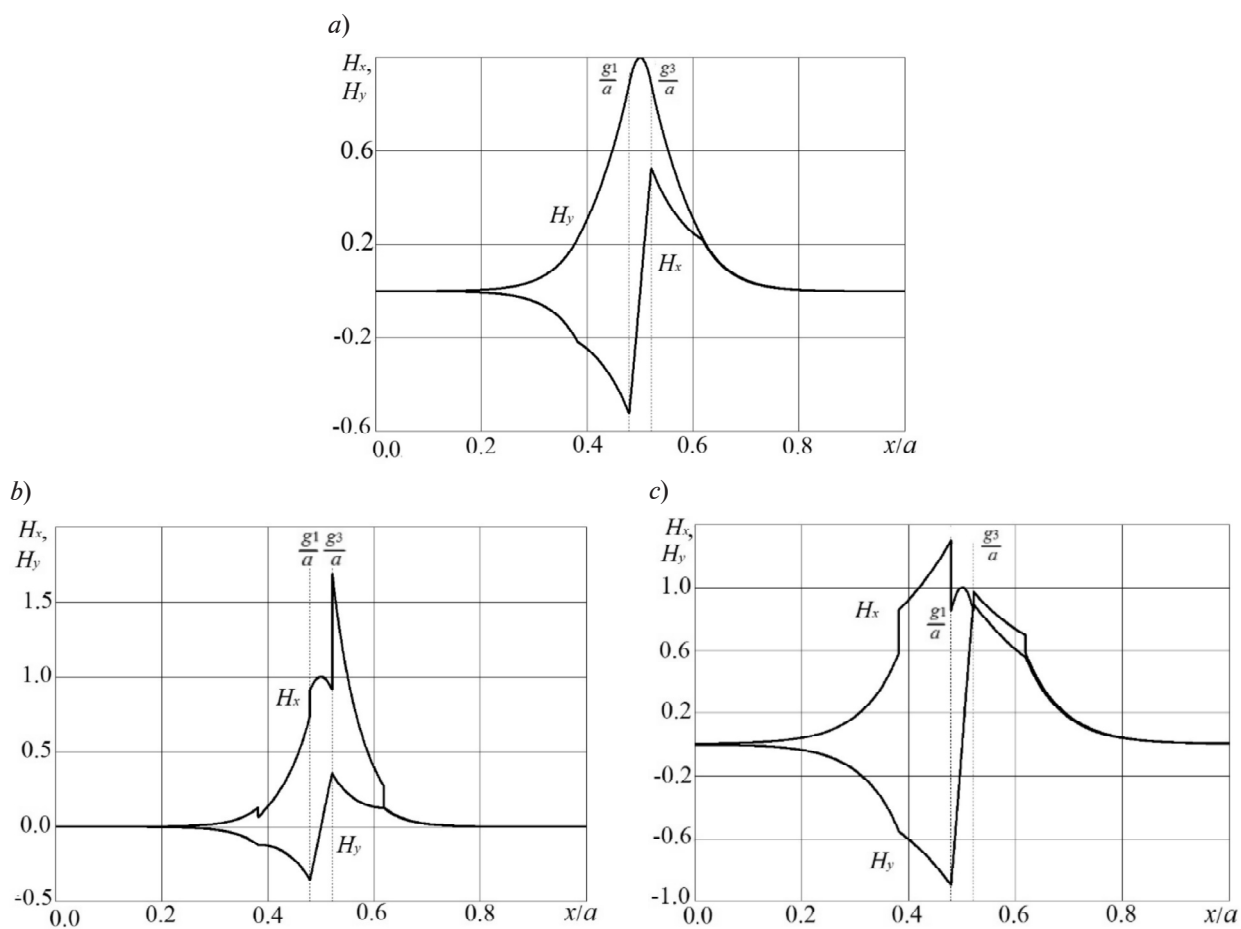


Fig. 6. Results of calculation of the magnetic field distributions (the  $H_x$  and  $H_y$  components) in the FDF structure for its demagnetized state (a) and for the maximum values of magnetization (b, c); the magnetic permeability  $\mu_a = 0$  (a);  $+0.5$  (b);  $-0.5$  (c).

The fields are normalized by  $H_{y\max}$  with  $\mu_a = 0$



the right-hand plate, differs greatly from circularly polarized. Therefore, as can be seen from the graph in Fig. 2, the slope of the  $q(\mu_a)$  dependence is steeper for negative  $\mu_a$ .

### Conclusion

The problem of propagation of waves in a rectangular waveguide containing a three-layer ferrite-dielectric-ferrite structure has been solved rigorously in the study. The proposed approach allows to investigate the modes of electromagnetic oscillations with no dependence of the fields on the coordinate directed along the bias field. We have established that the obtained relations also describe oscillation

modes for an open FDF waveguide. In an open FDF structure, it is the main oscillation mode that determines the key properties of the integrated phased array antennas, such as the scanning angle and the beamwidth. Applying the proposed approach to investigation of an open FDF waveguide eliminates the need for cumbersome numerical methods taking considerable computational time. This greatly simplifies calculating the performance of integral phased antenna arrays.

The results obtained can also be used to create ferrite phase shifters [9, 10] based on a closed rectangular waveguide with a three-layer FDF structure.

### REFERENCES

- [1] E.F. Zaytsev, A.S. Cherepanov, A.B. Guskov, New electrically scanning antennas of millimeter wave range, *Radioelectronics and Communication Systems*. 46 (4) (2003) 3–12.
- [2] A.S. Cherepanov, K.V. Guzenko, I.A. Kroutov, The slot integrated phased array, *St. Petersburg State Polytechnical University Journal. Computer Science, Telecommunications and Control Systems*. No. 2 (145) (2012) 41–45.
- [3] E.F. Zaytsev, A.S. Cherepanov, A.B. Guskov, New millimeter-wave electrically scanned antennas, *St. Petersburg State Polytechnical University Journal*. (2) (2001) 47–52.
- [4] A.G. Gurevich, *Ferrity na sverkhvysokikh chastotakh* [Microwave ferrite devices], Fizmatgiz, Moscow, 1960.
- [5] G.A. Gurevich, N.A. Bogomaz, Nonreciprocal phase shifts and a decay factor in the phase-loaded waveguide, *J. Commun., Techn. & Electron.* 3 (9) (1958) 1133 – 1343.
- [6] E.F. Zaytsev, A.S. Cherepanov, A.B. Guskov, *Elementarnaya teoriya integralnykh fazirovannykh antennoykh reshetok* [Elementary theory of integrated phase arrays], St. Petersburg State Technical University Publishing House, St. Petersburg, 1999. Dep. v VINITI, No. 3849–V99.
- [7] G.A. Sharov, *Volnovodnye ustrojstva santimetrovyh i millimetrovyh voln* [Waveguide devices of centimeter and millimeter waves], Goryachaya Liniya Telekom, Moscow, 2016.
- [8] G.A. Sharov, *Osnovy teorii sverkhvysokochastotnyh linij peredachi cepej i ustrojstv* [Foundations of the theory of microwave link communications for chains and devices], Goryachaya Liniya Telekom, Moscow, 2016.
- [9] S.V. Katin, A.V. Nazarov, E.A. Popov, M.S. Rozhkova, *Elektro-magnitnye volny v kruglom otkrytom sloistom ferrit-dielektricheskom volnovode* [Electromagnetic waves in the circular open layered ferrite-dielectric waveguide], *Antennas*. (8) (2012) 20–24.
- [10] N.P. Milevskij, O.V. Trekhovickij, *Nekotorye voprosy upravleniya ferritovym fazovrashchatelem* [Some aspects of a ferrite phase-shifter control], *Radioengineering*. (4) (2012) 84–92.

*Received 16.01.2018, accepted 30.01.2018.*

### THE AUTHOR

**CHEREpanov Andrey S.**

*Peter the Great St. Petersburg Polytechnic University*

29 Politechnicheskaya St., St. Petersburg, 195251, Russian Federation

ASCherSPb@mail.ru

## QUANTIZATION OF THE ENERGY DENSITY IN A CLOSED UNIVERSE

**N.N. Gorobey, A.S. Lukyanenko**

Peter the Great St. Petersburg Polytechnic University, St. Petersburg, Russian Federation

The energy of a closed universe is represented as a difference of two positive definite quantities, one of which includes the energy of matter and the energy of gravitational waves on the expanding universe background. The second quantity relates to the universe expansion and is called the energy of space. The whole energy of the universe equals zero provided the classical gravitational constraints are taken into account. In quantum theory a principle of the energy density of the matter minimum is formulated in the condition that the quantum gravitational constraints are also fulfilled in average. The states of the universe which satisfy the conditional minimal principle have different degree of the physical degrees of freedom excitation and, according to the gravitational constraints, corresponding excitation of space. The state of minimal excitation is proposed to be taken as the Beginning of the universe, and all the set of solutions, correspondingly, as admitted physical states of the universe at different moments of a cosmic time.

**Keywords:** energy; time; expanding universe; gravitational constant; quantum state; reference frame

**Citation:** N.N. Gorobey, A.S. Lukyanenko, Quantization of the energy density in a closed universe, St. Petersburg Polytechnical State University Journal. Physics and Mathematics. 11 (1) (2018) 94 – 101. DOI: 10.18721/JPM.11114

### Introduction

The Wheeler – de Witt equation (WdW) [1, 2] is the cornerstone of modern quantum cosmology. The equation can be written in the following condensed form:

$$\hat{H}|\Psi\rangle = 0, \quad (1)$$

where  $\hat{H}$  is the Hamiltonian of the Universe given in an arbitrary frame of reference.

This theory uses Dirac's covariant approach to quantization of dynamical systems with constraints [3], with the physical state of the system determined by the conditions that the quantum constraints equal zero. As a result, the quantum state of the Universe does not depend on any parameters of the frame of reference, including the coordinate time (the problem of time in the 'frozen' formalism of quantum gravity theory [4, 5]). In this case, the time parameter should be sought among the dynamic variables of the theory. For this purpose, it seems natural to take the variables directly related to the expansion of the Universe, as

they are contained in its scale factor

$$\Omega(x) = [\det g_{ik}(x)]^{1/6},$$

where  $g_{ik}(x)$ ,  $i, k = 1, 2, 3$  is the field of the metric tensor of 3D geometry of the spatial section  $\Sigma$ .

This choice of cosmic time is the main one in analyzing the solutions of the Einstein equations near the cosmological singularity (where  $\Omega(x) \rightarrow 0$ ) [6]. Below, we are going to give a general justification for this natural choice within the framework of the Hamiltonian formalism. Time is closely related to energy, so it should be expected that the solution of the time problem is also connected with the definition of energy in a closed Universe.

Eq. (1) has the form of a stationary Schrödinger equation with zero eigenenergy. In this paper, the zero energy of the Universe will be interpreted to mean that the positive energy of matter filling the Universe (this includes the energy of gravitational waves) is completely compensated by the negative energy of the



gravitational field, associated with the scale factor, which arises in case of a closed space (a 100 % mass defect). First of all, the gravitational field energy in a closed Universe is divided into two parts with opposite signs: the part of the energy that includes the energy of gravitational waves in an expanding Universe, and the energy of space expansion itself. The proposed approach is based on the theorem of positive energy of the gravitational field, which was originally formulated for an island mass distribution with asymptotically flat space-time geometry [7, 8]. The Hamiltonian formulation of this result, together with the new complex canonical variables of general relativity (GR) theory, was proposed in [9]. Ref. [10] offered a generalization of this theorem to the case of a closed Universe, where the Hamiltonian had the form of a linear combination of GR constraints  $H_\mu$ ,  $\mu = 0, 1, 2, 3$  (the constraints are the densities of weight +1, see the Ref. [11] for their explicit form):

$$H = \int_{\Sigma} d^3x N^\mu H_\mu. \quad (2)$$

The coefficients  $N^\mu$  are called the lapse and shift functions, and determine the geometry of the (3+1)-partition of space-time into space and time. The Witten identity [7, 8] using auxiliary bispinor fields on the spatial section  $\Sigma$  takes the central place in this analysis.

In case of asymptotically flat space-time geometry, the auxiliary spinor field that is the solution of the Dirac equation on the spatial section enters directly into the expression for the energy of the gravitational field. It does not have the physical meaning of a force field but determines the equally important result of the action of the gravitational field that is the speed of time at each point of the spatial section [8]. In the case of a closed Universe, the Witten identity produces the sought representation of Hamiltonian (2) as a difference of two positive definite quantities:

$$H = h - D^2, \quad (3)$$

one of which,  $h$ , coincides in form with the positive energy of the gravitational field in asymptotically flat space-time, and the second,  $D^2$ , is connected with the scale factor  $\Omega(x)$  and can be called the energy of the expansion of space

or simply the energy of space. Representation (3) arises by using a special parametrization of the lapse and shift functions  $N^\mu$  with the components of the Dirac bispinor field  $\psi$  on the spatial cross section  $\Sigma$  [12]. Now the components of the bispinor  $\psi$  determine the frame of reference and the corresponding geometry of space-time foliation, so we will call it the gauge spinor. Both terms in expression (3) are quadratic forms on the space of bispinor fields, in particular,

$$h = (\psi, \hat{h}\psi), \quad (4)$$

where the round brackets denote the scalar product in the space of bispinor fields.

In the presence of matter fields, their energy, proportional to the energy-momentum tensor, also enters quadratic form (4) with a positive sign [7]. From now on we will refer to this value as the energy of matter. According to the constraint equations,

$$H_\mu \approx 0, \quad (5)$$

Hamiltonian (2) is equal to zero, which means that the difference in the energies of matter and space in a closed Universe is equal to zero.

Having at our disposal the quantity of energy of matter in a closed Universe, with the value of this energy bounded from below, we can set the task of finding its minimum in quantum cosmology. This problem was formulated in [13], where it is proposed to regard the corresponding ground state as the Beginning of the Universe. In this paper, we have formulated the principle of the minimum (extremum) of the energy of matter and the equations that follow from it as a basis for the definition of physical states of the Universe in quantum cosmology, alternative to the WdW equation (1). In ordinary quantum mechanics, the stationary Schrödinger equation

$$\hat{h}|\Psi\rangle = E|\Psi\rangle \quad (6)$$

arises naturally in the problem of the minimum (extremum) of the mean energy value (see, for example, Ref. [14]):

$$\langle W \rangle = \frac{\langle \Psi | \hat{h} | \Psi \rangle}{\langle \Psi | \Psi \rangle} \quad (7)$$

on a Hilbert space of states of an isolated system.



This problem itself makes sense insofar as the energy operator  $\hat{h}$  is bounded from below. The closed Universe is an ideal isolated system, and according to the statement we have made above, the energy of matter in it is positive definite. Under quantization, quadratic form (4) becomes an operator

$$\hat{h} = (\psi, \hat{h}\psi), \quad (8)$$

acting in the space of states of the Universe  $|\Psi\rangle$ , where the two ‘hats’ now indicate the operator acting in the space of bispinors  $\psi$  and simultaneously in the space of states of the Universe.

Thus, the minimum (extremum) problem must be formulated for the functional

$$\rho = \frac{\langle \Psi | (\psi, \hat{h}\psi) | \Psi \rangle}{\langle \Psi | (\psi, \psi) | \Psi \rangle}. \quad (9)$$

This quantity has the dimension of the energy density because the denominator in the normalizing quadratic form  $(\psi, \psi)$  involves integration over the volume of the Universe. However, the difficulty in formulating this minimum principle is that physical degrees of freedom of matter (and of gravitational waves) also interact with the scale factor  $\Omega(x)$ . The scale factor determines the volume of the Universe, but we have excluded it from the physical degrees of freedom. The interaction in question is that both terms on the right-hand side of expression (3) depend on all parameters of 3D geometry.

In order to take this dependence into account, it is sufficient to supplement the principle of the minimum of the mean energy density by additional conditions imposed by quantum constraints on the physical states of the Universe:

$$\langle \Psi | \hat{H}_\mu | \Psi \rangle = 0. \quad (10)$$

Notice that Gaussian constraints of gauge theories that underlie the standard model of matter [15] are added to gravitational constraints (5). Let us denote these Gaussian constraints as

$$G_a \approx 0, \quad (11)$$

where  $a$  is the numbering index.

This addition occurs automatically, since constraints (11) are contained in the energy-

momentum tensor of matter fields. As a result, we obtain the conditional principle of the minimum (extremum) of the mean energy of matter in a closed Universe for the functional

$$\frac{\langle \Psi | (\psi, \hat{h}\psi) | \Psi \rangle}{\langle \Psi | (\psi, \psi) | \Psi \rangle} + \int_\Sigma \sqrt{g} d^3x [l^\mu \langle \Psi | \hat{H}_\mu | \Psi \rangle + A^a \langle \Psi | D_a | \Psi \rangle], \quad (12)$$

where  $l_\mu(x), A^a(x)$  are the Lagrange multipliers.

The following section contains the necessary definitions and the explicit form of representation (3) of the Hamiltonian of a closed Universe. An operator representation of gravitational constraints is derived from the Witten identity; the choice of the scale factor of the Universe as an internal (‘multi-arrow’) time parameter in the expanding Universe is substantiated. Then we obtain a system of equations, including the sought-for ‘stationary’ Schrödinger equation, from conditional minimum principle (12).

### Hamiltonian of a closed Universe

Let us introduce the spinor variables present in the Witten identity and in the proof of the theorem on the positive energy of the gravitational field [7, 8]. A spinor field is a pair of complex numbers  $\lambda_A \in C^2, A = 0, 1$ , given at each point of the spatial section  $\Sigma$ , which has certain transformational properties under the transformation of spatial coordinates (the necessary definitions and notations of spinor algebra are given in [15]). When dealing with spinor variables, it is also convenient to use complex canonical variables  $(\sigma_{iAB}, M^{kCD})$  for describing the gravitational field. These variables are defined by the relations

$$\sigma_{iAB} \sigma_k^{AB} = g_{ik}, \quad \sigma_{iAB} \sigma^{iCD} = \varepsilon_{(A}^C \varepsilon_{B)}^D, \quad (13)$$

$$M^{kCD} \equiv \pi^{kl} \sigma_l^{CD}, \quad (14)$$

and also by the Hermitian condition for the spin coefficients of the metric:

$$\sigma_{iAB}^+ \equiv 2n_A^{C'} n_B^{D'} \bar{\sigma}_{iC'D'} = -\sigma_{iAB}, \quad (15)$$

where  $\pi^{lm}(x), l, m = 1, 2, 3$  are the canonical impulses conjugate to the 3D metric tensor (they are the tensor density of weight +1); to-



gether with  $g_{ik}(x)$  they form the real canonical variables of the gravitational Arnowitt – Deser – Misner field (ADM) (see [11]). The overbar indicates the operation of complex conjugation.

The spin tensors and  $n^{AB'}$ , determined by the relations  $\varepsilon_{AB} = -\varepsilon_{BA}$ ,  $\varepsilon_{01} = 1$  and

$$n^{AA'} n^B_{A'} = \frac{1}{2} \varepsilon^{AB}, \quad (16)$$

are, respectively, a metric tensor and an arbitrary unitary spin tensor in the space of spinors  $C^2$ . The spinor indices become superscripts or subscripts using  $\varepsilon_{AB}$  and acquire a prime through the operation of complex conjugation of the spinor (two primes annihilate).

Of all the canonical Poisson brackets (PB) for the new variables, let us concentrate on only one PB relation associated with the scale factor  $\Omega$  of the Universe:

$$\{\ln \Omega^2(x), M(y)\} = \delta^3(x - y), \quad (17)$$

where  $M \equiv M^{kCD} \sigma_{kCD}$ .

The scale factor determines the 3D volume of the Universe:

$$V = \int_{\Sigma} \Omega^3 d^3x. \quad (18)$$

Let us introduce complex connection into the space of spinor fields [17]:

$$A_{kMN} = \Gamma_{kMN}(\sigma) + \frac{i}{\sqrt{2g}} M_{kMN}, \quad (19)$$

where  $\Gamma_{IMN}(\sigma)$  is the ordinary torsion-free spin connection which obeys the Hermitian condition of the form (15).

It determines the covariant derivative

$$\nabla_k \lambda_A \equiv \partial_k \lambda_A + A_{kA}^B \lambda_B \quad (20)$$

in the space of spinor fields. We also require Dirac bispinors

$$\psi \in C^2 \otimes \bar{C}^2.$$

Let us define a 3D Dirac operator on the space of bispinor fields

$$\widehat{D}\psi \equiv i\sqrt{2} \begin{pmatrix} n_A^{B'} \sigma^k_{B'}{}^C \nabla_k \lambda_C \\ n_{A'}^B \bar{\sigma}^k_B{}^{C'} \bar{\nabla}_k \bar{\mu}_{C'} \end{pmatrix}, \quad \psi = \begin{pmatrix} \lambda_A \\ \bar{\mu}_{A'} \end{pmatrix} \quad (21)$$

and introduce a Hermitian scalar product

$$(\psi_1, \psi_2) \equiv \int_{\Sigma} \sqrt{g} d^3x n_{AA'} (\bar{\lambda}_1^{A'} \lambda_2^A + \mu_1^A \bar{\mu}_2^{A'}), \quad (22)$$

Dirac operator (21) is Hermitian with respect to this scalar product [12].

The Witten identity links the bilinear form of the squared Dirac operator  $\widehat{D}^2$  with the bilinear form of another positive definite operator, which (with a slight modification) is the required representation of the energy of matter in a closed Universe.

Using the notations we have adopted and omitting for simplicity the contribution of matter fields, we can write this identity in the form [12]:

$$(\psi_1, \widehat{D}^2 \psi_2) - (\psi_1, \widehat{w} \psi_2) = H[\psi_1, \psi_2], \quad (23)$$

where

$$(\psi_1, \widehat{w} \psi_2) \equiv \frac{1}{4} \int_{\Sigma} \sqrt{g} d^3x g^{ik} n_{AA'} \times (\bar{\nabla}_i \bar{\lambda}_1^{A'} \nabla_k \lambda_2^A + \nabla_i \mu_1^A \bar{\nabla}_k \bar{\mu}_2^{A'}), \quad (24)$$

and the bilinear form on the right-hand side is a linear combination of gravitational constraints.

In case of an asymptotically flat space-time geometry, the Witten identity makes it possible to express the energy of the island system, which is determined by the surface integral at spatial infinity through a positive definite quadratic form which is obtained from expression (24) with  $\psi_1 = \psi_2 = \psi$ , where the bispinor  $\psi$  is a solution of the Dirac equation

$$\widehat{D}\psi = 0 \quad (25)$$

with the given asymptotic value of  $\psi_0$ .

We should note that Witten actually did not expect an auxiliary spinor variable obeying differential equation (25) to appear in general relativity, in addition to the already existing fields of matter [7]. In this case, the bispinor  $\psi$ , as previously indicated, specifies the local properties of the globally inertial frame of reference in which the energy is determined.

In case of a closed Universe, there is no surface integral and no usual definition of energy, and the physical consequences of identity (23) will be somewhat different. Let us now take an arbitrary bispinor field  $\psi \neq 0$  on the space section  $\Sigma$ , and, assuming that  $\psi_1 = \psi_2 = \psi$  in identity (23), write the representation of the Hamiltonian of a closed Universe (in a frame of reference governed by  $\psi$ ) as a difference of two positive definite quadratic forms:

$$H[\psi] = (\psi, \hat{w}\psi) - (\psi, \hat{D}^2 \psi). \quad (26)$$

Here the Hamiltonian  $H[\psi]$  is given as a gauge [11]:

$$N^0 = \frac{1}{4\sqrt{2}} n_{AA'} (\lambda^A \bar{\lambda}^{A'} + \mu^A \bar{\mu}^{A'}), \quad (27)$$

$$N^k = -\frac{1}{4} \sigma^k_{AB} n^B_{A'} (\lambda^A \bar{\lambda}^{A'} + \mu^A \bar{\mu}^{A'}). \quad (28)$$

Thus representation (3) is proved. Being quadratic relative to the canonical momenta of matter and the geometry of space-time, the Hamiltonian of a closed Universe also produces the geometry of the configuration space of GR (superspace). It is evident from the representation of Hamiltonian (26) that this geometry is pseudo-Riemannian in any frame of reference.

Let us now propose a physical interpretation of both terms on the right-hand side of (26). The first term is nonzero for any  $\psi$ , since Dirac operator (21) is an elliptic operator on a compact manifold  $\Sigma$ , so that its spectrum is discrete and separated from zero. Notice that this operator contains only the momentum  $M \equiv M^{kCD} \sigma_{kCD}$ , which, according to relation (17), is canonically conjugate to the scale factor of 3D geometry (more precisely, to the value  $\ln(\Omega^2)$ ). For this reason, we shall refer to this contribution to the Hamiltonian as the energy of expansion of the 3D space of the Universe. However, the momentum  $M$ , which is proportional to  $\Omega$  and determines the kinetic energy of the expansion of space, is also contained in the second quadratic form of the Hamiltonian (26). Its contribution can be ‘extracted’ from there in a covariant manner by introducing completely symmetric spin tensors [12]

$$\varphi^{MNA} \equiv \sigma^{iMN} \nabla_i \lambda^A + \frac{2}{3} \varepsilon^{A\{M} \sigma^{iN\}{}_P \nabla_i \lambda^P, \quad (29)$$

$$\chi^{MNA} \equiv \sigma^{iMN} \nabla_i \mu^A + \frac{2}{3} \varepsilon^{A\{M} \sigma^{iN\}{}_P \nabla_i \mu^P. \quad (30)$$

It is easy to verify that these spin tensors do not contain the canonical momentum  $M$ . Now the representation of the Hamiltonian of a closed Universe takes the following final form:

$$h[\psi] - \frac{11}{9} (\psi, \hat{D}^2 \psi) = H[\psi], \quad (31)$$

where

$$h[\psi] \equiv (\psi, \hat{h}\psi) = \frac{1}{2} \int_{\Sigma} \sqrt{g} d^3 x n_{AA'} n_{MM'} n_{NN'} \times \quad (32)$$

$$\times (\varphi^{A'M'N'} \varphi^{AMN} + \chi^{A'M'N'} \chi^{AMN}) + (\psi, \hat{T}\psi).$$

Here the ‘hats’ denote the operators acting in the space of bispinor fields.

We have added the contribution of ordinary matter proportional to the corresponding energy-momentum tensor [7] to this expression for the energy of the gravitational field and will treat all of this together as the energy of the physical degrees of freedom in a closed Universe. The first term in (32) represents the part of the energy of the gravitational field that includes the energy of gravitational waves in the expanding Universe.

We should note that this expression for the energy in a closed Universe coincides with that obtained for the island mass distribution with the asymptotically flat geometry of space-time, since in this case the bispinor  $\psi$  obeys the Dirac equation (25). This can be seen from the operator form of (32):

$$\hat{h} = -\frac{1}{2} \Delta + \frac{2}{9} \hat{D}^2 + \hat{T}, \quad (33)$$

where

$$\Delta \psi \equiv \frac{1}{\sqrt{g}} \left( n_A^{A'} \bar{\nabla}_i (\sqrt{g} g^{ik} n_{A'}^B \nabla_k \lambda_B) \right) \quad (34)$$

$$\left( n_{A'}^A \nabla_i (\sqrt{g} g^{ik} n_A^{B'} \bar{\nabla}_k \bar{\mu}_{B'}) \right)$$

is the Beltrami–Laplace operator in the space of bispinor fields.

The first term on the right-hand side of equality (33) is, like this entire expression, a positive definite operator and represents the operator of the energy of the gravitational field in case of asymptotically flat space-time geometry.

Witten’s identity (23) itself, which is valid for any  $\psi_1, \psi_2$ , leads to an operator equality on the space of bispinor fields, namely,

$$\hat{h} - \frac{11}{9} \hat{D}^2 = 0, \quad (35)$$

if gravitational constraints (5) are satisfied.

Equality (35) can be solved explicitly with respect to the Dirac operator:

$$\hat{D} = \pm \sqrt{\frac{9}{11}} \hat{h}, \quad (36)$$



where the square root of a positive definite Hermitian operator (33) can also be defined as a Hermitian operator.

Here the operators act in the space of bispinor fields. Since the Dirac operator is linear with respect to  $M$ , we can conclude that the system of gravitational constraints is solved with respect to the canonical momenta conjugate to the dynamic variable  $\ln(\Omega^2(x))$ .

This representation of gravitational constraints can be used as a basis for a noncovariant form of quantum gravity with classical 'multi-arrow' time [10] whose role is naturally played by the  $\ln(\Omega^2(x))$  variable (there is an arrow of time for each point  $x$  of the spatial section  $\Sigma$ ).

However, operator equation (36) does not in itself describe the evolution of the Universe until a specific observer is fixed. In quantum theory this equation only takes the form of a nonstationary Schrödinger equation with a single cosmic time parameter in the projection onto an arbitrary gauge spinor  $\psi(x)$ :

$$(\psi, \widehat{D}\psi) = \pm \left( \psi, \sqrt{\frac{9}{11}} \widehat{h}\psi \right). \quad (37)$$

This is a clear violation of covariance, since the gauge spinor is fixed arbitrarily. In the next section, we offer an alternative description of quantum dynamics of the Universe without an explicit violation of covariance. Instead of extracting the square root in operator equation (35) and introducing the classical time parameter, associated with the scale factor  $\Omega(x)$  and 'projected' onto an arbitrary gauge spinor  $\psi(x)$ , we formulate a quantum theory based on the principle of minimum (extremum) energy of matter (12), in which the scale factor is quantized along with the other components of the 3D metric.

### Quantization of energy density in a closed Universe

Let us carry out the quantization in a standard manner, by replacing the canonical momenta  $p$  by the operators of variational differentiation on the space of states of the Universe  $|\Psi\rangle$ :

$$p(x) \equiv \frac{\hbar}{i} \frac{\delta}{\delta q(x)}, \quad (38)$$

where  $q(x) \equiv (\sigma_{iAB}(x), \phi(x))$  ( $\phi(x)$ ) is the set of matter fields.

Respectively, the operators in this space of states are the Hamiltonian of matter  $\widehat{h}$ , determined by substituting operators (38) into Hamiltonian (31) and expression (32), and gravitational constraints  $\widehat{H}_\mu$ . We should note that Gaussian constraints (11) with the corresponding Lagrange multipliers are already contained in the second term of operator (32). At this stage, there is a difficulty in determining these operators due to the ambiguity of the ordering of the non-commuting operator multipliers. We shall here regard this difficulty as technical and shall not discuss it in detail.

After the basic quantities are determined, the remaining operation is to write down the equations that follow from the conditional extremum principle (12). The variational parameters are the wave function of the Universe  $\Psi[\sigma, \phi]$ , the gauge bispinor  $\psi(x)$ , and the Lagrange multipliers  $\tilde{l}_\mu(x), \tilde{A}^a(x)$ .

The variation with respect to  $|\Psi\rangle$  gives the actual Schrödinger equation:

$$\begin{aligned} & \frac{(\psi, \widehat{h}\psi)}{(\psi, \psi)} |\Psi\rangle + \\ & + \int_\Sigma \sqrt{g} d^3x [\tilde{l}^\mu \widehat{H}_\mu |\Psi\rangle + \tilde{A}^a D_a |\Psi\rangle] = \rho |\Psi\rangle, \end{aligned} \quad (39)$$

where the mean value of the double energy operator  $\widehat{h}$  is calculated in the frame of reference determined by the gauge spinor  $\psi(x)$ . It remains an operator in the space of states  $|\Psi\rangle$  of the Universe.

The modified Lagrange multipliers  $\tilde{l}_\mu(x), \tilde{A}^a(x)$  differ from the initial ones by a normalization factor

$$\frac{\langle \Psi | (\psi, \psi) | \Psi \rangle}{(\psi, \psi)}. \quad (40)$$

Variation with respect to  $\psi(x)$  gives an equation for the gauge spinor:

$$\frac{\langle \Psi | \widehat{h} \Omega^3(x) | \Psi \rangle}{\langle \Psi | \Omega^3(x) | \Psi \rangle} \psi = \rho \psi, \quad (41)$$

where the mean value of  $\widehat{h}$  is calculated in the space of states of the Universe with the weight  $\Omega^3(x)$  and is an operator in the space of bispinor fields on  $\Sigma$ .



Thus, the distribution of energy of matter, determined by the operator  $\hat{h}$ , fixes the frame of reference corresponding to a given state of the Universe. Finally, the variation with respect to Lagrange multipliers  $l_\mu, A_0^a$  gives constraint equations (10) plus additional gauge constraints

$$\langle \Psi | G_a | \Psi \rangle = 0. \quad (42)$$

The constraint equations are sufficient for determining the Lagrange multipliers in equality (35); after that the self-consistent system of equations (39) and (41) forms a 'stationary' Schrödinger equation in quantum cosmology.

We should note that for a fixed  $|\Psi\rangle$ , the operator acting on  $\psi(x)$  on the left-hand side of equality (41), is, as well as  $\widehat{D}^2$ , elliptic on a compact manifold  $\Sigma$ . Its spectrum is discrete. We can assume that the spectrum of eigenvalues of  $\rho$  in this problem is also discrete, since  $|\Psi\rangle$  and  $\psi(x)$  are found self-consistently.

Thus, the parameter  $\rho$  that enters into equations (39) and (41) is numbered by some set of quantum numbers. In classical cosmology, the energy density of matter in an expanding Universe decreases with the passage of cosmic time, starting from an infinite value. In the quantum theory considered here, the solutions of the 'stationary' Schrödinger equation differ by the degree of excitation of the physical degrees of freedom of matter. There is a state of minimal excitation among them, which is called the basic state of the Universe in quantum cosmology in [13], where it was proposed as the Beginning of the Universe. In this state, the energy density of matter is maximal but finite.

Now it becomes necessary to interpret the entire set of solutions of the 'stationary' Schrödinger equation. The basic assumption that we make about the spectrum of admissible values of  $\rho$  is that they are realized in the quantum evolution of the Universe. This means that the cosmic time should be sought in the above-mentioned set of quantum numbers. In this picture of quantum evolution of the Universe, the time parameter is discrete. The continuous nature of evolution with continuous time should be expected, as usual, at high degrees of excitation of the energy of matter. Another element of the formalism is the additional field of the calibration spinor  $\psi(x)$  which determines

the local properties of the frame of reference that accompanies the distribution of matter at a given moment in cosmic time. The lapse function  $N^0(x)$  constructed from it, according to gauge (27), sets the speed of the standard clock located in each point of space. Thus, together with cosmic time, a frame of reference to which this time should be assigned is also fixed. There is no violation of covariance, since the parameters of the frame of reference are determined self-consistently with the actual distribution of matter in this quantum state. However, consistent development of this interpretation assumes knowledge of the structure of the quantum energy density spectrum.

### Conclusion

In this paper, we have proposed to consider the quantum evolution of the Universe in terms of the energy parameter, the mean energy density of matter. The basis for the new approach is that the dynamic structure of the general theory of relativity in the case of a closed Universe allows defining the quantities of the energy of matter (including gravitational waves) and the energy of space expansion. In any frame of reference given by the gauge spinor  $\psi$ , these quantities are sign-definite quadratic forms of  $\psi$  that cancel each other out if gravitational constraints are satisfied.

Thus, the concept of a closed Universe as an object with a 100 % mass-energy defect has been substantiated. In this case, the quantization of the theory can be based on the principle of minimum energy with respect to one part of the internal energy of the Universe, namely, to the energy of matter and gravitational waves.

As a result, a system of equations is obtained which serves as an equivalent of the stationary Schrödinger equation in ordinary quantum mechanics for a closed Universe. The system includes Eq. (39), whose solutions are the states of the Universe  $|\Psi\rangle$  with a certain mean energy density  $\rho$ . It is supplemented by Eq. (41) for the gauge spinor  $\psi$ , i.e., the frame of reference to which the physical state  $|\Psi\rangle$  should be assigned, and the quantization parameter is the value of the mean energy density  $\rho$ . The quantum-constraint equations (10) and (42) fix the uncertain Lagrange multipliers in Schrödinger's equation (39). In this





formalism there is no violation of covariance, since additional calibration conditions are not necessary for fixing the Lagrange multipliers. In contrast to the conventional covariant form of quantum theory based on the Wheeler – de Witt equations (1), observable parameters  $\rho$  and  $\psi(x)$  are present here, which together can be linked to cosmic time and the frame of reference in quantum cosmology. The cosmic

time is discrete in this formalism. Continuous evolution of the Universe should be expected only in the late stages corresponding to a high degree of excitation of the energy of matter.

### Acknowledgments

The authors thank Prof. V.A. Franke (St. Petersburg State University) and Dr. A.V. Goltsev for useful discussions.

### REFERENCES

- [1] **J. Wheeler**, Superspace and the nature of quantum geometrodynamics, In: C. DeWitt, J. Wheeler (eds), “Batelle Rencontres – 1967, Lectures in Mathematics and Physics”, Benjamin Inc., New York (1968) 242–307.
- [2] **C. DeWitt**, The quantization of geometry, In: L. Witten (ed.), “Gravitation: An Introduction to Current Research”, Wiley, New York 1962.
- [3] **P.A.M. Dirac**, The principles of quantum mechanics, 4th ed., Oxford Univ. Press, Oxford (1958) 35–36.
- [4] **C.J. Isham**, Canonical quantum gravity and the problem of time, arXiv:gr-qc/9210011v1, 1992.
- [5] **E. Anderson**, Problem of time in quantum gravity, arXiv:1206.2403v1 [gr-qc], 2012.
- [6] **I.M. Khalatnikov, A.Yu. Kamenshchik**, Lev Landau and the problem of singularities in cosmology, Sov. Phys. Usp. 51 (6) (2008) 609–616.
- [7] **E. Witten**, A new proof of the positive energy theorem, Commun. Math. Phys. 80 (3) (1981) 381–402.
- [8] **L.D. Faddeev**, The energy problem in Einstein’s theory, Sov. Phys. Usp. 25(3) (1982) 130–142.
- [9] **A. Ashtekar**, On the Hamiltonian of General Relativity, Physica. A. 124 (1–3) (1984) 51–59.
- [10] **A. Lukyanenko**, Lengthwise gravitation fields in General Relativity theory, Doklady Akademii Nauk SSSR. 289 (3) (1986) 579–583.
- [11] **C. Misner, K. Thorne, J. Wheeler**, Gravitation, W.H. Freeman and Company, San Francisco, 1973.
- [12] **N.N. Gorobey, A.S. Lukyanenko**, Three-dimensional volume of a closed universe as a canonical time parameter, Class. Quantum Grav. 10(11) (1993) 2329–2335.
- [13] **N. Gorobey, A. Lukyanenko**, Ground state of the universe in quantum cosmology, J. Mod. Phys. A. 31 (02n03) (2016) 1641014.
- [14] **V.A. Fock**, Nachala kvantovoy mekhaniki [Quantum mechanics principles], Nauka, Moscow, 1976.
- [15] **L.D. Faddeev, A.A. Slavnov**, Vvedeniye v kvantovuyu teoriyu kalibrovochnykh poley [An introduction to gauge field quantum theory], Nauka, Moscow, 1988.
- [16] **R. Penrose, W. Rindler**, Spinors and space-time, Vol. 1. Two-spinor calculus and relativistic fields, Cambridge Univ. Press, Cambridge, 1984.
- [17] **A. Ashtekar**, New Hamiltonian formulation of General Relativity, Phys. Rev. D. D 36 (6) (1987) 1587–1602.

*Received 23.09.2017, accepted 28.11.2017.*

### THE AUTHORS

**GOROBEY Nataliya N.**

*Peter the Great St. Petersburg Polytechnic University*

29 Politechnicheskaya St., St. Petersburg, 195251, Russian Federation  
n.gorobey@mail.ru

**LUKYANENKO Alexander S.**

*Peter the Great St. Petersburg Polytechnic University*

29 Politechnicheskaya St., St. Petersburg, 195251, Russian Federation  
alex.lukyan@rambler.ru

## DETERMINING THE CONTACT FORCE OF AN AXIAL COLLISION OF AN ELASTIC ROD WITH A RIGID IMPACTOR

**A.K. Belyaev<sup>1,2,3</sup>, A.O. Shurpatov<sup>2</sup>, Ch.-Ch. Ma<sup>4</sup>**

<sup>1</sup>Institute for Problems of Mechanical Engineering of RAS, St. Petersburg, Russian Federation;

<sup>2</sup>Peter the Great St. Petersburg Polytechnic University, St. Petersburg, Russian Federation;

<sup>3</sup>St. Petersburg State University, St. Petersburg, Russian Federation;

<sup>4</sup>National Taiwan University, Taipei, Taiwan

The problem of axial impact of a rigid body on elastic rod is considered. The Semi-Analytical Method (SEM) and Finite Element Method (FEM) are applied to handle the problem. The SEM of solving the problem implies the quasi-static Hertz theory and numerical integration of obtained differential equations. The number of necessary degrees of freedom of the FEM solution is determined and numerical simulation is carried out. The time of contact interaction and dependence of the contact force on the contact time are calculated. The longitudinal wave propagation in the rod is investigated. The obtained results are compared with the data from natural experiments. An inverse dependence between impacting mass and the accuracy of both methods is discussed. The results of comparison confirm the appropriateness of both methods for solving the problem.

**Key words:** axial collision; contact force; finite element method

**Citation:** A.K. Belyaev, A.O. Shurpatov, Ch.-Ch. Ma, Determining the contact force of an axial collision of an elastic rod with a rigid impactor, St. Petersburg Polytechnical State University Journal. Physics and Mathematics. 11 (1) (2018) 102 – 108. DOI: 10.18721/JPM.11113

### Introduction

Solving problems of dynamics and stability of thin rods under longitudinal impact requires knowledge of the form and amplitude of the force in the contact zone [1 – 3]. This paper is dedicated to determining the contact force in the axial collision of a rod and an impactor using three fundamentally different approaches: the semi-analytical method (mathematical modeling), the finite element method, and an experiment. Comparing the results obtained by these approaches is particularly interesting, as this allows to assess whether each approach is correct and can be used in the future.

### Problem statement

An elastic rod with a length  $l$  is considered; one of the rod's ends is fixed (displacements and rotations are forbidden for all points

of the cross-section). An impactor of mass  $m$  approaches the free end of the rod at the initial time with the velocity  $V_0$ , causing a contact interaction in the system (Fig. 1). The gravity forces of the rod and the impactor are not taken into account.

In the general case, the force of elastic contact interaction arises as a result of mutual vibrations of colliding bodies and can be determined from the analysis of their combined dynamic strain.

The goals of the study are to find the time of contact interaction between the rod and the impactor, to construct the dependence of the arising contact force on time, and to experimentally verify the calculations.

### Semi-analytical method

Description of the mathematical model. The condition for contact between the bodies

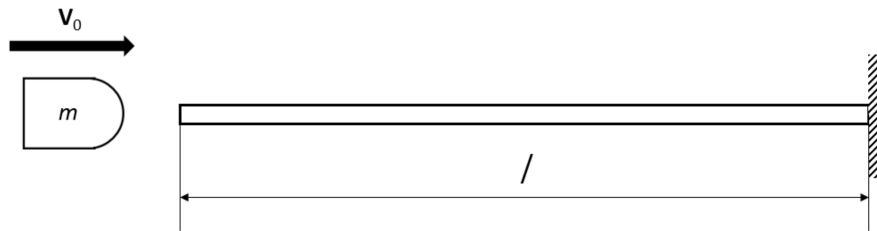


Fig. 1. Schematic for the problem statement (general case):  
 $l$  is the length of the elastic rod;  $m$  is the mass of the non-deformable impactor,  $\mathbf{V}_0$  is the vector of its initial velocity

is the coincidence of the coordinates of their contact points [4]:

$$v_0 t - \alpha - y_1 - y_2 = 0,$$

where  $\alpha$  is the linear convergence of the bodies due to contact deformations;  $y_1$  and  $y_2$  are the dynamic displacements of contact points of both bodies, caused by the contact force  $P(t)$  without taking into account local deformations;  $v_0$  is the initial velocity of the impactor.

As the contact area is small, we can neglect its mass. Then we are able to use Hertz's quasi-static contact theory, according to which the contact force  $P$  is related to the quantity  $\alpha$  by the dependence [5]:

$$P(\alpha) = k\alpha^{3/2},$$

Where  $k$  is the coefficient depending on the parameters of the contacting bodies.

In the case of the model under consideration, it has the form [6]:

$$k = \frac{2}{3(1-\mu^2)} E\sqrt{R},$$

where  $E$  and  $\mu$  are Young's modulus and Poisson's ratio, respectively (assuming that the rod and the impactor are made of the same material);  $R$  is the radius of the spherical profile of the impactor.

The displacements  $y_1$  and  $y_2$  can be expressed through the contact force, using the reaction of each of the colliding bodies to a unit impulse [7]:

$$y_1 = \int_0^t P(\theta) Y^{(1)}(t - \theta) d\theta,$$

$$y_2 = \int_0^t P(\theta) Y^{(2)}(t - \theta) d\theta,$$

where  $Y^{(1)}$ ,  $Y^{(2)}$  are the reactions to the unit impulse of the rod and impactor, respectively;  $t$  is the current time,  $\theta$  is the integration variable; the moment of contact of bodies is taken as the origin.

Substituting these expressions into the contact condition, we obtain an integral equation that determines the contact force:

$$\int_0^t P(\theta) Y(t - \theta) d\theta + [P(t) / k]^{2/3} = v_0 t,$$

where  $Y(t) = Y^{(1)}(t) + Y^{(2)}(t)$ .

Since the integral term of this equation depends on the values of the contact force at all times  $\theta$  preceding the one under consideration, with a sufficiently small integration step over the time  $\Delta t$ , we can neglect the change in the force in the integral sum over the interval

$$t - \Delta t \leq \theta \leq t.$$

In view of the above, the expression for determining the contact force can be written in the following form [8]:

$$P(t) = k[v_0 t - \int_0^{t-\Delta t} P(\theta) Y(t - \theta) d\theta - P(t - \Delta t) \int_0^{\Delta t} Y(\theta) d\theta]^{3/2}.$$

Thus, using a small step  $\Delta t$  with the help of numerical integration, we calculate the dependence of the contact force on time step by step. In this case, for the system under consideration, the reaction of the rod to a unit impulse is as follows [9]:

$$\text{with } 0 < t < \frac{2l}{a}$$

$$Y^{(1)}(t) = l^2 / [(2EFa)(at / l)^2];$$

with  $\frac{2l}{a} < t < \frac{4l}{a}$

$$Y^{(1)}(t) = l^2 / \{(2EFa)[8 - (4 - at/l)^2]\};$$

with  $\frac{4l}{a} < t < \frac{6l}{a}$

$$Y^{(1)}(t) = l^2 / \{(2EFa)[8 + (at/l - 4)^2]\}$$

and so on,

where  $a = \sqrt{\frac{E}{\rho}}$  is the speed of sound in the material of the rod.

Since this model does not consider the wave processes occurring in the impactor, its reaction to a unit impulse is determined by the following expression [10]:

$$Y^{(2)}(t) = \frac{t^3}{6m},$$

where  $m$  is the impactor mass.

The essence of the semi-analytic method consists in numerical integration of the equation obtained above for calculating the contact force [11].

Results of mathematical modeling. The dependence of the contact force on time was calculated by the semi-analytic method for systems with different parameters. It was obtained from these calculations that the contact force is a smooth time function which

has one to three maxima depending on the parameters.

An example of calculating the contact force with three maxima is shown in Fig. 2 (curve 1) and was obtained with the initial parameters of the system given in Table 1.

The rod and the spherical profile of the impactor were assumed to be made of steel with the characteristics also given in Table 1.

The results obtained were verified by finite element simulation of a system with identical parameters (see Table 1).

### Finite-element model

**Description of the model.** After studying the convergence of the finite element method, we have selected the model shown in Fig. 3. It includes about 300,000 knots and has about 1 million degrees of freedom. Since this problem involves investigating not only the contact interaction of the rod with the impactor but also the wave processes occurring in the rod itself [12], we decided not to condense the grid in the contact area. Thus, a uniform grid was used in the process of finite-element modeling.

The statement of the problem in this model is as follows.

The rod is made of linearly elastic material (as already noted above for the general model)

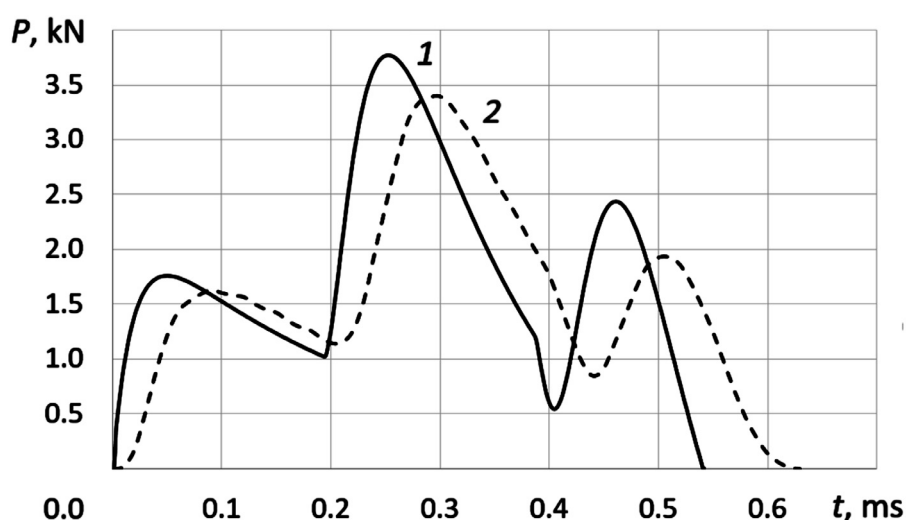


Fig. 2. Dependence of the contact force on time, obtained by the semi-analytic method (curve 1) and the finite element method (curve 2); the values of the initial parameters are given in Table 1

Table 1

Initial design and experimental parameters of the system

System element, material	Parameter	Notation	Unit	Value	
				Model	Experiment
Rod	Length	$l$	m	0.500	0.301
	Cross-section area	$S$	m <sup>2</sup>	$5.0 \cdot 10^{-5}$	$3.14 \cdot 10^{-6}$
Impactor	Mass	$M$	kg	0.5	0.13 – 8.46
	Spherical profile radius	$R$	m	0.01	1.58 – 6.36
	Initial velocity	$V_0$	m/s	1.0	0.3225
Steel	Young's modulus	$E$	N/m <sup>2</sup>	$2.1 \cdot 10^{11}$	$7.342 \cdot 10^{10}$
	Poisson's coefficient	$\mu$	—	0.30	0.34
	Density	$\rho$	kg/m <sup>3</sup>	7800.0	2696.6

Note: the initial calculated parameters for both models given in the Table are the ones deemed to be the most convenient by the results of the calculation

whose parameters are given in Table 1. One of the rod's ends is fixed, that is, both displacements and rotations are forbidden for all nodes. The opposite end of the rod is free (general model). In this problem, we assumed that gravity was absent, therefore, there is no curvature of the rod at the initial time and the rod is stationary. Unlike the rod, the impactor consists of two materials. Its front part is made of the same material as the rod (it is elastic), and the material of the rear part is perfectly rigid. This composition of the impactor was chosen for two reasons. Firstly, the materials in the contact area have to be identical to correctly compare the results with those obtained by the semi-analytical method [5]. Secondly, this

construction minimizes the influence of wave processes in the impactor on the model used [3]. Wave processes cannot occur in a perfectly rigid body, which allows to study only the wave processes that evolve directly in the elastic rod.

Displacement of the nodes of the perfectly rigid part of the impactor is only allowed along the axis of the rod, and all other displacements and rotations are forbidden. All the nodes of the impactor have a velocity directed along the axis to the free end of the rod at the initial time.

As already noted above, one of the goals of the study was to determine the dependence of the contact force on the impact time.

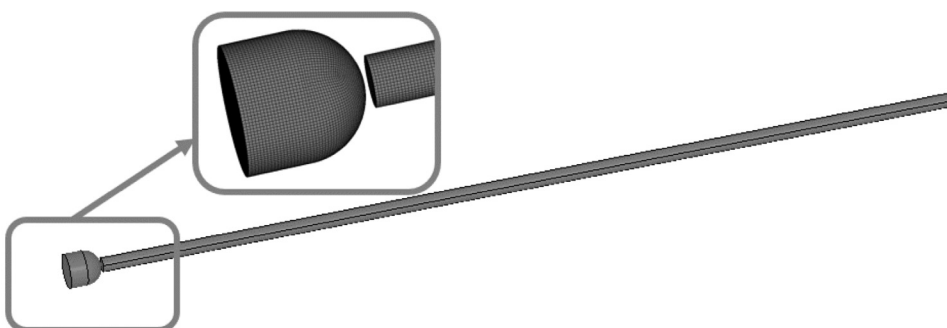


Fig. 3. Schematic of the finite-element model  
(an enlarged area of the contact between the rod and the impactor is additionally shown)



Results of finite-element modeling. This problem was modeled by the finite-element method with different parameters of both the rod and the impactor. The most noteworthy results were obtained for the initial parameters identical to those for a semi-analytical modeling method (see Table 1).

The obtained dependence of the contact force on time is shown in Fig. 2 (curve 2).

Depending on the input parameters, the number of maxima of the time function of the contact force can vary from one to three. It can be seen from the obtained results that in this case the graph has three local maxima.

Analysis of different results obtained during the simulation with different initial data indicates that the dependence of the contact force on the time under impact is a rather complex function that cannot be represented as simple functions such as, for example, the Heaviside function. In particular, analysis of dynamic loss of stability of a rod should include the possible forms of the function of the force applied to the end of the rod.

One of the advantages of the finite-element method over the semi-analytic method is that it is possible to determine the set of parameters at any time (for example, the values of displacements, deformations, stresses, etc.). This option makes it possible to focus closer on the wave processes evolving in the rod under impact, which ultimately determine the form of

the contact force. In particular, Fig. 4 shows the time dependence of the longitudinal displacement of the points of the cross-section located half the rod length away from the front end of the rod.

It can be seen that a superposition of waves propagating in the rod occurs. The method also makes it possible to compare the behavior of different points of the rod with the results of natural experiments.

### Comparison of the results obtained by two methods

Since these methods are based on different concepts and assumptions, it is particularly interesting to carry out comparative analysis of the simulation results. Fig. 2 shows such a comparison for the time dependences of the contact forces obtained by the semi-analytical and finite-element methods.

Comparing the obtained graphs, we can see the perfect qualitative agreement of their forms. Quantitative comparison of the calculated results reveals that the values of the contact time differ by 11 %, and the values of the local extrema of the functions by 9 %. Based on the simulation data, we can conclude that the results obtained by both methods are in good agreement, and that the contact force and contact time were determined correctly.

If we compare the obtained dependences in more detail, we can notice small oscillations

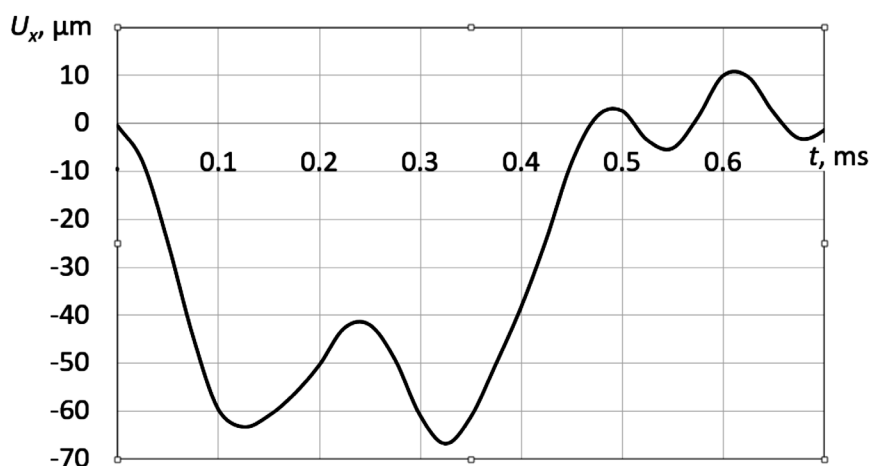


Fig. 4. Time dependence of the longitudinal displacement of the cross-section of the rod; the cross section is located half the rod length away from the front end of the rod (the result was obtained by finite element modeling)



on the curve obtained by the finite-element method, absent from the curve obtained by the semi-analytic method. These oscillations can be attributed to the influence of edge effects which the semi-analytic method does not take into account.

#### Comparison of the results of the natural experiment with the data of the two calculation methods

Natural experiments served to verify the semi-analytical and finite-element methods.

The natural experiment conducted at the National Taiwan University involved a cylinder with a radius of 10.0 mm and a length of 30.1 mm, made of a material whose parameters are given in Table 1.

One of the ends of the cylinder was fixed, and a steel impactor approached the second free end at the initial moment time at a speed of 0.3225 m/s (the impactor was ball-shaped). A piezoelectric film 28  $\mu\text{m}$  in thickness and  $7 \times 3$  mm in size, serving as a piezoelectric sensor, was attached to the free end of the rod. The principle of measuring the time of contact between the cylinder and the impactor was based on the piezoelectric effect; the time was measured depending on the mass of the impactor (Table 2).

A comparison of the results of finite-element simulation and semi-analytical calculation with the results of natural experiments is also given in Table 2.

It can be seen from the results given that the greatest error is observed for the finite-element method at intermediate values of the impactor mass. The error is minimal for the smallest and the largest of the selected masses.

A decrease in the error is observed for the semi-analytic method with increasing mass of the impactor. Thus, the minimal values of the impactor mass yield the greatest discrepancy between the results of the semi-analytic method and the results obtained in the natural experiment and by finite-element modeling. However, this discrepancy decreases with an increase in the mass of the impactor.

#### Conclusions

In this paper, we have used two fundamentally different methods (finite-element and semi-analytic) to study the dynamic process of an impact on a perfectly elastic rod in the longitudinal direction. In particular, the contact force and the interaction time have been determined. The wave processes occurring in the rod upon impact have also been studied.

The obtained results were in agreement, and it seemed logical to conduct a natural experiment to verify both methods. In addition, the approximation of the graphs makes it possible to use such functions to solve related problems. In particular, using approximated functions in studies on dynamic loss of rod stability can allow to correctly compare simulation with experimental results, since impact interaction is

Table 2

Comparison of the experimental results with the data obtained by the two calculation methods

Value of the impactor parameter		Time of the contact interaction, $\mu\text{s}$			Error of the method, %	
Diameter, m	Mass, g	Natural experiment	FEM	SEM	FEM	SEM
3.16	0.13	36.42	31.20	15.32	14.33	57.93
4.75	0.44	46.83	60.75	23.63	29.72	49.54
5.56	0.71	52.26	78.09	27.90	49.42	46.61
6.34	1.04	60.05	81.61	31.71	35.90	47.19
9.51	3.51	84.96	106.21	47.94	25.01	43.57
12.73	8.46	111.10	121.71	64.82	9.54	41.66

Abbreviations: FEM is the finite-element method, SEM is the semi-analytical method (mathematical modeling).

easier to carry out than, for example, step impacts. The latter are extremely popular in various model problems but using them in natural experiments is not possible yet.

The study was conducted within the framework of the Russian-Taiwanese grant of the Russian Foundation for Basic Research No. 16-51-52025 MHT\_a.

## REFERENCES

- [1] **A.K. Belyaev, N.F. Morozov, P.E. Tovstik, T.P. Tovstik**, Beating in the problem of longitudinal impact on a thin rod, *Mechanics of Solids*. 50 (4) (2015) 451–462.
- [2] **A.K. Belyaev, N.F. Morozov, P.E. Tovstik, T.P. Tovstik**, Parametric resonances in the problem of longitudinal impact on a thin rod, *Vestnik St. Petersburg University*. 3 (1) (2016) 53–67.
- [3] **A.K. Belyaev, Ch.-Ch. Ma, N.F. Morozov, P.E. Tovstik, T.P. Tovstik, A.O. Shurpatov**, Dynamics of rod under axial impact by a body, *Vestnik St. Petersburg University*. 4 (3) (2017) 310–317.
- [4] **V.L. Biderman**, *Teoriya mekhanicheskikh kolebaniy* [The theory of mechanical vibrations], Vysshaya shkola, Moscow, 1980.
- [5] **H.R. Hertz**, Über die Berührung fester elastischer Körper, *Journ. Reine Angew. Math. (Jour de Crelle)*. 92 (1881) 156–171.
- [6] **A.I. Lur'e**, *Teoriya uprugosti* [Theory of elasticity], Nauka, Moscow, 1970.
- [7] **S.P. Timoshenko**, *Kolebaniya v inženernom delye* [Vibrations in engineering], Nauka, Moscow, 1967.
- [8] **Ya.G. Panovko**, *Osnovy prikladnoy teorii kolebaniy i udara* [Fundamentals of applied theory of vibrations and shock], Politekhnik, Leningrad, 1990.
- [9] **E.V. Aleksandrov, V.B. Sokolinskiy**, *Prikladnaya teoriya i raschyoty udarnykh system* [Applied theory and calculations of shock systems], Nauka, Moscow, 1969.
- [10] **Ya.G. Panovko**, *Vvedeniye v teoriyu mekhanicheskogo udara* [Introduction to mechanical shock theory], Nauka, Moscow, 1977.
- [11] **A. Lyav**, *Matematicheskaya teoriya uprugosti* [Mathematical theory of elasticity], ONTI, Moscow, 1935.
- [12] **J.E. Sears**, On longitudinal impact of metal rods. Part 2, *Trans. Cambridge Phil. Soc.* 21 (1912) 49 – 106.
- [13] **S.D. Ponomarev, V.L. Biderman, K.K. Likharev, et al.**, *Raschyoty na prochnost v mashinostroyenii*, v 3 tt., Mashgiz, Moscow, 1956 – 1959. T. 3. Inertsionnyye nagruzki: Kolebaniya i udarnyye nagruzki. Vynoslivost, Ustoychivost [Strength calculations in mechanical engineering in 3 Vols, Vol. 3: Inertial loads: Vibrations and shock loads, Endurance, Resistance], Mashgiz, Moscow, 1959.

*Received 16.12.2016, accepted 13.11.2017.*

## THE AUTHORS

### **BELYAEV Alexander K.**

*Institute for Problems of Mechanical Engineering of RAS*  
61 Bolshoi Ave. V.Is., St. Petersburg, 199178, Russian Federation  
vice.ipme@gmail.com

### **SHURPATOV Anatoliy O.**

*Peter the Great St. Petersburg Polytechnic University*  
29 Politechnicheskaya St., St. Petersburg, 195251, Russian Federation  
a.shurpatov@gmail.com

### **MA Chin-Chin**

*National Taiwan University*  
No. 1, Section 4, Roosevelt Rd, Da'an District, Taipei City, 10617, Taiwan  
ccma@ntu.edu.tw